

---

Theses and Dissertations

---

Fall 2018

## Interactions of environmental and therapeutic particles with the airway microenvironment

Benjamin Michael King  
*University of Iowa*

Follow this and additional works at: <https://ir.uiowa.edu/etd>

 Part of the [Chemical Engineering Commons](#)

Copyright © 2018 Benjamin Michael King

This dissertation is available at Iowa Research Online: <https://ir.uiowa.edu/etd/6599>


---

### Recommended Citation

King, Benjamin Michael. "Interactions of environmental and therapeutic particles with the airway microenvironment." PhD (Doctor of Philosophy) thesis, University of Iowa, 2018.  
<https://doi.org/10.17077/etd.ds1a-z7ui>

---

Follow this and additional works at: <https://ir.uiowa.edu/etd>

 Part of the [Chemical Engineering Commons](#)

INTERACTIONS OF ENVIRONMENTAL AND THERAPEUTIC PARTICLES WITH  
THE AIRWAY MICROENVIRONMENT

by

Benjamin Michael King

A thesis submitted in partial fulfillment  
of the requirements for the Doctor of Philosophy  
degree in Chemical and Biochemical Engineering in the  
Graduate College of  
The University of Iowa

December 2018

Thesis Supervisor: Associate Professor Jennifer Fiegel

Copyright by  
Benjamin Michael King  
2018  
All Rights Reserved

Graduate College  
The University of Iowa  
Iowa City, Iowa

CERTIFICATE OF APPROVAL

---

PH.D. THESIS

---

This is to certify that the Ph.D. thesis of

Benjamin Michael King

has been approved by the Examining Committee for  
the thesis requirement for the Doctor of Philosophy degree  
in Chemical and Biochemical Engineering at the December 2018 graduation.

Thesis Committee:

---

Jennifer Fiegel, Thesis Supervisor

---

Eric Nuxoll

---

Julie Jessop

---

Charles Stanier

---

David Roman

To Mrs. F. H. Alley. You had so much love and faith in all of your great grandchildren and in the value of education.

It is good to love many things, for therein lies the true strength, and whoever loves much performs much, and can accomplish much, and what is done in love is well done.

Vincent van Gough

## Acknowledgements

First and foremost, I would like to thank Dr. Jennifer Fiegel. Throughout this process she was my greatest advocate, which also made her my harshest critic. She gave me a lot of freedom to take ownership of the direction of my research in this time. In this freedom she challenged me to think, to defend my ideas, and to go where the data leads. I will always be grateful for our many discussions that tended to move past research and into life advice. She has constantly challenged me to improve myself as a person as well as a scientist.

I would also like to thank all of my lab-mates throughout my time at Iowa. Special thanks to Dr. Mai Tu for training me on cell culture and helping me get started in the lab. Thanks to Dr. Dan Schenck, Dr. Sachin Gharse, Bharath kumar Gowdampolly, and Michael Crain-Zamora for your solidarity throughout this shared process. The mashup of graduate students from pharmaceuticals and chemical engineering made the Fiegel lab a wonderful place to work and study drug delivery. Working with all of these people highlighted the value of interdisciplinary research.

Throughout this research I was fortunate to have help from many undergraduate researchers whom I have had the pleasure of watching grow as scientists. Thanks to Alex Bess, Morgan Timm, Ojas Pradhan, Christine Czarnecki, Killian Tracey, Sarah Chou, Michael Leyden, Kevin Hillshafer, Kolten Hagens, Mohammed Moumen, Gil Gonzales, and Collin Waldron. Many of them contributed directly to this work, but I had the pleasure of working with all of them on various projects in my time at Iowa.

I would like to acknowledge the assistance of the Central Microscopy Research Facilities at The University of Iowa for their assistance with electron microscopy. Special

thanks to Joun “Sylvia” Lee and Chantal Allamargot for their assistance with sample preparation and analysis. I would also like to acknowledge the State Hygienic Lab at the University of Iowa for their assistance in quantifying uptake of metal nanoparticles and for trace metals analysis. I would like to thank Brian Wels specifically for his assistance in this.

The research presented in chapter 2 was partially supported by the University of Iowa Environmental Health Sciences Research Center (*NIH P30 ES005605*). I would like to acknowledge the collaborators and coauthors of that work: Nathan J. Janecek, Nathan Bryngleson, Andrea Adamcakova-Dodd, Traci Lersch, Kristin Bunker, Gary Casuccio, Peter S. Thorne, Charles O. Stanier, and Jennifer Fiegel. We all thank William H. Brune of Penn State University for use of his OFR system for this project.

The research presented in chapter 3 was performed in collaboration with David Roman, Joseph O’Brien, Michael Crain-Zamora, and Jennifer Fiegel. Thanks to David Roman and Joseph O’Brien for their expertise in measuring receptor expression. Thanks to Michael Crain-Zamora for his assistance with studying bacterial infectivity.

The office of the vice president of research at the University of Iowa and the department of chemical and biochemical engineering also provided funding that helped with this research. I am thankful to them for their support. There were also many collaborators and people who are unnamed but helped out in big and small ways that are too numerous to count.

Finally, I would like to thank all of the friends and family who have helped me throughout this process. Special thanks to my wife Caitlin. She watched me write late



into the nights and throughout the weekends. She listened to me talk about my data, let me practice presenting, and made sure I stopped to eat from time to time. Thanks to my parents for providing endless encouragement, and thanks to my fellow graduate students for going through this alongside me.

## Abstract

Particles that deposit in the respiratory airways can come from many sources, such as environmental pollution, particles created in the workplace, and inhalers that are designed to deliver medicines to the lungs. Once these particles deposit in the respiratory airways, they can interact in a variety of ways. Some particles are toxic and can cause damage to lung tissues, others may have little to no effect on health, and some may provide some benefit or therapy. Once particles land in the respiratory airways, the interactions they have with proteins can impact where they go and how they behave.

This thesis explores how particles that are inhaled may impact health through toxicity to lung cells. Aerosols produced from photooxidation of decamethylcyclopentasiloxane, an ingredient common in personal care products, were exposed to lung cells using an air-liquid interface exposure system to assess if these aerosols impact lung cell health. No significant impacts on lung cell health were observed. Copper oxide, a component of cigarette smoke, urban particulate matter, and e-cigarette vapor, was assessed for its role in lung disease. Copper oxide nanoparticles were exposed to lung cells, and their viability, expression of a platelet activating factor receptor (PAFR), and susceptibility to infection with a pneumonia-causing bacterium (*S. pneumoniae*) were measured. Copper oxide nanoparticles were found to be toxic to lung cells. At some doses, increases in PAFR were observed, but no clear differences in susceptibility to bacterial infection were observed. This research improves knowledge of how inhaled materials can impact health, providing insight into how particles from human-derived sources affect the lungs.

This thesis further explores how particles behave in the thin layer of fluid that covers the respiratory epithelium. This fluid contains a complex mixture of proteins, and this work aims to identify some of the ways these proteins interact with particles and influence behavior. This was accomplished by first investigating how individual proteins from this fluid interact with particles. Particle behavior was studied after exposure to these proteins, as well as the lung cell responses to the particles before and after interaction with individual proteins. These lung proteins were found to induce aggregation, significantly alter surface charge, and reduce cell uptake of particles. After studying how individual proteins might specifically affect particle behavior, particles were exposed to bronchoalveolar lavage fluid (BALF), a diluted lung fluid collected by rinsing lungs with saline. Particle responses to proteins in this fluid were compared to those in serum, a protein-rich blood extract. These studies identified differences in how various surface-functionalized polystyrene particles aggregated in BALF compared to serum. When particles were exposed to serum or BALF, they tended to be less likely to associate with lung cells. With some particle types studied, there were significant differences in how much BALF or serum reduced cell attachment and uptake. In addition to demonstrating that lung fluids impact particle behavior in a manner that differs from serum, a method was developed to increase the concentration of the proteins in BALF to partially undo the dilution that occurs during collection. After studying how protein adsorption can cause aggregation, cover up particle surfaces, and reduce attachment and uptake by lung cells, a polymer coating was synthesized to reduce particle interactions with these proteins and assist in stabilizing particles in lung fluids. This coating was tested in both BALF and serum to demonstrate its general utility at reducing undesired

interactions with proteins in biological fluids and was found to enhance particle stability in lung fluids as well as saline. This research enhances understanding of how particles behave in the respiratory airways, providing tools to further study how particles behave in lung fluids and demonstrating a polymer coating that is useful in this environment.

## Public Abstract

The first portion of this thesis investigates the effects of particles on lung cell health. Particles that are formed after a common personal care product ingredient reacts in the atmosphere were exposed to lung cells to study if they are toxic. These particles were not found to be toxic. Copper oxide, a chemical found in cigarette smoke and pollution, was also studied in lung cells. Particles made of copper oxide were toxic to lung cells, and they caused cells to produce more of a protein on their surface. This protein can be used by bacteria to attach to lung cells to cause infections. Bacteria were exposed to lung cells after copper oxide particles, and no significant increase in bacterial infection was observed.

The latter portion of this thesis investigates how proteins in lung fluid interact with particles and affect how they behave. Particles were exposed to proteins common in lung fluid, and their interactions measured. These individual proteins caused particles to stick together into clumps, changed the electrostatic charge on particles, and decreased uptake by lung cells. Particles were also exposed to a model lung fluid and a blood extract, and exposure to these fluids also caused particles to clump, changed the electrostatic charge on particles, and decreased uptake by lung cells. Finally, a polymer coating for particles was designed and tested that keeps proteins from sticking, reduces clumping, and does not interfere with particle uptake by lung cells. This research improves our understanding of inhaled particles, provides tools to further explore this field, and demonstrates a polymer that is useful in this space.

## Table of Contents

List of Tables.....	xvi
List of Figures .....	xvii
1 Introduction .....	1
1.1 Lung Disease.....	1
1.2 Structure and Function of the Airways .....	3
1.3 Particle Deposition in the Respiratory Airways.....	6
1.3.1 Particle Interactions After Deposition in the Airways.....	8
1.3.2 Factors That Influence Particle Behavior .....	8
1.3.3 Adsorption of Components from Blood onto Particles.....	12
1.3.4 Proteins Impact Particle Behavior in Biological Systems .....	13
1.3.5 Differences Between Serum and Lung Lining Fluid .....	19
1.4 Mitigation of Protein Interactions to Control Particle Behavior.....	20
1.5 Objectives .....	23
2 Lung Cell Exposure to Secondary Photochemical Aerosols Generated from OH Oxidation of Cyclic Siloxanes .....	27
2.1 Introduction.....	27
2.2 Materials and Methods.....	29
2.2.1 Aerosol Generation and Characterization.....	30
2.2.2 Cell Culture Preparation .....	35
2.2.3 Cell Exposures .....	35
2.2.4 Cell Responses to Oxidized D5 Aerosols and Gaseous Products.....	37
2.3 Results and Discussion .....	38
2.3.1 Exposure Characterization .....	38
2.3.2 Cell Responses to Oxidized D5 Aerosols and Gaseous Products.....	46
2.4 Conclusions.....	48
3 CuO Nanoparticle Exposure Reduces Lung Cell Viability and Upregulates PAFR.....	50

3.1	Introduction.....	50
3.2	Materials and Methods.....	52
3.2.1	Particle Preparation.....	52
3.2.2	Particle Imaging with TEM .....	53
3.2.3	Cell Culture Preparation .....	54
3.2.4	Cell Exposure to Nanoparticles .....	55
3.2.5	CuO Uptake Measurement.....	55
3.2.6	Cell Viability Analysis.....	57
3.2.7	Evaluation of PAFR Expression .....	58
3.2.8	CuO Effects on Cell Susceptibility to Infection .....	59
3.2.9	CuO Effect on Bacterial Viability.....	60
3.3	Results.....	61
3.3.1	Particle Imaging with TEM .....	61
3.3.2	Cell Viability.....	62
3.3.3	Correlation Between CuO Uptake and Cell Viability.....	63
3.3.4	Evaluation of Infectivity due to PAFR Upregulation .....	64
3.3.5	CuO Effect on Bacterial Viability.....	66
3.4	Discussion.....	66
3.5	Conclusions.....	68
4	Proteins Found in Lung Fluid Reduce Particle Stability and Uptake by Lung Cells.....	68
4.1	Introduction.....	68
4.2	Materials and Methods.....	73
4.2.1	Preparation of Protein-Coated Polystyrene Particles.....	73
4.2.2	Measurement of Protein-Coated Particle Uptake Using Flow Cytometry .....	74

4.2.3	Preparation of Protein-Coated Gold Particles.....	75
4.2.4	Hydrodynamic Size and Zeta Potential Measurements to Study Particle Behavior.....	76
4.2.5	Measurement of Adsorbed Protein Using the BCA Assay.....	77
4.3	Results and Discussion .....	77
4.3.1	Measuring Suspension Properties and Cell Responses to Coated Polystyrene Particles.....	77
4.3.2	Protein Interactions with Gold at Varying pH .....	83
4.3.3	DLVO Theory.....	91
4.4	Conclusions.....	95
5	Reconstitution of BALF as a Model to Study Inhaled Particle Behavior .....	98
5.1	Introduction.....	98
5.2	Materials and Methods.....	100
5.2.1	Concentration of BALF .....	100
5.2.2	Effects of Serum and rBALF Exposure on Particle Behavior .....	102
5.2.3	Flow Cytometry to Measure Coated Particle Uptake .....	104
5.3	Results.....	108
5.3.1	Effects of Serum and rBALF Exposure on Particle Behavior .....	108
5.3.2	Flow Cytometry to Measure Coated Particle Uptake .....	115
5.4	Discussion.....	117
5.4.1	Proteins in Serum and Lung Lavage Fluid Impact Particle Stability.....	117
5.4.2	Surface Chemistry Influences Cell Response More Than Fluid Composition.....	117
5.5	Conclusions.....	120
6	Zwitterionic pMPC Synthesized by Photoinitiated RAFT Polymerization Stabilizes Particles in BALF and Serum.....	121
6.1	Introduction.....	121
6.2	Materials and Methods.....	125



6.2.1	Polymer Design and Synthesis.....	125
6.2.2	Polymer Characterization.....	129
6.2.3	Gold Particle Synthesis.....	130
6.2.4	Polymer SAM Coating onto Gold Nanoparticles .....	132
6.2.5	Particle Characterization.....	133
6.2.6	Reconstitution of BALF.....	134
6.2.7	Protein Adsorption to Gold Nanoparticles.....	135
6.2.8	Cell Responses to Coated and Uncoated Gold Nanoparticles .....	136
6.3	Results.....	138
6.3.1	Polymer Characterization.....	138
6.3.2	Particle Characterization.....	142
6.3.3	Protein Adsorption to Gold Nanoparticles.....	151
6.3.4	DLVO Theory.....	153
6.3.5	Cell Responses to Coated and Uncoated Gold Nanoparticles .....	159
6.4	Discussion.....	162
6.5	Conclusion .....	164
7	Conclusions and Future Directions.....	166
7.1	Conclusions.....	166
7.2	Future Directions .....	170
7.2.1	Aerosols Produced Via Atmospheric Photooxidation of cVMS.....	170
7.2.2	Copper Oxide Nanoparticle Impacts on Lung Health.....	171
7.2.3	Impacts of Lung-Abundant Proteins on Particle Behavior.....	171
7.2.4	Reconstituted BALF to Study Inhaled Particles .....	172
7.2.5	pMPC-Coatings for Drug Delivery in the Lungs.....	173
	Appendix .....	175

A.1 Flow Cytometry Data.....	175
References .....	179

## List of Tables

Table 1.1. Review of studies investigating the adsorption of one to two proteins at a time to the surfaces of various particles, documenting the proteins and the techniques used to quantify adsorption. ....	17
Table 3.1 Approach to dilution of standards and samples to compensate for higher acid concentration in samples. ....	56
Table 3.2. Instrument settings for ICP-MS.....	57
Table 4.1. Composition data for proteins based on Uniprot sequences, <sup>185</sup> and the average zeta potential for gold particles coated with each protein. ....	87
Table 4.2. Constants for each protein used in DLVO calculations. * denotes calculated based on fit of MW versus occupied surface area from data in Cantarero et al. <sup>191</sup> † denotes generic protein Hamaker constant. <sup>31</sup> .....	93
Table 5.1. Manufacturer information for polystyrene particles used in protein-interaction studies. ....	103
Table 6.1 Steps in the synthesis of 100 nm gold nanoparticles with calculations of gold mass and number of particles remaining in the suspension at each step. Volumes are approximate as water is lost as vapor throughout the reaction. Concentration is estimated based on injected Au mass and particle size at each stage. ....	132
Table 6.2 Approach to dilution of standards and samples to compensate for higher acid concentration in samples. ....	137
Table 6.3 Instrument settings for the ICP-MS.....	138
Table 6.4. Definitions and units of symbols used in calculating electrostatic repulsive energy.....	155
Table 6.5. Definitions and values for constants used to calculate inverse Debye length.....	155

## List of Figures

Figure 1.1. Anatomy of the human respiratory system. Reprinted with permission. <sup>20</sup> .....	5
Figure 1.2. Illustration of deposition patterns for particles of varying aerodynamic diameter in different regions of the lungs. Reprinted with permission. <sup>16</sup> .....	7
Figure 1.3 Illustration of interparticle forces that influence the stability of particles in suspension. Forces include a) Van der Waals attractive forces, b) electric double layer repulsion, and c) steric repulsion. These components all contribute to the d) potential energies of particles across varying interparticle distances. Reproduced under the Creative Commons Attribution 3.0 Unported License. <sup>36</sup> – Published by The Royal Society of Chemistry.....	10
Figure 1.4 Illustration of protein corona formation around a nanoparticle in an equilibrium process. Reprinted with permission. <sup>53</sup> .....	12
Figure 1.5. Relative abundance of 31 common proteins in BALF (blue) and plasma (red). Y-axis represents the rank position among these proteins with 31 having the highest relative abundance in the respective fluid and 1 having the lowest relative abundance. Reprinted with permission. <sup>26</sup> .....	20
Figure 1.6. Zwitterionic functional groups and one zwitterated siloxane. Reprinted with permission. <sup>92</sup> Further permissions related to this material should be directed to ACS.....	22
Figure 2.1 Flow diagram of the experimental setup for generation of aerosols in the OFR and cell exposures. Incoming flowrate and RH, chamber pressure, ring flowrate, and downstream flowrate were measured at points 1, 2, 3, and 4 respectively on the diagram. Short dashed lines in the diagram indicate Teflon tubing, long dashed represent copper tubing, and solid lines represent conductive silicon tubing.....	30
Figure 2.2 Characterization of aerosol particles generated from the OFR. (a) Representative plot of mass concentration throughout a single experiment (from SMPS). (b) Average concentrations (from SMPS) of aerosol particles formed under different reactor conditions (error bars are equal to the standard deviation of the individual concentrations measured every 135 s during each experiment). .....	40
Figure 2.3 SEM and TEM images establishing particle morphology of the generated particles. SEM images of TPS samples are shown for (a) bright field and (b) secondary electron image, while TEM images of passive TEM samples are shown in (c) and (d). Panels (c) and (d) contrast two types of particles imaged by TEM – some had distinct boundaries, while others had indistinct borders. ....	41
Figure 2.4 Intercomparison of particle size distributions and size-resolved concentrations from experiment 12, which included SMPS, TPS sampling, and	

passive TEM sampling. The SMPS diameters are electrical mobility diameters; the SMPS (agglomerates) diameters are equivalent volume diameters of the agglomerate converted to number concentration with an assumed primary particle size of 25 nm; the TPS diameters are projected area diameters of agglomerates; the passive TEM diameters are projected area diameter of primary particles (not agglomerates). The passive TEM size distribution has been normalized to a maximum of  $6 \times 10^5 \text{ cm}^{-3}$ . ..... 43

Figure 2.5 EDS analysis of the chemical composition of particles from (a) TPS sample of Vitrocell exhaust and (b) passive TEM sample of aerosols deposited in Vitrocell wells. (a) EDS analysis of a particle agglomerate (see inset) collected during TPS sampling is shown in red and background grid is shown in blue. (b) Original electron micrograph illustrating the EDS sample region selection (blue crosshair) and comparative background region (orange crosshair) (bar = 50  $\mu\text{m}$ ); element mapping of silicon, oxygen, and carbon (bar = 50  $\mu\text{m}$ ); and EDS spectra of a particle obtained by passive TEM sampling confirmed that deposited aerosols are derived from siloxanes. .... 45

Figure 2.6 (a) Relative viability of cells exposed to filtered gases from the OFR (n=4, 5 replicates each), or OFR-generated aerosols (n=3, 5 replicates each) compared to no exposure and SDS controls (\*\*\*)  $p < 0.001$ . (b) Effect of dose dependent aerosol-exposure on relative viability of cells. Error bars=SD. .... 47

Figure 2.7 Concentration of IL-6, a cytokine marker for inflammation, in supernatants collected from A549 cells after exposure to aerosols (n=3, 5 replicates each) or gases (n=4, 5 replicates each) generated in the OFR reactor. Error bars=SD. .... 48

Figure 3.1 TEM Micrographs of CuO nanoparticles. A) A low-magnification image showing a variety of agglomerate shapes and sizes. b) A high-magnification image of smaller agglomerates with small primary particles distinguishable. .... 62

Figure 3.2: A549 cells imaged at 200x magnification after exposure to varying concentrations of CuO nanoparticles. A) No exposure, enlarged for reference. The remaining images correspond to cells exposed to B) 0.01 mg/mL C) 0.02 mg/mL D) 0.1 mg/mL E) 0.2 mg/mL F) 1 mg/mL G) 2 mg/mL of copper oxide nanoparticles. .... 63

Figure 3.3: a) Cell viability was measured as a response to applied dose (n=3, 4 replicates each). b) Cu mass observed in each sample as it relates to applied CuO nanoparticle dose (n=1, 3 replicates). Points with no error bars indicates that error bars were smaller than symbols. Error bars=SD. .... 64

Figure 3.4 a) Analysis of PAFR content (n=1, 3 replicates) and b) number of colony-forming bacteria attached to A549 cells exposed to varying doses of CuO nanoparticles (n=2, 3 replicates each). Error bars=SD. .... 65

Figure 3.5. Optical density of *S. pneumoniae* grown at various CuO doses over the course of 3h. Error bars=SD. .... 66

Figure 4.1 Size measurements for a) 200 nm and b) 1 $\mu$ m polystyrene particles exposed to buffers and proteins. Zeta potentials were similarly measured for c) 200 nm and d) 1 $\mu$ m particles (*= p<0.05, **p<0.01, ***p<0.001). n=1, replicates of 2. Error bars=SD. ....	79
Figure 4.2. Flow cytometry measurements of cell uptake of fluorescent a) 200 nm and b) 1 $\mu$ m polystyrene identifying the percentage of cells measured that were positive for fluorescence (*= p<0.05, ***p<0.001).n=1, replicates of 3. Error bars=SD.....	80
Figure 4.3. DLS was used to measure the hydrodynamic diameter of gold nanoparticles exposed to a) 1 mg/mL or b) 2 mg/mL of protein at varying pH. Zeta potentials were also measured for gold nanoparticles exposed to c) 1 mg/mL or d) 2 mg/mL of protein at varying pH. Using the BCA Assay, the mass of protein adsorbed to gold nanoparticles from solutions at e) 1 mg/mL and f) 2mg/mL protein was determined (ND=No Data). † denotes isoelectric point. n=1. Error bars=SD of multiple measurements. ....	86
Figure 4.4. Gold nanoparticles in buffers of varying pH. The clear tubes from left to right are saline at pH 4.4, 5.0, 5.4, 6.5, 8.7, and 11.0 respectively, and the far-right tube is gold in 2 mM sodium citrate. The clear liquids contain small black flecks. Gold in saline at pH 6.4 (lower left) and gold in 2 mM citrate (lower right) have been enlarged to illustrate visible aggregate formation (small black particles) versus dispersed gold nanoparticles (red/pink liquid).....	89
Figure 4.5. Classic DLVO theory was used to compare interaction energies of 100 nm gold particles in 2 mM sodium citrate and normal saline (154 mM sodium chloride).....	92
Figure 4.6. DLVO theory, Extended DLVO theory, and Extended DLVO theory with hydration were used to model attractive and repulsive energies between gold nanoparticles exposed to a) BSA, b) IgG, c) lactoferrin, and d) lysozyme. ....	94
Figure 5.1. Sample gating defined for a-c) yellow-green fluorescence using untreated A549 cells. Gate validation with exclusion of d-f) 200 nm PPS, g-i) 200 nm CML, and j-l) 200 nm APS particles in the absence of cells.....	107
Figure 5.2. Sample gating defined for a-c) red fluorescence using untreated A549 cells. Gate validation with exclusion of d-f) 500 nm CML particles in the absence of cells. ....	108
Figure 5.3. DLS measurements of a) 200 nm and b) 500 nm PPS particles after exposure to serum, rBALF, and BSA. Surface charge measurements of c) 200 nm PPS particles and d) 500 nm PPS particles exposed to serum and rBALF. e) Measurements of the mass of protein adsorbed to the surface of 200 nm and 500 nm PPS particles exposed to serum and rBALF (***p<0.001). n=1, 3 replicates. Error Bars=SD.....	110

Figure 5.4. DLS measurements of APS particles of a) 200 nm and b) 500 nm primary particle diameter exposed to serum and rBALF. Surface charge measurements of c) 200 nm and d) 500 nm APS particles exposed to serum and rBALF. e) Measure of the mass of protein adsorbed to the surface of 200 nm and 500 nm APS particles exposed to serum and rBALF (* p<0.05, **p<0.01, ***p<0.001). n=1, 3 replicates. Error bars=SD. ....	112
Figure 5.5. DLS measurements of CML particles of a) 200 nm and b) 500 nm primary particle diameter exposed to serum and rBALF. Zeta potential measurements of c) 200 nm and d) 500 nm CML particles exposed to serum and rBALF. e) Measure of the mass of protein adsorbed to the surface of 200 nm and 500 nm CML particles exposed to serum and rBALF (**p<0.01, ***p<0.001). n=1, 3 replicates. Error Bars=SD.....	115
Figure 5.6. Measurement of A549 cell association with fluorescent a) 200 nm PPS (n=1, 4 replicates), b) 200 nm APS (n=1, 4 replicates), c) 200 nm CML (n=1, 4 replicates), or d) 500 nm CML (n=1, 3 replicates) (*p<0.05, ***p<0.001). Error Bars=SD.....	116
Figure 6.1. Synthesis scheme for the photoinitiated polymerization of MPC in the presence of a trithiocarbonate RAFT agent using I2959 as the photoinitiator. ....	127
Figure 6.2. Synthesis scheme for the photoinitiated polymerization of MPC in the presence of a trithiocarbonate RAFT agent using I651 as the photoinitiator. ....	128
Figure 6.3. NMR spectra of a) MPC monomer before polymerization (taken at 300 MHz) and b) pMPC after polymerization (taken at 500 MHz). ....	140
Figure 6.4. Linear regression of log(M <sub>n</sub> ) for PEG standards.....	141
Figure 6.5. Representative GPC data for a) I651-cured pMPC and b) I2959-cured pMPC.....	142
Figure 6.6. Histogram of primary particle diameters determined from ImageJ analysis of TEM images. (n=253) .....	143
Figure 6.7. TEM micrographs of gold nanoparticles with a) no coating, b) pMPC coating 30:1 mass ratio. ....	143
Figure 6.8. Representative a) low-magnification and c) high-magnification TEM micrographs gold nanoparticles. Similar b) low-magnification and d) high-magnification micrographs were taken after coating with 6:1 mass ratio pMPC SAMs.....	145
Figure 6.9. Distributions of hydrodynamic diameters for a) gold and, b) 30:1 pMPC-coated gold exposed to serum and d) gold and e) 30:1 pMPC-coated gold exposed to BALF. ....	146

Figure 6.10. Zeta potential measurements for uncoated gold nanoparticles and gold nanoparticles coated with 30:1 pMPC, before and after exposure to a) serum and b) BALF. n=1, 3 replicates. Error bars=SD. ....	147
Figure 6.11. Distributions of hydrodynamic diameters of a) gold and b) 6:1 pMPC-coated gold nanoparticles exposed serum obtained by DLS. ....	150
Figure 6.12. Zeta potential measurements for pMPC-coated and uncoated gold nanoparticles exposed to a) serum and b) BALF. n=1, 3 replicates. Error bars=SD.....	151
Figure 6.13. Measurements of a) serum and b) BALF proteins adsorbed to 30:1 pMPC and uncoated gold nanoparticles using the BCA Assay. n=1, 3 replicates. Error bars=SD. ....	152
Figure 6.14. Measurements of serum proteins adsorbed to gold nanoparticles and 6:1 mass ratio pMPC-coated gold nanoparticles synthesized with either I2959 or I651 as the photoinitiator. * denotes that no measurable protein adsorption occurred in this dataset. (***) $p > 0.001$ n=1, 2 replicates. Error bars=SD. ....	153
Figure 6.15. Monomer structure of 3-[dimethyl(2-methacryloyloxyethyl)ammonium] propanesulfonate .....	158
Figure 6.16. Comparison of classic DLVO, Coated DLVO, and Coated DLVO+Hydration models for 100 nm gold nanoparticles in saline.....	159
Figure 6.17. Measurement of the toxicity of the various components that may be present in coated gold nanoparticle suspensions exposed to cells. Gold, RAFT agent, I-2959, and pMPC 2959: n=4, 3 replicates. MPC: n=4, 4 replicates. pMPC 651 and pMPC 651-coated gold: n=1, 3 replicates. Error Bars=SD. ....	160
Figure 6.18. ICP-MS measurement of gold nanoparticle uptake in A549 cells with and without coating after exposure to a) serum or b) BALF. c) comparison of uptake of gold nanoparticles with and without pMPC I2959 coating. n=1, 3 replicates. ....	161
Figure 6.19. Illustration of observed differences between a) settled stable particles and b) aggregates observed during analysis and exposure to proteins. ....	164
Figure A.1 Flow cytometry data for a-c) untreated, d-f) serum-treated, and g-i) BALF-treated 200 nm PPS particles exposed to A549 cells. ....	175
Figure A.2. Flow cytometry data for a-c) untreated, d-f) serum-treated, and g-i) BALF-treated 200 nm CML particles exposed to A549 cells. ....	176
Figure A.3. Flow cytometry data for a-c) untreated, d-f) serum-treated, and g-i) BALF-treated 200 nm APS particles exposed to A549 cells.....	177



Figure A.4. Flow cytometry data for a-c) untreated, d-f) serum-treated, and g-i) BALF-treated 500 nm CML particles exposed to A549 cells. .... 178

## 1 Introduction

### 1.2 Lung Disease

Diseases of the respiratory system account for a large fraction of the global burden of disease, with prevalence totaling over 500 million incidents per year collectively (including COPD, asthma, respiratory infections, and lung cancers).<sup>1,2</sup> This burden is increasing as the population increases, industrialization reduces air quality, and bacterial infections become more difficult to treat due to resistance. To better manage this increasing disease burden, it is critical to better understand how inhaled particles impact lung health, interact in the lung microenvironment, and interface with lung cells. Air is full of small particles that enter the airways during normal breathing. Many features of the airways are adapted to respond to this constant flux of foreign material into the body from both natural sources, such as pollen and dust, and human-derived sources, such as pollution or medicines.

Particles from environmental and industrial sources that end up in the lungs have been found to cause a variety of diseases. The World Health Organization has broadly identified impacts of urban particulate matter on lung health in humans as ranging from subclinical irritation to mortality.<sup>3</sup> Some common examples of exposures in the workplace that have led to significant disease are nanorods from asbestos leading to asbestosis and mesothelioma<sup>4</sup>, coal and silica dust leading to pneumoconiosis (commonly referred to as “black lung” and “silicosis” respectively)<sup>5</sup>, and artificial flavorings in the food industry leading to bronchiolitis obliterans (commonly referred to as “popcorn lung”)<sup>6</sup>. Smoking cigarettes is well-known to be associated with a number of diseases, both in the lungs and affecting various other organs.

In addition to directly causing disease, some particles have been identified to increase susceptibility to disease. Recent in vitro studies have found that the platelet-activating factor receptor, PAFR is upregulated in human lung cells after exposure to urban particulate matter (PM), cigarette smoke, and e-cigarette vapor.<sup>7-9</sup> A variety of respiratory bacterial pathogens, such as *Streptococcus pneumoniae*, non-typeable *Haemophilus influenzae*, and *Acinetobacter baumannii*, invade cells in the respiratory airways by binding to the platelet-activating factor receptor (PAFR) on the cell surface. The Grigg research group has been investigating mechanisms whereby inhaled particles lead to increased susceptibility to respiratory infections. Their studies involving urban PM<sub>10</sub> and PM<sub>2.5</sub><sup>10</sup>, cigarette smoke<sup>11</sup>, and e-cigarette vapor<sup>9</sup> all found that exposure to any of these particles upregulates PAFR expression in respiratory epithelial cells and increases susceptibility to infection with *S. pneumoniae*. They have further demonstrated that blocking PAFR with a competitive antagonist mitigates the increased susceptibility observed after particle exposure.<sup>10, 11</sup>

Inhaled particles can also play a role in the management and treatment of diseases. A variety of inhalable treatments for asthma are on the market, which allow delivery of drugs directly to the site of disease. This includes therapies that are taken daily for symptom management and rescue inhalers that are used during asthma attacks. Inhalable antibiotic therapies for the treatment of chronic pulmonary infections have received some attention in the medical and pharmaceutical industries. Some chronic diseases of the lungs, such as cystic fibrosis (CF), chronic obstructive pulmonary disorder (COPD), and non-CF bronchiectasis create environments in the lungs that are susceptible to infections. When infections occur in individuals with these disorders, they are more

difficult to treat than in normal individuals. Inhalable antibiotic therapies offer the opportunity to provide higher local concentrations of antibiotics at the site of infection versus a systemic route such as oral or injectable. Inhalable tobramycin for treatment of bacterial lung infections, for example, has been available since 1997.<sup>12</sup>

Despite the existence of effective and approved inhalable therapies such as these, there are gaps in our understanding of how inhaled drug particles behave in the lung space. A recent example of this can be found in the development of an inhalable formulation of ciprofloxacin to treat bacterial infections in the lungs. Ciprofloxacin is an effective antimicrobial that is used to treat infectious diseases of the lungs, but the delivery of a recent formulation of ciprofloxacin by inhalation did not have reliable clinical results.<sup>13</sup> Tobramycin and ciprofloxacin, two antibiotics that each can treat bacterial infections of the lungs, were developed as inhalable formulations, but only one of them was found to be effective as an inhalable product. Because these inhalable therapies are often evaluated based on clinical endpoints, the reason why one of these failed is not well understood. Whether or not a drug particle that deposits in the lungs is helpful depends on how that particle interacts with the local lung environment. Better understanding these particle interaction in the lung environment can lead to development of more successful inhalable therapies and provide insight into how inhaled particles impact human health.

### **1.3 Structure and Function of the Airways**

To understand how inhaled particles can potentially impact human health, it is useful to consider the structure and function of the respiratory system. As one breathes, air enters through either the nose or the mouth, passing through the pharynx into the

trachea, which branches into bronchi (Figure 1.1). Bronchi continue to branch into tubes of decreasing diameter eventually terminating in alveoli, small balloon-like sacs, after 23-28 branches.<sup>14</sup> When the lungs are partially to fully inflated, the total surface area has been estimated to be 70-130 m<sup>2</sup> with the alveolar air-exchange region accounting for 50-80% of this surface area.<sup>15</sup> This air-exchange region, which includes the respiratory bronchioles, alveolar ducts, and alveoli, are referred to collectively as the respiratory airways, whereas the region from the nose/mouth, through the trachea, bronchi, and bronchioles are referred to as the conducting airways.

The conducting airways are lined with many ciliated epithelial cells that are coated in a layer of fluid (~8 µm) on which a viscous mucus floats.<sup>16</sup> This mucus is rich in a glycoprotein called mucin that is crosslinked resulting in a viscoelastic gel.<sup>17</sup> A large portion of inhaled material becomes trapped in this mucus. The epithelial cells beat their cilia propelling mucus up into the throat, a process called mucociliary clearance, to recycle the fluids and transport foreign matter that deposits in the conducting airways out of the lungs where it can be expectorated or ingested. Mucus is produced in the conducting airways by another epithelial cell subtype called goblet cells, and both ciliated and goblet cell subtypes are derived from a third major subtype called club cells.<sup>18</sup> Club cells are a subtype formerly referred to as Clara cells; a consensus was reached in 2013 to refer to these cells as club cells.<sup>19</sup> This thesis will refer to club cells in-line with current conventions regardless of nomenclature choice in reference material.

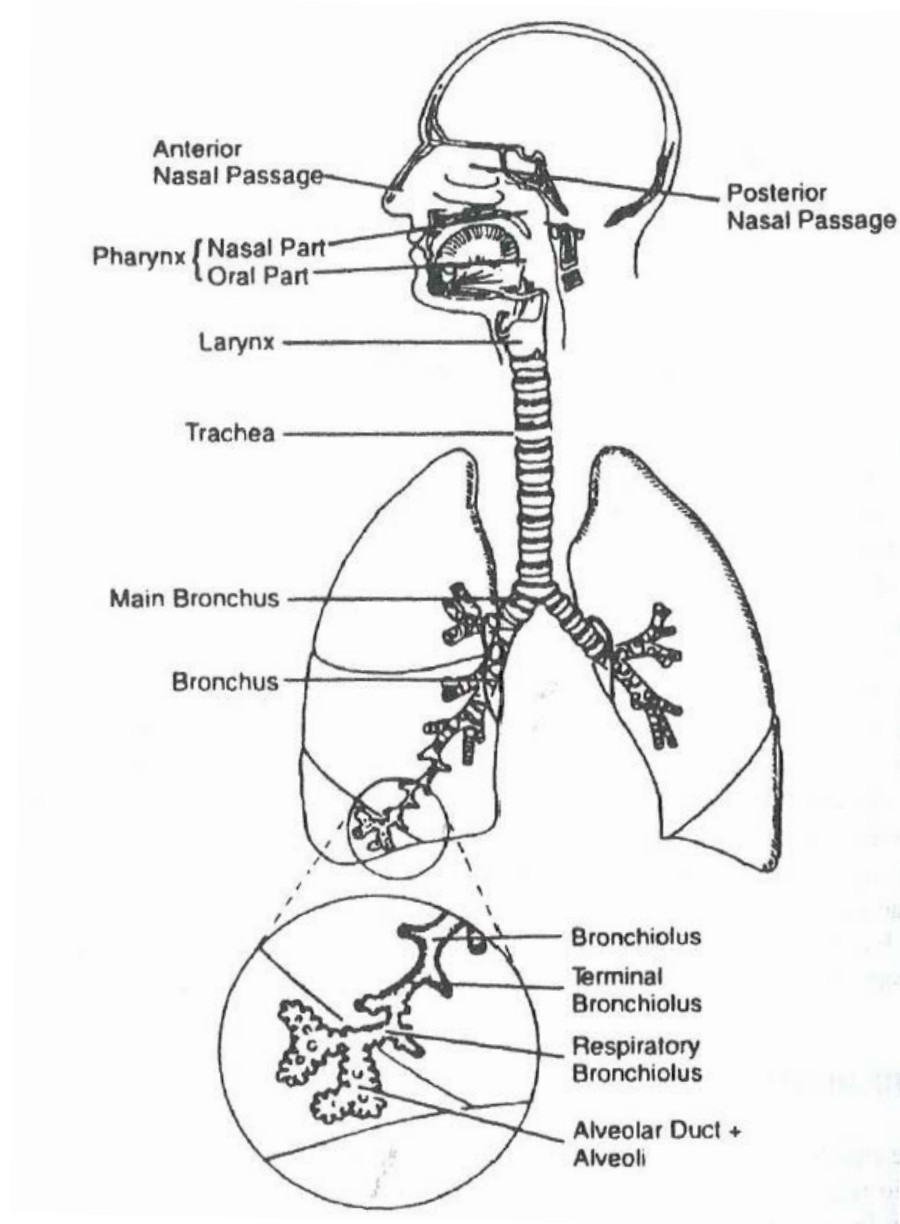


Figure 1.1. Anatomy of the human respiratory system. Reprinted with permission.<sup>20</sup>

Unlike the conducting airways, the respiratory airways are coated with a thin layer ( $<1 \mu\text{m}$ ) of alveolar lining fluid (ALF).<sup>21</sup> ALF is a protein-rich fluid with a surfactant layer on top. The surfactant layer reduces the surface tension of the fluid, which results in a lower force required to cause the lungs to expand. Many of the most

abundant proteins in this fluid either help transport and organize surfactant on the surface or provide some measure of host defense. Surfactant-associated proteins SP-B and SP-C maintain the surfactant at the air-liquid interface to facilitate the reduced surface tension.<sup>22</sup> High levels of IgG, IgA, transferrin, SP-A, SP-D, lactoferrin, lysozyme, and club cell protein, all of which have roles in host defense, have also been documented.<sup>23-26</sup>

Below the lung lining fluid is a thin layer of alveolar epithelium that acts as a membrane separating the airspace from blood. This epithelial layer is patrolled by macrophages from the immune system that help clean and protect the respiratory airways. These macrophages consume foreign materials that arrive in the alveolar lining fluid. They digest and kill bacteria, and they take particulate matter to the bronchioles where they are cleared via the mucociliary escalator.<sup>27</sup> The alveolar epithelium below this layer is thin, with cells having a thickness of  $<1 \mu\text{m}$ .<sup>16</sup> These cells form a barrier between the airspace and the blood, regulating the flow of materials back and forth by forming tight junctions.<sup>28</sup>

#### **1.4 Particle Deposition in the Respiratory Airways**

When inhaled, particles in the air deposit in different regions of the airways due primarily to their size. Particle shape and density alter the behavior of particles flowing in fluids by modifying drag and momentum, respectively. Deposition of particles in the lungs is often characterized by aerodynamic diameter, a term that compensates for shape and density (which are often not measured in complex mixtures of particles) and normalizes particle behavior to that of spheres with a density of  $1 \text{ g/cm}^3$ . Aerodynamic diameter ( $d_{\text{aero}}$ ) is calculated as shown in equation 1-1, where  $d_e$  is the diameter of a sphere of equivalent volume as the particle,  $\rho_p$  is the density of the material,  $\rho_0$  is the

density of water, and  $\chi$  is the shape factor. The shape factor is calculated from the drag force ( $F_D$ ) acting on a particle at a given velocity ( $v$ ) of a given viscosity ( $\eta$ ) as shown in equation 1-2.

$$d_{aero} = d_e \left( \frac{\rho_p}{\rho_0 \chi} \right)^{0.5} \quad (1-1)$$

$$\chi = \frac{F_D}{3\pi\eta v d_e} \quad (1-2)$$

As illustrated in Figure 1.2, aerosols inhaled through the mouth deposit in the airways efficiently when they have aerodynamic diameters from 1-10  $\mu\text{m}$ .<sup>16, 20</sup> This is based on normal mouth breathing. For the purposes of drug delivery, inspiration rate, breath holding, and inhaler type can all result in altered deposition efficiency for particles of various sizes.<sup>16</sup>

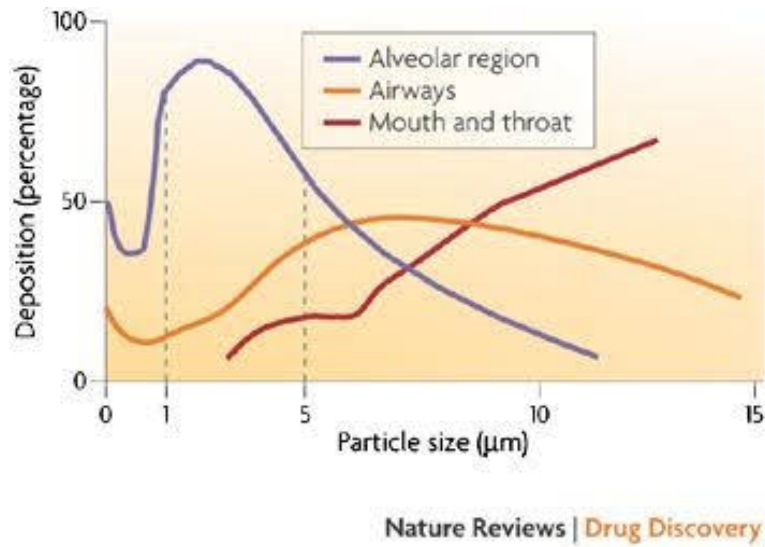


Figure 1.2. Illustration of deposition patterns for particles of varying aerodynamic diameter in different regions of the lungs. Reprinted with permission.<sup>16</sup>



#### 1.4.1 Particle Interactions After Deposition in the Airways

Once a particle has deposited onto the fluid that coats the airways, a variety of paths are available. Clearance rates for particles in the alveolar space are much lower than in the conducting airways, which can remove inhaled materials within a day via mucociliary clearance.<sup>29</sup> By comparison, some particles deposited in the alveolar space in animal models have been found to remain in the lungs for time periods ranging from weeks to years.<sup>30</sup> Particles can be transported across the alveolar epithelial cell membrane, or they can be sequestered by macrophages. Particles interact with the surfactant layer at the liquid-air interface where they deposit and interact with proteins in the aqueous subphase. In a recent review of drug delivery to the lungs, Patton et al. noted, “Our knowledge of how particle properties change over time due to adsorption of various fluid and surfactant components to the particle surface and how these interactions alter delivery is primitive.”<sup>21</sup> Particle behavior in air determines whether they can arrive in the respiratory airways, but particle behavior in aqueous systems determines what happens next.

#### 1.4.2 Factors That Influence Particle Behavior

In aqueous suspension, particles are acted on by a variety of forces, including buoyant force, gravity, drag, electrostatic forces, Van der Waals forces, and hydrophobic interactions as illustrated in Figure 1.3.<sup>20, 31, 32</sup> When forces are nearly balanced, particle suspensions tend to be stable, while force imbalances tend to destabilize suspensions. In the 1940s, Derjaguin, Landau, Verwey, and Overbeek identified the balance between Van der Waals and electrostatic forces as major determinants of colloidal stability, and the mathematical relationships they developed to describe colloids is referred to as DLVO

Theory.<sup>33, 34</sup> Van der Waals forces is a general term encompassing a number of forces dealing with features such as dipole interactions, potential induction, London dispersion forces, and others that result in a net attractive force that is related to  $1/d^6$  where  $d$  is the distance between two objects.<sup>35</sup> At very close distances, Van der Waals forces will cause two particles to stick together. These forces act over a very small distance (within a few nanometers), but they can be relatively strong. If particles have a surface charge, usually due to the presence of cationic or anionic chemistries, then the electrostatic charge exhibited by all of those groups on the surface pushes particles apart. This force is not as strong as Van der Waals forces at very close proximity ( $\sim 1$  nm), but it acts over a larger distance. This results in the electrostatic repulsive force pushing stable particles apart before they draw near enough for Van der Waals forces to engage. In the interplay between Van der Waals forces and electrostatic forces, the aqueous medium properties are more likely to influence electrostatic forces than Van der Waals forces. Electrostatic forces are related to the electronic double layer that forms around particles in suspension. This double layer is impacted by the ions in the aqueous medium; ion composition, concentration, and valence, which is a function of pH, impact the electronic double layer and can thus affect suspension stability.

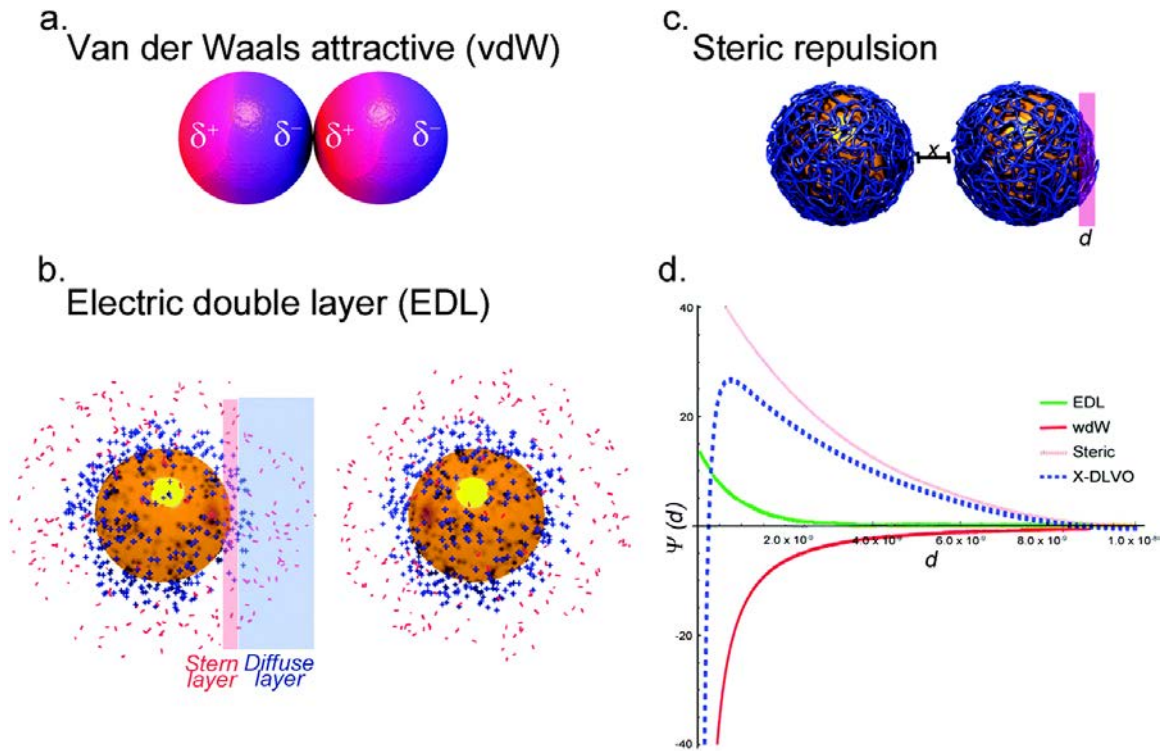


Figure 1.3 Illustration of interparticle forces that influence the stability of particles in suspension. Forces include a) Van der Waals attractive forces, b) electric double layer repulsion, and c) steric repulsion. These components all contribute to the d) potential energies of particles across varying interparticle distances. Reproduced under the Creative Commons Attribution 3.0 Unported License.<sup>36</sup> – Published by The Royal Society of Chemistry

The interparticle forces that affect suspension stability depend on the surface of the particles. Van der Waals forces are a function of the surface material properties, and surface chemistries imbue particles with surface charge providing electrostatic forces. Thus, changes in a particle surface can impact particle stability. Stable particles will remain dispersed in a fluid, whereas unstable particles will aggregate and settle out of a fluid. Stability is often measured by observing changes in particle size using light scattering approaches<sup>37-40</sup> or turbidimetric approaches<sup>40, 41</sup>.

Particles in biological media are rapidly coated with proteins, which results in a new particle surface.<sup>42</sup> The properties of this new surface can impact the stability of these

particles after proteins adsorb. When particles land in the respiratory airways, they interact with surfactant components or proteins in lung lining fluid. Our understanding of the interactions between inhaled particles and the fluid environment in the airways lags behind our understanding of these interactions in blood. The large volume of injectable therapies coupled with higher availability of blood and blood products has led to a large body of research into biomolecular interactions between blood and particulates.<sup>43-48</sup> The availability of blood relative to lung lining fluid is greater, both in terms of volume/person and in terms of ease of access. In one study, young adult males were found to have an average of 4.7 L of blood,<sup>49</sup> whereas alveolar lining fluid in an average person can be approximated to 0.01 L based on a surface area of 100 m<sup>2</sup> and a fluid thickness of 1 μm. Collecting blood is easier than collecting lung lining fluid. Blood is usually collected using a needle through the skin, whereas lung lining fluid is collected by threading a bronchoscope through the respiratory system to sample lung fluids. Difficulty of access to lung fluids, the small total volume of lung lining fluid, and a much smaller portfolio of therapies targeted to the lungs have all contributed to this large gap in understanding lung therapies compared to injectable therapies.

From research performed using injectable therapies, many of the features of particle behavior in lung lining fluid can be anticipated, and techniques developed to study injectable therapies can be translated for use in studying pulmonary therapies. For instance, studies of injectable therapies have identified that protein coronas tend to form around nanoparticles in biological environments, as illustrated in Figure 1.4.<sup>50-53</sup> These coronas can lead to particle aggregation, altering their behavior.<sup>54</sup> These coronas can additionally alter cellular responses to those particles.<sup>42, 55</sup>

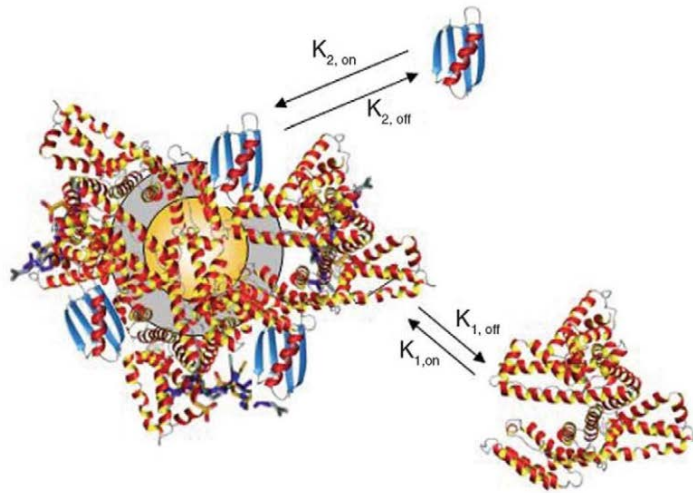


Figure 1.4 Illustration of protein corona formation around a nanoparticle in an equilibrium process. Reprinted with permission.<sup>53</sup>

### 1.4.3 Adsorption of Components from Blood onto Particles

To understand how interactions with fluids of the lungs may impact particle fate, it is useful to consider what has previously been discovered when particles interact with blood. When components from blood adsorb onto the surfaces of particles and induce aggregation, this can influence biodistribution and clearance rates of nanoparticles.<sup>56, 57</sup> These studies highlight the importance of particle stability in influencing cellular response and biodistribution of particles. They generally identify that aggregation can be a hindrance to cell uptake with some exceptions. When Malcolm et al. exposed polymer nanoparticles to increasing concentrations of serum in cell culture media for exposures *in vitro*, they found that at concentrations as low as 2% fetal bovine serum (FBS) their nanoparticles began to aggregate.<sup>58</sup> They also found that this aggregation limited cell uptake of their particles. Similarly, Albanese et al. found that aggregation of particles by the protein transferrin reduced cell uptake in two cell lines, but increased uptake in a third *in vitro*.<sup>56</sup> Muller et al. studied the impact of serum from different animals on particle

stability and human macrophage response. They found that particle aggregation varied across species, and that coronas formed in human serum reduced human macrophage uptake while mouse serum coronas enhanced human macrophage uptake *in vitro*.<sup>59</sup> When Mohr et al. studied protein adsorption onto particles in serum, they found that protein adsorption and particle aggregation influenced the organs in which particles accumulated in mice.<sup>57</sup>

The Muller study demonstrated that the different proteomes from various species each impacted particle behavior uniquely. This evidence of fluid proteome influencing particle behavior and cellular response supports the hypothesis that differences between the proteomes of lung lining fluid and serum will lead to differences in particle behavior in these two fluids. Studies based in blood can be used to infer the general trends and effects that may arise in studies using lung lining fluid. Moreover, techniques that have been developed using blood to characterize various aspects of the particle-protein relationship can be emulated to study the particle-protein relationship in the lung environment.

#### 1.4.4 Proteins Impact Particle Behavior in Biological Systems

The identity of adsorbed proteins in the protein corona has been shown to influence cellular responses. In the blood, two areas of research regarding protein identity focus on 1) identifying proteins that form in a corona from a large cohort of proteins or 2) studying how an individual protein interacts with particles. Unlike studies of stability, which tend to rely on light scattering and measurements of zeta potentials<sup>45, 56-63</sup>, these areas of study rely on more diverse analyses. The divergent approaches to investigating which proteins adsorb to the surfaces of particles underscores the difficulty of assessing

these complex interactions. Each technique and approach illuminates a different aspect of protein-particle interactions, identifying different factors that influence particle-protein interaction, as well as identifying various effects that these proteins can have on particles in biological environments.

Proteomic analyses of serum and lung fluid have identified over 1,500 unique proteins in either of these respective fluids.<sup>64</sup> Studies considering larger cohorts of proteins in serum have previously identified that these mixtures can influence particle stability, charge, and interactions with cells. Ehrenberg et al. combined SDS-PAGE to identify adsorbed proteins, light scattering to measure changes in size/aggregation, and flow cytometry to measure uptake of functionalized polystyrene particles exposed to serum.<sup>63</sup> They found that proteins adsorbed to the surfaces of particles, caused increases in size distribution, and increased attachment to vascular endothelial cells. In a similar study, Walkey et al. exposed gold and silver nanoparticles with a variety of anionic, cationic, and neutral surface coatings to serum.<sup>55</sup> They used light scattering to assess size, laser doppler anemometry to assess zeta potential, BCA assay to measure total protein adsorbed, separated and identified components in the corona using SDS-PAGE followed by LC-MS, and measured uptake in A549 cells using inductively coupled plasma optical emission spectroscopy (ICP-OES). They observed particle agglomeration in serum, and identified that characteristics such as size, zeta potential, and protein composition of the corona were predictive of cell response.

When considering the use of proteomics to approach studies of particle-protein interactions, the large number of distinct proteins identified in a corona can confound results and prevent accurate attribution of outcomes to any particular protein. The

specific contributions of individual proteins cannot be measured due to the large number of proteins present in each sample. In addition, proteomic analyses such as these tend to be costly and require specialized resources. An advantage to these studies is that they are physiologically relevant using naturally-derived fluids.

Studies focusing on the interactions of individual proteins with particles provide complementary information to these studies that use naturally derived fluids. A major advantage of single protein analyses is that they provide detailed information about how an individual protein affects particle behavior. The techniques typically require less expense and specialized equipment than techniques required for analyses of complex coronas formed in natural fluids. These studies have determined that individual proteins can have varying impacts on particle stability. They identify that there are clear three-way interactions between proteins, particles, and ions present in the solution or at the surface of particles that all influence both protein adsorption and particle stability. Galisteo-Gonzalez et al. investigated IgG adsorption to polystyrene beads by measuring the loss of IgG from the solution to the surface using absorbance at 280 nm (the wavelength proteins absorb).<sup>65</sup> Using optical dark-field microscopy and electrophoretic mobility measurements to measure stability and measuring protein adsorption using absorption spectroscopy at 280 nm, they determined that IgG adsorption destabilized these particle suspensions. Davalos et al. measured the effects of IgG and IgY adsorption on polystyrene particle stability.<sup>31</sup> Adsorption was quantified using 280 nm absorption spectrophotometry, and particle stability was studied using turbidimetry, light scattering, and measurements of electrophoretic mobility. They found that pH affected stability and adsorption for both proteins, and in addition to modulating the mass adsorbed, pH



affected whether the antibodies were oriented with the antigen-reactive group facing out or towards the surface. When Lopez-Leon et al. studied IgG interactions with polystyrene particles, they identified that ions present in solution influence the stability of protein-coated particles using light scattering techniques. Gun'ko et al. studied interactions between silica particles and BSA, ovalbumin, hemoglobin, and gelatin using light scattering and turbidimetry techniques alongside electrophoretic mobility to study suspension stability. Measurements of protein adsorption were performed using the Biuret test on the aqueous media after centrifuging particles. They found stability was influenced by the concentration and identity of proteins in solution as well as the concentration of salt. In a recent study, Meder et al. varied the concentration of sulfonate groups on the surface of alumina particles to assess how this surface functionality affected protein interactions.<sup>66</sup> They exposed these particles to BSA, lysozyme, and trypsin, and studied zeta potential through laser Doppler anemometry. Adsorption of proteins was measured using 280 nm absorption spectrometry. They found that adsorption of proteins was not dependent on particle zeta potential, but that it was related to the density of sulfonate groups on the surfaces of the alumina particles. They found that there were protein-specific effects, as increasing sulfonate caused BSA adsorption to decrease while lysozyme and trypsin adsorption increased. Thus, changes in surface chemistry can influence preferential adsorption of some protein species over others.

Most of the studies investigating the interactions of individual proteins with particles in suspension assess the mass of protein adsorbed to the surfaces of particles. Quantifying adsorption can identify the affinity of these individual proteins for adsorbing to a given surface. Additionally, quantifying adsorption can identify if a large or small

quantity of a given protein is needed to influence particle stability or cell response. To quantify the adsorption of individual proteins onto the surfaces of particles in these studies, a variety of techniques have been developed. Approaches developed to quantify adsorption rely either on separation and measurement of the protein removed from solution or on development of an in-situ measurement to monitor protein coatings on particle surfaces. Table 1.1 lists a brief review of literature (from oldest to newest) describing techniques used to quantify protein adsorption to the surfaces of particles. These measurements often involving perturbation of the system. Different techniques perturb in different ways and can introduce different sources of error. Among these, separation techniques require more sample processing, but do so at a very low cost. Comparatively, in-situ techniques eliminate errors introduced in separations, but require specialized and costly equipment as well as being compatible with fewer particle materials.

*Table 1.1. Review of studies investigating the adsorption of one to two proteins at a time to the surfaces of various particles, documenting the proteins and the techniques used to quantify adsorption.*

Reference	Protein(s) Studied	Separation Technique	Protein Quantification Technique(s)
Galiesteo-Gonzalez et al. <sup>65</sup>	IgG	Centrifuged	Absorbance at 280 nm
Rowe et al. <sup>67</sup>	BSA	Filtered	Absorbance at 280 nm
Davalos et al. <sup>31</sup>	IgG, IgY	Centrifuged	Absorbance at 280 nm
Gun'ko et al. <sup>68</sup>	BSA, Ovalbumin, Hemoglobin, Gelatin	Centrifuged	Biuret Test

Table 1.1 continued

Cedervall et al. <sup>51</sup>	HSA	In-situ	ITC, SPR
Reference	Protein(s) Studied	Separation Technique	Protein Quantification Technique(s)
Yoshimoto et al. <sup>69</sup>	BSA	In-situ	SPR
Baier et al. <sup>70</sup>	BSA, Ovalbumin, Hemoglobin, Gelatin	In-situ	ITC
Schulze et al. <sup>71</sup>	SP-A	Centrifuged	BCA Assay
Tsai et al. <sup>72</sup>	BSA	In-situ	ATR-FTIR, Fluorescence Spectroscopy
Meder et al. <sup>66</sup>	BSA, Lysozyme, Trypsin	Centrifuged	Absorbance at 280 nm NanoOrange
Huang et al. <sup>73</sup>	Ubiquitin, Fibrinogen	In-situ	ITC
Wang et al. <sup>74</sup>	GB3, Ubiquitin	In-situ	NMR
Wang et al. <sup>75</sup>	GB3	In-situ	NMR
Wang et al. <sup>76</sup>	GB3, Ubiquitin	In-situ	NMR
Givens et al. <sup>77</sup>	BSA	In-situ	ATR-FTIR

In summary, studies in blood have identified many features of particle-protein interactions and how they impact subsequent particle interactions. These studies have identified that particles exposed to blood, plasma, or serum adsorb a number of different proteins. Different particle surfaces tend to be covered with different sets of proteins and

those protein coronas impact cell uptake and association with particles. They identified how particle stability can be influenced by the identity of adsorbed proteins, ion conditions of the surrounding media, and pH. Based on this knowledge of injectable therapies, we can anticipate that particles in lung lining fluid will 1) be coated in protein coronas, 2) tend to form aggregates as a result of protein interactions, and 3) have cellular responses influenced by the presence of surface-adsorbed proteins.

#### 1.4.5 Differences Between Serum and Lung Lining Fluid

A particle that is surrounded by one group of proteins in blood will not necessarily have the same coating of proteins form in a fluid with a different composition. This was evidenced by the Muller study which compared the composition of proteins on the surfaces of particles exposed to serums from four different species.<sup>59</sup> The proteomic composition of lung lining fluid differs from serum. Chen et al. analyzed bronchoalveolar lavage fluid (BALF), a fluid obtained by using a bronchoscope to rinse the deep lungs and collect proteins and cells, and compared the proteome to serum; as illustrated in Figure 1.5, they found that the relative expression of a variety of proteins differs between these two biological fluids.<sup>26</sup> It is likely based on these differences in composition that some particles will have markedly different protein interactions in lung fluid than in serum based on differences in their respective proteomes. Using the knowledge and experimental approaches obtained from studies involving injected particles, these interactions must be studied in lung fluid to elucidate the specific needs and issues that arise with inhalable therapies.

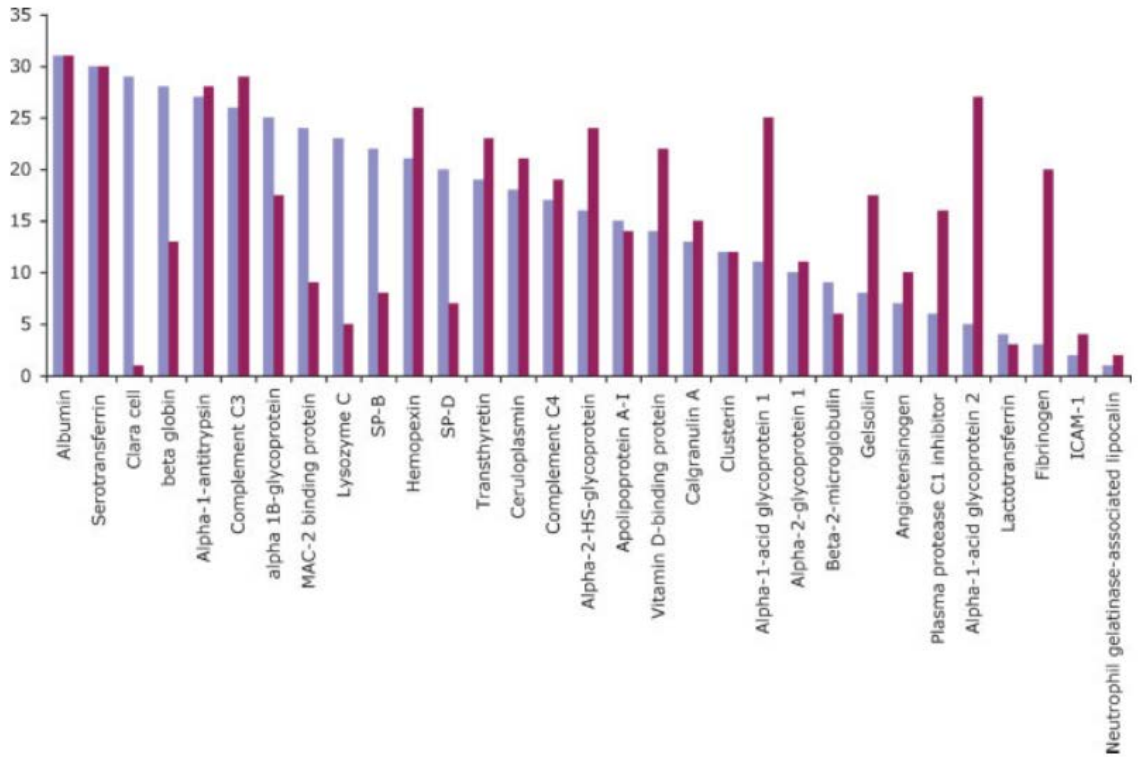


Figure 1.5. Relative abundance of 31 common proteins in BALF (blue) and plasma (red). Y-axis represents the rank position among these proteins with 31 having the highest relative abundance in the respective fluid and 1 having the lowest relative abundance. Reprinted with permission.<sup>26</sup>

## 1.5 Mitigation of Protein Interactions to Control Particle Behavior

The interactions between particles that arrive in blood or lung lining fluid and the complex mixture of proteins therein are overlooked in many *in vitro* studies of particle therapies. The rapid coating of proteins onto the surfaces of particles that are exposed to biological fluids mediates the particles' subsequent interactions with cells and tissues, making protein coronas strong determinants of the fate of particles in the human body. In many of the studies using blood, protein corona formation inhibited the ability of particles to enter cells and tissues. Thus, protein coronas can be an obstacle to effective particle-based therapies. To minimize interactions between particles and proteins in the body, surfaces are often functionalized with a layer of polyethylene glycol (PEG).<sup>44, 78, 79</sup>

PEG provides a highly hydrophilic surface that shields surfaces from nonspecific protein adsorption. PEG attachment was originally developed to provide a shield that prevented immune recognition of foreign proteins.<sup>80</sup> Over time, some immunogenicity of the PEG itself has been recognized, resulting in PEGylated products that may lose efficacy after multiple doses.<sup>81</sup> A recent study investigating anti-PEG antibody effects on clearance of PEGylated nanoparticles found that anti-PEG antibody response was associated with increased IgM and apolipoprotein content in the protein corona that formed on these particles, which can contribute to increased clearance.<sup>82</sup> Specifically, the binding of IgM antibodies serves to opsonize particles increasing immune recognition.<sup>83</sup>

In response to the potential immunogenicity of PEG, investigations into similar materials that can resist protein interactions have been performed. Around the time anti-PEG antibodies were being recognized, some analysis into the underlying properties that PEG and other protein-resistant materials shared was underway. One investigation into a number of resistant surfaces identified that a common feature was that they were composed of kosmotropes, or chemistries that are well hydrated and influence water structures in their vicinity.<sup>84</sup> Among the chemistries in that study were zwitterionic functionalities such as carboxybetaine.

The protein-resistant features of zwitterionic functionalities were not unknown when PEG antibodies were being discovered, but the chemical simplicity and cheap manufacture of PEG had made it dominant in the field for years. The discovery of anti-PEG antibodies has provided an in-road to promote the use of zwitterionic polymers in biomaterials. Zwitterionic polymers have been increasingly studied as biocompatible materials due to their minimal interactions with proteins and non-thrombogenic

properties.<sup>46, 85-91</sup> Zwitterions are materials that have ionic components, but the various positively and negatively charged components results in a net charge of zero for the material. A sample of some common zwitterionic functionalities can be seen in Figure 1.6. Many zwitterionic polymer coatings have been developed to resist adsorption to proteins. Investigations into these coatings have identified that a key feature in resistance to protein adsorption relates to interactions with water. The charged groups are attractive to water, which enhances hydration, but the spatial relationship between charged groups in a zwitterionic material affect how water molecules arrange themselves near the material.<sup>87, 92</sup> When water both hydrates a zwitterionic material and is structured in such a way that it resembles water in its bulk form, resistance to protein adsorption is achieved.<sup>92, 93</sup> Thus, maintaining good spatial orientation between cationic and anionic substituents of a zwitterionic material leads to surfaces that minimally interact with proteins in water. In a review of the use of zwitterions for biocompatible materials, Schelhoff noted that the cationic and anionic groups on a surface do not need to be attached to one another as long as some feature of surface construction facilitates their placement at an appropriate fixed distance.<sup>92</sup>

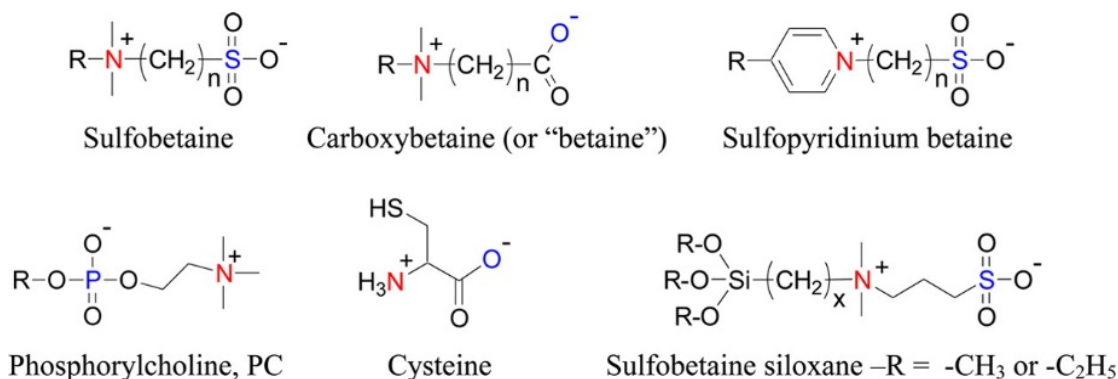


Figure 1.6. Zwitterionic functional groups and one zwitterated siloxane. Reprinted with permission.<sup>92</sup> Further permissions related to this material should be directed to ACS.

A variety of avenues involving non-fouling zwitterionic materials are being explored in medicine. One polymer, polymethacryloyloxyethyl phosphorylcholine (pMPC), has been used for many years in medical devices such as contact lenses.<sup>94</sup> In the case of drug delivery, some have demonstrated synthesis of pMPC copolymers for the formation of polymersomes to encapsulate and deliver drugs.<sup>95,96</sup> A carboxybetaine methacrylate has been demonstrated to stabilize liposomes to increase circulation time.<sup>97</sup> Beyond their potential use in particles for drug delivery, carboxybetaine and sulfobetaine functionalized polymers are being used to design materials for implants.<sup>89,98</sup> Sulfobetaine methacrylate has also been demonstrated as a potential coating for catheters to decrease formation of bacterial biofilms during use.<sup>99</sup> Thus, these materials show significant promise as biomaterials for the development of implants as well as therapeutic carriers for stealth delivery of drug and gene therapies.

## 1.6 Objectives

Inhaled particles can impact lung health and overall health. Some particles encountered in daily life may have unknown effects on health; others may be known to be toxic, but secondary effects on health and disease remain unknown. The research in this thesis begins with investigations into toxicity of a newly discovered aerosol photooxidation of components in personal care products. Due to the near ubiquity of this compound in a variety of personal care products, a large quantity of these aerosols can form in the environment. With the health effects of this new chemical species unknown, it is important to determine whether inhalation of these aerosols is a concern for human health.



In addition to exploring the effects of a previously-unknown aerosol on lung health, it is important to understand how known inhalation hazards harm the lungs. The investigation of copper oxide (CuO) nanoparticles, a component of toxic aerosols such as pollution, cigarette smoke, and e-cigarette vapor, was performed to identify the contributions of this chemical species to the toxic effects of these aerosols. We further studied whether CuO nanoparticles increase susceptibility of lung cells to infection with *S. pneumoniae* through upregulated expression of the platelet-activating factor receptor (PAFR), as is observed after exposure to urban PM, cigarette smoke, or e-cigarette vapor.

Particles that arrive in the respiratory airways interact with the proteome in lung lining fluid prior to contact with cells. The remainder of the research presented in this thesis is related to how protein-particle interactions in the lungs may impact particle behavior, and what factors influence these interactions. Investigations into these interactions seek to identify whether differences in the lung proteome meaningfully affect particle behavior compared to more well-studied systems such as blood. We hypothesized that distinct proteins found in the lungs adsorbed to particle surfaces would have varying effects on particle stability and properties in suspension. We further hypothesized that particles exposed to BALF would differ from those exposed to serum.

In addition to studying how particles interact with proteins, the development of materials that limit these interactions are of value in medicine. Based on the success of stealth materials such as PEG and zwitterionic polymers, the application of stealth systems was theorized to improve particle properties in the lung fluid environment. However, based on immunogenicity of PEG, zwitterionic polymers were explored for inhalable therapies. We hypothesized that the synthesis of a thiol-terminated zwitterionic

polymer would result in a surface coating that would reduce protein adsorption, stabilize nanoparticle suspensions, and have minimal impact on lung cell responses.

Objective 1: Evaluate the toxicity of two aerosols that are encountered through incidental exposure.

Specific Aim 1.1: Investigate lung cell toxicity of aerosols composed of photooxidized decamethylcyclotrisiloxane.

Specific Aim 1.2: Investigate the toxicity and uptake of copper oxide nanoparticles exposed to lung cells.

Specific Aim 1.3: Evaluate the impact of copper oxide nanoparticles on bacterial infections in lung cells.

Objective 2: Identify changes in particle physicochemical properties as a result of exposure to proteins found in the respiratory airways.

Specific Aim 2.1: Measure the effects of individual proteins common in lung lining fluid on polystyrene particle stability, surface charge.

Specific Aim 2.2: Measure particle stability, surface charge and quantify adsorption after exposing individual proteins common in lung lining fluid to gold nanoparticles at varying pH.

Objective 3: Identify changes in particle physicochemical properties and interactions with lung cells after exposure to serum and BALF.

Specific Aim 3.1: Develop a method to concentrate BALF proteins to nearer their physiological concentration.

Specific Aim 3.2: Measure particle stability, surface charge, and cellular response to coated particles upon exposure to human biological fluids.

Objective 4: Develop a zwitterionic polymer coating for nanoparticles to resist protein adsorption and stabilize particles in a model pulmonary environment.

Specific Aim 4.1: Synthesize a zwitterionic polymer that will form self-assembled monolayers onto gold nanoparticles.

Specific Aim 4.2: Characterize the polymer after synthesis for composition, conversion, and molecular weight.

Specific Aim 4.3: Assess polymer-coated particle stability in serum and BALF.

Specific Aim 4.4: Investigate the impact of this polymer coating on lung cell uptake of gold nanoparticles.

## 2 Lung Cell Exposure to Secondary Photochemical Aerosols Generated from OH Oxidation of Cyclic Siloxanes

### 2.1 Introduction

Over the past decade, research interest in siloxane and polysiloxane (silicone) compounds has increased markedly. While these compounds have been in-use since the 1940s, improved analyses have revealed the presence of organosiloxanes in a large number of previously unreported locations. Furthermore, complexity in the environmental degradation pathways has led to reassessment of conceptual models relying on conversion of parent compounds to silica ( $\text{SiO}_2$ ).<sup>100</sup> Demonstration of conversion of siloxane products into other organosiloxanes and the discovery of parent and daughter siloxanes in a variety of environments and biomes has further piqued interest regarding environmental and human health.<sup>100, 101</sup>

Cyclic volatile methyl siloxane (cVMS) compounds are of particular interest due to their volatility and their wide use in personal care products and industrial applications.<sup>100-102</sup> cVMS compounds, most commonly decamethylcyclopentasiloxane (D5), are used ubiquitously as emollients in antiperspirants and in hair and skin care products because their presence imbues skin and hair with properties described as smooth, silky, or soft to the touch. While estimates of cVMS compound emissions vary, a well-regarded air emission estimate for US D5 is 135 mg/person/day.<sup>103-105</sup> Further, recent literature indicates that cVMS are the largest source of VOC emissions in urban environments<sup>106</sup> and that cVMS are dominant pollutants (~1/3 of volatile carbon) in classroom air<sup>107</sup>.

The safety of the parent cVMS compounds has been extensively evaluated by both US and European oversight groups, with the conclusion that parent cVMS compounds pose a minimal health risk to humans and animals.<sup>108, 109</sup> These compounds generally evaporate quickly after application and thus are minimally absorbed. Human uptake of D5, typically by inhalation results in measurable bloodstream concentrations. The blood plasma half-life of D5 is approximately 2-3 days, and the compound is removed via partitioning into fat, exhalation from the airspaces, and metabolism into silanols.<sup>110, 111</sup> Further studies of D5 and similar cVMS compounds have generally found little to no toxicity,<sup>108, 112</sup> with some key exceptions observed for derivatives of the parent compounds.<sup>101, 102, 113</sup>

A large fraction of the cVMS are emitted to indoor and outdoor air after application due to their volatility, and thus become available for reaction in the atmosphere. cVMS react in the atmosphere with hydroxyl radicals (OH), generating a variety of products including non-volatile or semi-volatile compounds.<sup>114-117</sup> Recent work has established that siloxanes are widely distributed, with the highest concentrations in urban population centers and more diffuse concentrations in surrounding areas.<sup>118-123</sup> The primary removal mechanism for siloxanes in the environment is predicted to be via photooxidation with OH radicals;<sup>114, 124</sup> the OH reaction kinetics result in a long lifetime for D5 in the troposphere of approximately 10 days.<sup>114</sup> Chamber-based experiments have demonstrated that these non-volatile and semi-volatile cVMS oxidation products can nucleate or condense onto preexisting aerosol particles (cVMS + OH → o-cVMS (oxidized product) → particle species).<sup>116, 117, 125, 126</sup> Field measurements of the elemental composition of ambient aerosols further suggest that cVMS photooxidation may be a

source.<sup>118</sup> Further work demonstrated that the chemical conversion and incorporation of cVMS into aerosols modifies the transport and accumulation of cVMS in the environment.<sup>126-128</sup> The presence of these compounds in aerosols could result in human exposure to species that are unlike the pure cyclic siloxanes previously investigated. For soot and black carbon, increased toxicity of aerosols has been observed after oxidation in the atmosphere.<sup>129, 130</sup> In these studies, aerosol particles induced multiple-fold increases in toxicity to cells once oxidized compared to pre-oxidation. Recent advances in detection identifying a high prevalence of siloxane-containing aerosols coupled with greater toxicity associated with the atmospheric oxidation of aerosols necessitate an understanding of the effects of aerosols containing photooxidized D5 on human health.

In this study, we generated aerosols composed of “daughter” compounds produced by photooxidation of D5 and assessed their impact on human lung cells. An oxidation flow reactor (OFR) was used to photooxidize cVMS under controlled conditions that mimic reactions in the atmosphere<sup>131</sup>. Here we combine the OFR with an *in vitro* aerosol exposure system to assess potential health implications of photooxidized cVMS aerosols. The aerosol exposure system (Vitrocell 12/6) enabled the passive deposition of aerosols onto the surface of lung cells cultured under air-interfaces conditions, mimicking aerosol exposures and culture conditions that occur in the lungs<sup>132-134</sup>. The ability of photooxidized cVMS aerosols to induce inflammation and toxicity in lung cells was evaluated.

## 2.2 Materials and Methods

Thirteen experiments were conducted using the apparatus shown in Figure 2.1. Experiments were about 4-h in duration, with additional time for system stabilization

prior to aerosol characterization and/or cell exposure. Seven experiments included cell exposures and six were performed for system characterization. The apparatus has three major sections described below – aerosol generation using a potential aerosol mass (PAM) type OFR, *in vitro* cell exposure in the Vitrocell system, and effluent characterization by SMPS, filter samples, and ozone monitoring.

### 2.2.1 Aerosol Generation and Characterization

Vapor-phase D5 was oxidized in a 13.3 L OFR using UV lamps to generate OH radicals following previously published methods.<sup>131, 135, 136</sup> A 5-LPM, HEPA-filtered, humidified air stream flowed past a capped piece of Teflon tubing containing liquid D5 (Sigma-Aldrich, 97% purity) maintained at 70°C in a water bath to vaporize the D5, and was fed into the OFR chamber through the feed port.

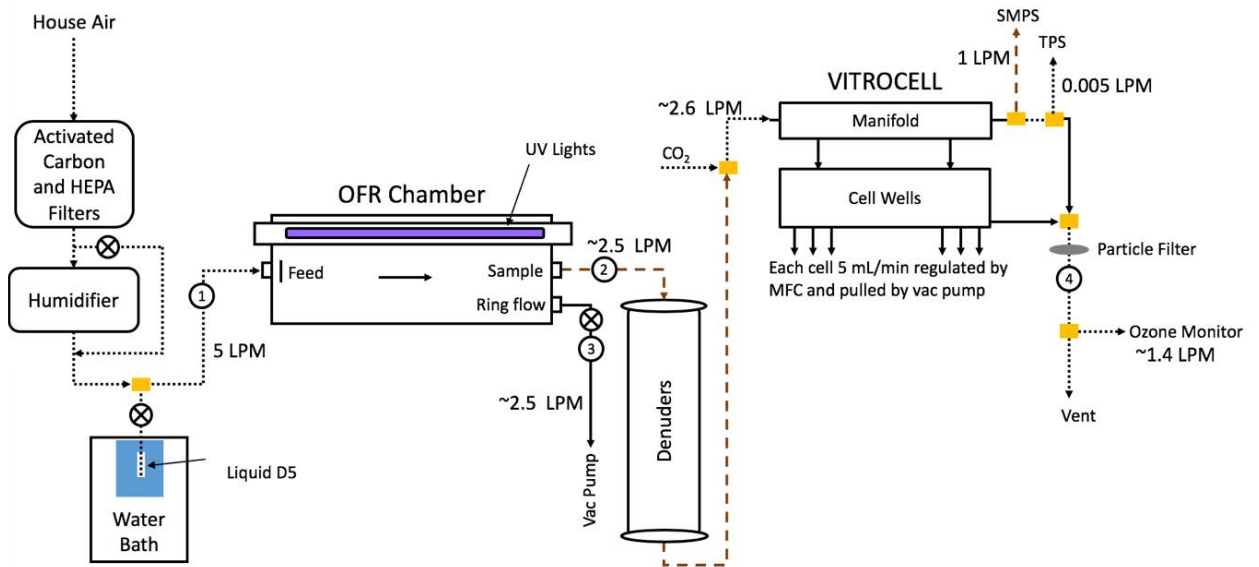


Figure 2.1 Flow diagram of the experimental setup for generation of aerosols in the OFR and cell exposures. Incoming flowrate and RH, chamber pressure, ring flowrate, and downstream flowrate were measured at points 1, 2, 3, and 4 respectively on the diagram. Short dashed lines in the diagram indicate Teflon tubing, long dashed represent copper tubing, and solid lines represent conductive silicon tubing.

The OFR feed stream was maintained at 30% RH, as measured directly prior to the OFR feed port, by adjusting the fraction of dry air bypassing the humidifier. OH generated from the OFR was estimated at about  $1.4 \times 10^{10}$  molec/cm<sup>3</sup> as measured from SO<sub>2</sub> oxidation kinetics for chamber conditions of maximum light intensity and 30% RH. This OH exposure is equivalent to approximately 17.6 days of atmospheric aging assuming an average atmospheric OH concentration of  $1.5 \times 10^6$  molec/cm<sup>3</sup>. Flow from the sample outlet on the terminal side of the OFR left at a rate of 2.4 – 2.7 LPM, and the remainder of the outlet flow with more chamber wall exposure (ring flow, ~50%) was vented through the ring flow outlet, filtered, and exhausted through a lab hood. OFRs generate substantial quantities of ozone (O<sub>3</sub>), which was observed in our first four experiments with the OFR and negatively impacted the health of exposed lung cells. Thus O<sub>3</sub> was removed from the sample stream using annular denuders containing Carulite 200 (manganese dioxide/copper oxide catalyst; Carus Corp.). An activated carbon (Fisher Scientific; 6x14 mesh size) denuder was placed in-line to absorb organic gases from the OFR effluent. The activated carbon denuder dimensions were 25 cm outside diameter (OD), 20 cm inside diameter (ID) by 125 cm, while the Carulite denuders had dimensions of 14 cm OD, 1 cm ID by 70 cm, and 8 cm OD, 1.5 cm ID by 54 cm. The denuders were packed with material between the OD and ID. After the denuders, CO<sub>2</sub> was added to the sample stream at a level of 5% v/v of the total stream, which provides enough partial pressure to stabilize the sodium bicarbonate buffer in cell media to maintain physiological pH for the lung cells. The CO<sub>2</sub> level was measured at the end of the system using a CO<sub>2</sub> monitor (TSI 9555X with 982 probe). The CO<sub>2</sub>-enriched sample stream then entered the Vitrocell glass manifold. Two sample outlets pulled a fraction of the flow off



the main stream for cell exposures (~15 mL/min each) and the remaining fraction of the main stream exited the manifold for characterization. After characterization, the remaining flow was vented through a HEPA filter and passed through a Thermo 49i O<sub>3</sub> monitor before venting into a lab hood.

Particle size distribution and concentration in the manifold effluent were determined using a TSI 3936L85 scanning mobility particle sizer (SMPS; TSI 3785 condensation particle counter, TSI 3080 classifier, and 3077 Kr-85 2mCi neutralizer). The size distribution was sampled from 9.7 – 422 nm and scans were repeated every 135 s. Aerosol size distributions were converted to aerosol mass concentrations assuming spherical particles of the liquid D5 density (0.959 g/cm<sup>3</sup>) and spherical diameters equal to the reported electrical mobility diameters. For both SMPS and O<sub>3</sub> measurements, the data was processed by removing time periods when the lines were opened for flow measurement or during supplemental sampling. SMPS data was additionally corrected by removing four instances of non-physical size distributions. The removed SMPS data constituted 63 min of data out of a total of 52 h of monitoring.

Particles were collected for evaluation using two sampling methods for electron microscopy. Samples downstream from the Vitrocell manifold were collected onto a carbon film supported by a 200 mesh nickel transmission electron microscopy (TEM) grid using a Thermophoretic Personal Sampler (TPS; model TPS100, RJ Lee Group, Inc.).<sup>137</sup> TPS samples were collected at 0.005 LPM for 25 min using hot and cold surface temperatures of 110°C and 25°C, respectively, and with 0.125 L total volume. TPS samples were analyzed at RJ Lee Group using a field emission scanning electron microscope (FE-SEM) with scanning transmission electron microscopy (STEM)

capabilities (S-5500, Hitachi High Technology Corporation). Compositional information was obtained using an energy dispersive X-ray spectroscopy (EDS) system (Quantax 800, Bruker AXS Microanalysis GmbH) incorporating a silicon drift detector (Bruker XFlash 4030). Information about the size, morphology, concentration, and elemental composition of the collected particles was obtained as part of the analysis.

A second, passive collection of aerosol particles for microscopy analysis occurred inside the Vitrocell system. To characterize the distribution, morphology, and composition of particles depositing in the wells of the Vitrocell system, TEM grids were placed in the exposure chambers as has been reported previously with similar air-liquid interface exposures systems.<sup>138, 139</sup> Grids were prepared by coating 300 mesh Cu grids with formvar and carbon type-B, placed in clean transwells, and mounted in the exposure chambers. To maintain similar environmental conditions to cell exposures, culture media was maintained on the basolateral side of the inserts during collection. However, to reduce direct exposure of the grids to the media, the volume was reduced to 12 mL per chamber. Grids were exposed to aerosols for 4 h under the same conditions as the cell exposures. Due to the ubiquity of siloxane sources among people who use personal care products, it was possible that silicon-containing compounds could be exposed in the preparation and processing of formvar-coated grids. To verify that silicon-based materials collected on TEM grids were derived from the OFR system, a single grid in a clean transwell was placed next to the exposure system to sample lab air during particle collection in the Vitrocell system. After exposure, the grids were placed in a HEPA-filtered biosafety cabinet overnight to evaporate excess moisture. The samples were then analyzed for particle size and elemental composition using a JEOL JEM-2100F field

emission TEM with an EDS system (Noran Nanotrace with NORVAR window). TEM images were analyzed using ImageJ software<sup>140</sup> to determine the diameters of individual particles and EDS spectra were analyzed using Noran System Six.

Testing the time-resolved concentration of 0.3 – 20  $\mu\text{m}$  particles with a GRIMM 1.108 aerosol spectrometer showed that agitation of the Carulite denuders could produce airborne dust in the system. Therefore, contamination from Cu and Mn containing dusts was tested for by chemical analysis of a filter sample, and by inspection of EDS spectra for Cu and Mn contamination. A 0.8-micron mixed cellulose ester (MCE) membrane filter was inserted after the denuders and sampled for 90 h at a flow rate of 1.95 LPM. The filter was digested and analyzed by inductively coupled plasma optical emission spectrometry (ICP-OES) at the State Hygienic Laboratory of the University of Iowa using a modified NIOSH 7300 method. Briefly, filters were treated with 3 mL of concentrated nitric acid and heated at  $98 \pm 5^\circ\text{C}$  in a hot block until the volume was reduced to approximately 0.5 mL. Another 3 mL of concentrated nitric acid was added, and the volume was again reduced to 0.5 mL. Samples were removed from the hot block and the volume was brought up to 25 mL using 5%  $\text{HNO}_3$ , 5%  $\text{HCl}$ . Analysis was performed on an ICP-OES instrument (Perkin-Elmer, Optima 5300DV) using external calibration with matrix-matched standards. Spectral interferences were minimized using inter-element correction factors and background correction.

To minimize non-D5 sources of elemental silicon causing false readings, silicon conductive tubing was minimized, with its only use in flexible adaptors to and from the Vitrocell manifold and connections to and within the SMPS system. A copper tube was

used to connect the Vitrocell manifold effluent to the SMPS. The remainder of the system used Teflon tubing.

To measure the role D5 plays in particle formation in the system, experiments were performed with the OFR operating, but with a feed stream containing no D5. This was accomplished by closing the valve connecting the liquid D5 evaporation tube to the humidified air stream. The remaining experimental parameters were left unchanged, and particle analysis was performed using the SMPS.

### 2.2.2 Cell Culture Preparation

A549 cells (ATCC) from passages 5-15 were cultured in RPMI 1640 (Gibco) medium supplemented with 10% FBS (Atlanta Biologicals, lot C0089) and 1% penicillin-streptomycin, then incubated at 37°C in a humidified 5% CO<sub>2</sub> environment. Upon reaching confluence (5-7 days), cells were rinsed with phosphate-buffered saline (PBS) and treated with a 0.25% Trypsin-EDTA solution (Gibco) for 8 min to dissociate cells. Cells were suspended in culture medium and 0.5 mL aliquots were seeded onto 12 mm transwell inserts (Corning, 0.4 µm pore size, polycarbonate) at a concentration of  $1.25 \times 10^5$  cells/mL with 0.53 mL of modified RPMI 1640 under the basal side of each transwell. The cells were grown to confluency under submerged conditions for 24 h. The apical media was then aspirated, and cells were allowed to adapt to an air interface for 12 h according to previously established methods.<sup>141, 142</sup>

### 2.2.3 Cell Exposures

The aerosol generation system was brought online 14-24 h prior to cell exposures (water bath temperature set at 40 – 55°C). Three hours before cell exposure, the D5

temperature was increased to its operational temperature of 70°C, and approximately 2 h before exposure, denuders and ring flow were added.

Six transwells were mounted in a Vitrocell 12/6 air-liquid interface exposure chamber (Vibrocell Systems, Waldkirch Germany) with 16 mL of culture medium under the basal side in each compartment. The chambers were maintained at 37°C by circulating heated water through the stainless-steel jacket surrounding the chambers. The exposure system was set up using the glass manifold distributor as described previously.<sup>142</sup> The humidified, CO<sub>2</sub>-enriched inlet stream passed into the Vitrocell manifold distributor at a flow rate of 2.4 – 2.7 L/min. The concentration of particles in the gas phase averaged 150 µg/m<sup>3</sup> as measured by SMPS. The aerosol flow delivered to the cells (5 mL/min) was regulated by separate mass flow controllers (GFC17, Aalborg Instruments) downstream of the exposure chambers. Assuming a deposition efficiency of 70%, based on previous characterization of the Vitrocell system,<sup>142</sup> the average expected dose was 364 ng per transwell after 4-h exposure. The 4-h exposure time was selected from pilot studies incubating cells in the Vitrocell system under filtered air supplemented with 5% CO<sub>2</sub> at experimental flow rates. Exposure times greater than 4 h resulted in viability losses in these pilot studies, whereas no viability losses were observed at 4 h. The outlet streams from the six mass flow controllers were combined, filtered through a HEPA filter, and vented to a fume hood. Control experiments were run to determine the role of gas-phase components generated in the OFR by filtering out aerosols via a HEPA filter (TSI 1602051) placed after the denuders and exposing the cells to particle-free OFR effluent.

After exposure to the particle-laden effluent, particle-free effluent, or D5 in PBS, cells were gently rinsed with 500  $\mu$ L of PBS and the PBS collected and centrifuged at 14,000 $\times$ g for 30 min to remove cell debris. The supernatant was stored at -80°C for analysis of inflammatory markers. The cells were immediately processed to determine cell viability.

#### 2.2.4 Cell Responses to Oxidized D5 Aerosols and Gaseous Products

Cells were assessed to measure effects of exposure on cell viability using an MTS proliferation assay (Promega), a colorimetric assay for assessing cell metabolic activity. Prior to running the assay, transwells were treated with 250  $\mu$ L of PBS-based, enzyme-free, cell dissociation buffer and incubated for 8 min at 37°C. Culture media (250  $\mu$ L) was then added to each transwell, pipetted multiple times to loosen cells, and 100  $\mu$ L aliquots transferred to a 96-well plate. Negative controls were cells exposed to clean air and positive controls were cells exposed to 250  $\mu$ L of a 2% sodium dodecyl sulfate (SDS) solution in PBS. Each well was measured via absorption spectrometry at a wavelength of 490 nm (SpectraMax 384 Plus, Molecular Devices, and Epoch, BioTek). Absorbance values were normalized to controls to assess the relative viability of exposed to unexposed cells.

Cellular generation of inflammatory cytokines, tumor necrosis factor-  $\alpha$  (TNF- $\alpha$ ) and interleukin-6 (IL-6), were measured using ELISA kits (Life Technologies). Positive controls were cells exposed to lipopolysaccharide (LPS) from Gram-negative bacteria, a known inducer of inflammation.<sup>138</sup> A549 samples grown on transwells were exposed to 500  $\mu$ L of 10-40  $\mu$ g/mL LPS (L 2880, Sigma) in 90% PBS with 10% Hanks buffered salt solution (HBSS) for 6 h.

## 2.3 Results and Discussion

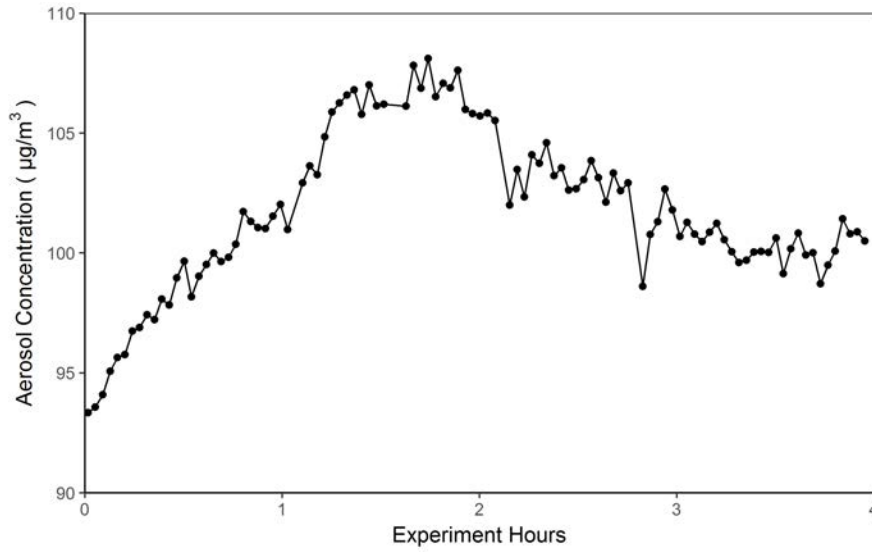
### 2.3.1 Exposure Characterization

The environmental relevance of the OFR has been demonstrated through correlation of aerosol-OH reaction time with photochemical age in the atmosphere by normalizing against measured diurnal OH averages.<sup>136</sup> In the current study with a flowrate of 5 lpm through the OFR and an OH concentration of  $\sim 10^{10}$  molec/cm<sup>3</sup>, we estimate the OH exposure to be equivalent to  $\sim 17.6$  days of atmospheric aging. This is not unreasonable given that D5 has a lifetime of  $\sim 10$  days in the atmosphere.<sup>114</sup>

The OFR and denuder system produced stable aerosol samples with low ozone concentrations. Typical aerosol number and mass concentrations measured downstream of the denuders and the Vitrocell manifold by SMPS were  $2.8 \times 10^5 - 1.2 \times 10^6$  cm<sup>-3</sup> and  $82 - 220$   $\mu\text{g}/\text{m}^3$ , respectively. This measurement reflects the concentration and size distribution of particles flowing through the Vitrocell after any losses caused by the denuders. Figure 2.2a shows typical temporal variability of mass concentration from the OFR over the course of a 4-h cell exposure period. The OFR aerosol output was stable during cell viability or microscopy experiments. Aerosols generated in the OFR could be removed by placing a HEPA filter inline after the OFR output (Figure 2.2b), suggesting that particles were outside than 0.2-0.3  $\mu\text{m}$  range at which HEPA filters are least efficient<sup>143</sup>. Negligible particle counts were observed when humid air (no D5) flowed through the OFR while the UV lamps were activated, indicating that the OFR itself did not produce aerosol particles, and when air flowed through the system with the OFR off, indicating that the air stream did not contain significant quantities of particles. Additionally, no particles were detected when D5 flowed through the system with the UV lights off (data

not shown), signifying that aerosol particles were only generated when D5 was exposed to UV light in the OFR.

a)



b)

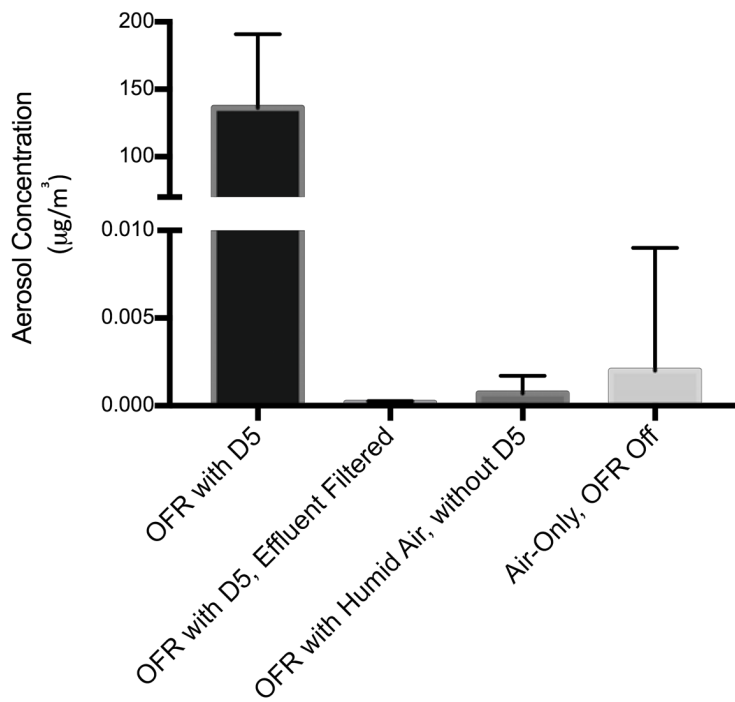




*Figure 2.2 Characterization of aerosol particles generated from the OFR. (a) Representative plot of mass concentration throughout a single experiment (from SMPS). (b) Average concentrations (from SMPS) of aerosol particles formed under different reactor conditions (error bars are equal to the standard deviation of the individual concentrations measured every 135 s during each experiment).*

Figure 2.3 shows a comparison of electron micrographs of aerosols exhausted from the Vitrocell manifold via collection in the TPS sampler (a and b) and aerosols deposited in the Vitrocell system via collection by sampling onto TEM grids in the Vitrocell wells (c and d). Particle agglomerates or clusters of particles consisting of 2-30 primary particles, as well as a few lone particles, were observed at both sampling locations. In many of the images agglomerates can be seen where the primary particles have distinct borders (Figure 2.3c), while other agglomerates consisted of particles with poorly defined boundaries as illustrated in Figure 3d. Indistinct boundaries as shown in Figure 2.3d may indicate liquid or partially liquid particles. Both microscopy labs found that particles demonstrated stability under temporary storage (5-days).

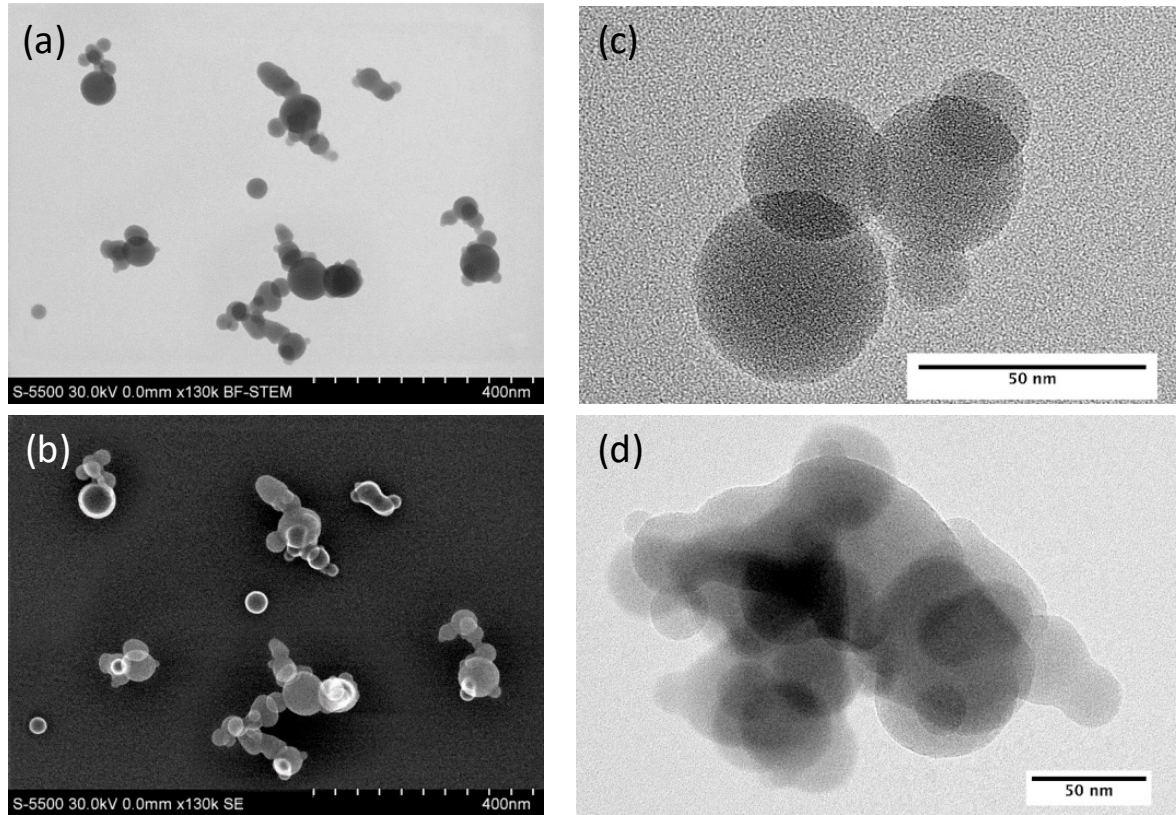
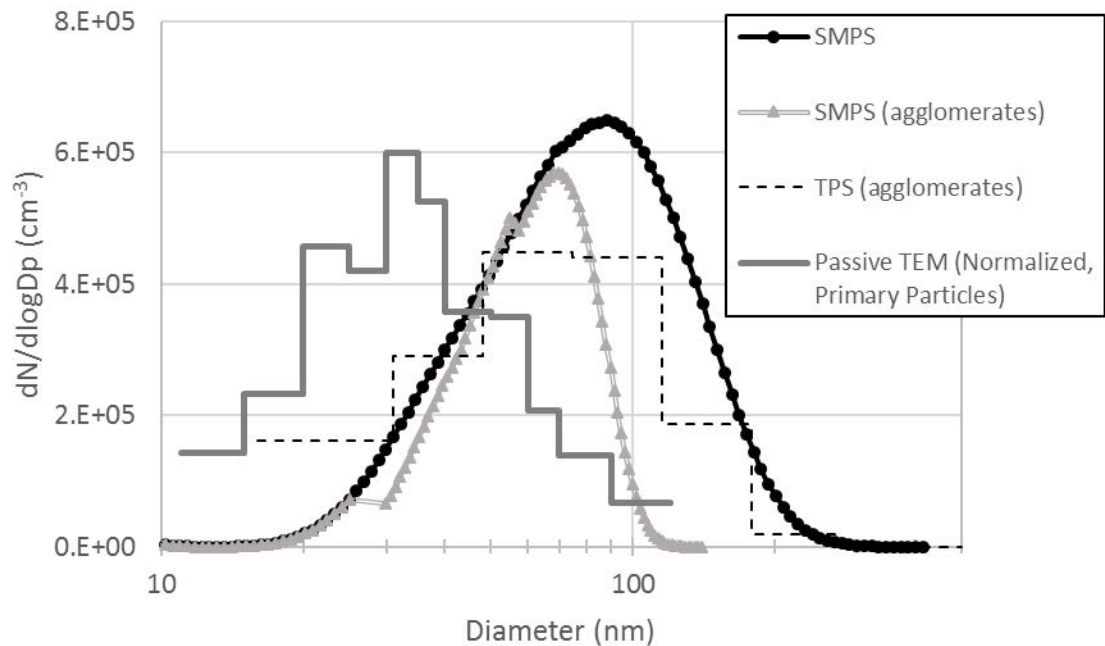


Figure 2.3 SEM and TEM images establishing particle morphology of the generated particles. SEM images of TPS samples are shown for (a) bright field and (b) secondary electron image, while TEM images of passive TEM samples are shown in (c) and (d). Panels (c) and (d) contrast two types of particles imaged by TEM – some had distinct boundaries, while others had indistinct borders.

Figure 2.4 shows the aerosol size distribution measured during experiment 12, where the particle size distribution and morphology was assessed by SMPS, TPS sampling, and passive TEM sampling. All size distributions are shown, after converting to a normalized concentration size distribution function ( $dN/d\log D_p$ ). Two SMPS size distributions are shown – one uses the measured electrical mobility diameter (labeled SMPS), while the other uses a calculated equivalent volume diameter assuming agglomerates with primary particle diameter of 25 nm (based on the most prevalent

primary particle size observed in the passive TEM analysis). For the equivalent volume diameter, SMPS number concentration data was reanalyzed using the Spectrometer Nanoparticle Aggregate Mobility Analysis Software Module distributed with Aerosol Instrument Manager v10.2 (TSI Inc). This software can correct SMPS data to account for agglomerates using a user-provided primary particle size.

The aerosol size distribution mode in these analyses varied between 32 – 89 nm. For non-agglomerated spherical particles, the electrical mobility and volume equivalent diameter are equal. Accordingly, the shift in the size distribution based on equivalent volume diameter to smaller sizes shows the sensitivity of the distribution to particle morphology. Previous reports of Si-containing aerosols identified particles in the 20-50 nm range,<sup>118, 144</sup> which are similar to the particles produced in the OFR with D5.



*Figure 2.4 Intercomparison of particle size distributions and size-resolved concentrations from experiment 12, which included SMPS, TPS sampling, and passive TEM sampling. The SMPS diameters are electrical mobility diameters; the SMPS (agglomerates) diameters are equivalent volume diameters of the agglomerate converted to number concentration with an assumed primary particle size of 25 nm; the TPS diameters are projected area diameters of agglomerates; the passive TEM diameters are projected area diameter of primary particles (not agglomerates). The passive TEM size distribution has been normalized to a maximum of  $6 \times 10^5 \text{ cm}^{-3}$ .*

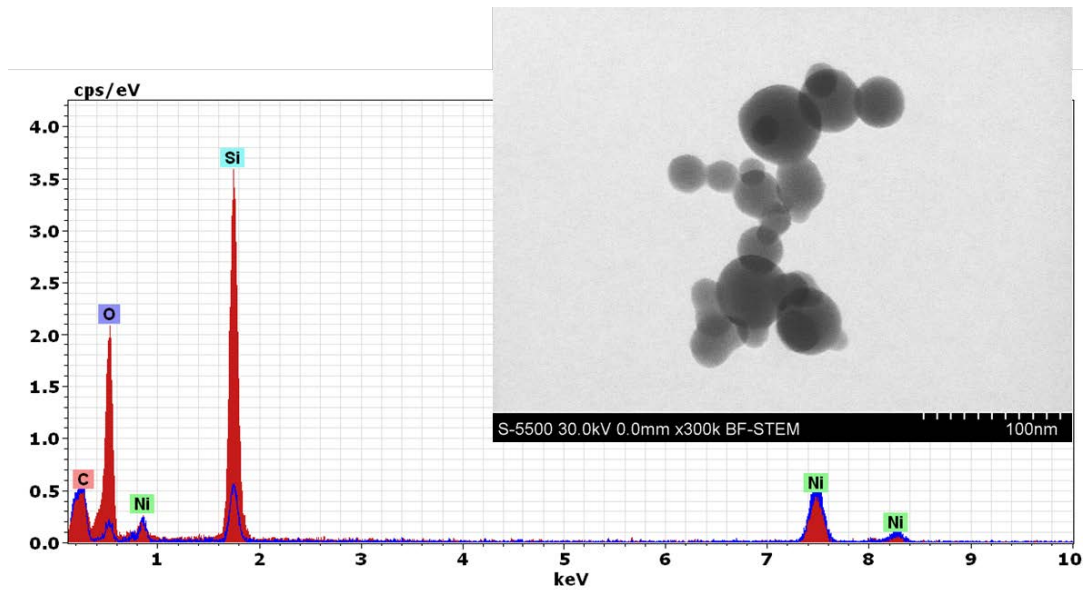
Projected area diameters were measured using ImageJ on the TPS samples for 1412 structures including agglomerates. The SMPS and TPS size distributions are relatively similar in total number and size distribution. The diameters obtained from the passive TEM samples ranged widely from about 10-100 nm, with a count median diameter of the 214-particle population of 31 nm. As the TEM sizes are based on measurement of primary particles making up the agglomerates using ImageJ (projected area diameter of 214 particles), agreement with the distributions based on the agglomerates is not expected.

The chemical composition of particles containing siloxanes was confirmed in both the TPS samples and passive TEM samples measured by EDS, both indicating strong silicon and oxygen signatures (Figure 2.5). Silicon and oxygen were uniformly distributed within the particles at high concentration compared to the background, whereas carbon, a component of the grid, was uniformly distributed across the scan area (Figure 2.5b). This composition is consistent with aerosols formed primarily from oxidized derivatives of D5. Background peaks consistent with the nickel TPS grid and the copper passive TEM grid were evident in the spectra. In addition, the carbon film on the

TPS grids and formvar coating on the passive TEM grids created background carbon signals.

O<sub>3</sub> was removed from the reactor outlet stream using Carulite 200 denuders and an activated carbon denuder as as ozone is known to damage lung cells.<sup>145-147</sup> Typical O<sub>3</sub> concentrations downstream of the denuders was 2.5 ppb. Peak O<sub>3</sub> concentrations (20-s averaging) were 5 ppb when limiting analysis to cell exposure periods only, and 43 ppb considering all denuded OFR effluent. As the Carulite used in the denuders is a manganese dioxide/copper oxide catalyst, we further tested the OFR effluent to ensure no catalyst contamination was present. ICP-OES analysis of filter samples found both components to be below detection limits, 0.3 and 0.5 µg/m<sup>3</sup> for Cu and Mn, respectively.

a)



b)

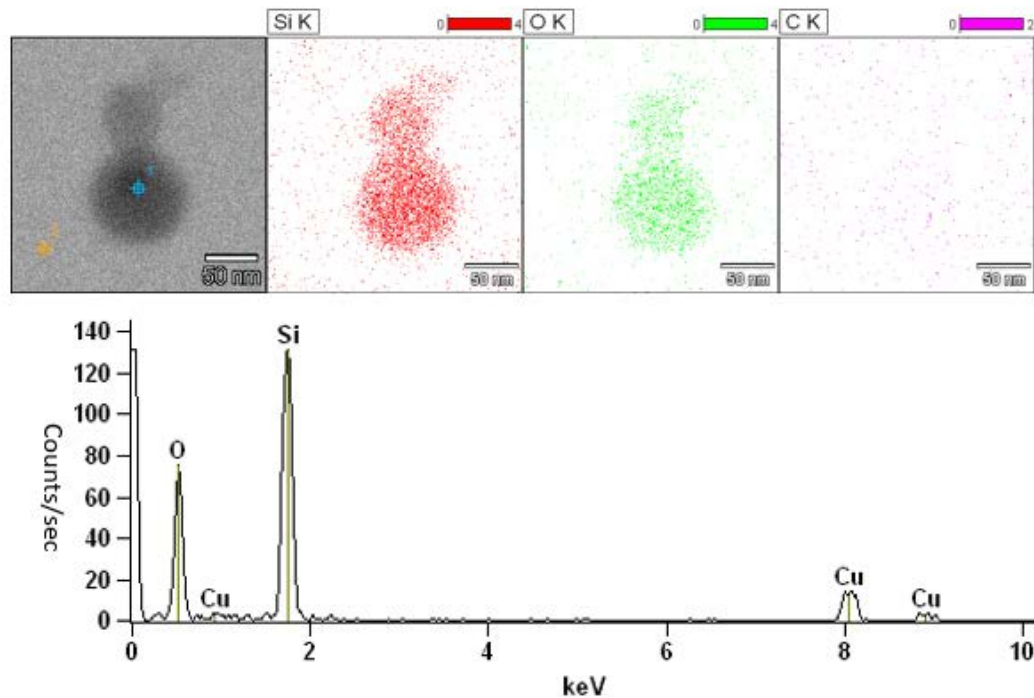


Figure 2.5 EDS analysis of the chemical composition of particles from (a) TPS sample of Vitrocell exhaust and (b) passive TEM sample of aerosols deposited in Vitrocell wells. (a) EDS analysis of a particle agglomerate (see inset) collected during TPS sampling is shown in red and background grid is shown in blue. (b) Original electron micrograph illustrating the EDS sample region selection (blue crosshair) and comparative background region (orange crosshair) (bar = 50  $\mu\text{m}$ ); element mapping of silicon, oxygen, and carbon (bar = 50  $\mu\text{m}$ ); and EDS spectra of a particle obtained by passive TEM sampling confirmed that deposited aerosols are derived from siloxanes.

EDS analysis of deposited aerosols (Figure 2.5) also indicated no signs of contamination by Cu- and Mn-containing particles. No Mn was detected in any of the six TPS samples. A small Cu peak was observed for some samples, likely originating from the sample holder. TEM-EDS analysis of the passive TEM samples collected in the Vitrocell chamber also did not detect Mn. A strong Cu signal was present in the spectra due to generation of extraneous X-rays from the Cu TEM grid.

### 2.3.2 Cell Responses to Oxidized D5 Aerosols and Gaseous Products

Exposure to OFR effluent reduced viability in A549 cells compared to no-exposure controls (Figure 2.6). Contributions from the secondary aerosols generated from D5 were not significantly different from the OFR effluent effects on viability. Furthermore, no dose-dependence in cell toxicity was observed (Figure 2.6b). Losses in viability were observed when the OFR product stream was filtered to remove aerosols. When cells were exposed to OFR effluent, but with the OFR lamps not on, no reduced viability was observed (data not shown). These results imply that photooxidation reactions occurring in the reactor are producing one or more gaseous products that are both toxic to cells and not fully removed by the denuders. The three primary products of this OFR are  $O_3$ ,  $OH$ , and  $HO_2$ ,<sup>131, 135</sup> while measurement and catalytic removal of  $O_3$  was performed, the quantities of  $OH$  and  $HO_2$  in the reactor effluent were not quantified. These reactive oxygen species are known to be toxic to cells, which indicates that  $OH$  and  $HO_2$  are likely contributors to the reduced viability observed in the absence of particles. In a similar set of experiments using this reactor system, losses of viability in A549 cells were not observed after exposure to filtered reactor effluent.<sup>148</sup> Other notable differences in that study include a different exposure system and a different approach to viability measurements (testing 24 hours after exposure rather than immediately). These results suggest that aerosols produced from oxidized D5 derivatives are not likely to be highly toxic, though they may be responsible for some of the observed decrease in cell viability.

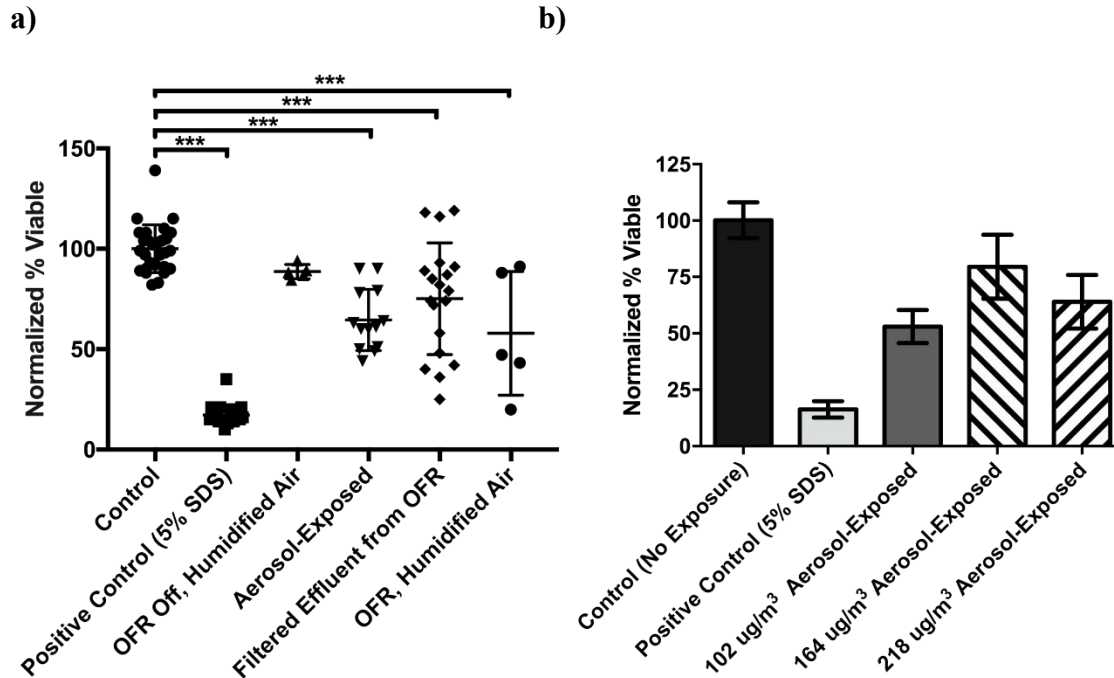


Figure 2.6 (a) Relative viability of cells exposed to filtered gases from the OFR ( $n=4$ , 5 replicates each), or OFR-generated aerosols ( $n=3$ , 5 replicates each) compared to no exposure and SDS controls (\*\*\*)  $p < 0.001$ . (b) Effect of dose dependent aerosol-exposure on relative viability of cells. Error bars=SD.

Cellular stress and damage may occur in cases where death does not occur; in those instances, cells may exhibit signs of inflammation indicative of that stress.<sup>149</sup> Two markers of inflammation released as a stress response in A549 cells are TNF- $\alpha$  and IL-6.<sup>150, 151</sup> TNF- $\alpha$  secretion increases flow from the blood to the tissue to bring innate immune proteins and immune cells into the space, while IL-6 activates white blood cells and signals antibody production.<sup>83</sup> After 4-h exposure to oxidized-D5 aerosols, no increase in secretion of TNF- $\alpha$  or IL-6 was observed. However, after exposure to LPS, a dose-dependent response of IL-6 was elicited (Figure 2.7). LPS failed to elicit a measurable response of TNF- $\alpha$  in the same cases (data not shown). These results indicate that the cytotoxicity measured in acutely exposed cells was not accompanied by a pro-inflammatory response.



For future studies with the OFR, especially those involving cell or animal exposures to determine toxicity, it is critical that the gas-phase components of the reactor effluent be well-characterized. Use of an in-line GC-MS may elucidate the gas-phase components and provide insight into the cause of the observed toxicity.

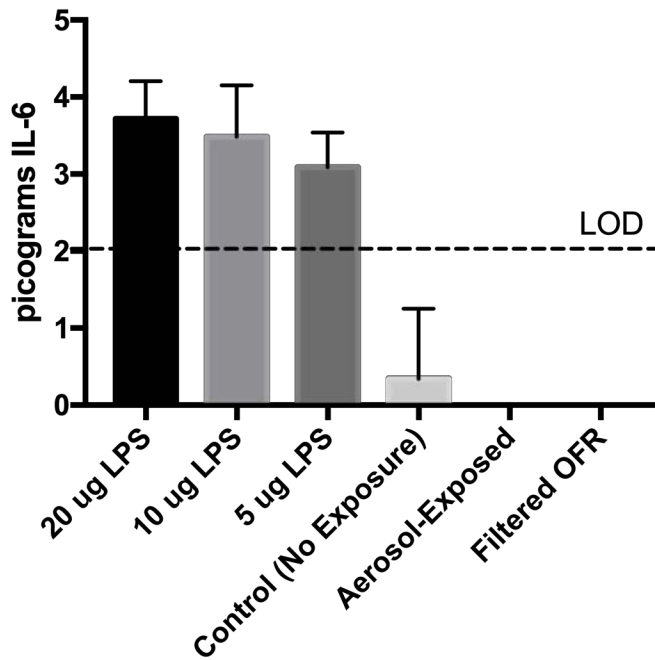


Figure 2.7 Concentration of IL-6, a cytokine marker for inflammation, in supernatants collected from A549 cells after exposure to aerosols ( $n=3$ , 5 replicates each) or gases ( $n=4$ , 5 replicates each) generated in the OFR reactor. Error bars=SD.

## 2.4 Conclusions

While many chemicals become more toxic after oxidation, this effect was not observed with D5. Aerosols that form after photooxidation of D5 under laboratory conditions were found to have no significant impact on lung cell health. The aerosols generated herein were found to be similar to those observed in the environment, indicating that the OFR-generated aerosols are likely representative of the atmospheric

aerosols. Further exploration of the health impacts of these aerosols in an *in vivo* model should be performed to identify if toxicity occurs in other organs or at the systemic level.

### 3 CuO Nanoparticle Exposure Reduces Lung Cell Viability and Upregulates PAFR

#### 3.1 Introduction

The airways have a wide range of defenses to protect the human body from assault by pathogens and foreign material, including mucociliary clearance, macrophage and neutrophil clearance or killing, and production of defense molecules such as antimicrobial and antiviral agents. However, lung infections remain a major cause of morbidity and mortality in the world, especially for young children, and these infections can be exacerbated by inhalation of a variety of indoor and outdoor pollutants. The World Health Organization (WHO) recently reported that the risk for lower respiratory tract infections in children under the age of 5 was 3-times greater at high levels PM<sub>2.5</sub> exposure (in the range of 250-600 µg/m<sup>3</sup>) and remained 2-times greater when PM<sub>2.5</sub> exposure was decreased to ~100 µg/m<sup>3</sup>.<sup>152</sup>

One way that bacteria and viruses evade the lungs' natural defenses is by binding to the lung tissues, which anchors the pathogens in the lungs. A variety of phylogenetically distinct respiratory bacterial pathogens, such as *Streptococcus pneumoniae*, non-typeable *Haemophilus influenzae*, and *Acinetobacter baumannii*, invade host cells in the airways by binding to the platelet-activating factor receptor (PAFR) on the cell surface. This process is mediated by interaction of host PAFR with surface lipooligosaccharides containing phosphorylcholine (ChoP), a molecular mimic of platelet activating factor (PAF), expressed on the bacterial surface.<sup>153-156</sup> Cellular uptake of these pathogens is dependent on the ChoP content of the bacterial surface, with higher ChoP content promoting colonization and persistence in the lungs. ChoP expression also

reduces opsonization of bacteria and delays pulmonary clearance, which enables bacteria to remain in the lung space longer.<sup>157</sup>

Recent in vitro studies have found that PAFR is upregulated in human lung cells after exposure to urban particulate matter (PM), cigarette smoke, and e-cigarette vapor.<sup>7-9</sup> Mushtaq et al. found that urban PM<sub>10</sub> and PM<sub>2.5</sub> enhance adhesion and intracellular penetration of *S. pneumoniae* in a dose-dependent manner in A549 cells and primary bronchial epithelial cells.<sup>10</sup> Bacterial penetration was not associated with changes in lung cell viability or metabolic stability; thus, cell damage was not the cause of enhanced penetration. Bacterial adhesion was attenuated by PAFR antagonists, confirming the role of the PAF receptor in mediating adherence. A follow-up study by the same group produced similar findings with PAFR upregulation in lung cells and an increase in *S. pneumoniae* adhesion following cell exposure to cigarette smoke.<sup>11</sup> Again bacterial adhesion was attenuated by PAFR antagonists. Additionally, an increase in PAFR transcription was observed in mice exposed to cigarette smoke, as well as in active human smokers (compared to those who have never smoked), suggesting a link between foreign materials in the lungs and bacterial infection through PAFR upregulation. In a more recent study, this group observed upregulation of PAFR in humans, A549 cells, and mice after exposure to e-cigarette vapor.<sup>9</sup> Mice were also found to be more susceptible to *S. pneumoniae* infection after exposure to the e-cigarette vapor.

The degree of PAFR upregulation in lung cells exposed to PM was dependent on the source, with differences observed between PM obtained from the UK compared to Ghana.<sup>10</sup> This suggests that the chemical makeup of PM has a direct impact on the ability of PM to modulate susceptibility to infection. While the composition of urban particulate

matter and cigarette smoke are complex, potential sources of PAFR upregulation are carbonaceous particles or metals present in both sources. One common metal nanoparticle emission is copper oxide, which has become relevant because of its use and synthesis in metal catalysts, heat transfer fluid, semiconductors, and antimicrobial preparations.<sup>158, 159</sup> Metal oxide nanoparticles, particularly those made of copper oxide, have been shown to increase pulmonary risk of infection to gram-negative bacteria in mice, further implicating this species.<sup>160</sup> Finally, copper was identified as a component in e-cigarette vapor associated with upregulated PAFR expression.<sup>9</sup>

In the current work, the potential for CuO nanoparticles to enhance pneumococcal infection in lung cells *in vitro* via PAFR upregulation was determined. The dose-dependent viability, PAFR expression, and level of bacterial infection of A549 human lung epithelial cells was evaluated upon CuO nanoparticle exposure. Cellular uptake of copper was also measured to assess the level of CuO entry into lung cells. The role of PAFR in cell infection was confirmed by attenuation of infection using PAFR antagonists.

## **3.2 Materials and Methods**

### **3.2.1 Particle Preparation**

Copper oxide (CuO) nanoparticles (Nanoscale and Amorphous Materials, Lot: 0296JY), were weighed and suspended in 1 mL of RPMI 1640 (sans serum and antibiotics) immediately prior to exposure. To ensure particles were well-dispersed, they were alternatively mixed using a sonic bath and a vortex mixer (> 5 cycles) until the suspension became fully opaque, ink-black in appearance. After dispersion, nanoparticles were further diluted to working concentrations (0.005-2 mg/mL) in RPMI 1640. Fresh

nanoparticle suspensions were prepared directly prior to each experiment to minimize dissolution effects and contributions of soluble copper.

### 3.2.2 Particle Imaging with TEM

The size and morphology of CuO nanoparticles were analyzed by transmission electron microscopy (TEM). TEM grids were prepared by coating in formvar to create an electron-transparent substrate to support the particles. A clean glass microscope slide was coated in formvar by dipping into a formvar solution in ethylene dichloride. After drying, the corners of the slide were abraded using a razor to separate the formvar on the two broad faces of the slide from the edges. The slide was inserted vertically into the water causing the coating to float away from the sides of the slide onto the water's surface. 300-mesh copper TEM grids were gently placed onto the formvar film. Parafilm was placed on top of the grids, sandwiching them between the formvar and parafilm. The coated grids were collected by perforating the formvar in a circle around each grid and gently lifting them from the parafilm with tweezers.

Nanoparticle samples were prepared by placing droplets of the CuO suspensions in RPMI 1640 onto formvar-coated TEM grids for 30 sec, then gently wicking the liquid away with clean filter paper. Dilutions of CuO ranging from 0.001-0.1 mg/mL were used to find an optimum density of particles in the TEM field to image. Grids were allowed to dry for 24 h on a clean piece of filter paper with a glass dish above to prevent ambient dust from settling onto them. The grids were imaged using a JEOL-JEM-1230 Transmission Electron Microscope, with image analysis performed using ImageJ.<sup>140</sup>

### 3.2.3 Cell Culture Preparation

Immortalized alveolar epithelial cells, A549 (ATCC), were cultured adhered in T75 flasks (Gibco) using RPMI 1640 (Gibco) supplemented with 10% FBS (Atlanta Biologics) and 1% penicillin/streptomycin (Gibco). Cells were maintained in a humidified 37°C cabinet with 5% v/v CO<sub>2</sub>. When cells were mostly confluent, 4-7 days after inoculation, they were rinsed with sterile phosphate buffered saline (PBS, Gibco) and treated with 3 mL of 0.25% trypsin with ethylenediaminetetraacetic acid (EDTA) (Gibco) for 8 min at 37°C to dissociate cells. 10 mL of culture media was added to stop the trypsinization. The cell suspension was gently mixed until well-dispersed, and a 20 µL sample was removed for counting. To this, 20 µL of trypan blue solution was added as a live/dead indicator. Samples were loaded onto a hemocytometer slide and four 1x1 mm areas were counted. The concentration of cells was determined using the equation:

$$\text{Concentration} \left( \frac{\text{cells}}{\text{mL}} \right) = \# \text{ of cells counted} * \frac{2 (\text{dilution factor in Trypan Blue})}{4 (\text{number of quadrants counted})} * 10,000 \text{ cells/mL}$$

Using the concentration determined by hemocytometry, the cell suspension was diluted with culture media to a concentration of  $2 \times 10^5$  cells/mL and seeded onto 12-well tissue culture plates in 1 mL aliquots. These plates were incubated overnight to allow cell attachment.

Although the process of aliquoting out multiple plates of cells occurred quickly, lasting approximately 5 min, it was noted that the cell density from plate to plate was inconsistent when a large volume of cell suspension at  $2 \times 10^5$  cells/mL was prepared and used for all 4 plates. This was attributed to the settling of cells in the suspension creating concentration gradients. Much less plate-to-plate variation was observed when 13-14 mL

of suspension was prepared for each plate immediately prior to the plate being seeded. This was accomplished by inverting the high-concentration stock suspension 5 times to ensure good dispersion, followed by immediate transfer of an inoculation and dilution in fresh culture media.

### 3.2.4 Cell Exposure to Nanoparticles

A549 cells were rinsed three times in sterile PBS to remove the culture media, then exposed to 1 mL doses of nanoparticle suspensions ranging from 0.005-2 mg/mL in RPMI 1640. Initially, each plate received 4 doses in replicates of 3, but eventually the dosing regimen was altered to 3 doses of 4 replicates per plate to increase available material for analysis. These samples were incubated for 4 h, then rinsed three times with sterile PBS to remove excess particles. Samples were photographed at 200× magnification through the eyepiece of an Axiovert 25 invert microscope using a Nexus 5x camera.

### 3.2.5 CuO Uptake Measurement

After exposure to CuO nanoparticles, A549 cells were removed from the well plates using 0.25% trypsin-EDTA cell dissociation buffer and collected into microcentrifuge tubes. The tubes were centrifuged at 1,000×g for 5 min, and the supernatant removed. Samples were stored at -20°C until transportation. Cu content in each sample was measured by inductively coupled plasma mass spectrometry (ICP-MS) at the State Hygienic Lab at the University of Iowa.

Lung cells were digested in nitric acid and hydrogen peroxide. A 50% solution of nitric acid was prepared by mixing equal volumes of concentrated nitric acid (Fisher A467, Optima grade) and reagent water (18 MΩ). Previously collected cells were



submitted for analysis in 1.5-mL microcentrifuge tubes. To each tube was added 500  $\mu\text{L}$  of the 50% nitric acid solution. A reagent blank was prepared containing only the 50% nitric acid. A laboratory control sample was prepared containing the 50% nitric acid and spiked with 0.1  $\mu\text{g}$  of copper derived from a commercially prepared copper standard (SPEX, PLCU1-2X). The tubes were placed in a water bath at 85-90°C for 1 h. After cooling for 20 min, 100  $\mu\text{L}$  of 30% hydrogen peroxide was added and the tubes were heated for another 1 h. After cooling, samples were diluted to 1.0 mL using reagent water.

Copper was determined at the State Hygienic Lab using a Perkin Elmer NexION 350D, Inductively Coupled Plasma Mass Spectrometer (ICP-MS). Intermediate working calibration standards were prepared from a commercial stock solution in 2% (v/v)  $\text{HNO}_3$  (Fisher Trace Metal Grade or equivalent) at 0, 5, 50, 100, 250, and 500  $\mu\text{g}/\text{L}$ . Working standards and samples were diluted 10-fold with an internal standard solution composed of 2% (v/v)  $\text{HNO}_3$  and 10  $\mu\text{g}/\text{L}$  rhodium. Compensation for the higher acid concentration in the samples is outlined in Table 3.1.

*Table 3.1 Approach to dilution of standards and samples to compensate for higher acid concentration in samples.*

Solution type	mL of 20% $\text{HNO}_3$	mL of 2% $\text{HNO}_3$	mL of internal standard	Total volume (mL)
Standards	0.5	-	4.0	5.0
Samples	-	0.5	4.0	5.0

Instrument settings are shown in Table 3.2. Selected calibration standards were analyzed as samples at the beginning and end of the run to validate accuracy of the calibration and a second-source copper standard was prepared at 100 µg/L and analyzed as a sample to validate the calibration source.

Table 3.2. Instrument settings for ICP-MS.

Parameter	Setting
Rf Power	1450 W
Ion lens voltages	Optimize for sensitivity
Sweeps / reading	30
Readings / replicate	1
Replicates	3
Isotopes monitored	<sup>63</sup> Cu, <sup>65</sup> Cu, <sup>103</sup> Rh
Dwell time	100 ms for Cu, 50 ms for Rh
Scan mode	Peak hopping
Detector mode	Dual
Blank subtraction	After internal standard

### 3.2.6 Cell Viability Analysis

Cell viability after exposure was measured using the MTS assay (Promega CellTiter 96) according to the prescribed protocol. Briefly, a 1:5 mixture of assay reagent and culture media was prepared, and 500 µL of this mixture was added to each well. The plates were incubated for 1h, and four 100 µL aliquots were transferred from each well to

96-well plates for measurement in a Biomate Epoch well plate reader. Absorbance was measured at 490 nm to determine relative viability of cells.

### 3.2.7 Evaluation of PAFR Expression

To assess whether PAFR expression in lung cells was affected by copper oxide, PAFR was measured in cells exposed to varying doses of CuO nanoparticles. Cells exposed to CuO nanoparticles for 4 h were gently rinsed three times with 400  $\mu$ L of PBS to remove loose particles. Cells were immersed in 500  $\mu$ L of cold (4°C) NP-40 lysis buffer for 15 min. NP-40 lysis buffer was prepared using 150 mM NaCl (RPI), 50 mM Tris-Cl (RPI), and 1.0% Nonidet P-40 substitute (RPI) according to existing protocols.<sup>161</sup> After lysis, cell debris was scraped and collected from well plates. Cell lysates were agitated for 30 min at 4°C to extract proteins. Coarse cell material was separated from dissolved proteins using a centrifuge at 14,000 $\times$ g for 30 min cooled to 4°C. The supernatants were collected and stored at -80°C until analysis by western blot.

To determine dose-dependent changes in lung cell PAFR expression due to CuO nanoparticle exposure, cellular expression of PAFR was measured by western blot. Detailed protocols have been previously described.<sup>162</sup> The anti-PAFR polyclonal antibody from AbCam (#ab104162) served as the primary antibody for cell experiments.<sup>163, 164</sup> Secondary antibody for detection was an Anti-rabbit IgG-Horseradish Peroxidase conjugate. Cell lysates were prepped and normalized for protein content using a Bradford Protein Quantification assay (DC Assay, BioRad). Proteins were run on SDS-PAGE for separation by size and transferred to Immobilon (Millipore) Poly membrane using the wet sandwich method. The membrane was blocked with bovine serum albumin, washed, and incubated with anti-PAFR antibody overnight. The next day, membranes

were washed, and the secondary antibody added. Following secondary antibody incubation, the membranes were washed and developed using SuperSignal Pico ECL reagent for visualization on a gel imaging station equipped with an ultra-sensitive CCD camera for ECL detection. Results were normalized to actin to account for differences in total protein expression in various samples.

### 3.2.8 CuO Effects on Cell Susceptibility to Infection

PAFR has already been implicated as a pathway for increased pathogenicity of certain bacteria in the lungs. This study aims to determine whether changes in lung cell PAFR regulation due to exposure to CuO nanoparticles is correlated with increased susceptibility to infection with a PAFR-targeting bacterium. A pathogenic strain of *Streptococcus pneumoniae*, D39 (virulent strain type 2, NCTC 7466, obtained from NHS), was chosen as it has been widely used in the study of the pathogenesis of pneumococcal disease.<sup>165</sup> In addition, it has been used in adhesion studies to A549 cells after smoke exposure.<sup>7</sup> *S. pneumoniae* were grown in brain heart infusion (BHI) media to the log phase, approximately 12 h after inoculation.

In toxicity studies, cell detachment from well plates was observed for higher doses of CuO nanoparticles. To reduce loss of cells, collagen coatings were added to wells prior to cell seeding to improve cell attachment. A type-1 collagen solution was prepared by dissolving 250 mg of bovine Achilles tendon in 250 mL of 0.1 M acetic acid (EMD). This 0.1% solution was sterilized by autoclave. To prepare collagen coated plates, the collagen solution was diluted in sterile water to 0.01% and 500  $\mu$ L of this solution was added to each well and allowed to coat overnight. After preparation in collagen, cells were seeded onto plates and exposed to CuO nanoparticles in the manner

described above. After exposure to CuO nanoparticles for 4 h, cells were inspected under a microscope, and were found to be adhered to wells at every CuO dose. Visible changes in cell morphology were observed for higher doses; however, this morphology shift was no longer accompanied by cell detachment in the presence of collagen-coatings.

A549 cells after exposure to CuO nanoparticles were gently rinsed three times with sterile PBS. 0.5 mL of RPMI 1640 was added to each well, and the plates were incubated briefly while bacteria were prepared. To each well 500  $\mu$ L of brain heart infusion (BHI) media with *S. pneumoniae* grown to just after log phase, approximately  $2.7 \times 10^{11}$  CFU/mL, were added, and the plates incubated for 2 h. After 2 h, unattached bacteria were removed by gently rinsing with sterile PBS. The A549 cells were lysed with cold water, scraped, and the resulting solution was centrifuged at  $6,500 \times g$ . The lysate was plated onto Columbia agar with 5% sheep blood (BD), and placed in a humidified incubator at  $37^\circ\text{C}$  supplemented with 5%  $\text{CO}_2$ . After 24 h, colonies were counted on the plates to measure infectivity.

### 3.2.9 CuO Effect on Bacterial Viability

A549 cells exposed to CuO still retain CuO nanoparticles after rinsing due to uptake and adhesion. To observe the effect these residual particles on bacterial health during infectivity studies, *S. pneumoniae* growth was measured in the presence of CuO nanoparticles at relevant concentrations. Bacteria grown to just after log phase, about 12h, and 5 mL of the suspension was diluted with 5 mL of fresh BHI media containing CuO nanoparticles. Based on ICP-MS analysis of copper remaining associated with A549 cells after exposure, the mass of CuO to which bacteria would be exposed was determined. Based on this analysis, *S. pneumoniae* were exposed to CuO concentrations

ranging from 0.05-0.6  $\mu\text{g}/\text{mL}$  and placed in a humidified incubator at  $37^\circ\text{C}$  supplemented with 5%  $\text{CO}_2$ . Optical density at 650 nm was measured every hour for three hours. Bacterial growth, relative to a particle-free control, was assessed hourly at each dose level to identify any bacteriostatic or antibacterial properties imbued by the CuO nanoparticles.

### 3.3 Results

#### 3.3.1 Particle Imaging with TEM

Copper nanoparticles imaged via TEM formed large agglomerates composed of small primary particles. These agglomerates varied in size from as small as 100 nm to over 1  $\mu\text{m}$  in diameter (Figure 3.1a). Higher magnification images (Figure 3.1b) confirmed that the primary particle size was in agreement with manufacturer specifications (nominal diameter of 25 nm). Previous high-resolution TEM analysis of these CuO nanoparticles at the University of Iowa identified average primary particle size in this batch to be 12 nm.<sup>160</sup>

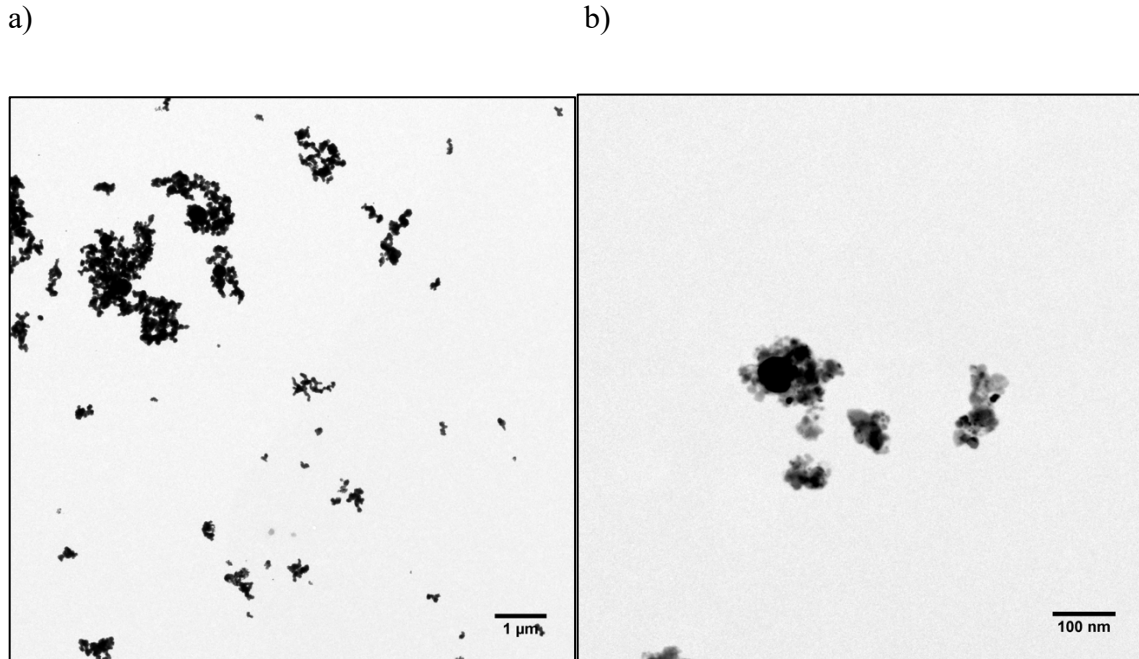


Figure 3.1 TEM Micrographs of CuO nanoparticles. A) A low-magnification image showing a variety of agglomerate shapes and sizes. b) A high-magnification image of smaller agglomerates with small primary particles distinguishable.

### 3.3.2 Cell Viability

A549 viability decreased exponentially with dose. Complete cell death was observed at CuO nanoparticle doses  $\geq 1$  mg/mL (Figure 3.2a). When cells were visually inspected after exposure, cell morphology was altered at higher CuO nanoparticle doses (Figure 3.2). At a dose of 0.2 mg/mL (Figure 3.2E), cells began to visibly ball up and detach from the well plate. Cell detachment resulted in low concentrations of proteins for western blot and reduced the number of cells remaining on plates for infectivity studies. Thus, CuO nanoparticle doses less than 0.2 mg/mL were used in further studies. Higher doses also resulted in visible deposition of the CuO nanoparticles apparent as brown/black regions amid the cell debris (Figure 3.2F and G).

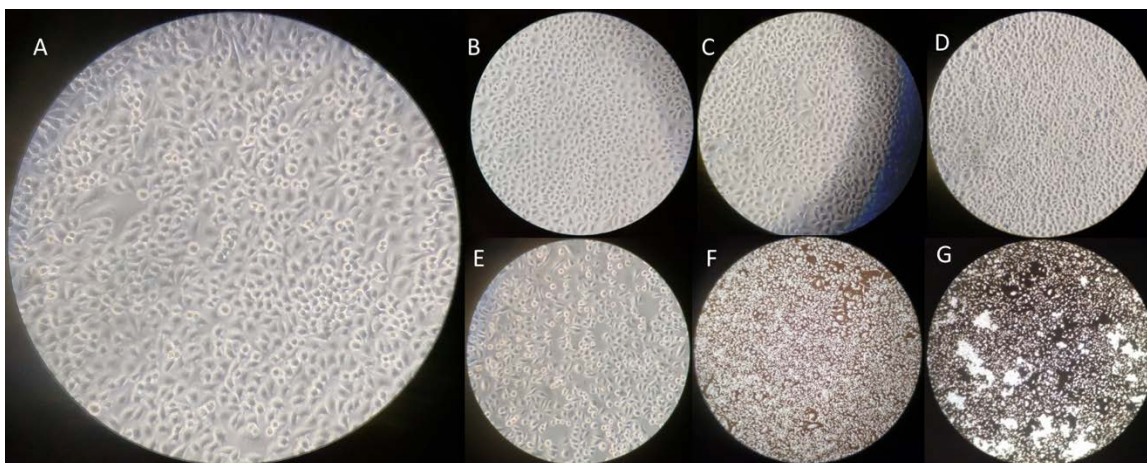


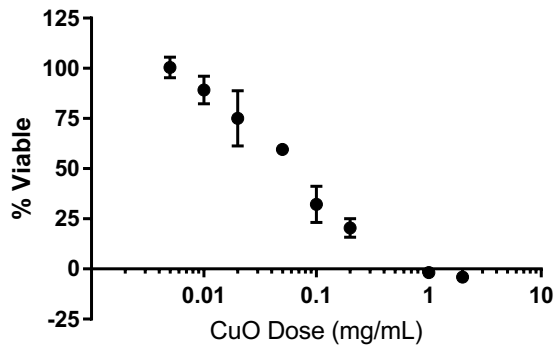
Figure 3.2: A549 cells imaged at 200x magnification after exposure to varying concentrations of CuO nanoparticles. A) No exposure, enlarged for reference. The remaining images correspond to cells exposed to B) 0.01 mg/mL C) 0.02 mg/mL D) 0.1 mg/mL E) 0.2 mg/mL F) 1 mg/mL G) 2 mg/mL of copper oxide nanoparticles.

### 3.3.3 Correlation Between CuO Uptake and Cell Viability

Cell viability analysis identified dose-dependent toxicity in lung cells exposed to CuO nanoparticles. As illustrated in Figure 3.3a, at 0.005 mg/mL dose levels, no losses in viability were observed, while cells exposed to doses at and above 1 mg/mL were non-viable. All doses greater than or equal to 0.01 mg/mL resulted in significantly decreased viability as measured by MTS ( $p < 0.001$ ). ICP-MS analysis of the Cu content of cells exposed to varying doses of CuO nanoparticles identified a dose-dependent uptake. As illustrated in Figure 3.3b, the relationship between applied dose and Cu mass in each sample was linear across the dose range studied.



a)



b)

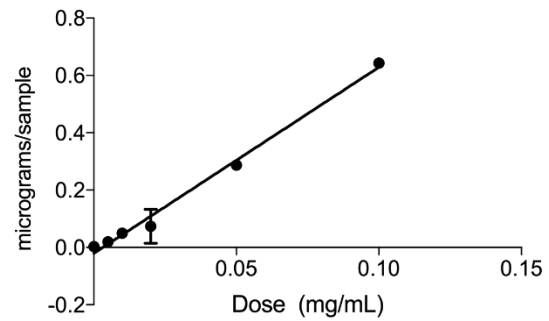


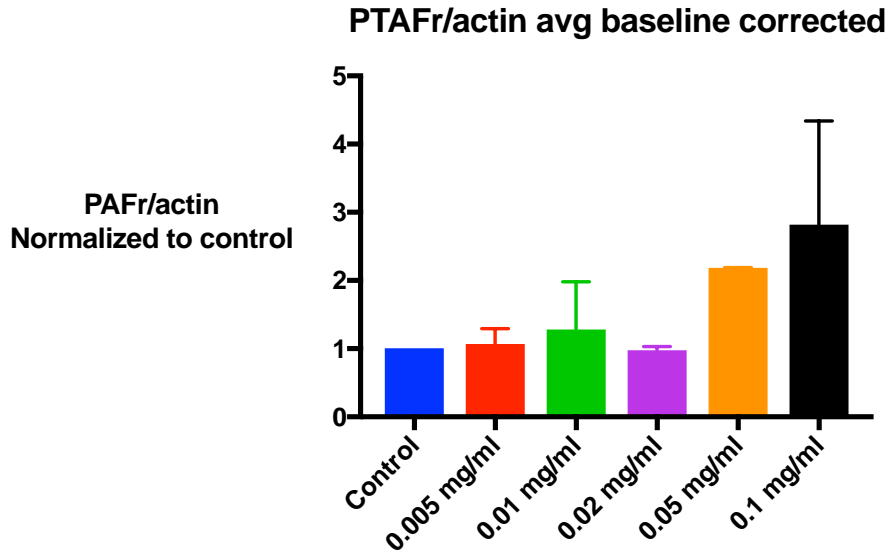
Figure 3.3: a) Cell viability was measured as a response to applied dose ( $n=3$ , 4 replicates each). b) Cu mass observed in each sample as it relates to applied CuO nanoparticle dose ( $n=1$ , 3 replicates). Points with no error bars indicates that error bars were smaller than symbols. Error bars=SD.

### 3.3.4 Evaluation of Infectivity due to PAFR Upregulation

The expression of PAFR in A549 cells has been previously observed to be upregulated by cellular exposure to urban particulate matter and cigarette smoke.<sup>7,8</sup> When PAFR expression was measured in lung cells exposed to CuO nanoparticles at concentrations ranging from 0.005-0.1 mg/mL PAFR expression increased at higher doses. Elevated levels of PAFR were observed with A549 cells exposed to 0.05 mg/mL CuO nanoparticles (Figure 3.4A).

To assess effects of CuO on lung cell susceptibility to infection, *S. pneumoniae* from cold water lysates generated in the A549 infection study were placed onto agar plates and colony forming units (CFUs) counted. Figure 3.4b illustrates that adhered and internalized bacteria increase somewhat as CuO dose to A549 cells increase. Cells exposed to 0.05 mg/mL of CuO nanoparticles were found to have the highest number of *S. pneumoniae* CFUs, though no significant differences were observed.

a)



b)

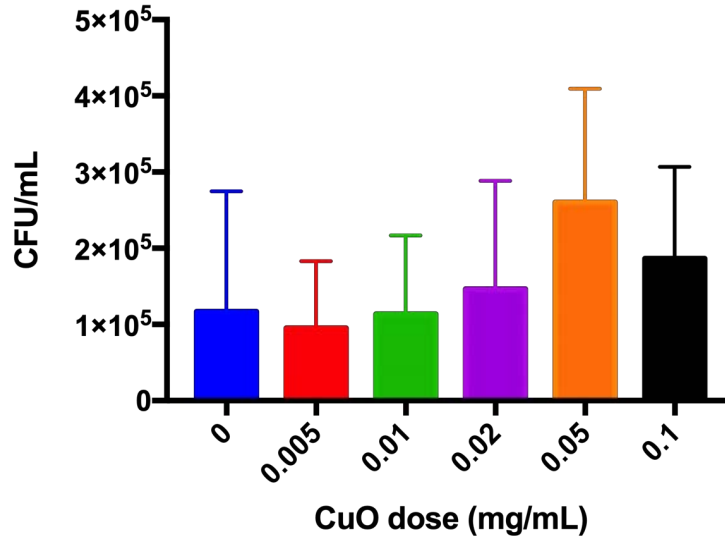


Figure 3.4 a) Analysis of PAFR content ( $n=1$ , 3 replicates) and b) number of colony-forming bacteria attached to A549 cells exposed to varying doses of CuO nanoparticles ( $n=2$ , 3 replicates each). Error bars=SD.

### 3.3.5 CuO Effect on Bacterial Viability

To assess whether CuO nanoparticles affected infectivity due to bacteriostatic or antimicrobial properties, bacterial growth in the presence of CuO nanoparticles was measured. As can be seen in Figure 3.5, there was no discernable change in bacterial growth for *S. pneumoniae* exposed to CuO levels present during infectivity studies over 3 h of log-phase growth, which exceeds the 2 h bacteria spend exposed to lung cells to measure infectivity.

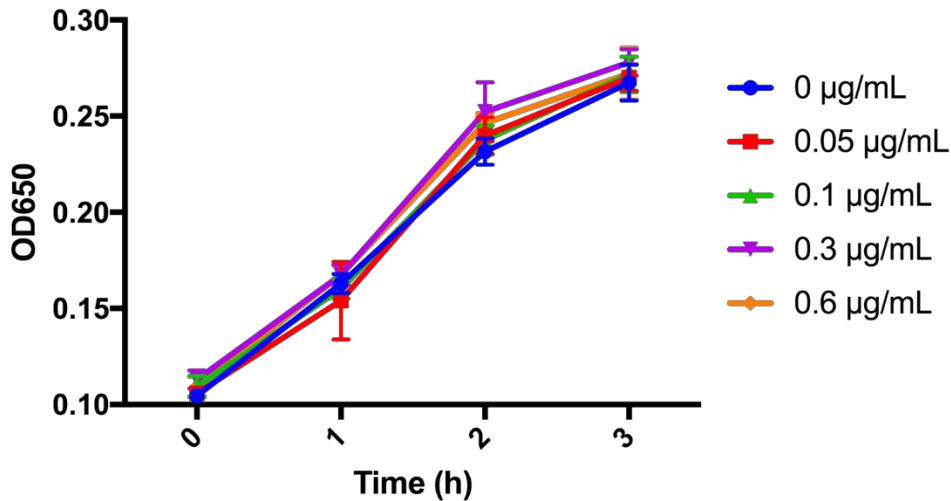


Figure 3.5. Optical density of *S. pneumoniae* grown at various CuO doses over the course of 3h. Error bars=SD.

### 3.4 Discussion

In this study, the effects of nanoparticles composed of CuO on lung cell viability and susceptibility to infection. In an *in vitro* model using A549 alveolar epithelial cells, viability in response to CuO nanoparticle exposure identified that losses in lung cell viability occurred in the dose range of 0.005-1 mg/mL CuO. The decrease in viability with increasing dose indicates that the dose-response relationship in this dose range is one of exponential decay. This dose range encompasses the entire region in which

changes in viability can be observed from no change in viability to no measurable viability. Cell detachment resulted in low concentrations of proteins for western blot and reduced the number of cells remaining on plates for infectivity studies. Thus, CuO nanoparticle doses less than 0.2 mg/mL were used in further studies of particle uptake, bacterial infectivity, and PAFR expression. Focusing on the 0.005-0.1 mg/mL range of doses, cell uptake of copper was measured using ICP-MS. The linearity of this relationship simplified further analyses, identifying that the dose/uptake relationship for CuO nanoparticles in A549 cells is directly proportional.

*When these cells were exposed to CuO nanoparticles, PAFR levels increased indicating that elevated PAFR expression is one component of acute cellular response to these particles. At higher doses, 2-fold increases in PAFR expression were observed, which is consistent with observed increases in PAFR expression in lung cells exposed to cigarette smoke and urban PM.<sup>10, 166</sup> This finding supports the conclusion that copper oxide is a contributing component to increased PAFR expression observed after exposure to cigarette smoke and some types of urban PM. The mechanism by which CuO nanoparticles enhance expression of PAFR is unclear. As with other materials that induce this effect, CuO is associated with oxidative stress responses.<sup>167, 168</sup> While some species-specific effects are critical to the upregulation of PAFR,<sup>10</sup> this oxidative stress component may be a major factor in the upregulation pathway.*

Infectivity studies using *S. pneumoniae*, D39, indicated that prior exposure to copper oxide led to increases in bacterial adherence to and internalization by lung cells. Further, the dose at which maximum infectivity occurred is consistent with the dose at which the highest level of PAFR expression measured by western blot was observed (Figure 3.5). These data implicate PAFR overexpression in lung cells exposed to CuO nanoparticles as a factor in increased susceptibility to infection with *S. pneumoniae*. These findings further corroborate previously published work indicating that subtypes of pathogenic bacteria of the lungs that express phosphorylcholine in their LOS exhibit increased infectivity via PAFR-mediated attachment and entry into lung cells.<sup>153-156</sup>

CuO, along with other oxidation states of copper, is known to have antimicrobial properties.<sup>169,170</sup> When relevant concentrations of CuO were exposed to bacteria during log phase, growth was unaffected. The absence of any observable differences in bacterial growth at these CuO nanoparticle concentrations indicates that residual CuO present during bacterial challenge does not directly impact bacterial growth. In the absence of any observed effect on bacterial viability, it is likely that differences in attachment and uptake of *S. pneumoniae* by A549 cells are solely due to impacts CuO nanoparticles have on the lung cells, especially by enhancing PAFR expression.

### **3.5 Conclusions**

Foreign materials that enter the respiratory airways can modulate disease progression. Herein we have identified a chemical component that when presented in nanoparticulate form can impact lung health by direct toxicity as well as indirectly inducing upregulation of the surface receptor PAFR. The increased expression of PAFR is associated with increased susceptibility to pathogens, such as *S. pneumoniae*, that synthesize and present lipooligosaccharides on their membranes that contain ChoP. CuO is a chemical present in urban particulate matter, cigarette smoke, and e-cigarette vapor that in this study was found to elicit similar responses to these aerosols in lung cells, including upregulation of PAFR and subsequent susceptibility to bacterial infection.

## **4 Proteins Found in Lung Fluid Reduce Particle Stability and Uptake by Lung Cells**

### **4.1 Introduction**

The lung proteome, like most fluid systems in the body, is diverse and complex, performing varied functions. Two major functions of the lungs are the protection of the

body from foreign materials in the air and rapid and efficient exchange of gases between the air and the blood. These are accomplished by anatomical features of the lungs; the structural features of the conducting airways limit entry of aerosols into the respiratory airways and the large number of alveoli provide high surface area for gas exchange. These anatomical features are complemented and enhanced by fluids in the lungs. In the conducting airways, fluids are rich with mucins MUC2, MUC5AC, and MUC5B, glycoproteins which give mucus its gel-like viscoelastic properties that help entrap and remove foreign materials that enter the lungs.<sup>171</sup> In the respiratory airways, the surfactant compounds, compounds that reduce surface tension and facilitate alveolar sac opening while breathing, are maintained at the air-liquid interface by surfactant-associated proteins SP-B and SP-C.<sup>22</sup> Early studies of the composition of bronchoalveolar lavage fluid (BALF), a fluid obtained by rinsing the deep lung with saline to collect cells and other materials therein, identified IgG, IgA, and transferrin as making up a greater portion of lung lavage than serum.<sup>23</sup> Further analyses identified elevated levels of proteins SP-A, SP-D, lactoferrin, lysozyme, and Club cell proteins in BALF.<sup>24-26</sup> Most of the proteins expressed at high levels in BALF have a role in host defense, indicating that many of these compounds are likely secreted to protect against foreign materials and organisms that enter the lungs.

Foreign materials in the lung space interact with a large cohort of proteins prior to any potential interactions with cells. In the absence of proteins, a foreign object coming into contact with a cell would result in a direct surface interaction between the material surface and the cell membrane or membrane-bound proteins/receptors. However, protein coronas form rapidly on the surfaces of foreign materials exposed to biological fluids;

these coronas become the new surfaces for those materials affecting their behavior and interactions.<sup>42, 50, 51, 53</sup>

These new surfaces created when protein coronas form around foreign materials change interactions with other materials, biomolecules, and cells. Some recent *in vitro* studies of nanoparticle interactions in vascular endothelium and also in epithelium have indicated that the protein corona is significant in cell adhesion and particle uptake.<sup>63, 172</sup> Using A549 cells, an alveolar epithelial cell line, Walkey et al. demonstrated the significance of protein corona composition on cellular uptake focusing on the influence of individual proteins in the corona on cellular response.<sup>55</sup> While some correlations between individual proteins and uptake, whether enhancing or inhibiting, were observed in that work, the presence of a large number of unique proteins in each sample prohibited direct attribution of positive or negative effects to any single protein.

When an individual protein is interacting with a foreign material's surface, that interaction is affected by properties of both the protein and the surface. Electrostatic interactions can influence how two objects in suspension interact. For instance, polystyrene particle manufacturers indicate that protein adsorption to the surface of particles is maximized at the isoelectric point of a protein.<sup>173</sup> This implies that pH changes can neutralize charged groups, either on proteins or on a foreign material surface, and the resulting changes in hydration and/or electrostatic repulsion may increase or decrease adsorption. Walkey et al. demonstrated the significance of particle surface charge on the mass of protein adsorbed and corona composition by using cationic, anionic, and neutral particle coatings to study corona formation in serum.<sup>55</sup> In addition to charged groups present on the surface of foreign materials, ions in solution, especially

phosphate, have also been shown to modify adsorption behavior of proteins.<sup>174, 175</sup> Thus, the presence of ionic/charged groups in the interaction space between proteins and foreign matter appears to play a role in mediating those interactions, affecting the adsorption of various proteins and the overall makeup of the protein corona formed in biological fluids.

The adsorption of a single protein in the lung space to the surface of a foreign material is related to its presence, abundance, affinity for the surface, and competition with other proteins. Simulating adsorption in a controlled environment without competition eliminates confounding from a large host of biomolecules. This can provide insight into those more complex systems by elucidating the substituent pieces that make up those systems. For example, identifying whether large or small quantities of individual proteins are necessary on the surfaces of particles to induce changes in particle behavior *in vitro* can inform how strongly a given protein can be expected to affect particle stability *in vivo*.

This study explores the role of prevalent lung fluid proteins on particle behavior and cellular responses to particles in the lung space as well as probing conditions that contribute to adsorption and particle stability. To probe the specific contributions of individual proteins, while maintaining a focus on the lung space, a small sample of proteins shown to be expressed at higher levels in the lungs was selected for analysis. Beyond being elevated in the lungs, proteins were selected based on known functions that may or may not affect adsorption and cellular responses. Proteins selected were BSA, IgG, lactoferrin, and lysozyme. BSA and lysozyme were adsorbed onto the surfaces of 200 nm and 1  $\mu\text{m}$  polystyrene particles following protocols laid out by the manufacturers



of these beads. Particles were characterized after treatment to determine effects of proteins on particle aggregation and particle zeta potential, and lung cell responses to particles were measured to measure the effect of proteins on cell uptake. Polystyrene is stable in physiological environments, can be obtained as monodisperse spheres of various sizes, and can be purchased functionalized with fluorescent tags. These features make polystyrene particles a good model system for these studies. The two sizes were selected to study whether particles of differing size are impacted differently by protein adsorption, especially considering cellular response.

In addition to studying polystyrene particle behavior after protein adsorption, the adsorption of BSA, IgG, lactoferrin, and lysozyme on the surface of 100 nm gold particles was studied across a range of pH to identify protein-specific impacts on particle behavior and clarify the role pH has in protein adsorption. The selection of gold nanoparticles for use in these studies is based on their high density relative to water, which simplifies separation of these particles from protein solutions. Derjaguin, Landau, Verwey, and Overbeek (DLVO) theory was used to model particle behavior before and after proteins adsorbed to the surface of gold particles and assessed for its ability to accurately predict particle behavior. After studying particle behavior for both polystyrene and gold particles exposed to protein, data for BSA and lysozyme were compared across both materials to identify if effects were generally ascribable to the individual proteins, or if there were material-specific contributions.

## 4.2 Materials and Methods

### 4.2.1 Preparation of Protein-Coated Polystyrene Particles

Lysozyme, being expressed abundantly in lung fluids as well as having a role in innate immunity, was selected for analysis. BSA was selected for its ubiquity in bodily fluids as well as its frequent use in a variety of studies of protein adsorption allowing for comparison to others work.

According to polystyrene bead manufacturers, proteins best adsorb to microspheres at or near isoelectric pH conditions.<sup>173</sup> After determining the isoelectric points for lysozyme (pI 11.4, RPI)<sup>176</sup> and BSA (pI 4.7, RPI)<sup>70</sup>, carbonate-bicarbonate (CB, pH 11) and citrate-phosphate (CP, pH 4.7) buffers were selected for adsorption as these buffers were recommended by polystyrene bead manufacturers at their respective pH<sup>173</sup>. CB buffer was prepared containing 0.1 M sodium bicarbonate (EMD Chem) and 0.1 M sodium carbonate (Fisher) with pH adjusted to 11. CP buffer was prepared containing 0.1 M sodium citrate (RPI) and 0.2 M dibasic sodium phosphate (Sigma), with pH adjusted to 4.7. Proteins were dissolved in the buffer nearest their pI at 5 mg/mL each to generate protein coating solutions that fell within a range of 3-10 times excess protein based on theoretical monolayer calculations as recommended by the polystyrene bead manufacturer.<sup>173</sup>

Fluoresbrite 200 nm and 1  $\mu$ m polystyrene microspheres (Polysciences) were prepared for adsorption by washing in CB or CP buffer depending on the desired protein coating. Particles were suspended in 1 mL buffer in 1.5 mL microcentrifuge tubes at concentrations of  $2 \times 10^9$  particles/mL and  $2 \times 10^8$  particles/mL for 200 nm and 1  $\mu$ m particles respectively. These were vortexed and sonicated alternately for three cycles,

then particles were separated by centrifuge (Eppendorf 5424) for 30 min at 12,000×g and 8,000×g for 200 nm and 1 μm particles respectively. The buffer supernatant was removed, and the particles suspended in 5 mg/mL protein-coating solutions. These suspensions were gently agitated for 4 h at room temperature. Samples were then allowed to further equilibrate overnight at 4°C. Particles were separated from the protein solutions by centrifugation at 2300×g for 15 min. Particles were washed in the respective buffer and pelleted a second time to remove loosely-bound proteins. These pellets were suspended in DI water for characterization.

#### 4.2.2 Measurement of Protein-Coated Particle Uptake Using Flow Cytometry

To measure the effect of protein-coatings on cell uptake in the lungs, human bronchoepithelial lung cells (16HBE14o-) were exposed to protein-coated particles and their interactions measured. 16HBE14o- cells were obtained from Dr. Gruenert (Children's Hospital Oakland Research Institute) and cultured in DMEM supplemented with 10% FBS (Atlanta Biologics), 1% L-Glutamine (Gibco) and 1% penicillin-streptomycin (Gibco). Cells were grown at 37°C in a humidified 5% CO<sub>2</sub> environment. Upon reaching confluence, cells were rinsed with PBS and treated with a 0.25% Trypsin-EDTA (Gibco) solution for 8 min to dissociate cells. These cells were suspended in fresh media and seeded in 24-well plates onto 12 mm collagen-coated coverslips in aliquots of 100 μL containing 2x10<sup>5</sup> cells. Cells attached and grew to 80% confluence overnight. The culture media was removed, and cells were washed twice using serum-free DMEM in preparation for particle exposure.

Protein-coated polystyrene particles tagged with fluorescein isothiocyanate (FITC) were prepared as described above. For cell uptake, protein-coated particles were

suspended in serum-free DMEM (with L-Glutamine and penicillin-streptomycin) at a concentration of  $5 \times 10^7$  particles/mL. 100  $\mu$ L of particles in suspension were added to each well and incubated for 4 h. This concentration exposed cells at a dose of 25 particles per cell. After the incubation, cells were rinsed with cold PBS three times followed by addition of 200  $\mu$ L of enzyme-free cell dissociation buffer (Gibco) at room temperature for 2 min. Dissociation buffer was removed, followed by addition of 200  $\mu$ L of dissociation buffer for 15-20 min in the incubator until detachment was observed under the microscope. Cells were exposed in replicates of 4 wells, and these replicates were pooled and collected in 12 $\times$ 75 mm tubes (BD). Cells were separated from dissociation buffer using a centrifuge at 270 $\times$ g for 10 min at 4°C. The supernatant was removed, and the cells suspended in 400  $\mu$ L of PBS. Cells were kept on ice during transport until to analysis by flow cytometry.

Particle association with 16HBE14o- cells was measured by flow cytometry using a Beckton Dickinson LSR II using a 488 nm laser. Gates were set and validated against untreated cells as described previously,<sup>177</sup> particles in suspension, and a mixture of these samples combined immediately prior to analysis. Analyses were collected for 10,000 samples (n=4). The percent of cells positive for FITC was determined in FlowJo using the Enhanced Normalization Subtraction (ENS) method.

#### 4.2.3 Preparation of Protein-Coated Gold Particles

Gold nanoparticles were synthesized using a citrate-stabilized reduction of tetrachloroauric acid as described in Chapter 6. After synthesis, gold particle concentration was calculated to be 0.175 mg/mL in suspension. For each sample, 5.7 mL of the suspension (1 mg of gold) was placed in a glass centrifuge tube, and the particles

sedimented at  $1,000\times g$  for 15 min followed by removal of the supernatant. Lysozyme, lactoferrin (pI=8.7, Sigma)<sup>178</sup>, IgG (pI=6.3-8.9, RPI)<sup>179</sup> and BSA were dissolved in saline solutions at protein concentrations of 1,000 and 2,000  $\mu\text{g/mL}$  with pH adjusted to 4.4, 5.0, 5.4, 6.5, 8.7, and 11.0. These points were selected based on their proximity to isoelectric points of the proteins and the pKa values of citrate. Proteins in saline were exposed to 100 nm spherical gold nanoparticles, and the particles suspended in the protein solutions by pipetting to disperse the pellets. Additionally, gold particles were suspended in saline at the various pH. To identify if any observed aggregation was due to particles being forced together into a pellet in the centrifuge, particles were also dispersed in fresh citrate buffer after separation from their initial suspension in the centrifuge.

#### 4.2.4 Hydrodynamic Size and Zeta Potential Measurements to Study Particle Behavior

To study how exposure to individual proteins or aqueous solutions alter particle aggregation, hydrodynamic diameters were measured by dynamic light scattering (DLS, Malvern Nano ZS). Polystyrene particles were measured at their prepared concentrations of  $2\times 10^9$  particles/mL and  $2\times 10^8$  particles/mL for 200 nm and 1  $\mu\text{m}$  particles respectively. In addition to the particles prepared as described, stock 200 nm and 1  $\mu\text{m}$  particles were suspended in water without treatment for suspension characterization. Gold nanoparticles were similarly measured as prepared at a concentration of 1 mg/mL ( $\sim 2 \times 10^{11}$  particles/mL). Particle suspensions were placed in clear disposable polystyrene cuvettes. Hydrodynamic size was measured 13 times per run and run three times per sample.

Particles prepared for hydrodynamic size measurements were placed in folded capillary zeta cells (Malvern, DTS1070) and the zeta potential measured in a Malvern

Nano ZS. The zeta method was set to run a minimum of 10 times, and a maximum of 100 times or until confidence in the result was achieved. This analysis was run three times per sample.

#### 4.2.5 Measurement of Adsorbed Protein Using the BCA Assay

Quantification of protein mass adsorbed to the surfaces of gold particles was performed to assess differences in adsorption behavior of the proteins at varying pH. Adsorbed mass was calculated by adding 1 mg of gold particles to protein solutions prepared as described above at a protein concentration of 1,000-2,000  $\mu\text{g/mL}$  and allowing coatings to form for 1 h. Afterwards, the samples were centrifuged at  $1,000\times g$  to separate the gold nanoparticles. Total protein contents of the various protein solutions were measured using the bicinchoninic acid (BCA) assay (Thermo) before and after exposure to particles. The well-plate variant of the BCA assay was used, and well plates were read at 560 nm using a BioMate spectrophotometer (Epoch) The difference in solution protein content before and after exposure was assumed to be the mass adsorbed to the surface of particles.

### 4.3 Results and Discussion

#### 4.3.1 Measuring Suspension Properties and Cell Responses to Coated Polystyrene Particles

After exposure to proteins in buffers, polystyrene particles' hydrodynamic diameters were measured using DLS (Figure 4.1a). For 200 nm particles, lysozyme induced the formation of large aggregates ( $\sim 1,500$  nm), whereas BSA did not. Additionally, the polydispersity of lysozyme-coated particles (PDI=0.836) was much higher than BSA-coated particles (PDI=0.175), which led to large error bars in average

hydrodynamic diameter measurements. CB and CP buffer exposure each resulted in some aggregation of 200 nm particles. The BSA-exposed particles had the smallest hydrodynamic diameters (270 nm) of all samples tested, though no significant differences were observed. Zeta potential measurements (Figure 4.1c) for these samples found that lysozyme-coated particles were the most neutral with a zeta potential of -4.3 mV. BSA adsorption to the surface of particles resulted in a zeta potential of -39.1 mV. Particle exposure to CB or CP buffer resulted in different zeta potentials of -60.2 mV and -6.7 mV respectively.

For 1  $\mu\text{m}$  particles, all buffer and protein exposures resulted in the formation of aggregates (Figure 1b). BSA exposure resulted in the smallest aggregates with an average hydrodynamic diameter of 2,495 nm. Lysozyme exposure resulted in large aggregates with an average hydrodynamic diameter of 4,100 nm. Exposure to CB and CP buffers resulted in aggregate hydrodynamic diameters of 3,556 nm and 3,092 nm respectively. Zeta potential measurements (Figure 4.1d) determined that lysozyme-exposed particles were the most neutral with a zeta potential of 1.9 mV. BSA adsorption to these particles resulted in a zeta potential of -60.8 mV. Exposure to CB and CP buffers resulted in zeta potentials of -60.5 mV and -70.4 mV respectively.

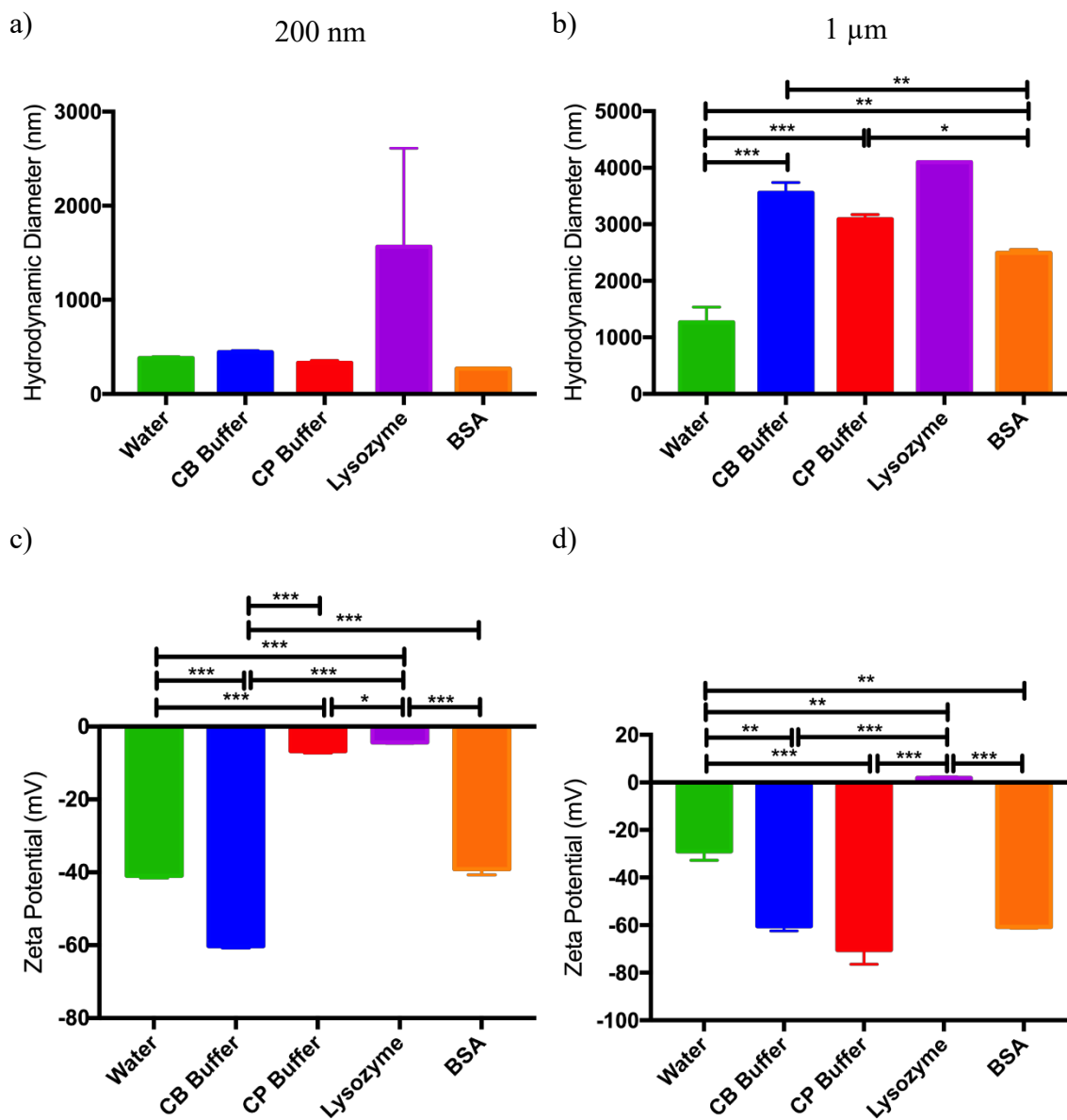


Figure 4.1 Size measurements for a) 200 nm and b) 1 μm polystyrene particles exposed to buffers and proteins. Zeta potentials were similarly measured for c) 200 nm and d) 1 μm particles (\*=  $p < 0.05$ , \*\* $p < 0.01$ , \*\*\* $p < 0.001$ ).  $n = 1$ , replicates of 2. Error bars = SD.

Flow cytometry was used to measure the cell uptake/association of protein-coated particles using 16HBE14o- cells, with results shown in Figure 4.2. For all proteins studied, coatings on polystyrene particles resulted in reduced association with cells relative to particles exposed only to buffer solutions. Among 200 nm particles, those



coated with lysozyme had the lowest uptake by the cells, with only 19% of cells identified as positive for fluorescent particles. When 200 nm particles had been coated with BSA, 23% of cells were positive for particles, which was not significantly lower than for particles exposed to CB buffer (33%) and CP buffer (25%). For 1  $\mu\text{m}$  particles, 16% cells were positive for lysozyme-coated particles. BSA-coating of 1  $\mu\text{m}$  particles limited uptake, as only 11% of cells were positive for particle uptake/association. The majority of cells incubated with particles exposed to CB buffer were positive for fluorescent particles (66%). When particles had been exposed to CP buffer, uptake was observed in 23% of cells.

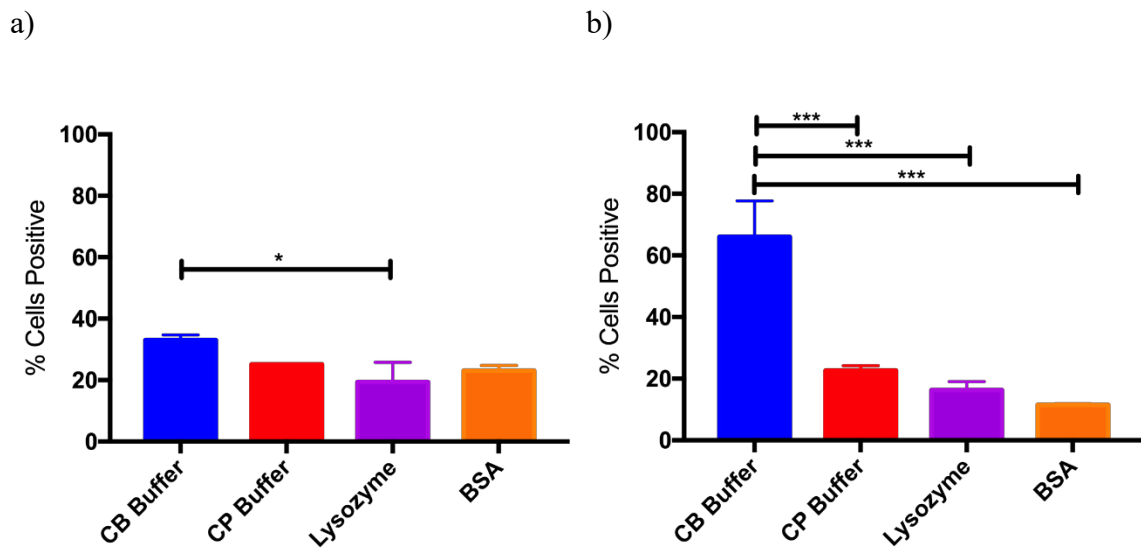


Figure 4.2. Flow cytometry measurements of cell uptake of fluorescent a) 200 nm and b) 1  $\mu\text{m}$  polystyrene identifying the percentage of cells measured that were positive for fluorescence (\*=  $p < 0.05$ , \*\*\* $p < 0.001$ ).  $n=1$ , replicates of 3. Error bars=SD.

For polystyrene particles exposed to lysozyme, particle zeta potential measurements indicated that protein interactions resulted in large changes in surface charge for both 200 nm and 1  $\mu\text{m}$  particles; the resulting zeta potentials near zero mV

indicate that neutralization of surface charge due to lysozyme adsorption may play a role in particle aggregation observed with this protein. BSA exposure resulted in no change in the surface charge of 200 nm polystyrene particles relative to water but resulted in a more negative surface charge of 1  $\mu\text{m}$  particles. In fact, BSA exposure had an apparent stabilizing effect on particle suspensions relative to buffers and lysozyme for both 200 nm and 1  $\mu\text{m}$  particles, resulting in minimal aggregation in both cases. For 200 nm particles, this effect was pronounced, and resulted in a smaller average hydrodynamic diameter for BSA-coated particles than for stock particles suspended in water. Across size measurements for both particle sizes the same trend is observed if exposures are ranked from largest aggregates to smallest: lysozyme>CB buffer>CP buffer>BSA. This apparent stabilizing effect of BSA has been previously observed.<sup>36, 173, 180</sup> Exposure to CP buffer resulted in a zeta potential of -6.7 mV for 200 nm particles, which is far from the typical value of -41 mV observed for particles in water. This strongly contrasts with observations made of 1  $\mu\text{m}$  particles where CP buffer exposure resulted in negatively charged particles with a zeta potential of -70 mV. This may indicate interactions between the ionic components of buffers and particle surfaces that affect particle stability.

For 200 nm particles, cell uptake decreased in the presence of proteins on the surface. Size and surface charge did not correlate with cell responses to particles. Particle treatments (whether buffer or protein) appeared to have a consistent relative effect on cell response with similar trends observed for 200 nm and 1  $\mu\text{m}$  particles. CB buffer exposure consistently resulted in the highest cell association with particles, with CP buffer following. Exposure to lysozyme or BSA resulted in lower cell association with particles for both sizes studied.

The differences observed in particle behavior, particle properties, and cellular responses to particles indicate that buffers impacted particles as well. The differences in buffers were pH and ionic composition. A possible pH-related difference could be in the CB buffer extracting residual surfactant from the surfaces of particles. The polymerization process for manufacturing these beads involves the use of a sulfate-containing surfactant. The specification sheets for these products indicate that trace levels of residual surfactant are embedded in the surfaces of these particles, and that it has a sulfate head group. Considering sodium dodecyl sulfate (SDS), a common sulfate-containing surfactant, is likely similar to if not the surfactant used. Assuming that SDS is representative, pH effects may be inferred. The critical micelle concentration of SDS increases with pH, indicating that SDS solubility is higher at alkaline pH.<sup>181</sup> Thus, higher pH aqueous solutions, like CB buffer, may modify particle surfaces by surfactant removal. The adsorption of buffer ions onto particle surfaces may further affect particle behavior and cellular responses. Phosphate, having been identified previously as active in surface interactions with materials, is likely to be responsible for some of the observed differences between particles exposed to CB or CP buffer.<sup>174, 175</sup>

There are multiple determinants of particle stability and cellular responses to particles. Particle size can determine which cellular uptake pathways are utilized,<sup>182</sup> and, as Walkey et al. demonstrated, surface charge has a contributing effect on cellular uptake.<sup>55</sup> The size and zeta potentials for BSA-coated particles is similar to that of CB buffer exposed particles, but particles exposed to CB buffer experienced a high level of uptake relative to BSA-coated particles. While BSA exposed particles were the least aggregated (i.e. smallest) and negatively charged they experienced the poorest association

with lung cells. The data presented here indicate that exposure to specific ionic components and lung proteins can impact cellular uptake.

There is a potential role that process pH can play in determining cell response. As previously demonstrated using BSA, protein conformation can change in different pH environments,<sup>77, 183</sup> which can result in different portions of the protein being exposed for interactions with cells. The protocols followed here for maximizing protein adsorption appear to have been developed primarily as a means of producing antibody-coated particles for immunolabeling. Isoelectric points for IgG antibodies fall in a pH range from 6.3-8.9, which is centered around physiological pH (7.4).<sup>179</sup> The development of these protocols, and the optimization of adsorption at the isoelectric point of IgG does not place the protein in a pH environment that differs greatly from the native physiological environment. Thus, the use of isoelectric points, while reasonable as it reduces potential electrostatic repulsion between proteins and a surface, may be more likely to induce conformational changes the farther a protein's pI is from physiological pH.

#### 4.3.2 Protein Interactions with Gold at Varying pH

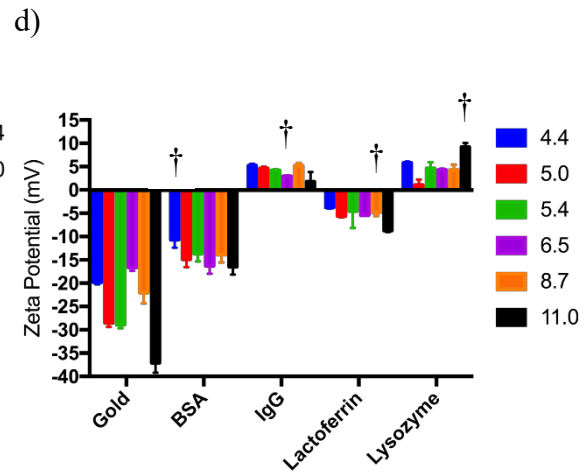
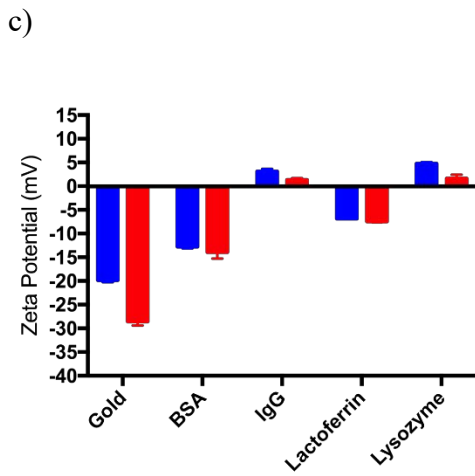
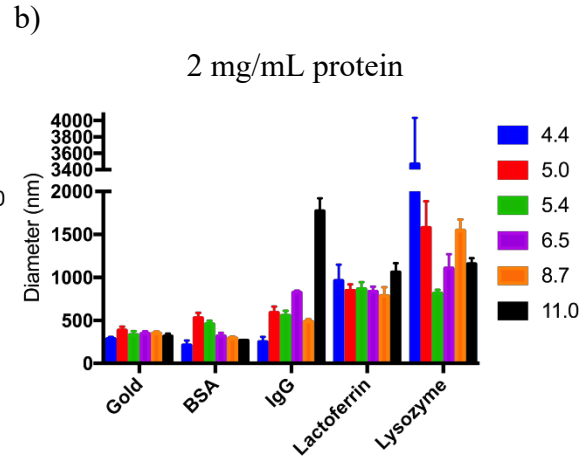
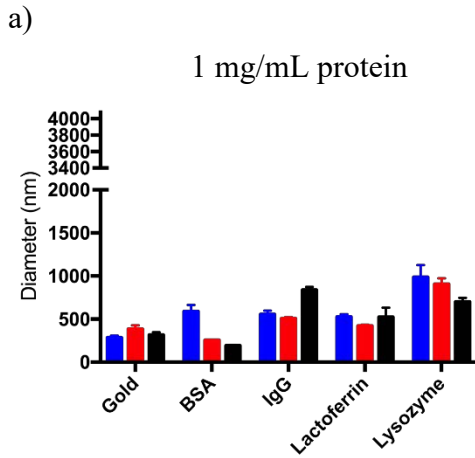
Protein-exposed gold nanoparticles were characterized using DLS. For each protein studied, particle aggregation changed with pH. Comparing protein-based effects, lysozyme induced the most aggregation overall while BSA induced the least aggregation. At both 1 mg/mL and 2 mg/mL, BSA-exposed gold particles tended to agglomerate at low pH, with the largest observed hydrodynamic diameters appearing at pH of 4.4 and 5.0 respectively. IgG-exposed gold tended to aggregate at pH 11 for both concentrations. Lysozyme exposure produced aggregates at all pH, but no specific trends were observed in particle aggregation. For the 2 mg/mL exposure, large aggregates (over 3  $\mu\text{m}$ ) were

observed at pH 4.4. Aggregation of gold particles due to lactoferrin exposure did not vary appreciably at any pH studied. Comparing against gold nanoparticles in saline at varying pH, exposure to most proteins in this study resulted in much larger aggregates. In the protein-free saline samples at varying pH, gold nanoparticles fell out of suspension over relatively short timescales (minutes to hours). This trend was consistent for all pH.

For all protein-coated gold nanoparticles, zeta potentials fell between -20 mV and 15 mV. The low-magnitude zeta potentials are consistent with the aggregates observed in all cases. For BSA-coated gold, the lowest-magnitude zeta potential occurred at pH 4.4. This is consistent with the highest observed aggregation for this protein-gold combination. Similarly, the pH at which IgG-coated gold had a zeta potential nearest zero was 11, the same pH at which the largest aggregates were observed. When lysozyme-coated gold nanoparticles were measured in various pH environments, zeta potentials ranged from 1-10 mV. The lowest magnitude value was observed at pH 5.0. As with the DLS measurements, zeta potential measurements for lysozyme did not follow any clear pattern. Zeta potential measurements of gold nanoparticles in protein-free saline at varying pH identified low-magnitude zeta potentials of -19.8 and -16.6 mV at pH of 4.4 and 6.5 respectively.

The BCA assay was used to determine the mass of protein adsorbed to 1 mg of gold nanoparticles exposed to lysozyme, lactoferrin, IgG or BSA at various pH at two concentration levels. For the 1,000  $\mu\text{g/mL}$  protein exposures, the highest adsorbed masses were observed for BSA, lactoferrin, and lysozyme at pH 4.4. Lactoferrin had a second point of high adsorption at pH 8.7. IgG adsorption was highest at pH 5.0 for the 1,000  $\mu\text{g/mL}$  exposure. For the 2,000  $\mu\text{g/mL}$  exposures, BSA, IgG, and lactoferrin

experienced high levels of adsorption at pH 5.4. Lysozyme experienced maximum adsorption at pH 6.5 for the 2,000 µg/mL exposure. At this concentration, low levels of adsorption were observed for all proteins at pH 4.4.



e)

f)

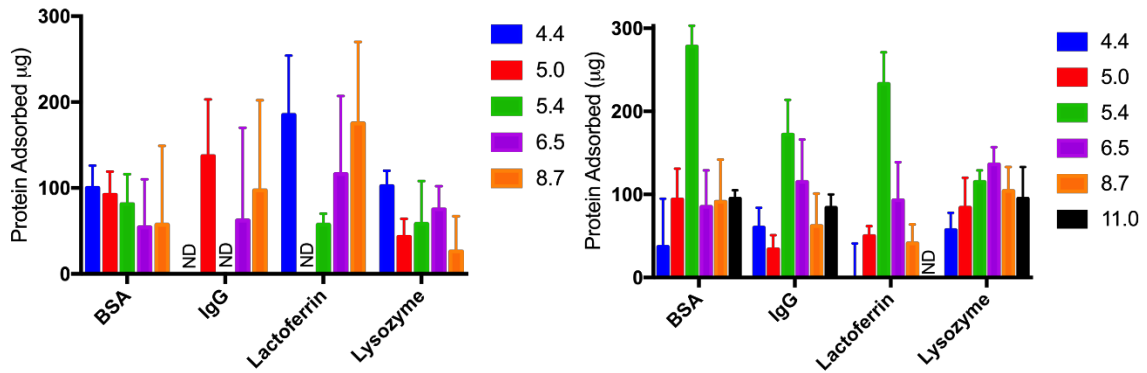


Figure 4.3. DLS was used to measure the hydrodynamic diameter of gold nanoparticles exposed to a) 1 mg/mL or b) 2 mg/mL of protein at varying pH. Zeta potentials were also measured for gold nanoparticles exposed to c) 1 mg/mL or d) 2 mg/mL of protein at varying pH. Using the BCA Assay, the mass of protein adsorbed to gold nanoparticles from solutions at e) 1 mg/mL and f) 2mg/mL protein was determined (ND=No Data). † denotes isoelectric point.  $n=1$ . Error bars=SD of multiple measurements.

Size and zeta potential data trend overall from BSA to Lysozyme. The zeta potentials for each protein-gold combination tended to be in a similar range for all pH studied. Aggregate size tended to increase with more neutral zeta potentials. Proteins are listed in the graphs from left to right in order of increasing isoelectric point. The two proteins that induced the largest aggregates (lactoferrin and lysozyme) may also be more hydrophobic than BSA and IgG. Lactoferrin is an antimicrobial peptide with the ability to interact with bacterial membranes.<sup>184</sup> This would require some hydrophobic characteristics to aid in binding to lipid bilayers. Thus, increased aggregation may be due to a mixture of low surface charge and hydrophobic properties imbued by these proteins.

While pH had some effect on measured responses of gold particles to proteins, protein identity appeared to be much more important at determining particle aggregation and surface charge. The primary structure of these proteins was analyzed to assess amino acid composition effects on zeta potential of gold particles coated in the respective

proteins. Specifically, the amine-functionalized arginine, histidine, and lysine content was compared to the carboxylate-functionalized aspartic acid and glutamic acid content of the proteins listed. As illustrated in Table 4.1, the average zeta potential of protein-coated particles across the pH studied tends to increase with increasing content of amine-functionalized residues relative to carboxylate-functionalized residues in the protein structure. The IgG ratio was determined based on a partial sequence covering the conserved Fc region. The Fab amino acid sequences change depending on the antibody's target antigen, so the amino acid composition for that portion of IgG is not listed in the Uniprot database. Despite only having knowledge of the Fc region, or approximately 2/3 of the IgG composition, the zeta potential data measured for protein-coated gold particles correlates with cationic and anionic content of proteins. The aggregation of protein-coated gold particles also increased with increasing amine content in the protein, though this may be due to effects on zeta potential.

*Table 4.1. Composition data for proteins based on Uniprot sequences,<sup>185</sup> and the average zeta potential for gold particles coated with each protein.*

Protein	Amine Residues	Carboxylate Residues	Total Residues	Amine/Carboxylate Ratio	Average Zeta Potential (mV)
BSA	103	99	607	1.04	-14.1
IgG (Fc portion)	43	30	330	1.43	3.5
Lactoferrin	101	79	711	1.27	-5.9
Lysozyme	19	9	147	2.11	4.4

The aggregation of gold in saline at various pH is likely due to the lack of stabilizing citrate in the solution. Indeed, when gold nanoparticles were collected into



pellets in the centrifuge, and dispersed in fresh citrate buffer, stable suspensions of gold nanoparticles were observed. This is clearly illustrated in Figure 4.4, where the citrate suspension is translucent and red, while the various saline suspensions are clear with small black particulates visible. Suspension color is a useful indicator with gold nanoparticles, as the diameter of gold particles affects the wavelengths of light absorbed by particle suspensions resulting in distinct colors for each diameter. Spectrophotometry to measure absorption in the visible spectrum has been demonstrated to be a reliable method for measuring the size of gold nanoparticles in suspension.<sup>186</sup> When DLS measurements of the citrate-stabilized suspension were taken, particle size was measured to be 120 nm in diameter. This contrasts with the saline-suspended particles. Particle size for saline-suspended ranged from 280-390 nm for the various pH tested. Aggregate size for particles in saline with BSA at various pH were similar to the saline-only samples. In some cases, the BSA-exposed particles had smaller average hydrodynamic diameters than those exposed to saline. This implies that for gold nanoparticles to remain stable in suspension, they must be maintained in either a buffer with appropriate stabilizing ions (e.g. citrate) or when exposed to a biological medium, a stabilizing protein needs to be present, such as albumin.

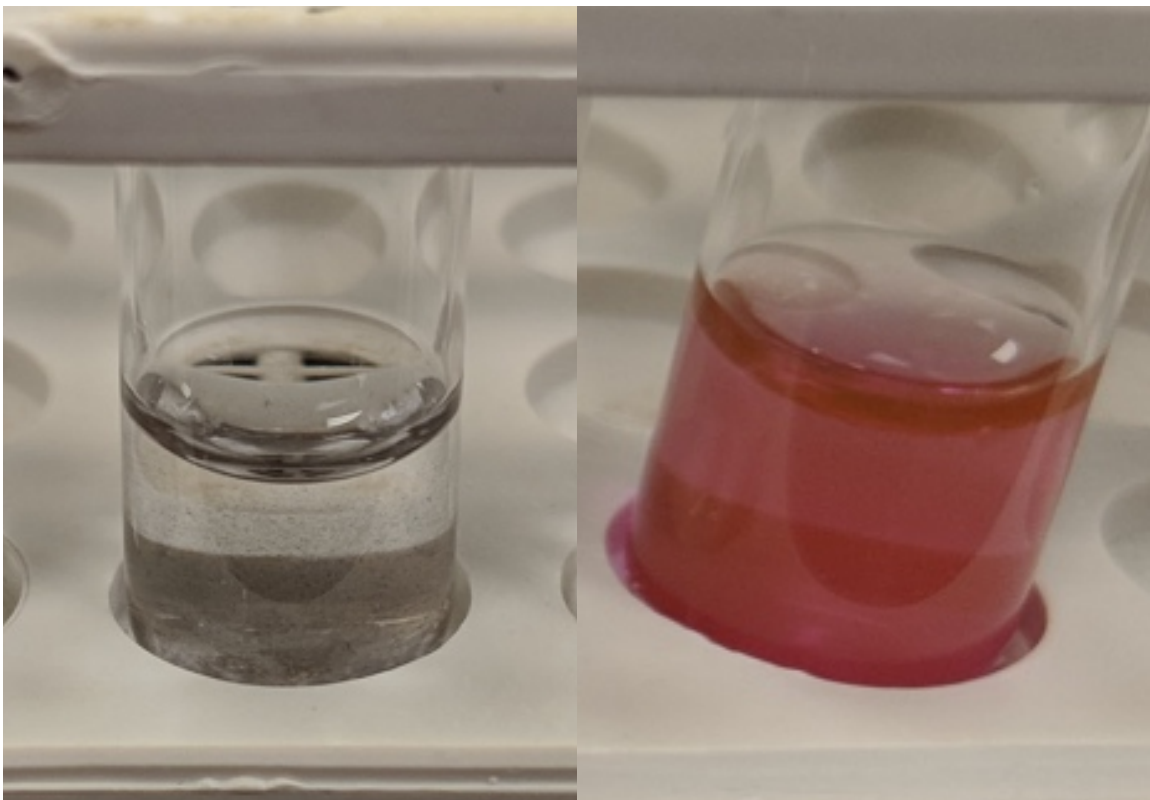
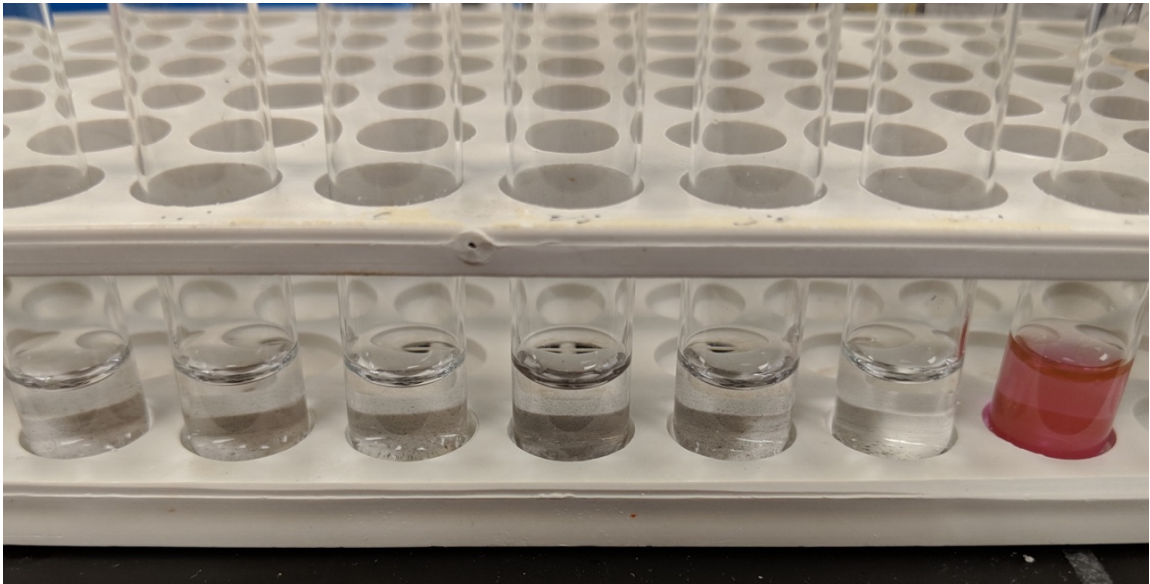


*Figure 4.4. Gold nanoparticles in buffers of varying pH. The clear tubes from left to right are saline at pH 4.4, 5.0, 5.4, 6.5, 8.7, and 11.0 respectively, and the far-right tube is gold in 2 mM sodium citrate. The clear liquids contain small black flecks. Gold in saline at pH 6.4 (lower left) and gold in 2 mM citrate (lower right) have been enlarged to illustrate visible aggregate formation (small black particles) versus dispersed gold nanoparticles (red/pink liquid).*

Gold nanoparticles in suspension are often referred to as “citrate-stabilized” due to the synthesis reaction that involves citrate as an electron donor for the reduction of ionic gold. The reaction results in gold that nucleates into seeds which then grow into spherical nanoparticles as the reaction progresses. At all stages, the surface of these particles is covered with stabilizing acetone dicarboxylate, the compound produced as citrate provides electrons via oxidative decarboxylation, as well as citrate. These two compounds are a triacid and a diacid respectively. And their presence on the surface of gold nanoparticles imbues them with a negative surface potential. The  $pK_a$  values for the three carboxylate groups of citrate are 3.1, 4.8, and 6.4 at 20°C.<sup>187</sup> The 4.8 and 6.4 values correspond with the two low magnitude zeta potentials observed at pH 4.4 and 6.5, which indicates that the citrate or acetone dicarboxylate may play varying roles in protein adsorption to the surfaces of gold nanoparticles as substituent acid groups gain or lose protons. This potential contribution of citrate and its derivative is despite washing and replacing buffer with saline. Carboxylate moieties have an affinity for gold surfaces where they form complexes that can contribute to particle stability in the case of citrate.<sup>188</sup> These are reportedly weak, but likely provide enough energy to maintain many surface-attached carboxylate groups after rinsing and resuspension with a citrate-free medium.

Despite bringing stabilizing citrate into saline suspensions, gold nanoparticles were markedly less stable in this aqueous medium. The concentration and composition of ions in solution affects adsorption of proteins to surfaces as well as suspension stability.<sup>189, 190</sup> Further, as citrate acquires or loses protons to its carboxylate moieties

with changing pH, the complex interaction is affected. It remains unclear whether the changes occurring at the surface are due to surface-attached groups becoming more or less charged with changing pH, or whether the addition and removal of protons is affecting the affinity of citrate and acetone dicarboxylate for gold surfaces resulting in changes in conformation or facilitating removal. Either case could affect protein adsorption to these gold surfaces.

One example of citrate potentially affecting protein adsorption is illustrated in protein adsorption data at pH 4.4. At 1 mg/mL protein concentration, this was the pH at which all proteins measured exhibited maximum adsorption. At 2 mg/mL protein concentration, this was the pH at which adsorption was the lowest for BSA, lactoferrin, and lysozyme, and the second lowest for IgG. This pH is also near one of the  $pK_a$  values for citrate. Further evidence of changes in citrate groups complexed on gold nanoparticle surfaces at this pH was observed as zeta potential was nearer to zero at this pH than most others. The other case of low-magnitude zeta potential for gold particles in saline occurred at pH 6.5, corresponding with a second  $pK_a$  value for citrate.

#### 4.3.3 DLVO Theory

Modeling of interaction energies between gold nanoparticles in suspension was achieved using DLVO theory. The approach to this theory is detailed in chapter 6, and after validation of the model with previous results the model was tested on gold nanoparticles by predicting particle behavior in 2 mM sodium citrate vs 154 mM sodium chloride (saline). The zeta potential values used were -27 mV for particles in citrate buffer, and -25.5 mV for particles in saline. These were experimental values, with the saline value being an average of zeta potentials for gold in saline at all pH studied. The

results, presented in Figure 4.5, correctly predicted that low-concentration sodium citrate provided enough repulsive energy, reaching a maximum energy of 15.7 k<sub>B</sub>T, to resist aggregation while the more concentrated sodium chloride solution resulted in a maximum energy of -1.1 k<sub>B</sub>T, implying that aggregation would occur. These results aligned well with experimental observations, enhancing confidence in model performance.

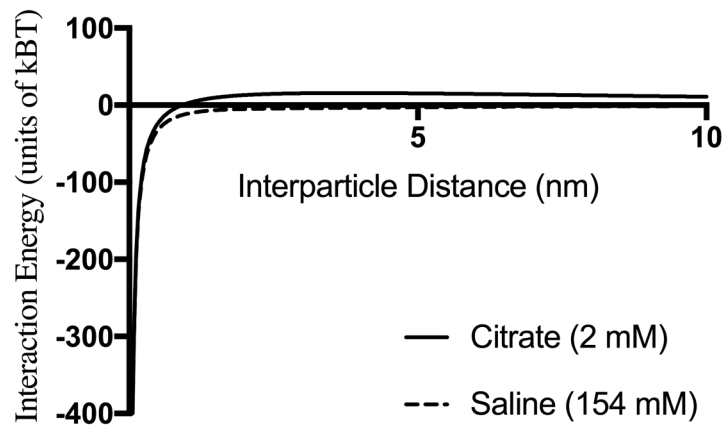


Figure 4.5. Classic DLVO theory was used to compare interaction energies of 100 nm gold particles in 2 mM sodium citrate and normal saline (154 mM sodium chloride).

Using modifications to DLVO theory, as described in detail in chapter 6, the theoretical interaction energies of BSA, IgG, lactoferrin, and lysozyme were predicted. Using data on the area occupied by proteins on a surface, a relationship between surface area occupation and protein molecular weight was found to be linear and used to predict the surface areas for lactoferrin and lysozyme. Proteins were assumed to be spherical, with the diameter of the sphere representing both the surface area covered by each protein as well as the monolayer thickness. Material constants used in extended DLVO calculations can be found in Table 4.2. For protein Hamaker constants, if they were reported as the constant in a medium (e.g. water), then the Hamaker constant in a vacuum was calculated from that value using Eq. 6-4.

Table 4.2. Constants for each protein used in DLVO calculations. \* denotes calculated based on fit of MW versus occupied surface area from data in Cantarero et al.<sup>191</sup> † denotes generic protein Hamaker constant.<sup>31</sup>

	Hamaker Constant (vacuum) (J)	Monolayer Thickness (nm)
BSA	9.5E-21 <sup>192</sup>	6.9 <sup>191</sup>
IgG	8.2E-21†	10.4 <sup>191</sup>
Lactoferrin	8.2E-21†	6.9*
Lysozyme	1.1E-20 <sup>193</sup>	4.5*

The addition of hydration effects to extended DLVO theory was based on research into adsorption behavior of IgG compared to IgY. A hydration constant for IgG ( $1.2 \times 10^{-20}$  J) was used to account for hydration in DLVO.<sup>31</sup> No hydration constants were available for other proteins, so the constant for IgG was used as an estimate to calculate the hydration portion of interaction energies for the remaining proteins. For each protein, classic DLVO, extended DLVO, and extended DLVO with hydration were used to plot interaction energy versus interparticle distance (Figure 4.6).

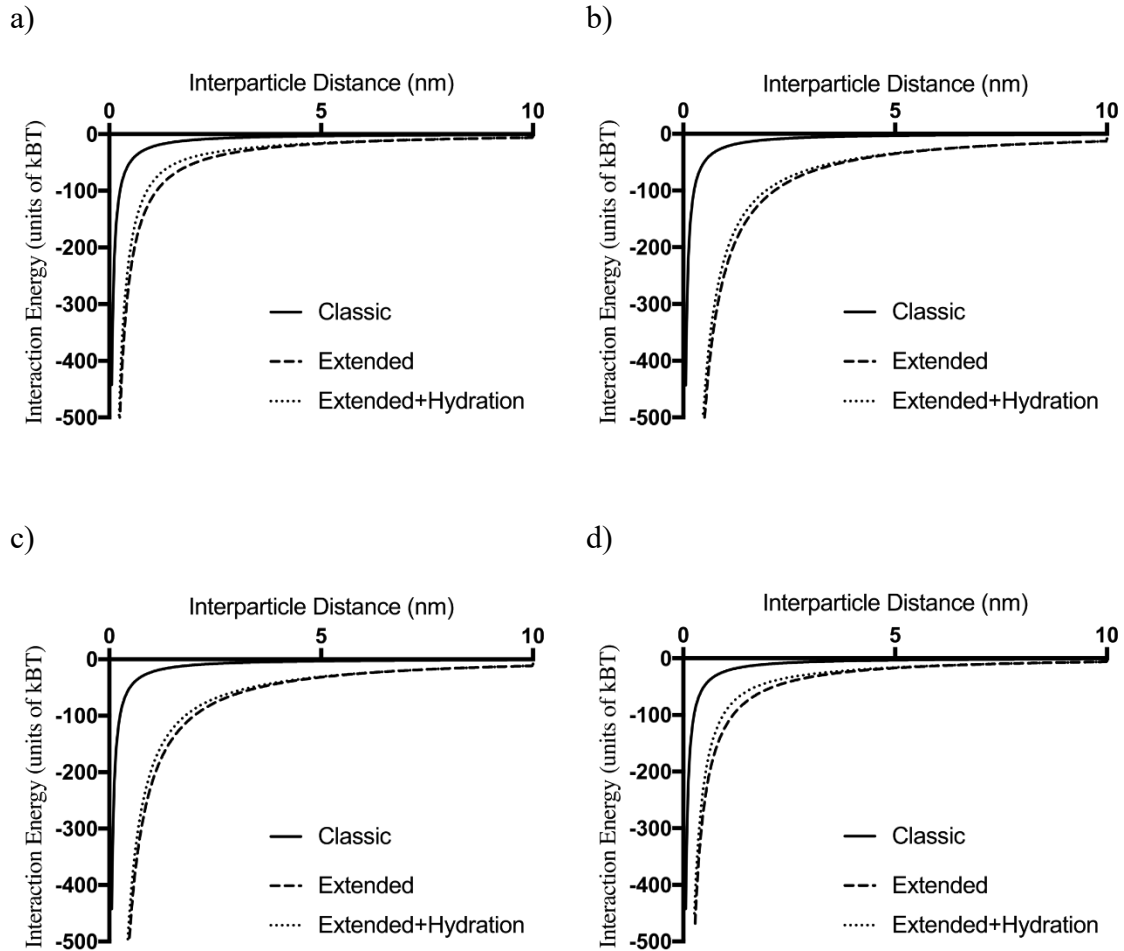


Figure 4.6. DLVO theory, Extended DLVO theory, and Extended DLVO theory with hydration were used to model attractive and repulsive energies between gold nanoparticles exposed to a) BSA, b) IgG, c) lactoferrin, and d) lysozyme.

For all protein coatings modeled, all variations on DLVO theory indicated particle aggregation as none of the models tested predicted an interaction energy greater than or equal to Brownian motion ( $\sim 1.5 \text{ k}_B\text{T}$ ). Classic DLVO predicts near-zero interaction energies for all particles, with a similarly steep drop in energy as Van der Waals attractions become prominent. Once the contribution of the surface protein layer is incorporated in extended DLVO, the added thickness and consideration of more complex

interactions between particles, proteins, and media resulted in more negative values. Additionally, extended DLVO exhibited more protein-specific differences in the interaction energy curves in alignment with experimental observations. Hydration effects, though not large, did shift the energies towards more stability.

Modifications to DLVO theory resulted in interaction energy versus interparticle distance curves that were more responsive to protein properties. Extended DLVO results were sensitive to monolayer thickness and the Hamaker constant for the proteins. Inclusion of hydration added a factor other than surface charge that can contribute to suspension stability. In these models, BSA-coated particles had the highest interaction energy at all interparticle distances of all the proteins studied. This correlated with the observation that BSA-coated particles formed the smallest aggregates. Energies of interaction did not further correlate with aggregate size for the proteins studied. This may be due to assumptions made for some constants used in this approach, or due to a determining factor that is not incorporated in this model.

#### **4.4 Conclusions**

While lysozyme and BSA both influence particle stability in 200 nm and 1  $\mu\text{m}$  polystyrene particles, only lysozyme significantly reduced uptake for both particle sizes. Significant differences were observed in zeta potentials of particles exposed to CB buffer, CP buffer, lysozyme, and BSA in this study. Significant differences in charge as well as in cell uptake of the 1  $\mu\text{m}$  particles after exposure to these two buffers indicate that ion composition of aqueous media can also impact particle behavior. Thus, buffer selection should be carefully considered when studying particle interactions with proteins and cells.



The role of pH in protein-particle interactions was studied using four proteins with 100 nm gold particles across a range of pH. For the proteins studied, pH did not strongly affect protein adsorption in a consistent manner. Indeed, the suggestion that adsorption of proteins is maximized at or near their isoelectric points was not confirmed by these studies. However, residual citrate may have affected protein-particle interactions that are pH dependent. Small changes in particle surface charge and particle interactions with protein were observed at pH where changes in the ionization states of citrate occur.

Once adsorbed, proteins affect the surface charge of particles. The resulting surface charge depends on the identity of the protein adsorbed. The relative abundance of amine-functionalized and carboxylate-functionalized amino acid residues correlated with the zeta potentials of coated particles. Further, as zeta potentials moved from more negative charge towards neutral/positive, the size of aggregates tended to increase. When DLVO theory was used to describe particle interactions, it predicted when gold particles would and would not aggregate. Inclusion of hydration predicted an increase in the interaction energy for extended DLVO with hydration compared to extended DLVO. Thus, BSA stabilization of particles, resulting in little to no aggregation, may be due in part to hydration effects.

In gold nanoparticles, ion interactions at the particle surface were evident in the high stability in citrate buffer compared to stability in saline. Additionally, the changes in gold particle behavior in the presence of proteins observed at pH corresponding to  $pK_a$  values for citrate indicated that citrate ions were transported on particle surfaces into saline. This further supports the conclusion that exposure to ionic components present in

solution at various stages in particle processing can affect particle surface interactions in later processing steps and subsequently when interacting with cells.

## 5 Reconstitution of BALF as a Model to Study Inhaled Particle Behavior

### 5.1 Introduction

Foreign materials that enter the human body, regardless of introduction route, undergo a variety of surface interactions with the large cohort of biomolecules present in the various fluids of the body. The most common of these interactions is the adsorption of proteins to the materials' surfaces. For large-scale materials, this phenomenon is generally referred to as biofouling, whereas for nanomaterials the phenomenon is referred to as the formation of a protein corona due to the thin protein shell that surrounds the exterior of these materials.

Nanomaterials, due to their small size, can easily be transported to various tissues and even into cells. Their interactions with cells and tissues are influenced by a variety of factors including size, shape, and surface properties. Surface properties, such as hydrophobic/hydrophilic nature, surface charge, and the presence of specific functional groups can influence the responses of cells and tissues to foreign materials. However, prior to accessing cells and tissues, protein coronas that form on foreign materials create new surfaces.<sup>50</sup> These new surfaces are believed to be what ultimately interacts with cells and tissues.<sup>42, 55</sup>

With a large quantity of injectable therapies that utilize small particles entering the market, studies probing surface interactions between particles and proteins frequently focus on the blood proteome. Blood and serum, blood with cells and coagulation factors removed, are widely-available biological components for use in assessing behavior of nanomaterials in a clinically-relevant environment. Studies measuring interactions between nanomaterials and serum proteins have determined that protein adsorption to the

surfaces of particles strongly impacts biological fate.<sup>36, 55, 70, 172, 194</sup> Indeed, some have demonstrated that the composition of the corona proteomes formed in serum varies with different material and surface properties of particles, and that the varying composition of those coronas impact cell response.<sup>55</sup>

In addition to influencing cell responses, the surface properties imbued by proteins on nanomaterials, especially hydrophobic/hydrophilic nature and charge, further influence the stability of particles in aqueous media.<sup>55, 70, 172, 194</sup> This was explored in chapter 4, which identified that individual proteins can have varying impacts on particle stability. Particle instability has been observed in complex mixtures of proteins such as serum as well.<sup>36, 45</sup> Aggregation of particles that have been destabilized by protein coronas can impact transport in biological environments. Agglomerates can form that are too large to cross barriers that would have been permissive to the smaller primary particles. Additionally, large agglomerates may be relegated to alternative clearance pathways for removal from the body.<sup>195</sup>

While blood and serum have good clinical relevance for injectable therapies, proteomic analysis has shown that the composition of mucosal fluids and lung lining fluids are distinct from serum.<sup>24, 25, 196-198</sup> These analyses have found similar concentrations of albumin, the most prominent protein in either solution, as well as similarly high levels of some immunoglobulins such as IgG. However, differences in concentrations of proteins involved in host defense, e.g. collectins, immunoglobulins IgA and IgM, antimicrobial proteins, and the presence of lung-function specific proteins result in a fluid that is not well represented by serum as a model system. Indeed, a number of proteins are produced in the lungs such as the surfactant proteins SP-A, SP-B, SP-C, and

SP-D, as well as club cell proteins.<sup>24</sup> Surfactant proteins SP-A and SP-D, two collectins whose function is to aid in foreign object removal, have been shown to direct cellular uptake by alveolar macrophages.<sup>199</sup>

We hypothesized that particle surface interactions with biomolecules in lung fluids differed from those in serum due to the differences in the proteomes, which would result in distinct particle behavior. This study assessed the impact of human serum and concentrated bronchoalveolar lavage fluid (BALF) on the aggregation behavior, zeta potential, cell uptake, and amount of protein in the corona of polystyrene particles. We further assessed differences in particle behavior based on particle size and surface functionalities in both fluids.

## **5.2 Materials and Methods**

### **5.2.1 Concentration of BALF**

Bronchoalveolar lavage fluid (BALF), was obtained from our collaborator, Dr. David Stoltz (University of Iowa Hospitals and Clinics), who collected the sample from a nonsmoking healthy male aged 34. After collection, cells were removed and protease inhibitors (Pierce) were added to prevent degradation. The fluid was stored at -80°C when not in use. BALF total protein content was measured by bicinchoninic acid assay (BCA, Thermo) and found to be  $93 \pm 6 \mu\text{g/mL}$ . The process of collecting BALF from the lung space results in significant dilution as the lungs are rinsed with volumes of saline that dilute the very small initial volume of lung fluid. Since volumes collected by BALF are substantial (50-100 mL), the fluid can be concentrated to obtain more physiologically relevant protein concentrations. To concentrate BALF, saline needs to be extracted from the sample. A two-step process was developed to first remove salt, then remove water.

For salt removal, a buffer exchange column for proteins was selected over dialysis. Excess salts were removed using BioRad buffer-exchange columns with P6 gel. Columns were prepared by exchanging the storage buffer with type-1 water from a Direct-Q UV-R (Millipore) three times followed by centrifugation at  $1,000\times g$  for four min to draw the excess fluid through the gels. After the gels had been prepared in type-1 water, 100  $\mu\text{L}$  of BALF was added to each column, and the columns were centrifuged for two min at  $1,000\times g$ . Four samples were pooled, and the water was removed by evaporation in a speedvac (SC100, Savant) for 3 h with the heat setting on medium ( $\sim 40^\circ\text{C}$ ) to a resulting volume of  $\sim 100 \mu\text{L}$ , an approximate 75% volume reduction. This sample was analyzed using BCA and bromocresol green (BCG) assays to test for total protein content and albumin content respectively. This sample was found to have  $309\pm 29 \mu\text{g/mL}$  total protein and  $281\pm 67 \mu\text{g/mL}$  albumin. This was a 3.3-fold increase in protein concentration. Based on this pilot study, the following protocol was used to produce reconstituted BALF (rBALF) for use in studying particle behavior in model lung fluids and serum.

P6 gel columns were prepared by exchanging the storage buffer with type-1 water from a Direct-Q UV-R (Millipore) three times followed by centrifugation at  $1,000\times g$  for four min to draw the excess fluid through the gels. After the gels had been prepared in type-1 water, 100  $\mu\text{L}$  of BALF was added to each column, and the columns were centrifuged for two min at  $1,000\times g$ . Sets of 10 exchanged samples were pooled, and pooled samples ( $\sim 1 \text{ mL}$  each) were placed into microcentrifuge tubes and dried in a speedvac (SC100, Savant) for 3 h with the heat setting on medium ( $\sim 40^\circ\text{C}$ ) to a resulting volume of  $\sim 100 \mu\text{L}$ . Dried samples were again pooled to a total volume of just over 2 mL. Protein concentration of the rBALF was analyzed using BCA. One mL aliquots were

taken from the pooled samples for exposure to particles. Three batches of rBALF were prepared for this study, with protein concentrations measured to be  $1386 \pm 201$   $\mu\text{g/mL}$ ,  $1706 \pm 153$   $\mu\text{g/mL}$ , and  $126 \pm 5$   $\mu\text{g/mL}$ . Despite being much less concentrated, this last sample was used due to having more than enough protein to fully coat particles. To coat 1 mg of 200 nm particles with a monolayer requires approximately 10  $\mu\text{g}$  of protein. Thus, even with this concentration, an excess of protein is available. When the differences in concentration were considered, the mass of protein adsorbed varied with total protein concentration in the fluids, but particle properties did not vary with protein concentration. This low concentration case was included based on this low dependence of particle properties on total protein content.

### 5.2.2 Effects of Serum and rBALF Exposure on Particle Behavior

To identify the effects proteins from serum and BALF on particle aggregation, polystyrene particles with various surface functionalities were used. Particle sizes included 200 and 500 nm particles, and surface functionalities included plain polystyrene (PPS), aliphatic amine-functionalized polystyrene (APS), and carboxylate-functionalized polystyrene (CML). PPS is referred to as plain or non-functionalized. However, the particles have surface sulfate groups present from the initiator used in polymerization, and a small contribution from trace residual sulfate-containing surfactant used in the synthesis.<sup>200</sup>

Normal saline was prepared using sodium chloride (RPI). Phosphate buffered saline (PBS) was prepared using sodium chloride (RPI), monobasic sodium phosphate (RPI), monobasic potassium phosphate (Sigma), and potassium chloride (Fisher). 1 mg aliquots of particles were added to samples of normal saline, PBS, rBALF, or diluted

serum and mixed for 1 h. Hydrodynamic size distributions were measured using a Malvern Nano ZS in clear plastic disposable polystyrene cuvettes (VWR). The size method was set to record 13 size distributions per measurement. The intensity versus size values were exported and overlaid for each particle type and size to compare effects of exposure on particle stability.

Table 5.1. Manufacturer information for polystyrene particles used in protein-interaction studies.

Size (nm)	Functionalization	Manufacturer	Lot #	Groups/Particle
220	PPS	Polysciences	671232	N/A
190	CML	Invitrogen	1148837	$9.5 \times 10^4$
200	APS	Invitrogen	813620	$3 \times 10^5$
510	PPS	Polysciences	655980	N/A
520	CML	Polysciences	710373	N/A
500	APS	Polysciences	708245	N/A

Particles prepared for hydrodynamic size measurements were placed in folded capillary zeta cells (Malvern, DTS1070) and the zeta potential measured in a Malvern Nano ZS. The zeta method was set to run a minimum of 10 times and a maximum of 100 times or until confidence in the result was achieved. This analysis was run three times per sample and the mean and standard deviation of these three values reported.

Protein adsorption to particles was determined by adding 1 mg of 500 nm particles or 0.4 mg of 200 nm particles to BALF or diluted serum and allowing coatings to form for 1 h. Selection of these quantities of particles was based on maintaining constant surface area available to the proteins across all samples. Serum was diluted to match the concentration of protein in the rBALF sample being used. An exception was



made in the case of the low concentration sample, where serum was diluted to 1,000 µg/mL to provide a basis for comparison to other particles. After 1 h of exposure, the samples were centrifuged at 3,200×g for 15 min to separate the particles from the solutions. Total protein content of the samples was measured using BCA before and after exposure to particles. The difference in solution protein content before and after exposure was calculated to be the mass adsorbed to the surface of particles.

### 5.2.3 Flow Cytometry to Measure Coated Particle Uptake

Polystyrene particles were exposed to rBALF and serum to measure the effects of exposure to either fluid on uptake of PPS, CML, and APS particles. For these studies, Fluospheres (Molecular Probes) with particle diameters of 0.2 µm and yellow-green fluorescent tags were obtained in PPS (Sulfate, Lot:30151W), CML (Lot: 714135), and APS (Lot: 513683). Additionally, 0.5 µm CML (Lot: 417442) particles were obtained with a red fluorescent tag. Aliquots of 1 mg of 500 nm particles or 60 µg of 200 nm particles were dispersed in either diluted serum or concentrated BALF for 1 h. These selections were based on maintaining an equal number of particles per mL regardless of size. Particles were separated from the respective biological media by centrifugation for 30 min at 12,000×g for 200 nm particles and 10,000×g for 500 nm particles. The BALF and serum supernatants were removed, and the particles were suspended in 1 mL of RPMI 1640. Dilutions from these stock solutions were made to a concentration of 10 µg/mL for all particle sizes for uptake studies. This dose was based on a previous study comparing effects of media with and without serum on the uptake of similarly sized fluorescent polystyrene beads.<sup>201</sup>

A549 cells were cultured and seeded onto 12-well tissue culture plates (Gibco) in 1 mL of culture media (RPMI 1640 with 1% penicillin streptomycin and 10% FBS) at a concentration of  $2 \times 10^5$  cells/mL and allowed to attach and grow overnight. Cells were rinsed three times with sterile PBS (Gibco) and exposed to 1 mL aliquots of coated or uncoated (control) particles in RPMI 1640 for 4 h under incubation. After exposure, excess particles were removed by rinsing with sterile PBS 3x. Cells were detached from culture plates using 300  $\mu$ L of versene (Gibco, Lot: 1962329) for 10-14 min at 37°C until cell detachment was observed. Cells were dislodged and collected by gently pipetting the suspension onto the wells 10 $\times$  for each well. Each treatment was repeated in 3-4 wells. All wells sharing the same exposure were pooled and collected into 5 mL 12 $\times$ 75 mm falcon tubes (BD). Cells were separated from versene in a Jouan CR 422 centrifuge for 10 min at 1,000 $\times$ g and 4°C. The versene was poured off, and cells were suspended in 0.9-1.2 mL of sterile PBS (0.3 mL per replicate well) for flow cytometry. Tubes were kept on ice until analysis to maintain sample integrity. Samples were vortexed briefly to disperse cells immediately prior to measurement.

Samples were analyzed using a BD LSR II with violet laser upgrade. Data was collected using FACSDiva software, with the yellow-green fluorescent beads measured using a 480 nm excitation laser and the red fluorescent beads measured using a 561 nm excitation laser. Gates were developed using cells without beads to identify the population of cells of interest using side-scatter area (SSC-A) versus forward-scatter area (FSC-A) to sort based on size and granularity. From this population, forward-scatter width (FSC-W) versus FSC-A was used to identify single cells and separate from double cells. Fluorescent beads without cells and cells without beads were used as controls to

determine the intensity threshold for bead-positive cells and verify that particles alone were largely excluded from gates. Data were analyzed using FlowJo 10.5.0. Results of gating for the yellow-fluorescent 200 nm particles is displayed in Figure 5.1, and the gating for the red-fluorescent 500 nm particles are shown in Figure 5.2. A small population of false positive particles was observed in the gating for 200 nm CML particles (Figure 5.1h). This is likely due to weak fluorescence observed in these particles (Figure 5.1i). Due to their small size, these particles are less likely to trigger a recordable event in the instrument without strong fluorescence. The small population observed is likely agglomerates that fell inside the gates developed for A549 cells, as more scattering would be required in the absence of strong fluorescence to trigger a recordable event.

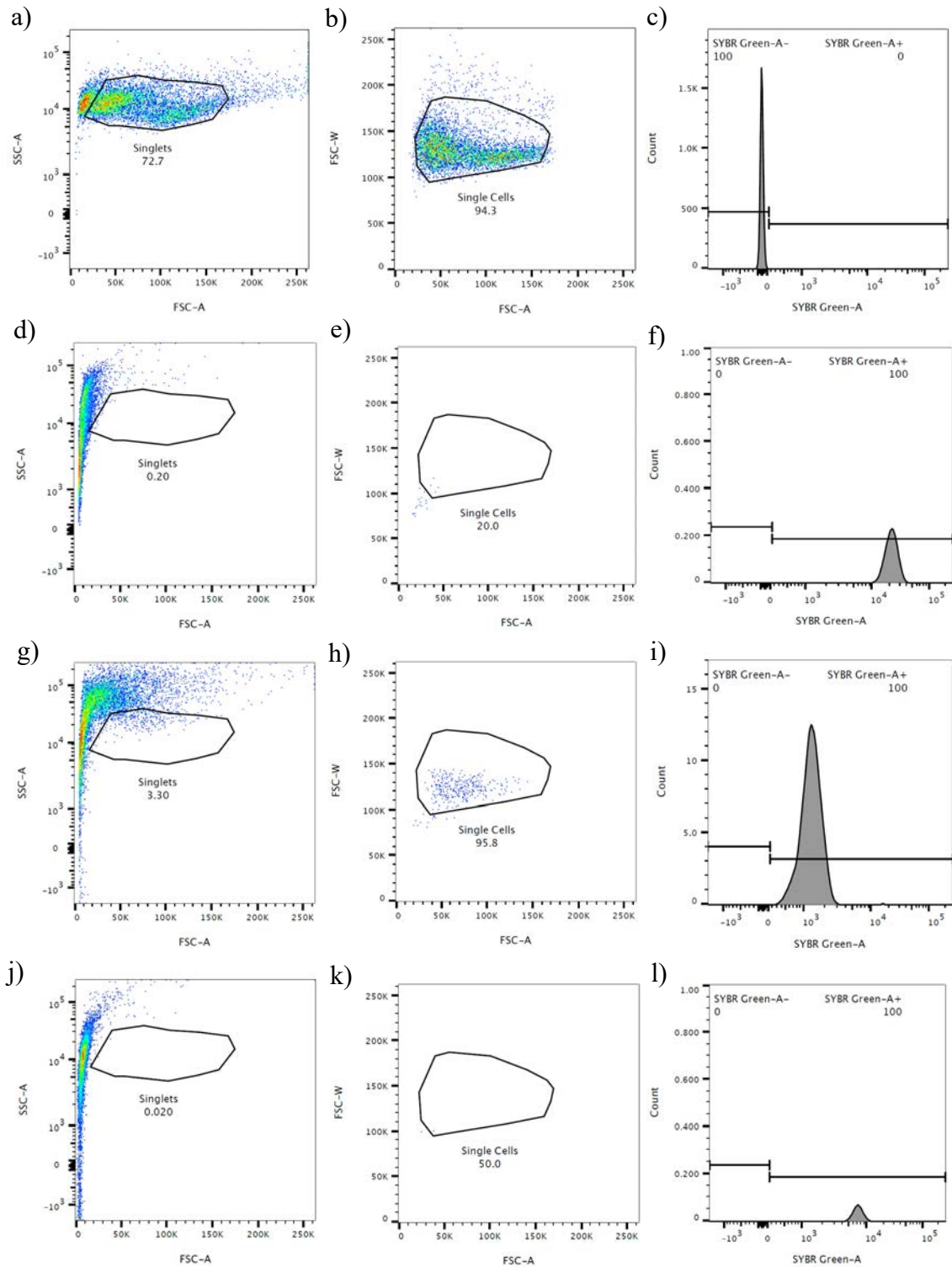


Figure 5.1. Sample gating defined for a-c) yellow-green fluorescence using untreated A549 cells. Gate validation with exclusion of d-f) 200 nm PPS, g-i) 200 nm CML, and j-l) 200 nm APS particles in the absence of cells.

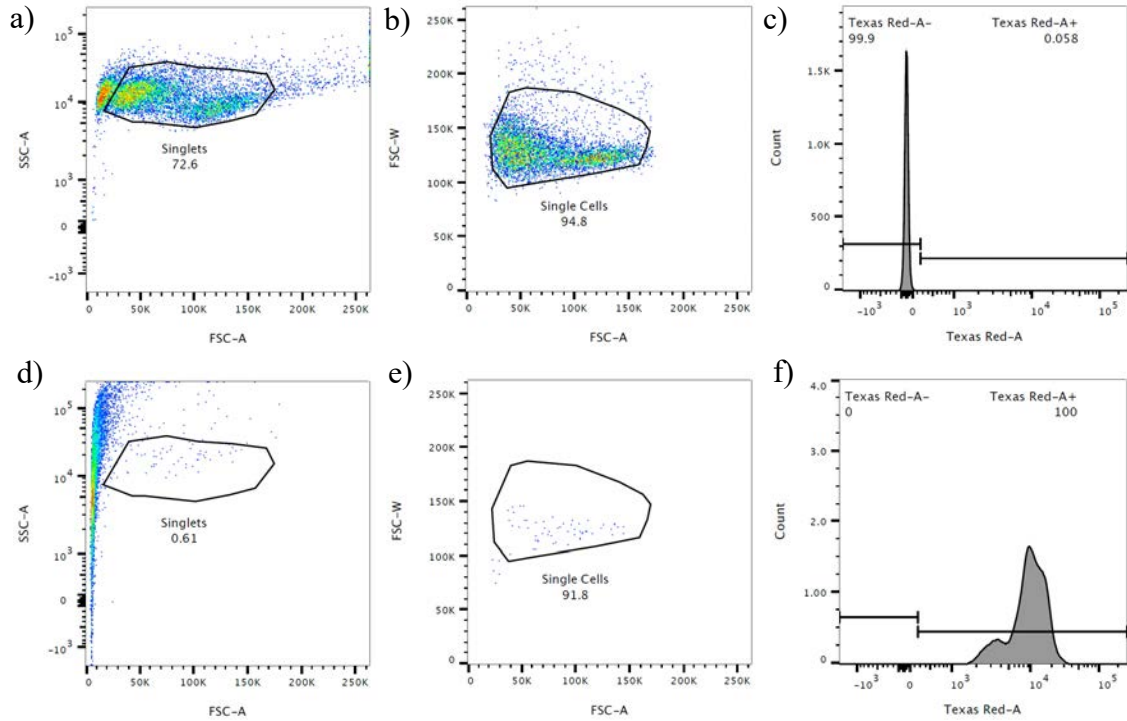


Figure 5.2. Sample gating defined for a-c) red fluorescence using untreated A549 cells. Gate validation with exclusion of d-f) 500 nm CML particles in the absence of cells.

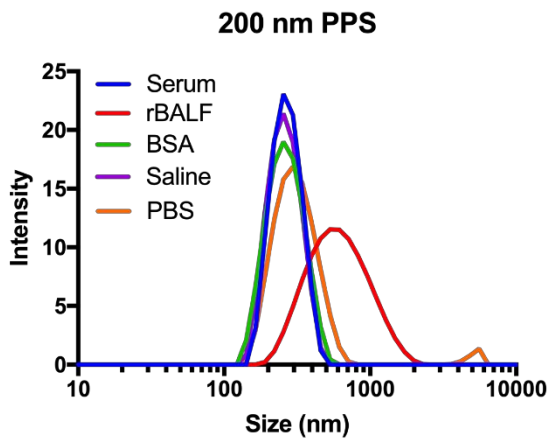
## 5.3 Results

### 5.3.1 Effects of Serum and rBALF Exposure on Particle Behavior

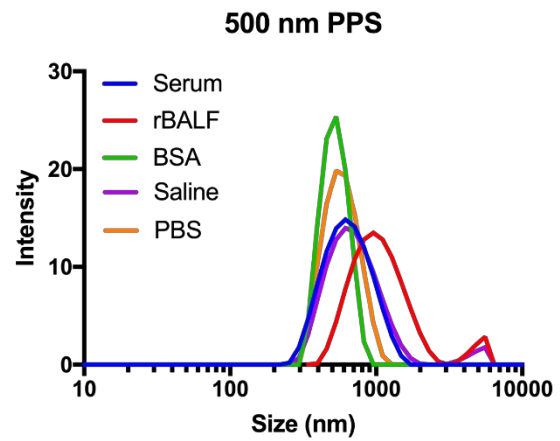
For PPS particles with primary particle diameters of 200 and 500 nm, the most significant effects were observed in the particles exposed to rBALF, which resulted in size distributions shifted towards larger particles indicating increased size due to protein adsorption and particle agglomeration (Figure 5.3a&b). Additionally, rBALF exposure to 500 nm PPS resulted in the appearance of a small population near 10  $\mu\text{m}$  at the limit of measurement for light scattering. This indicates that a population of large agglomerates forms in rBALF. Serum exposure resulted in particle size distributions that were matched to saline for both particle sizes. As with rBALF, a small peak at large particle sizes was observed for 500 nm PPS in serum. Size distributions recorded for particles exposed to

BSA did not vary from saline and PBS for 200 nm PPS particles. For 500 nm particles, BSA exposure resulted in a narrowed distribution. For PPS, serum exposure altered the zeta potential to approximately -20 mV for both particle sizes (Figure 5.3c&d). rBALF exposure, altered the zeta potential to approximately 0 mV for both particle sizes. Using the BCA assay, it was determined that 200 nm PPS particles adsorbed 277  $\mu\text{g}$  of protein from serum and 383  $\mu\text{g}$  of protein from rBALF. 500 nm PPS particles adsorbed 256  $\mu\text{g}$  of protein from serum and 426  $\mu\text{g}$  of protein from rBALF.

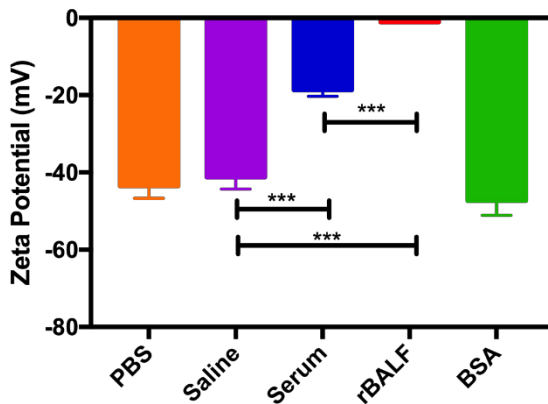
a)



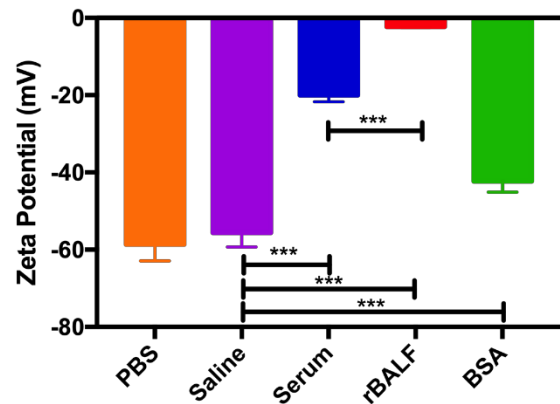
b)



c)



d)



e)

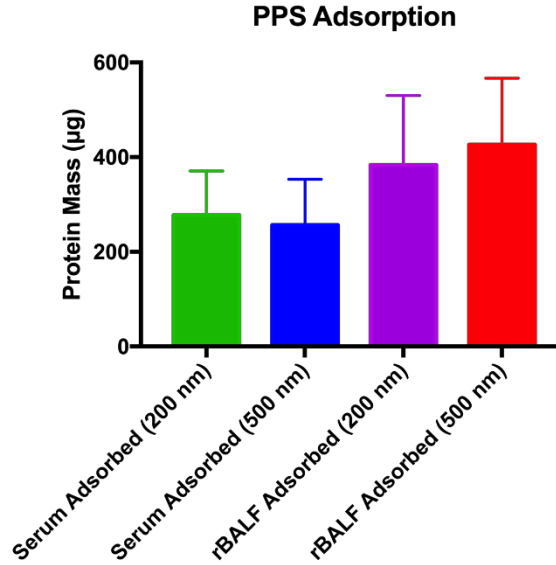
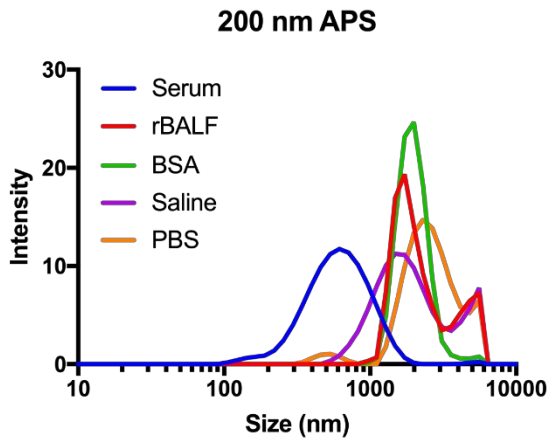


Figure 5.3. DLS measurements of a) 200 nm and b) 500 nm PPS particles after exposure to serum, rBALF, and BSA. Surface charge measurements of c) 200 nm PPS particles and d) 500 nm PPS particles exposed to serum and rBALF. e) Measurements of the mass of protein adsorbed to the surface of 200 nm and 500 nm PPS particles exposed to serum and rBALF (\*\* $p < 0.001$ ).  $n = 1, 3$  replicates. Error Bars = SD.

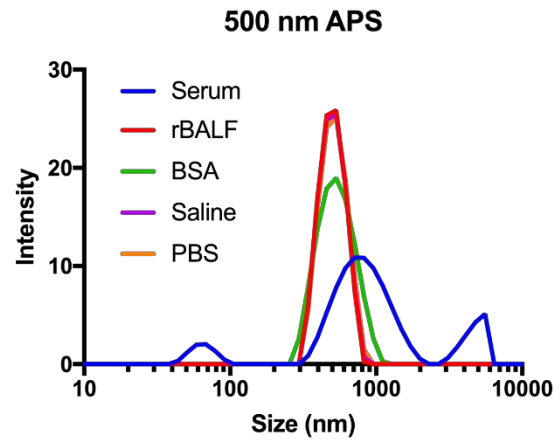
200 nm APS particles formed large aggregates in all suspensions tested. Particles exposed to rBALF, saline, and PBS all had primary peaks around 2000 nm, and secondary peaks that were beyond the measurement range of the instrument ( $>10 \mu\text{m}$ ). Serum exposure resulted in smaller hydrodynamic diameters for these particles. BSA exposure resulted in a particle size distribution at 2000 nm. 500 nm APS particles exposed to rBALF, saline, PBS, and BSA had hydrodynamic diameters around 500 nm. Serum exposure induced aggregation, with a primary peak around 800 nm, and a secondary peak beyond the instrument's measurement range. The 200 nm APS particles had slightly negative zeta potentials ranging from -4 mV to -10 mV for all solutions tested. The 500 nm APS particle zeta potentials of -26 mV after exposure to rBALF and BSA. PBS exposure resulted in a zeta potential of -24 mV, while particles exposed to

saline had a zeta potential of -31 mV. 500 nm APS particle exposed to serum resulted in a zeta potential of -8 mV. 200 nm APS particles adsorbed 23  $\mu\text{g}$  of protein from serum and 11  $\mu\text{g}$  of protein from rBALF. 500 nm APS particles adsorbed 181  $\mu\text{g}$  of protein from serum, and 153  $\mu\text{g}$  of protein from rBALF.

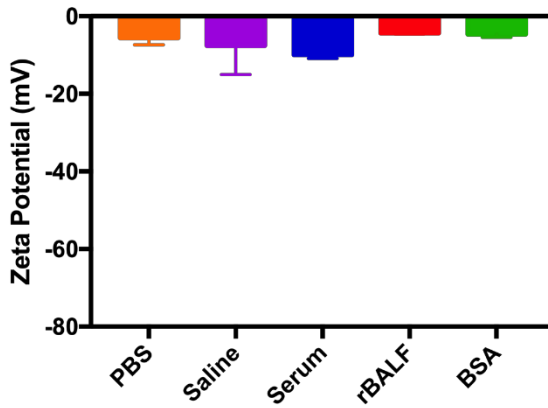
a)



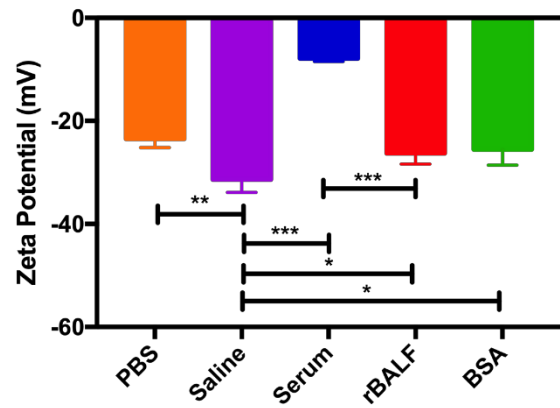
b)



c)



d)





e)

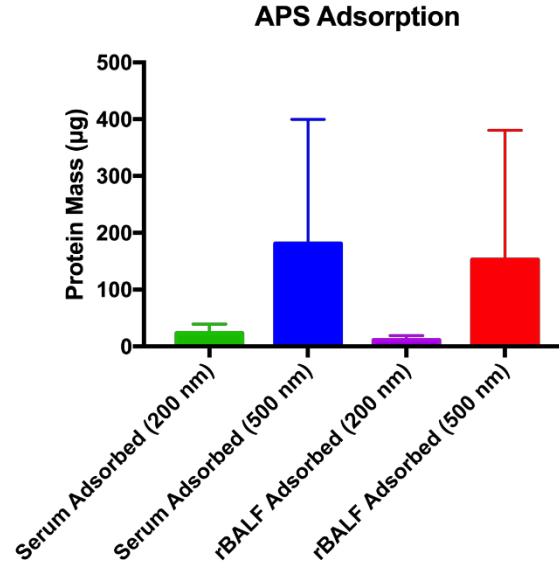
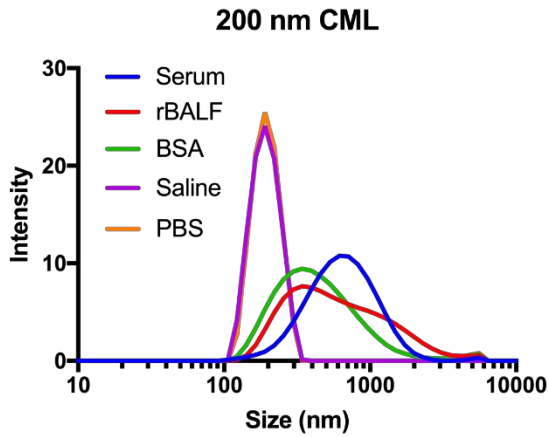


Figure 5.4. DLS measurements of APS particles of a) 200 nm and b) 500 nm primary particle diameter exposed to serum and rBALF. Surface charge measurements of c) 200 nm and d) 500 nm APS particles exposed to serum and rBALF. e) Measure of the mass of protein adsorbed to the surface of 200 nm and 500 nm APS particles exposed to serum and rBALF (\*  $p < 0.05$ , \*\*  $p < 0.01$ , \*\*\*  $p < 0.001$ ).  $n = 1$ , 3 replicates. Error bars = SD.

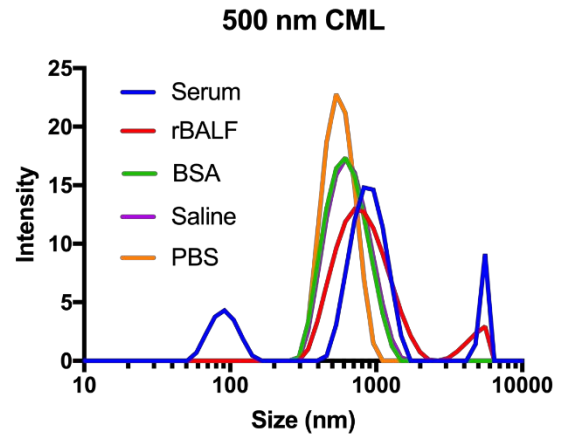
For CML particles with primary particle diameters of 200 and 500 nm, exposure to both rBALF and serum resulted in the formation of aggregates (Figure 5.5a&b). For the 200 nm CML particles, serum exposure resulted in a distribution centered around 700 nm. When 200 nm CML particles were exposed to rBALF, they aggregated into a bimodal distribution with peaks centered around 400 nm and 1,500 nm. BSA-exposed 200 nm CML particles formed aggregates with a distribution centered around 400 nm. 200 nm CML particles exposed to PBS or saline were monodisperse and distributions were centered around 200 nm, the primary particle size. When 500 nm CML particles were exposed to rBALF, they formed aggregates, with a distribution centered around 800 nm and a second distribution at the edge of the instrument's detection range (~10 µm).

Serum-exposed 500 nm CML particles formed slightly larger aggregates, with a distribution centered around 900 nm, and a second distribution at the limit of detection similar to rBALF. 500 nm CML particles exposed to saline and BSA were monodisperse and distributions were centered around 600 nm. PBS exposure to 500 nm CML particles resulted in a monodisperse distribution centered around 500 nm. CML particles exposed to serum and rBALF were further characterized by their zeta potentials (Figure 5.5c&d). Serum-exposure to 200 nm CML particles resulted in a zeta potential of -9 mV. When rBALF was exposed to CML particles, the zeta potential was -6 mV. BSA exposure to the 200 nm CML particles resulted in a zeta potential of -13 mV. 200 nm CML particles in PBS and saline exhibited zeta potentials of -43 mV and -39 mV respectively. When 500 nm CML particles were exposed to serum, the resulting zeta potential was -7 mV. rBALF exposure to these particles resulted in a similar zeta potential of -9 mV. When BSA was exposed to 500 nm CML particles, the zeta potential was -30 mV. 500 nm CML particles suspended in PBS or saline had zeta potentials of -35 mV and -45 mV respectively. Protein adsorption to CML particles exposed to serum and rBALF was measured using the BCA assay (Figure 5.5e&f). When 200 nm CML particles were exposed to serum, they adsorbed 60  $\mu\text{g}$  of protein. When these particles were exposed to rBALF, they adsorbed 3  $\mu\text{g}$  of protein. When 500 nm CML particles were exposed to serum, they adsorbed 107  $\mu\text{g}$  of protein. When these 500 nm particles were exposed to rBALF, they adsorbed 48  $\mu\text{g}$  of protein.

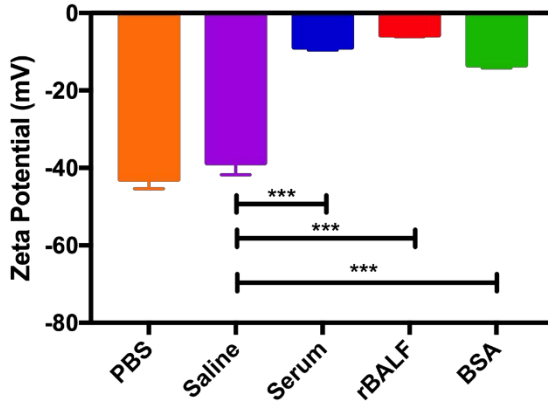
a)



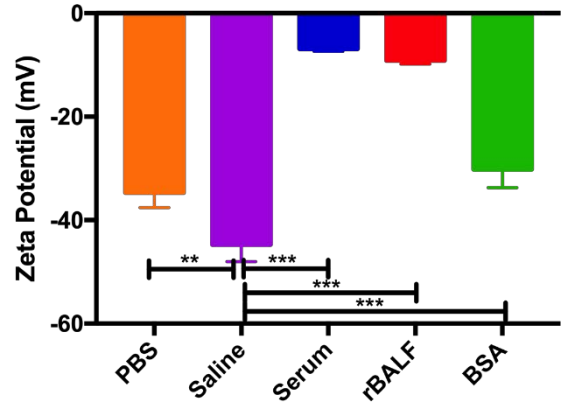
b)



c)



d)



e)

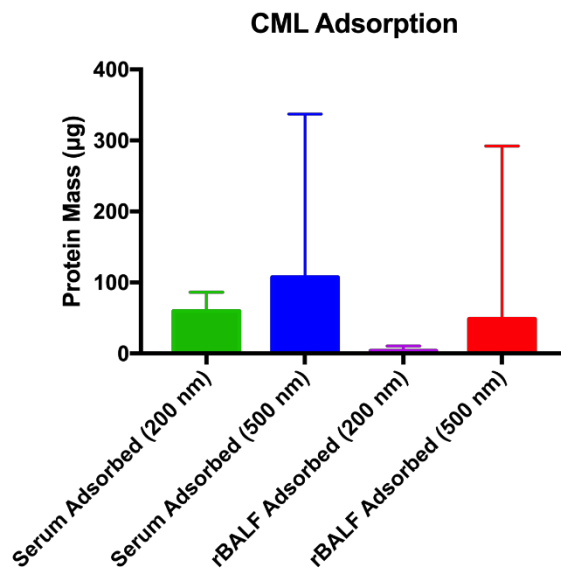


*Figure 5.5. DLS measurements of CML particles of a) 200 nm and b) 500 nm primary particle diameter exposed to serum and rBALF. Zeta potential measurements of c) 200 nm and d) 500 nm CML particles exposed to serum and rBALF. e) Measure of the mass of protein adsorbed to the surface of 200 nm and 500 nm CML particles exposed to serum and rBALF (\*\* $p < 0.01$ , \*\*\* $p < 0.001$ ).  $n = 1$ , 3 replicates. Error Bars = SD.*

### 5.3.2 Flow Cytometry to Measure Coated Particle Uptake

Flow cytometry was used to assess the impacts of particle exposure to serum or rBALF on lung cell association. As illustrated in Figure 5.6a, protein coronas from both serum and rBALF impacted uptake of 200 nm PPS particles the most. The fraction of cells positive for particles was less than 20% for both serum and rBALF-exposed particles compared to 87% of cells positive for untreated particles. For the 200 nm APS particles, serum exposure resulted in reduced uptake relative to controls and rBALF. 200 nm CML particles exposure to serum or rBALF did not significantly affect the percentage of cells positive for particles relative to untreated controls. 500 nm CML particles exposed to serum and rBALF were less likely to be associated with cells than untreated controls. Particles exposed to rBALF were more likely to be associated with cells than those exposed to serum ( $p = 0.046$ ).

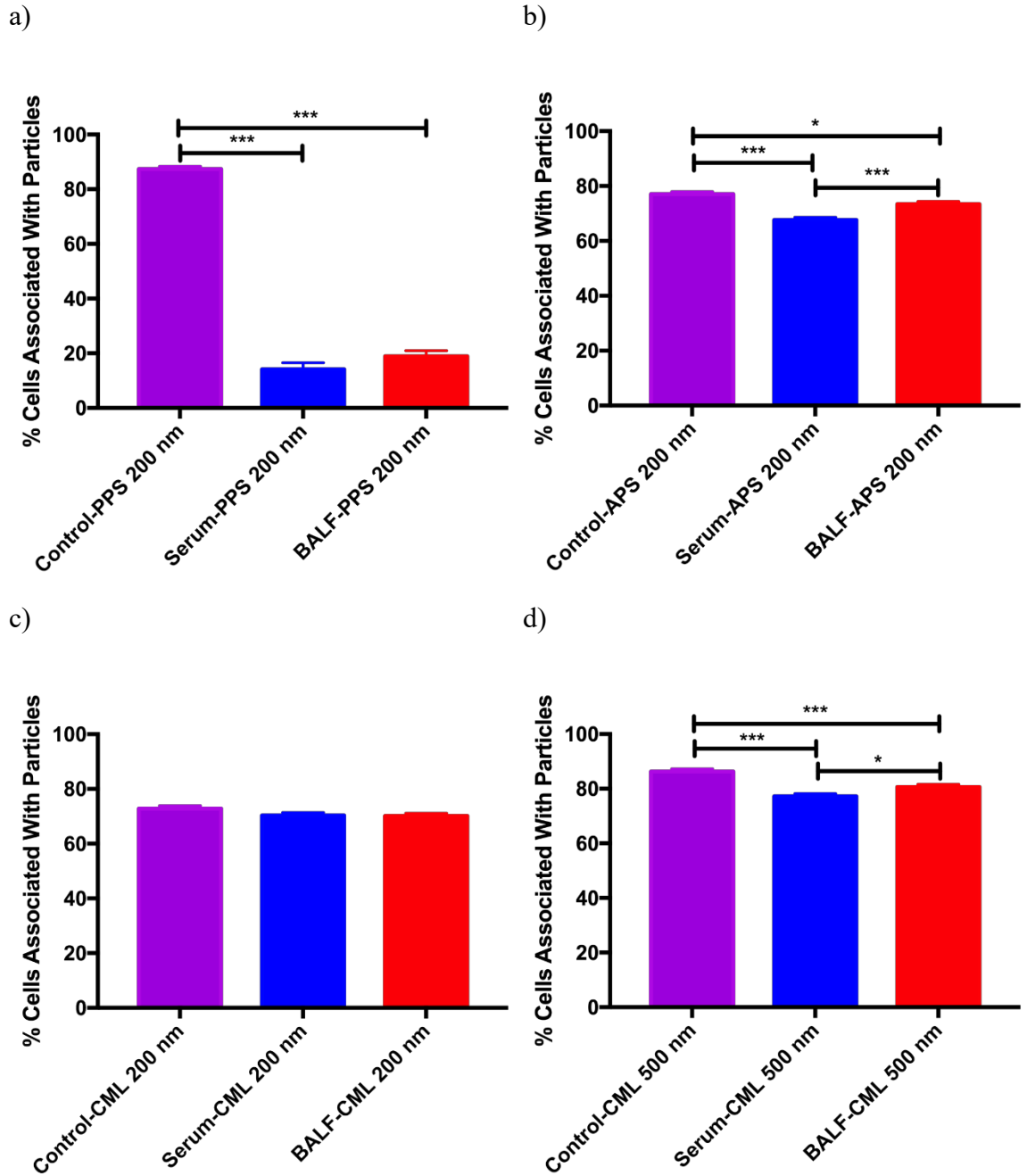


Figure 5.6. Measurement of A549 cell association with fluorescent a) 200 nm PPS ( $n=1$ , 4 replicates), b) 200 nm APS ( $n=1$ , 4 replicates), c) 200 nm CML ( $n=1$ , 4 replicates), or d) 500 nm CML ( $n=1$ , 3 replicates) ( $*p<0.05$ ,  $***p<0.001$ ). Error Bars=SD.

## 5.4 Discussion

### 5.4.1 Proteins in Serum and Lung Lavage Fluid Impact Particle Stability

For PPS particles and APS particles, the size distributions of particles exposed to rBALF differed from those exposed to serum for both particle sizes studied. For 200 nm PPS, 500 nm PPS, and 500 nm APS, this corresponded with differences in zeta potentials for rBALF-exposed particles compared to serum-exposed particles. For 200 nm and 500 nm CML particles, size distributions for particles exposed to serum or rBALF tended to overlap, which corresponded with very similar zeta potentials for particles in both fluids. This was also despite the order-of-magnitude difference in protein concentration in the rBALF. This indicates that a small quantity of adsorbed protein is capable of significantly altering particle charge and behavior. For all functionalities studied, no significant differences in protein adsorption were observed between particles of different size. Particles were exposed such that surface area remained constant, so any potential size-related effects would be based on surface curvature rather than available area. For all particle functionalities and sizes studied, aggregates tended to form when particle zeta potentials were nearer to zero. This is consistent with electrosteric forces being a strong contributor to the stability of particles in suspension as was discussed in Chapter 4.

### 5.4.2 Surface Chemistry Influences Cell Response More Than Fluid Composition

In the case of PPS particles, rBALF resulted in slightly more adsorption for both particle diameters, but mass adsorbed from serum was similar in each case. CML and APS particles adsorbed less mass than the PPS particles. Additionally, while PPS particles adsorbed more protein from rBALF than serum, the CML and APS particles adsorbed more protein from serum than rBALF. CML particles adsorbed the least protein

mass of any particle type studied. This was surprising given the aggregation and shifts in zeta potential observed for CML particles exposed to both serum and rBALF.

Additionally, while rBALF did not induce aggregation or a shift in zeta potential for APS particles, similar levels of protein adsorption to serum were observed. The large mass adsorbed from serum to PPS with little aggregation observed in DLS indicate that large quantities of protein adsorption is not the cause of particle aggregation in these fluids.

When we consider how serum and lung proteins adsorbed to particles impact lung cell response, a large difference is observed in the 200 nm PPS particles compared to other particles studied. Serum or BALF adsorption to these particles resulted in a large decrease in cell association. When considering differences in particle type, amine particle association with cells was significantly reduced in rBALF and serum, but no significant differences were observed in 200 nm CML. This implies that these surface variants likely result in a different protein corona fingerprint, similarly to those observed by Walkey et al. Differences in particle size or zeta potential did not correlate with the observed interactions with cells. Particle surface, whether through direct interactions or based on influencing protein adsorption, appears to impact cell response more than particle charge and aggregation after exposure to protein. This is consistent with prior work, where changes in surface chemistry were found to influence cell responses to particles exposed to serum.<sup>55</sup> While aggregation did not correlate with cell responses in this case, there is a limit to the size of an aggregate that could feasibly enter a cell. Thus, particle size is still important to consider for cell and tissue interactions.

The 200 nm APS particles had zeta potentials much nearer to zero for all solutions tested, whereas the 500 nm APS particles had much more negative zeta potentials. A

discussion with technical support at Bangs Labs (affiliated with Polysciences) revealed that amine-functionalized particles are produced there by addition of ethylenediamine to carboxylate-modified polystyrene particles.<sup>202</sup> Thermo/Invitrogen/Molecular Probes lists on their product page for aliphatic amine polymer microspheres that the amine functional groups are on 6-carbon spacers,<sup>203</sup> and their certificate-of-analysis forms list both amine and carboxylate functionalities on the particles.<sup>204</sup> Thus it is likely that Thermo/Invitrogen/Molecular Probes produces amine-functionalized polystyrene by reacting hexamethylenediamine with carboxylate-modified polystyrene particles. The more aminated 200 nm particles tended to aggregate significantly more than the more negatively charged 500 nm particles. These particles are technically zwitterionic, having a mixture of amine and carboxylate functional groups (and some quantity of sulfate) on their surface, resulting in a net neutral charge. As will be discussed in more detail in Chapter 6, a feature of zwitterions that contributes to their stabilizing properties in water is related to the spatial relationship between cationic and anionic groups.<sup>92</sup> The 6-carbon spacer on the aminating group creates a large space between the terminal amines and the unreacted surface-bound carboxylates. With a non-optimum spatial relationship, this results in a neutral particle that does not have the requisite hydration necessary to remain stable in suspension. Based on this understanding of the differences in surface chemistry of these two APS particle sizes, it is likely that many of the differences observed in zeta potentials and aggregate formation are functions of differences in particle surface, rather than a particle size-related effect.

In almost all cases, little to no effect was observed when exposed to pure BSA.

This implies that the effects observed in serum and rBALF are not due to albumin despite



it being the most abundant protein in each fluid. In many cases, serum and rBALF had markedly different impacts on aggregation and changes in zeta potential relative to saline or PBS. This indicates that studies of protein coronas in serum are not strong predictors of behavior in lung fluids.

## **5.5 Conclusions**

Despite having proteomic overlap, effects of serum and rBALF exposure onto polystyrene nanoparticles varied. Aggregation behavior, zeta potential, total mass of protein adsorbed, and cell uptake after exposure to serum or rBALF varied with particle surface functionality and with primary particle diameter. Based on these results, investigations into behavior of inhaled particles, whether in an environmental exposure or drug delivery context, should consider potential interactions with the proteomes of lung fluids. Lung lavage is a minimally invasive diagnostic procedure to collect cells from the deep lungs that can provide access to BALF as a better model for the characterization of such inhaled particle behavior. We have demonstrated here that BALF can be reconstituted to a higher total protein content for use in such characterizations.

## 6 Zwitterionic pMPC Synthesized by Photoinitiated RAFT Polymerization Stabilizes Particles in BALF and Serum

### 6.1 Introduction

Biomaterials that resist nonspecific protein adsorption (or biofouling) have a wide variety of uses in drug delivery, medical devices, and marine engineering. Nonspecific protein adsorption, resulting in the formation of a protein corona, can destabilize particle suspensions causing aggregation or otherwise modifying particle behavior in the body. This can impair the ability of drug-containing particles to cross various biological barriers or induce clearance as part of the foreign body response. Recent *in vitro* studies of nanoparticle interactions in vascular endothelium and in epithelium have indicated that the protein corona plays a role in cell adhesion and particle uptake.<sup>63, 172</sup> Walkey et al. demonstrated the significance of particle surface charge effects on both protein corona composition and cellular uptake,<sup>55</sup> indicating a strong relationship between surface chemistry of particles and biological interactions. In this study protein corona formation on the surfaces of most particles studied resulted in decreased cell uptake of particles. This ability of proteins to coat particles and interfere with cellular response, as demonstrated in chapters 4 and 5, is undesirable for therapeutic particles.

To mitigate protein adsorption from blood, zwitterionic polymers have been used resulting in protein adsorption as low as 0.4 ng/cm<sup>2</sup> in plasma.<sup>46</sup> Zwitterionic polymers, those with positively and negatively charged moieties but a net neutral charge, are a class of non-fouling materials that can be developed with many chemistries. Zwitterionic polymers are selected with a cation-anion pair that result in a net-neutral overall charge. Cationic groups are typically amines, but anionic groups tend to vary, with common

examples being carboxylate and sulfate moieties.<sup>87</sup> These zwitterionic pairs are typically collocated on a polymer side-chain, although some have demonstrated similar results grafting cationic and anionic brushes in equal proportion onto surfaces<sup>46</sup> or creating a peptide with alternating cationic and anionic amino acids<sup>85</sup>.

The prevalent theories regarding why many surfaces resist fouling/protein adsorption tend to focus on the behavior of water. One such theory is that strong hydration through electrostatic forces<sup>205</sup> or through hydrogen bonding can create a barrier to proteins adsorbing to a surface.<sup>87</sup> The polar nature of water results in strong interactions with the ionic components of a zwitterionic surface. A charged surface made up of purely cations or anions would induce orientation of water molecules with the oxygen towards cationic groups or the hydrogens towards anionic groups. This results in water being oriented with either the oxygen or the hydrogens faced towards the surface. When both groups are present in a close spatial orientation, this can result in water that is not oriented with all of the oxygen or hydrogen groups towards the surface. A similar, if slightly different approach to describing the role water plays in fouling-resistant surfaces is in the ordering of water molecules in the immediate vicinity of a surface.<sup>84</sup> One group described the behavior of water near zwitterionic surfaces as “ice-like”, as an explanation of both protein-resistance and low friction observed for some of these surfaces when wetted.<sup>206</sup>

Polymers functionalized with phosphorylcholine, a biomimetic zwitterionic functional group consisting of phosphate and quaternary ammonium, have been developed as fouling-resistant materials, and their resistance to protein adsorption as well as low friction properties have been studied.<sup>46, 206, 207</sup> One polymer,

polymethacryloyloxyethyl phosphorylcholine (pMPC), has been used in medical devices such as contact lenses<sup>94</sup> and a small number of drug-delivery particles used in research labs. In the case of drug delivery, most systems using phosphorylcholine involve the incorporation of pMPC into copolymers for the formation of polymersomes to encapsulate and deliver drugs.<sup>95, 96</sup>

Copolymers containing pMPC have been developed as coatings onto gold surfaces. These systems have been designed to coat gold using initiator chemistry to generate thiol end-functionality<sup>69</sup> or using the pMPC-containing copolymer as the reducing agent to facilitate gold nanoparticle formation by reduction of tetrachloroauric acid<sup>208</sup>. Further, block copolymers containing pMPC have been synthesized as proof-of-concept work to demonstrate compatibility with radical addition fragmentation chain-transfer (RAFT) agents.<sup>96</sup>

Resistance to protein adsorption could make pMPC an effective polymer for delivering inhalable medicines to treat lung infections. To test the potential of pMPC in pulmonary medicine, a nanoparticle system with a surface coating of pMPC was designed. Gold nanoparticles were selected as the core since they have demonstrable antimicrobial properties<sup>209-212</sup> are composed of an inert and insoluble material, and for the ease of thiol-SAM coating materials onto their surfaces<sup>213</sup>. Production of gold nanoparticles by reducing tetrachloroauric acid with sodium citrate was developed in 1951 by Turkevich et al., and is a commonly used method of manufacturing citrate-stabilized, monodisperse gold nanoparticles of various sizes.<sup>186, 214, 215</sup> Citrate-stabilized gold nanoparticles are easily functionalized with self-assembled monolayers (SAMs) of

thiol-containing compounds by exposure in an ethanol environment over a short time.<sup>216-</sup>

218

This study has focused on polymethacryloyloxyethyl phosphorylcholine (pMPC), a zwitterionic polymer with ammonium and phosphate moieties, and its potential utility as a biomaterial in pulmonary drug delivery using nanoparticles. A synthesis route for pMPC using a photoinitiated reaction with a RAFT agent to produce polymers with thiol end-functionality was developed. RAFT agents are central to the polymer synthesis scheme presented here due to their utility in providing thiol end-functionalization, which allows for polymers to be easily grafted to the surfaces of gold nanoparticles.<sup>219</sup> The synthesis scheme presented here presents advantages compared to previously demonstrated approaches to pMPC syntheses; polymer synthesis and processing occur in ethanol and water at ambient conditions. These solvent and temperature conditions are less likely than most polymerization approaches to denature proteins or drug molecules, allowing the potential use of this approach to perform polymerizations in the presence of a therapeutic product. The polymers were characterized and coated onto gold nanoparticles, and the resulting system was tested for interactions with proteins and lung cell responses. This study specifically assessed particle toxicity, uptake, and behavior in lung lining fluids and serum. While lung fluids are important for pulmonary drug delivery, inhaled particles can quickly enter the bloodstream. Inclusion of serum for comparison in this study allowed further characterization of materials. Additionally, as BALF is a more limited resource, the use of serum allowed for method development without depleting limited supplies of a rarer material. Using classic DLVO theory, particle behavior in aqueous media is determined based on surface charge and material

properties that affect Van der Waals forces. Herein, we demonstrate how classical DLVO theory fails to describe how zwitterionic polymers stabilize particles and demonstrate the incorporation of hydration as an additional force to the theory to account for such effects.

## 6.2 Materials and Methods

### 6.2.1 Polymer Design and Synthesis

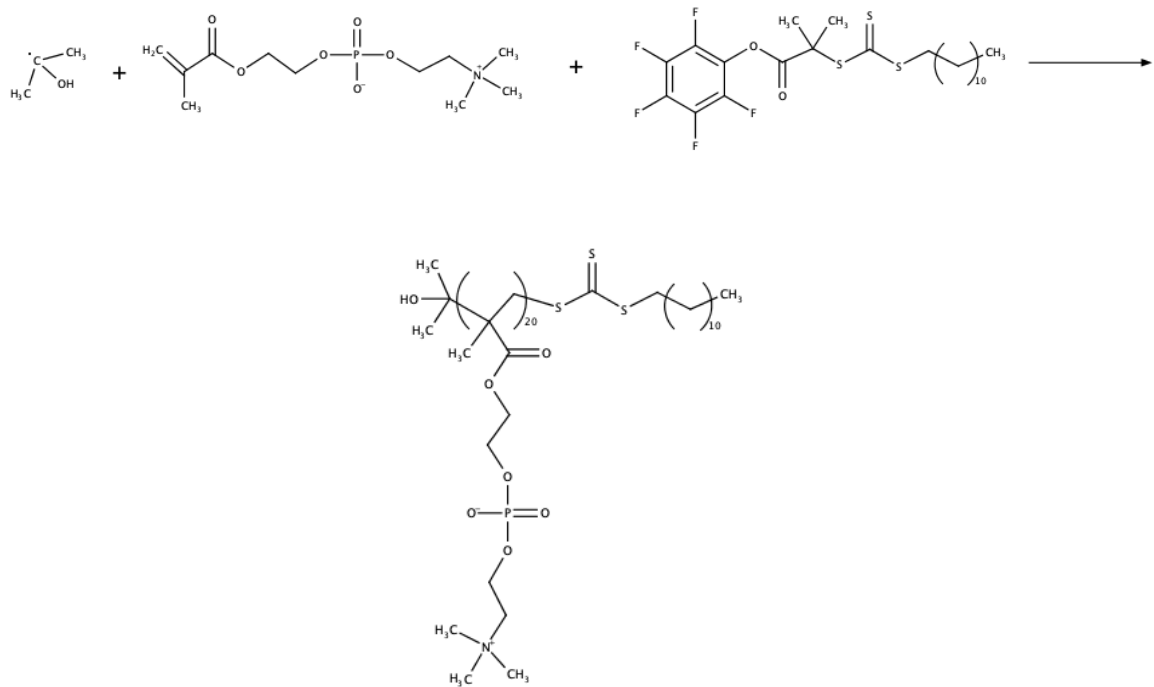
A synthesis route for thiol-terminated methacrylates at ambient conditions was developed to produce polymer brushes to be grafted onto the surfaces of gold nanoparticles. To provide a system with thiol end-functionality, a free-radical polymerization in the presence of a RAFT agent was used. Photoinitiation was selected to allow for polymerization at ambient conditions and in bio-compatible solvents (ethanol and water). These polymers were synthesized in glass to minimize potential interactions with the container. The ratio of initiator to RAFT agent can affect reaction rate and polydispersity of the polymer produced, with reported initiator:RAFT agent ratios ranging from 1:3 to 1:20 for similar systems.<sup>220</sup> The 1:3.6 initiator:RAFT agent molar ratio was selected in this case to maximize RAFT agent content relative to the number of active chains. The RAFT agent in this case provides the thiol-end functionality, so a higher ratio of RAFT agent provides more sources of this end-group. The RAFT agent, 2-(dodecylthiocarbonothioylthio)-2-methylpropionic acid pentafluorophenyl ester (Sigma, Lot: MKBK1986V), was dissolved in 200-proof ethanol. 10 mL of this solution was used to dissolve approximately 50 mg of 2-methacryloyloxyethyl phosphorylcholine (MPC, Sigma, Lot MKBX8895V). To this, 1 mg of photoinitiator, IRGACURE 2959 (I2959, Ciba, Lot: 1744H2) or IRGACURE 651 (I651, Ciba, Lot: 72501S), was added. I2959 was initially selected as the photoinitiator due to the tolerance of I2959 in various cells.<sup>221</sup> A

study using photoinitiators as reducing agents for the synthesis of metal nanoparticles have identified that the benzoyl radical generated in the photoinitiation step quickly reacts into and 4-(2-hydroxyethoxy)benzoic acid (2-HEBA), which was found to stabilize metal nanoparticle suspensions similarly to citrate.<sup>222</sup> I651 was included later to troubleshoot polymer characterization. I651 was selected as an alternative commonly used initiator.<sup>223, 224</sup> Both photoinitiators have similar efficiencies, with values of 0.29 and 0.3 for I2959 and I651 respectively.<sup>220, 225, 226</sup> To initiate polymerization the system was stirred under a 340 nm lamp at an intensity of 20 mW/cm<sup>2</sup> for 15 min. After polymerization, the thiocarbonothioylthio group was degraded via the addition of 1 mL of ethylamine (70 wt% in water) to the reaction mixture to yield thiol end-groups.<sup>220</sup> Representative synthesis schemes are presented in Figure 6.1 and Figure 6.2 for I2959 and I651 respectively.

1)



2)



3)

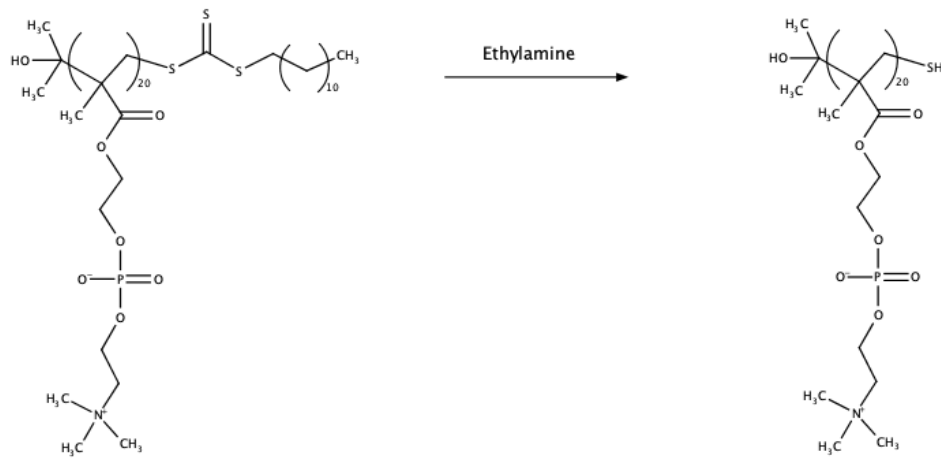
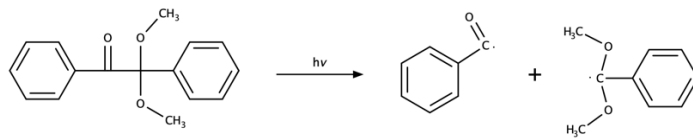


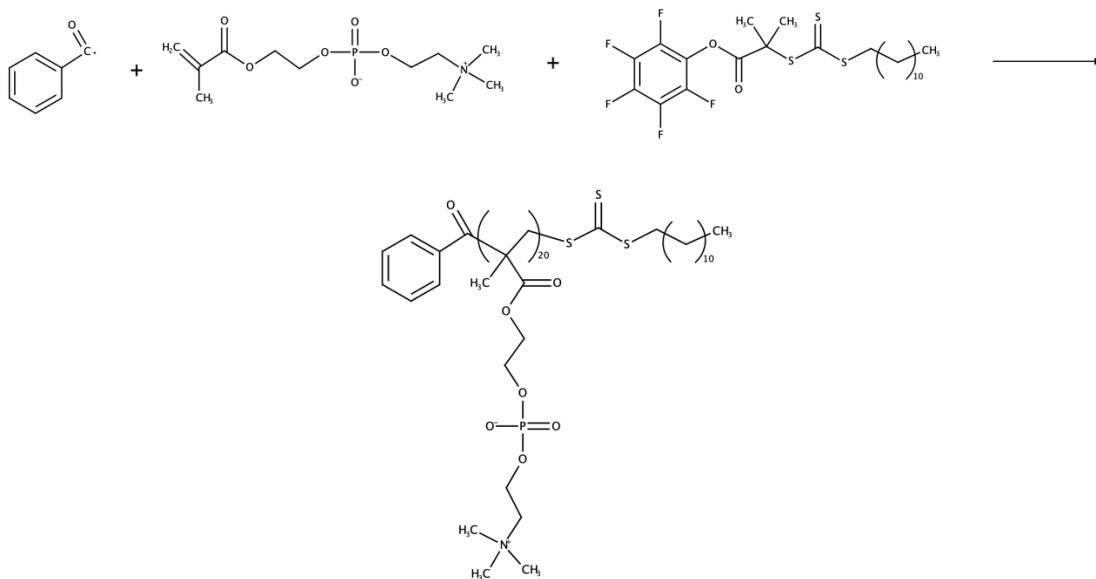
Figure 6.1. Synthesis scheme for the photoinitiated polymerization of MPC in the presence of a trithiocarbonate RAFT agent using I2959 as the photoinitiator.



1)



2)



3)

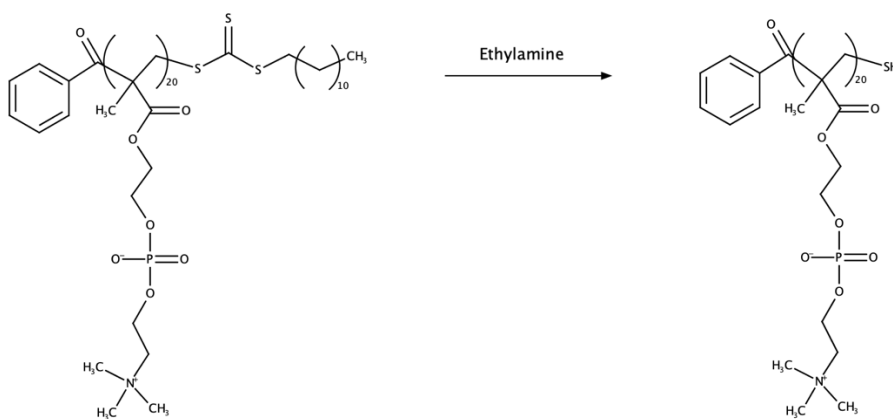


Figure 6.2. Synthesis scheme for the photoinitiated polymerization of MPC in the presence of a trithiocarbonate RAFT agent using I651 as the photoinitiator.

## 6.2.2 Polymer Characterization

Polymer conversion was measured using Raman spectroscopy. A monomer mixture with the RAFT agent and photoinitiator was prepared as described above. Prior to photoinitiation, a 2 mL sample was collected. Another 2 mL sample was collected after lamp exposure. These two samples were dried in the hood to remove ethanol, then dissolved in 150  $\mu\text{L}$  of water each. Raman spectra were taken, and the peak heights compared at  $1640\text{ cm}^{-1}$  to quantify conversion using the equation:

$$\text{conversion (\%)} = 100 \times \left(1 - \frac{\text{Polymer Peak Height}}{\text{Monomer Peak Height}}\right)$$

Polymer chemistry and monomer conversion were confirmed by  $^1\text{H}$  NMR. MPC and pMPC were dissolved in  $\text{D}_2\text{O}$  at a concentration of 8 mg/mL. MPC was analyzed using a Bruker Dpx-300 spectrometer with a 6.9 Tesla field. The pMPC was analyzed using a Bruker Av500 NMR with a 11.5 Tesla field. Peaks were matched to literature values for monomer and polymer to confirm chemistry.<sup>95, 227-229</sup> Conversion was qualitatively confirmed by monitoring the reduction of two alkene peaks at 5.6 and 6.1 ppm.

Polymer molecular weight was determined using gel permeation chromatography (GPC). Polymer samples (5-10 mg each) were dried in a hood and dissolved in 1 mL of 0.1  $\mu\text{m}$ -filtered, degassed, 0.2 M sodium acetate (pH 4) buffer. These samples were injected in 20  $\mu\text{L}$  aliquots into a GPC using a 0.2 M sodium acetate mobile phase (pH 4) equipped with an Ultrahydrogel 250 aqueous GPC column (Waters, 7.8 x 300 mm). For some samples, a 0.1  $\mu\text{m}$  syringe filter was fitted to the syringe to inject samples in lieu of a guard column. No differences were observed in the results from the instrument when a

filter was used compared to an unfiltered sample. This may be an effective approach to prolonging column life in the absence of a guard column. The column operated at 0.500 mL/min, and the pressure value recorded on the pump for this flowrate ranged from 18-19 bar on different days; however, within an experimental run pressure changes did not exceed 0.2 bar. Initial analyses were conducted with the pH of the eluent at a value of 7.0, but lower pH (4.0) was found to improve signal on both detectors, as well as decrease elution time of the polymer. The  $dn/dc$  used for analysis of pMPC was 0.142, which was obtained from literature.<sup>96</sup> Samples were analyzed using a Heleos II (Wyatt) light scattering detector coupled with a T-rEX (Wyatt) differential refractive index monitor. Molecular weight was initially determined using the Astra 6 software suite. The system was validated using PEG standards (Polymer Standards Services) ranging from 400 to 20,000 Da. Calibration standards identified large errors in molecular weight determination using the Astra software system, so a more traditional analysis was performed by plotting the log of molecular weight versus elution time of the monodisperse PEG standards to calculate pMPC molecular weight.

### 6.2.3 Gold Particle Synthesis

Gold nanoparticle synthesis via reduction of tetrachloroauric acid by sodium citrate was originally developed by Turkevich et al.<sup>214</sup> The reaction to generate these particles involves thermal oxidation of citrate to acetonedicarboxylate. This provides the electrons for the reduction of the gold from  $Au^{3+}$  to  $Au^{1+}$  as well as fixing the AuCl in reaction complexes during the subsequent disproportionation, which results in the complete reduction of some gold to Au and oxidation of the remaining gold to  $Au^{3+}$ . While the Turkevich synthesis was originally developed in the 1950s, the kinetics and

intermediate equilibrium conditions were discovered later. Studies determining the kinetics and intermediate equilibrium conditions led to protocols that decrease size variation between batches and reduce the width of particle size distributions.<sup>230-234</sup>

Gold particles with a diameter of 100 nm were produced using a modification to the Turkevich protocol developed by Bastus et al. for larger diameter particles.<sup>186</sup> Briefly, 150 mL of 2 mM sodium citrate (Sigma, Lot: MKBW0372V) in water was brought to a boil in a 3-neck round-bottom flask with a condenser mounted in the central neck recirculating chilled water at 6°C. The other two necks were kept plugged with ground glass stoppers except during addition or removal of material from flask. A 23 mM HAuCl<sub>4</sub> solution was prepared by dissolving gold (III) trichloride (Sigma, Lot: MKCF1650, MKVBV9850V) in water. Every 30 min, 1 mL injections of 23 mM HAuCl<sub>4</sub> were added. 30 min after every even-numbered injection, 50 mL of the reaction volume was replaced with fresh 2 mM sodium citrate to dilute the system. This regular dilution of particles favors nanoparticle growth by condensation rather than nucleation into new particles or collision-induced fusion of larger particles.<sup>186</sup> A total of 20 injections of HAuCl<sub>4</sub> results in particles approximately 100 nm in diameter. Table 6.1 lists the steps in the synthesis with actions and estimations of the contents of the reaction flask. The particle concentration uses an initial value based on the seed concentration provided by Bastus et al.<sup>186</sup> The concentration in subsequent steps is calculated as a dilution of this initial value based on removal of reaction volume and addition of fresh citrate and HAuCl<sub>4</sub>.

#### 6.2.4 Polymer SAM Coating onto Gold Nanoparticles

After synthesis, gold nanoparticles were coated with polymers. To accomplish this, thiol-functionalized methacrylate polymers in ethanol were added to the aqueous gold suspensions and agitated overnight to allow formation of self-assembled monolayers on the particles' surfaces. A polymer to gold mass ratio ranging from 6:1 to 30:1 was used for these coating, and an optimum selected based on characterization of behavior in fluids and interactions with protein. The resulting suspensions exhibited high stability over time, so particles were left in the ethanol-citrate buffer mixtures until use. Settling occurred over time; however, inversion of the tube containing these suspensions would

*Table 6.1 Steps in the synthesis of 100 nm gold nanoparticles with calculations of gold mass and number of particles remaining in the suspension at each step. Volumes are approximate as water is lost as vapor throughout the reaction.*

*Concentration is estimated based on injected Au mass and particle size at each stage.*

Time (min)	Reaction Vol. (mL)	Action	Au Mass (mg)	Au Conc. (mg/mL)	Au Conc. (Particles/mL)
0	150	Warm citrate soln. to 100°C	0.00	0.000	
0	150	1 mL HAuCl <sub>4</sub> inject	4.92	0.033	
30	150	1 mL HAuCl <sub>4</sub> inject	9.85	0.066	
60	95	50 mL Removed	6.24	0.066	3.00E+12
60	150	Citrate added, then gold	11.16	0.074	
90	150	1 mL HAuCl <sub>4</sub> in	16.09	0.107	
120	95	50 mL Removed	10.19	0.107	1.90E+12
120	150	Citrate added, then gold	15.11	0.101	
150	150	1 mL HAuCl <sub>4</sub> in	20.04	0.134	
180	95	50 mL Removed	12.69	0.134	1.20E+12
180	150	Citrate added, then gold	17.61	0.117	
210	150	1 mL HAuCl <sub>4</sub> in	22.54	0.150	
240	95	50 mL Removed	14.27	0.150	7.62E+11
240	150	Citrate added, then gold	19.20	0.128	
270	150	1 mL HAuCl <sub>4</sub> in	24.12	0.161	
300	95	50 mL Removed	15.28	0.161	4.83E+11
300	150	Citrate added, then gold	20.20	0.135	
330	150	1 mL HAuCl <sub>4</sub> in	25.13	0.168	

Table 6.1 continued

Time (min)	Reaction Vol. (mL)	Action	Au Mass (mg)	Au Conc. (mg/mL)	Au Conc. (Particles/mL)
360	95	50 mL Removed	15.91	0.168	3.06E+11
390	150	Citrate added, then gold	20.84	0.139	
420	150	1 mL HAuCl <sub>4</sub> in	25.76	0.172	
450	95	50 mL Removed	16.32	0.172	1.94E+11
450	150	Citrate added, then gold	21.24	0.142	
480	150	1 mL HAuCl <sub>4</sub> in	26.16	0.174	
510	95	50 mL Removed	16.57	0.174	1.23E+11
510	150	Citrate added, then gold	21.49	0.143	
540	150	1 mL HAuCl <sub>4</sub> in	26.42	0.176	
570	95	50 mL Removed	16.73	0.176	7.77E+10
570	150	Citrate added, then gold	21.66	0.144	
600	150	1 mL HAuCl <sub>4</sub> in	26.58	0.177	
630	150	Finished, heat off	26.58	0.177	4.92E+10

result in an immediate return to a well-dispersed state. SAM-coated particles were cleaned at time of use to remove any residual components and solvents from the polymerization process.

#### 6.2.5 Particle Characterization

Average particle size and size distribution were measured via dynamic light scattering (DLS), and the zeta potential was measured via laser Doppler velocimetry using a Malvern Nano ZS. As before, DLS measurements were taken in clear disposable polystyrene cuvettes (VWR), using measurement settings to execute 13 runs per measurement for 3 measurements. Zeta potentials were measured in disposable zeta cells (DTS1007, Malvern). Measurements were set to run a minimum of 10 to a maximum of 100 runs per measurement, or until confidence in the result was achieved. This was also measured in triplicate. Samples were analyzed while suspended in sodium citrate directly taken from the reaction mixture. Measurements of particles after interaction with proteins

were taken directly in diluted saline, BALF, or reconstituted BALF respectively. Particle morphology and primary particle size were determined with transmission electron microscopy (TEM). Samples were prepared by placing a droplet of gold nanoparticles suspended in sodium citrate buffer onto formvar-coated TEM grids for 30 s followed by removal of excess liquid with a clean piece of filter paper. Grids were placed under a glass dish overnight to allow residual water to evaporate without accumulating dust on the grids. Images were collected using a JEOL JEM-1230 TEM. Beam current density was maintained between 10-20 pA/cm<sup>2</sup>, with exposures between 1-2 s, and particle measurements from images was performed using ImageJ.<sup>140</sup>

#### 6.2.6 Reconstitution of BALF

Bronchoalveolar lavage fluid (BALF), was obtained from a nonsmoking healthy male aged 34 by our collaborator, Dr. David Stoltz at the University of Iowa Hospitals and Clinics. After collection, cells were removed by centrifugation, and the fluid was stored at -80°C. After obtaining BALF from Dr. Stoltz, protease inhibitors (Pierce, Lot:PF200530) were added to maintain protein concentration throughout use. As-received BALF was relatively dilute with a total protein concentration of 100 µg/mL. To bring it to a more physiologically relevant concentration, a method was developed to desalt the solution and dry the BALF.

Salts were removed from BALF using P6 buffer exchange columns (BioRad). P6 gel columns were prepared by exchanging the buffer with 500 µL of water 3 times and the water drawn through the column at 1,000×g. After this, 100 µL of BALF was passed through each column. Multiple samples were pooled, and the pooled samples dried in a

SpeedVac (SC100, Savant) for 3 h. This led to a 2 to 15-fold increase in protein concentration as measured by bicinchoninic acid (BCA, Thermo) assay.

#### 6.2.7 Protein Adsorption to Gold Nanoparticles

To test the ability of the polymer coatings to resist nonspecific protein adsorption, coated and noncoated gold nanoparticles were exposed to two different protein environments: type AB human serum (Pel-Freez, Lot: 23535) and reconstituted BALF. Initial studies used serum diluted to 2,000  $\mu\text{g}/\text{mL}$  and BALF as-received. Serum was diluted to this concentration so that studies would be performed within the linear range of the BCA assay for accurate analysis. After development of BALF reconstitution techniques, serum solutions were prepared by dilution in saline to match the concentration of the reconstituted BALF to provide a basis for more direct comparison.

Gold nanoparticle suspensions containing 1 mg of gold were centrifuged at 1,000 $\times$ g for 15 min. The supernatant was removed, and the nanoparticles were washed with saline (pH 7.4) three times to remove excess polymer, reactants, or other solution components from their preparation. Diluted serum or reconstituted BALF was added to these samples, and the system was gently agitated for 30 min. Particles were characterized at this point using DLS and laser Doppler velocimetry to characterize size distributions and zeta potentials. The particles were separated using a centrifuge at 1,000 $\times$ g for 15 min, and the supernatants were collected and analyzed using the BCA assay to determine the quantity of protein not adsorbed to the particles. By measuring the change in protein mass in the coated nanoparticles relative to uncoated gold, the fouling resistance of the pMPC-coating was determined.



## 6.2.8 Cell Responses to Coated and Uncoated Gold Nanoparticles

A549 cells (ATCC), an immortalized lung epithelial cell line, were used to assess lung cell responses to coated and uncoated gold nanoparticles, as well as components used in the synthesis of coatings, *in vitro*. A549 cells were cultured in RPMI 1640 (Gibco) supplemented with 10% fetal bovine serum (FBS, Atlanta Biologics) and 1% penicillin streptomycin (Gibco). They were grown in a humidified incubator at 37°C supplemented with 5% CO<sub>2</sub>. Cells were seeded into 12-well tissue culture plates (Gibco) at a density of 200,000 cells/well. Cells were exposed to 1 mL doses of 1, 5, or 10 µg/mL of gold nanoparticles, polymer components, polymer, or 6:1 mass ratio polymer-coated gold nanoparticles in RPMI 1640 for 4 h. This was done to ensure that if toxicity was observed in coated gold nanoparticles, sources of toxicity could be identified or ruled out.

After exposure to nanoparticles and polymer components, cells were rinsed 3x with PBS and incubated for 1 h in RPMI 1640 containing MTS reagent (Promega CellTiter 96) to assess viability. After incubation, 100 µL aliquots were taken from the wells and measured using an Epoch microplate spectrophotometer (BioTek). Additionally, cells exposed to pMPC-coated and citrate-stabilized gold nanoparticles were rinsed with PBS and collected from well plates using 0.25% trypsin-EDTA cell dissociation buffer (Gibco). The collected cells were centrifuged at 1,000×g for 7 min and the supernatant discarded. Samples were sent to the State Hygienic Laboratory of the University of Iowa for ICP-MS analysis to measure cellular uptake of gold.

Lung cells were digested in a freshly prepared mixture of one-part nitric acid (Fisher, Trace Metal Grade, A509) with three-parts hydrochloric acid (Fisher, Trace Metal Grade, A508). Previously collected cells were submitted for analysis in 1.5-mL

microcentrifuge tubes. To each tube was added 500  $\mu\text{L}$  of the acid solution. A reagent blank was prepared containing only the acid mixture. A laboratory control sample was prepared containing the acid mixture spiked with 0.1  $\mu\text{g}$  of gold derived from a commercially available gold standard. The tubes were placed in a water bath at 85-90°C for 1 h. After cooling for 20 min 100  $\mu\text{L}$  of 30% hydrogen peroxide was added and the tubes were heated for another hour. After cooling, samples were diluted to 1.0 mL using reagent water.

Gold was quantified using an Agilent 7700, Inductively Coupled Plasma Mass Spectrometer (ICP-MS). Intermediate working calibration standards were prepared from a commercial stock solution in 3% (v/v) HCl (Fisher Trace Metal Grade or equivalent) at 0, 100, 200, 500, and 1000  $\mu\text{g}/\text{L}$ . Working standards were diluted 10-fold with an internal standard solution composed of 10  $\mu\text{g}/\text{L}$  iridium in 3% (v/v) HCl. As needed, samples were diluted 100-fold. Compensation for the higher acid concentration in the samples is outlined in Table 1.1.

*Table 6.2 Approach to dilution of standards and samples to compensate for higher acid concentration in samples.*

Solution type	mL of 20% HCl	mL of 3% HCl	mL of internal standard	Total volume (mL)
Standards (0.5 mL)	0.5	-	4.0	5.0
Samples, 10x (0.5 mL)	-	0.5	4.0	5.0
Samples, 100x (0.05 mL)	-	0.95	4.0	5.0

Instrument settings are shown in Table 6.3. Selected calibration standards were analyzed as samples at the beginning and end of the run to validate accuracy of the calibration and a second-source gold standard was prepared to validate the calibration source.

Table 6.3 Instrument settings for the ICP-MS.

Parameter	Setting
Rf Power	1550 W
Ion lens voltages	Optimize for sensitivity
Sweeps / replicate	50
Replicates	3
Isotopes monitored	<sup>197</sup> Au, <sup>193</sup> Ir
Integrateion time/mass	90 ms
Analysis mode	Spectrum
Peak pattern	3 points
Stabilization time	30 s
Background subtraction	Count subtraction except for internal standard

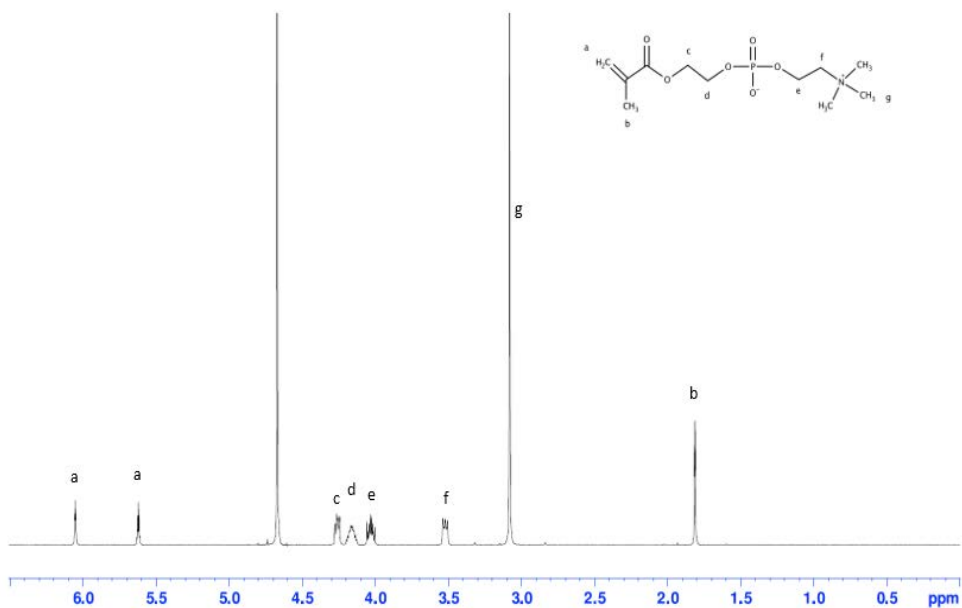
## 6.3 Results

### 6.3.1 Polymer Characterization

After synthesis, pMPC conversion was determined using Raman spectroscopy. Monomer peak height at  $1640\text{ cm}^{-1}$  was measured to be 396.98 counts whereas the peak height for the polymer was measured to be 199.66. Conversion was determined to be 49.7% by peak height comparison. Polymer chemistry was verified using <sup>1</sup>H NMR. Using peak area measurements in TopSpin 4.0.3 (Bruker), the MPC monomer peak areas were integrated, and a molar concentration of 1 was assigned to the peak at 5.6 ppm. When the remaining peaks were integrated based on this calibration, the areas were found to correspond to the molar ratios of protons illustrated in the inlaid structure (Figure 6.3a). The locations of these peaks were confirmed to match those for this monomer.<sup>12</sup> NMR analysis for the polymer confirmed polymer chemistry. The spectrum obtained for this polymer (Figure 6.3b) was found to correspond to previously reported spectra of pMPC.<sup>33-35</sup> As seen in Figure 6.3, the polymer spectrum does not have peaks as clearly defined as in the monomer. This may be due to proximity of neighboring

phosphorylcholine groups in the polymer chain and the presence of other reaction components in the polymerized samples. Chemical shifts were matched to previously reported NMR spectra of pMPC-containing polymers to confirm polymer chemistry.<sup>95, 227-229</sup> Conversion was qualitatively confirmed with NMR by monitoring the disappearance of the two peaks at 5.6 and 6.1 ppm corresponding to the removal of C=C bonds from the system.

a)



b)

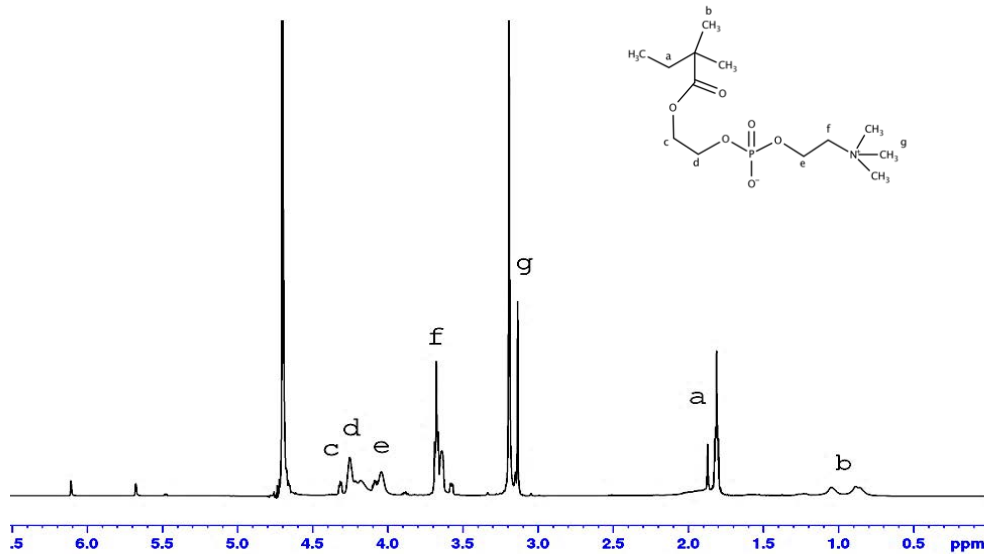


Figure 6.3. NMR spectra of a) MPC monomer before polymerization (taken at 300 MHz) and b) pMPC after polymerization (taken at 500 MHz).

Polymer molecular weight was determined using GPC. GPC analysis determined that 4 batches of pMPC synthesized using I651 as the photoinitiator had an average  $M_N$  of 68,000 Da with a standard deviation of 8,000 Da based on the molecular weight curve (Figure 6.4). Elution times were 10.07 min, 9.68 min, 6.68 min, and 9.68 min corresponding to  $M_N$  values of 55,800 Da, 77,300 Da, 77,200 Da, and 72,500 Da respectively for the four analyses. Multiple batches of pMPC synthesized using I2959 were analyzed using GPC, but there were consistent issues with detection of polymer in the system. Typically, the light scattering detector would measure particles at approximately 9 min (within 1 min of I651 polymer elution times), but no changes in differential refractive index were measured concurrently. The elution time for I2959 from

the light scattering detector at 8.6 min corresponded with a  $M_N$  value of approximately 148,000 Da. Elution graphs for pMPC made with I651 and I2959 are provided in Figure 6.5.

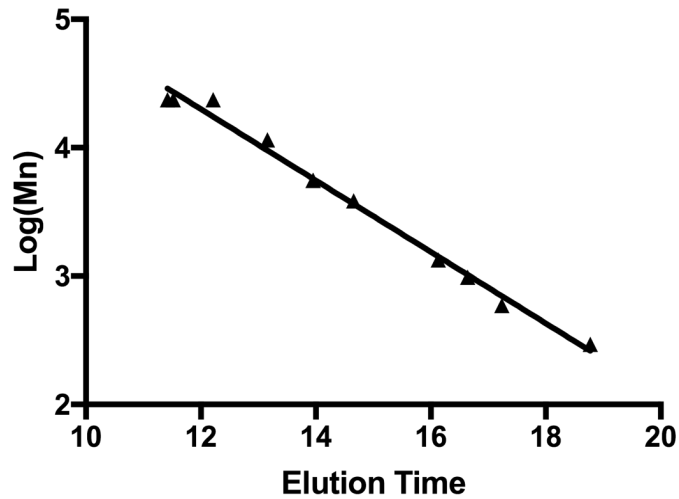
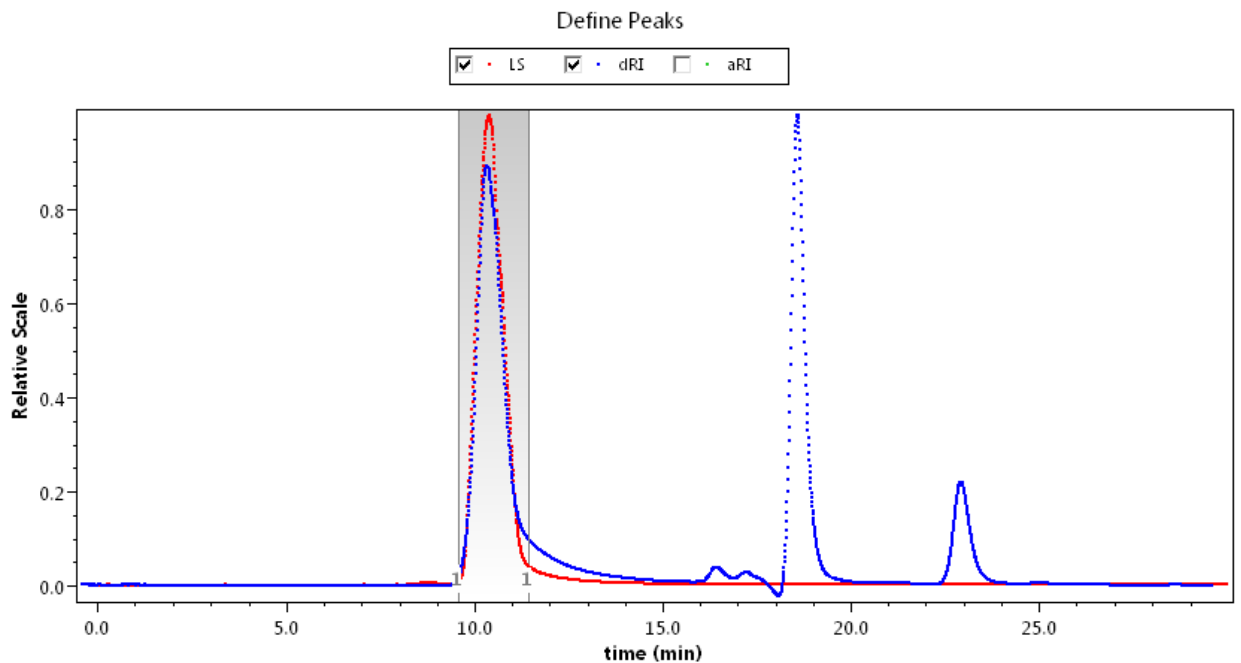


Figure 6.4. Linear regression of  $\log(M_n)$  for PEG standards.

a)



b)

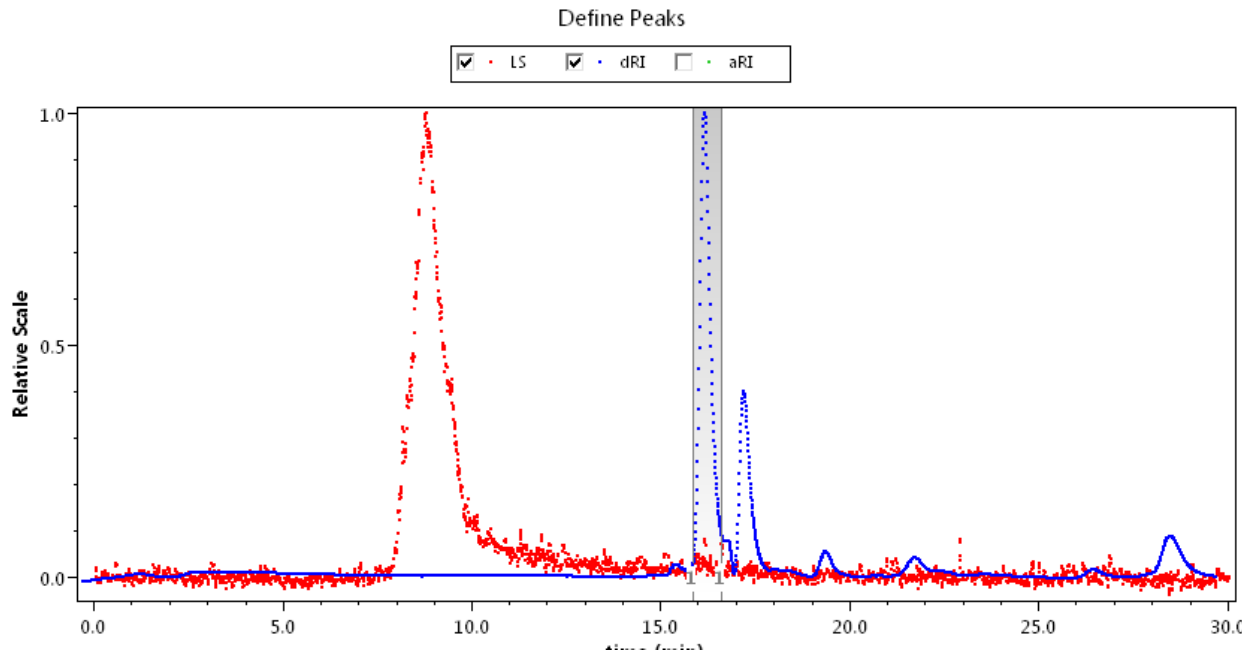


Figure 6.5. Representative GPC data for a) I651-cured pMPC and b) I2959-cured pMPC.

### 6.3.2 Particle Characterization

Gold nanoparticles synthesized via the modified Turkevich protocol were analyzed by TEM imaging. Analysis of TEM images using ImageJ identified a monodisperse distribution of roughly spherical primary particles with an average diameter of 90 nm (Figure 6.6). Additionally, a small population of very small particles (10-20 nm) was observed (Figure 6.6, arrow); these are the nucleation seeds that can form at any time during synthesis. The small number of these observed in TEM imaging is indicative of reaction conditions heavily favoring particle growth over new particle formation.

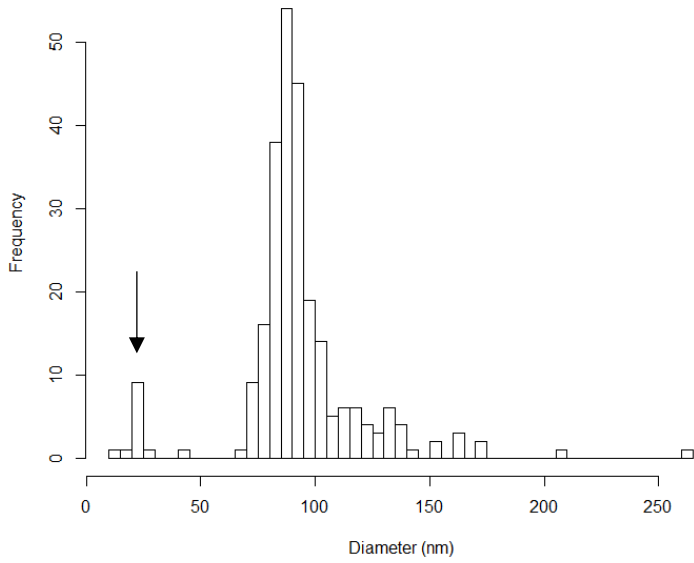


Figure 6.6. Histogram of primary particle diameters determined from ImageJ analysis of TEM images. ( $n=253$ )

When pMPC coatings were formed onto gold nanoparticles at high polymer:gold mass ratios (30:1), TEM imaging captured particles that were agglomerated, and associated with polymer globs that appear as shaded regions (Figure 6.7b). The gold nanoparticles were located inside the shaded polymer regions in these images.

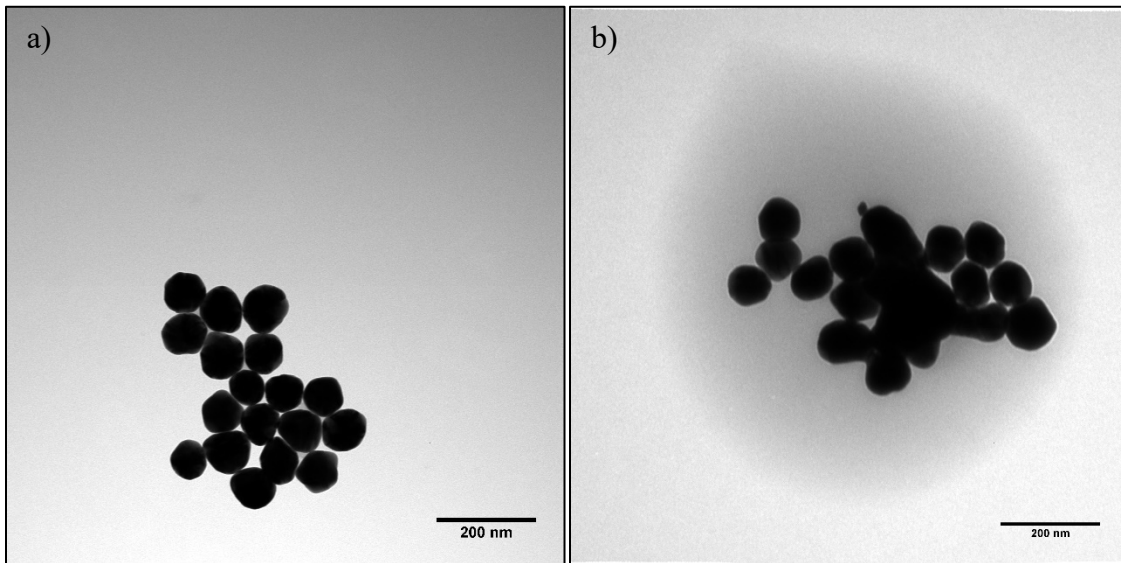


Figure 6.7. TEM micrographs of gold nanoparticles with a) no coating, b) pMPC coating 30:1 mass ratio.



When pMPC coatings were formed on gold nanoparticles at low polymer:gold mass ratios (6:1), TEM imaging showed no changes in primary particle morphology (Figure 6.8d), but particles were much more dispersed on the formvar membrane in pMPC-coated gold compared to bare gold, as illustrated in Figure 6.8a&b. It is likely that while the nanoparticle suspensions were drying on the membrane, uncoated gold particles aggregated as the water evaporated. In contrast, the pMPC-coated gold nanoparticles remained stable during the drying process resulting in TEM images more representative of their in-suspension distribution. Additionally, the polymer portion of these pMPC-coated gold nanoparticles were not substantial enough to interfere with the electron beam, remaining invisible in TEM images (Figure 6.8d).

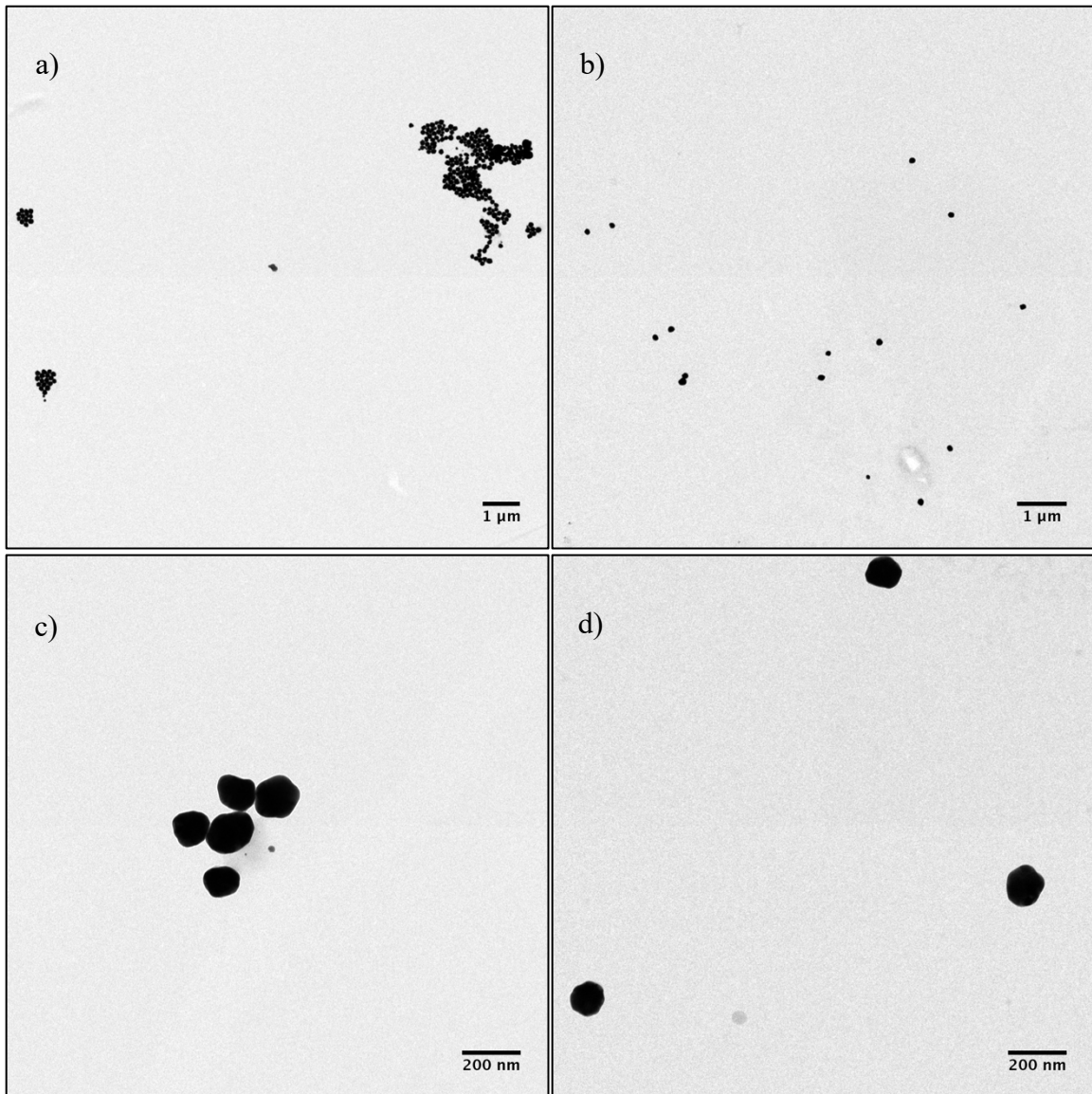


Figure 6.8. Representative a) low-magnification and c) high-magnification TEM micrographs gold nanoparticles. Similar b) low-magnification and d) high-magnification micrographs were taken after coating with 6:1 mass ratio pMPC SAMs.

DLS measurements, as illustrated in Figure 6.9, indicated a monodisperse distribution of uncoated gold with the particle hydrodynamic diameter centered at approximately 100 nm (Figure 6.9a), in good agreement with primary particle measurements taken of TEM images. When gold nanoparticles were exposed to serum, particle size increased (Figure 6.9a). When 30:1 pMPC-coated gold particles were

exposed to serum, particle size decreased (Figure 6.9b). When gold particles were exposed to BALF, the resulting size distribution was nearly identical to serum (Figure 6.9a). As in serum exposure, BALF exposure to these 30:1 pMPC-coated nanoparticles resulted in decreased particle size (Figure 6.9b).

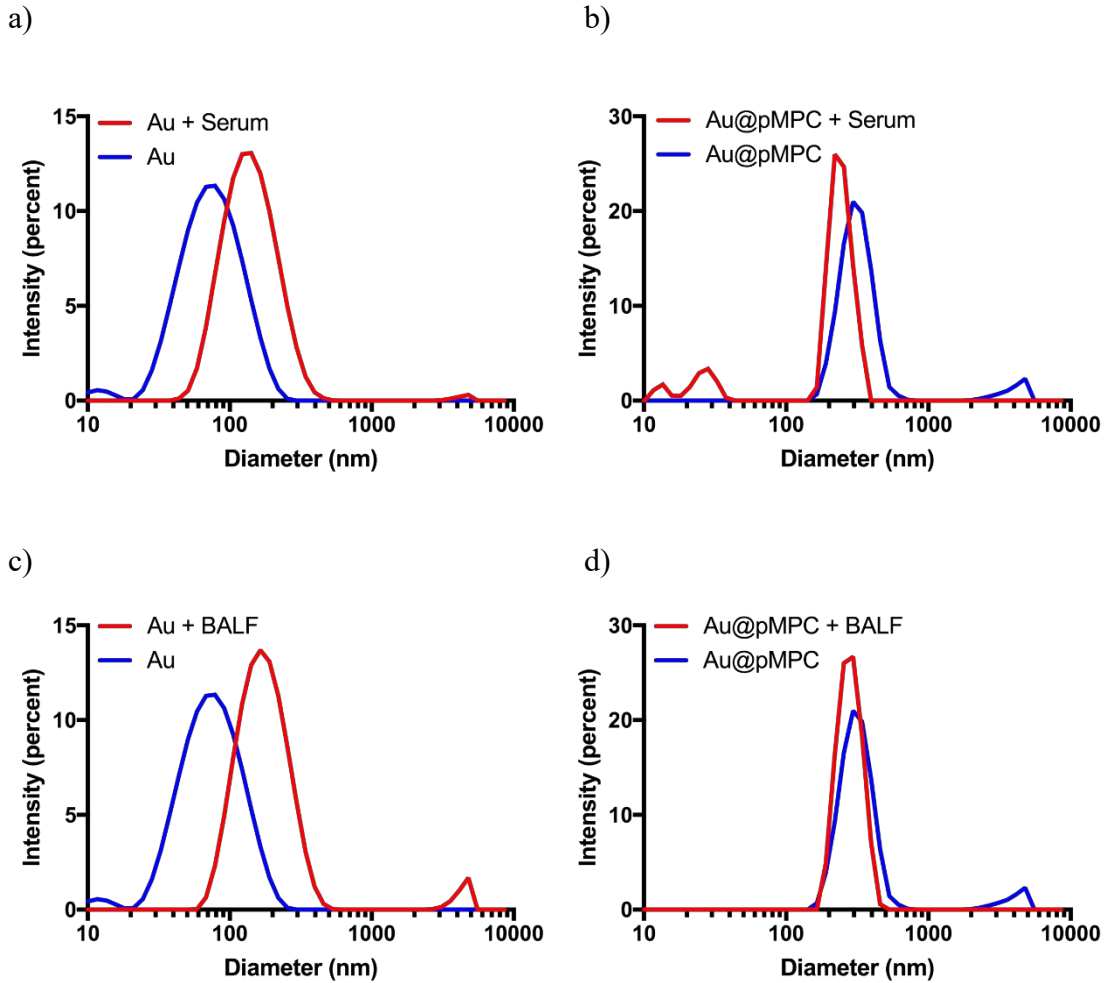


Figure 6.9. Distributions of hydrodynamic diameters for a) gold and, b) 30:1 pMPC-coated gold exposed to serum and c) gold and d) 30:1 pMPC-coated gold exposed to BALF.

Zeta potentials were measured for 30:1 pMPC-coated and uncoated gold particles before and after exposure to serum (Figure 6.10a) or BALF (Figure 6.10b). When gold nanoparticles were exposed to serum, zeta potential increased to -2.5 mV. Gold

nanoparticles coated in pMPC experienced an increase in zeta potential to 5.2 mV when exposed to serum. As with serum, BALF exposure to gold nanoparticles resulted in particle zeta potential increasing, with a slightly positive value resulting. After exposure to BALF, pMPC-coated gold particle zeta potentials shifted to about -8 mV. Significant differences in zeta potentials were observed for all groups studied here.

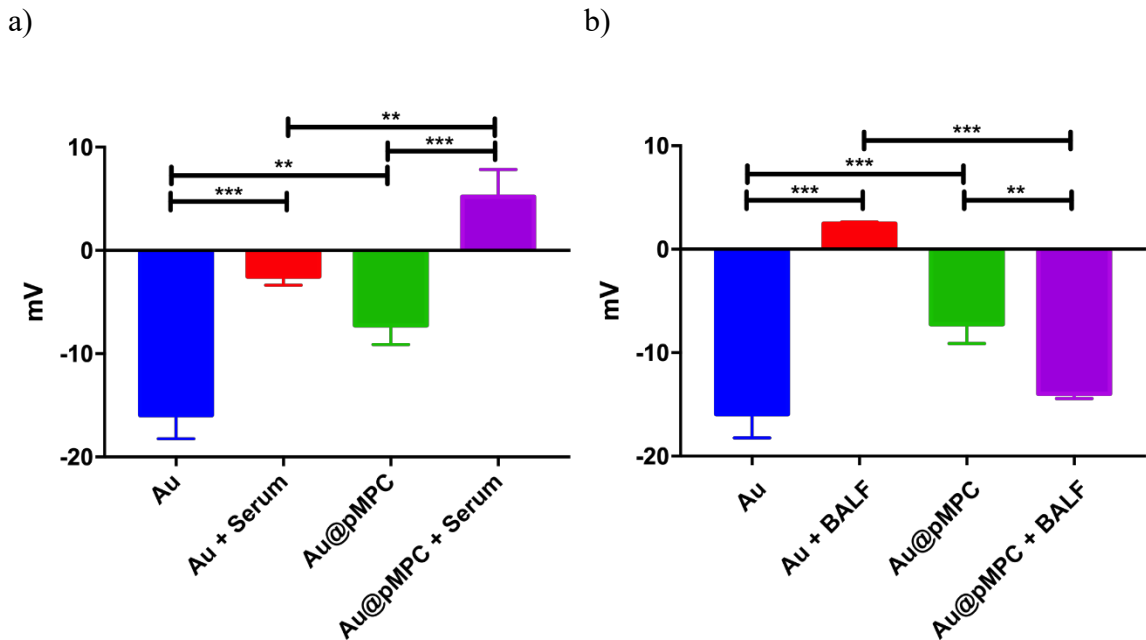


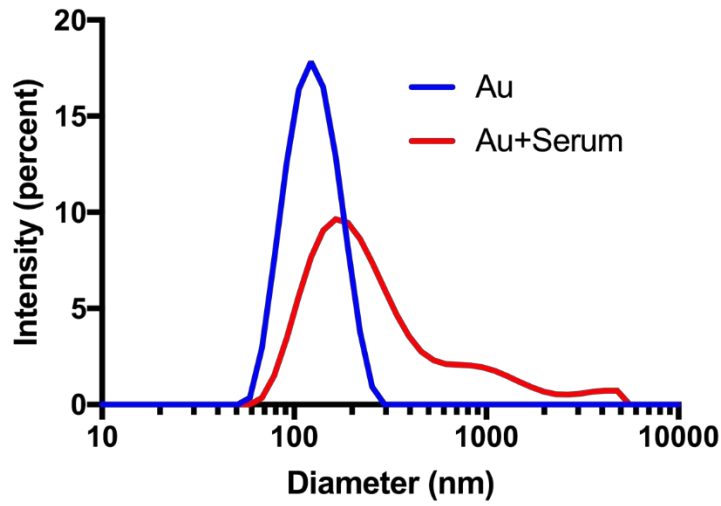
Figure 6.10. Zeta potential measurements for uncoated gold nanoparticles and gold nanoparticles coated with 30:1 pMPC, before and after exposure to a) serum and b) BALF.  $n=1$ , 3 replicates. Error bars=SD.

After coating in a 6:1 w/w polymer:gold ratio, gold particles were similarly characterized. Hydrodynamic size measured after exposure to human serum resulted in a shift in distribution to larger sizes, as well as a transformation into a multimodal polydisperse mixture. Particles in the micrometer and larger size range tend to be less accurately measured using DLS, but exposure to serum induces significant aggregation. DLS indicated that after coating in pMPC particles remained similarly dispersed in

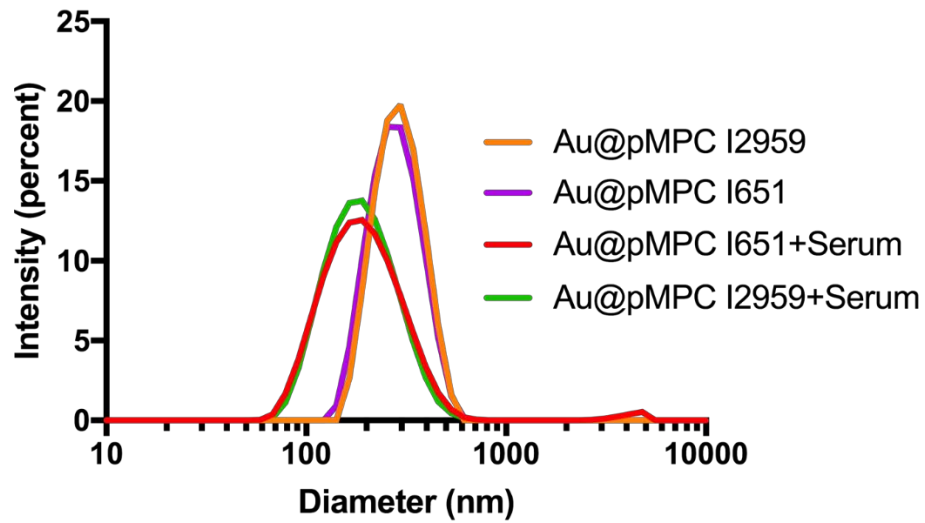
suspension to uncoated gold, with a shift in hydrodynamic diameter to approximately 230 nm for polymers using either initiator (Figure 6.11). The observed dispersion of pMPC-coated particles in TEM images indicate that larger hydrodynamic diameters observed in DLS data are the result of a polymer coating rather than aggregation induced because of exposure to these polymers. When pMPC-coated particles were exposed to serum, the hydrodynamic diameter decreased to slightly larger than uncoated gold without serum, and remained monodisperse, though some large aggregates may be forming based on a small peak at the limit-of-detection near 10  $\mu\text{m}$ . Choice of photoinitiator did not have any measurable effect. Like serum, when uncoated gold particles were exposed to BALF, particle size increased, as did the breadth of the distribution with the addition of aggregates at very large hydrodynamic diameters. When pMPC-coated gold particles were exposed to BALF, much smaller changes in particle size distributions occurred. For I659-generated polymer brushes, the distribution broadened and shifted slightly towards smaller hydrodynamic diameters. For I2959-generated polymer brushes, the distribution broadened slightly, and shifted similarly to coated particles in serum.

In samples stored in suspension over longer time periods (weeks) more settling was observed for uncoated gold nanoparticles than for pMPC-coated gold nanoparticles. Additionally, the settled particles were easily dispersed in the case of the pMPC-coated particles.

a)



b)



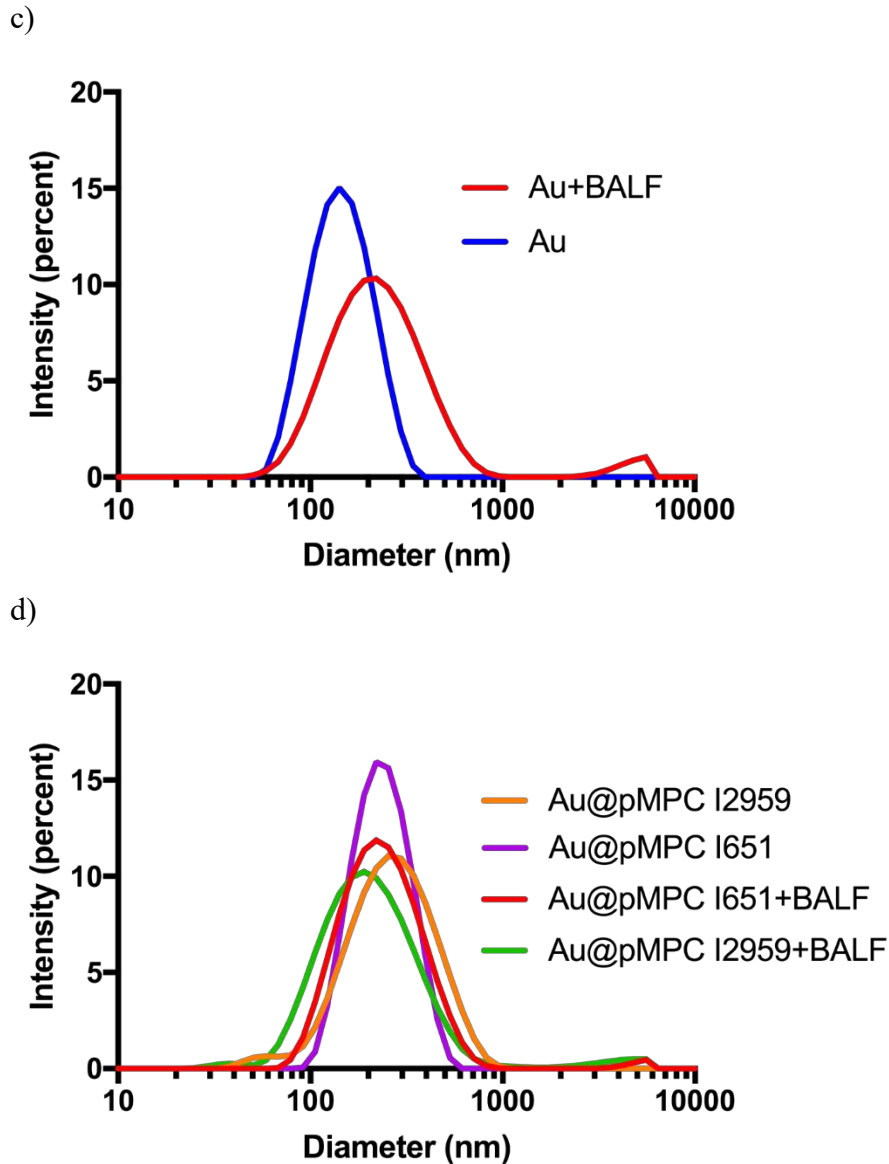


Figure 6.11. Distributions of hydrodynamic diameters of a) gold and b) 6:1 pMPC-coated gold nanoparticles exposed serum obtained by DLS.

Zeta potentials of gold nanoparticles were measured before and after exposure to serum or BALF (Figure 6.12). Uncoated gold nanoparticles exhibited an increase in zeta potential after exposure to serum. Similarly, the zeta potentials for pMPC-coated gold nanoparticles increased after exposure to serum, though not as much as uncoated gold.

For gold nanoparticles exposed to BALF, zeta potential increased more than in serum. For pMPC-coated gold nanoparticles, zeta potentials increased, but similarly to serum, the increase was not as large as for uncoated gold.

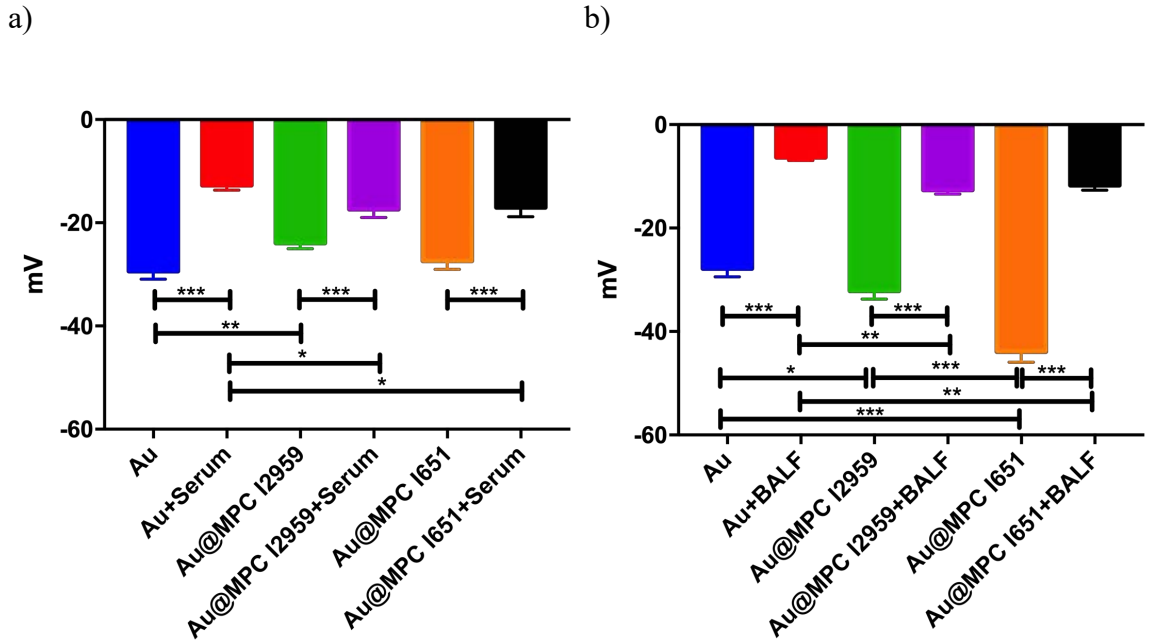


Figure 6.12. Zeta potential measurements for pMPC-coated and uncoated gold nanoparticles exposed to a) serum and b) BALF.  $n=1$ , 3 replicates. Error bars=SD.

### 6.3.3 Protein Adsorption to Gold Nanoparticles

The BCA assay was used to measure proteins adsorbed to the surfaces of coated and uncoated nanoparticles (Figure 6.13). Coating with pMPC in a 30:1 polymer:gold mass ratio did not alter serum protein adsorption to gold particles. When these particles were exposed to BALF, much less total protein was adsorbed to all particle types, but this may be due to the low total protein concentration of BALF. With BALF, the pMPC coating adsorbed less protein than gold, but the difference was not significant.



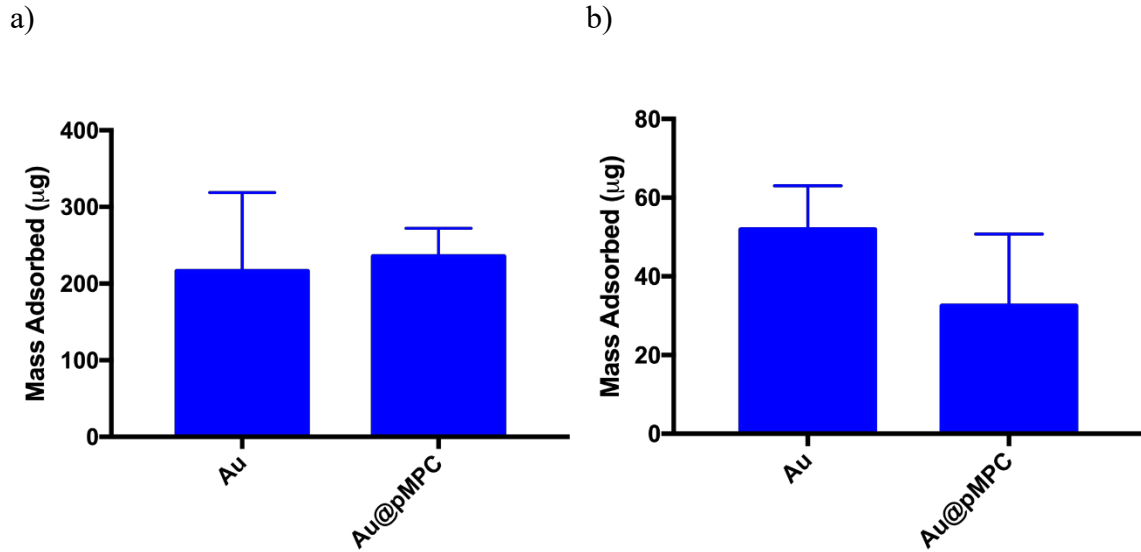


Figure 6.13. Measurements of a) serum and b) BALF proteins adsorbed to 30:1 pMPC and uncoated gold nanoparticles using the BCA Assay.  $n=1$ , 3 replicates. Error bars=SD.

When gold particles were coated with pMPC in a 6:1 mass ratio and exposed to serum diluted to 1,000  $\mu\text{g}/\text{mL}$ , large reductions in protein adsorption compared to bare gold were measured (Figure 6.14). For pMPC initiated with I2959, a reduction in adsorption of 80% compared to bare gold was observed, and for pMPC initiated with I651, no measurable adsorption was recorded. Both of these effects were significantly different from controls for this coating.

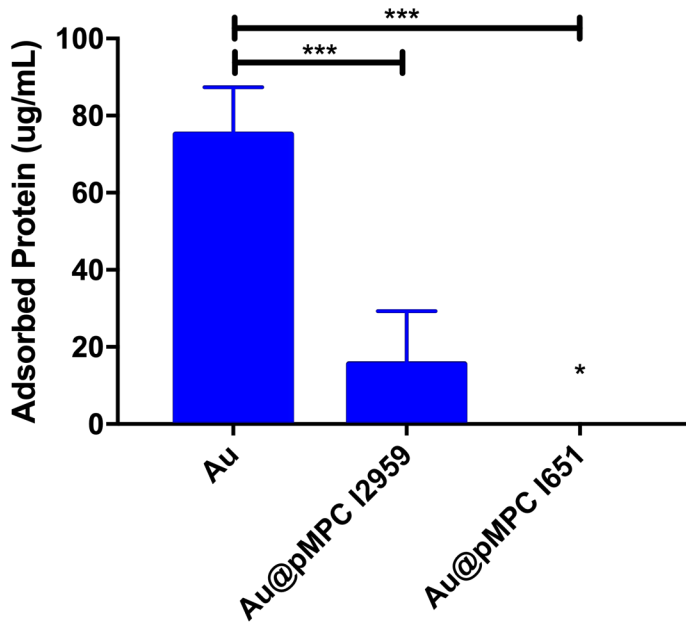


Figure 6.14. Measurements of serum proteins adsorbed to gold nanoparticles and 6:1 mass ratio pMPC-coated gold nanoparticles synthesized with either I2959 or I651 as the photoinitiator. \* denotes that no measurable protein adsorption occurred in this dataset. (\*\*\*) $p > 0.001$   $n = 1, 2$  replicates. Error bars=SD.

#### 6.3.4 DLVO Theory

DLVO theory, named for Derjaguin, Landau, Verwey, and Overbeek<sup>33, 235</sup>, was used to assess the stability of protein-coated particles in saline. DLVO theory models the behavior of particles in suspension by adding attractive Van der Waals forces (Equation 6-1)<sup>236</sup> with repulsive electrostatic forces (Equation 6-2)<sup>32</sup> to predict the net force of interaction (Equation 6-3) between two particles. These two forces are often dominant in affecting particle interactions, so the theory has been used to predict and describe the behavior of various colloids.<sup>32, 54, 237</sup>

$$\Phi_{VDW} = -\frac{A_{212}}{12} f(x, y) = -\frac{A_{212}}{12} \left( \frac{y}{x^2 + xy + x} + \frac{y}{x^2 + xy + x + y} + 2 \ln \left( \frac{x^2 + xy + x}{x^2 + xy + y + x} \right) \right) \quad (6-1)$$

$$\Phi_{\text{Elec}} = 2\pi r \epsilon \epsilon_0 \Psi_0^2 \ln(1 + \exp(-\kappa S_0)) \quad (6-2)$$

$$\Phi_{\text{Net}} = \Phi_{\text{VDW}} + \Phi_{\text{Elec}} \quad (6-3)$$

In these equations,  $\Phi_{\text{VDW}}$  and  $\Phi_{\text{Elec}}$  are the energies of Van der Waals attraction and electrostatic repulsion respectively and their sum  $\Phi_{\text{Net}}$  represents the total energy of interaction (in Joules) between two particles. Van der Waals attraction is a function of the Hamaker constant,  $A_{212}$ , of particles (2) in the medium (1) and two variables  $x$  and  $y$ , where  $x = S_0/2r_1$  and  $y = r_2/r_1$  with  $S_0$  representing the distance between two particles,  $r_1$  representing the radius of particle 1, and  $r_2$  representing the radius of particle 2 (if the particles are not the same size). The Hamaker constant for particles in media was either sourced from literature or calculated using equation 6-4 where  $A_{22}$  and  $A_{11}$  are the self-interaction Hamaker constants for materials in a vacuum.

$$A_{212} = (\sqrt{A_{22}} - \sqrt{A_{11}})^2 \quad (6-4)$$

Electrostatic repulsion is calculated using variables and constants defined in

Table 6.4. Values for  $\epsilon$  and  $\epsilon_0$  are constant at 80.1 and  $8.85 \times 10^{-12} \text{ C}^2/(\text{J m})$  respectively. The zeta potential,  $\Psi_0$ , was measured experimentally. Values for  $S_0$  were plotted to solve for interaction energy at various distances, and the inverse Debye length,  $\kappa$ , was calculated using Equations 6-5 and 6-6.

Table 6.4. Definitions and units of symbols used in calculating electrostatic repulsive energy.

Symbol	Definition	Units
r	Particle Radius	m
$\epsilon$	Dielectric Constant of Water	
$\epsilon_0$	Permittivity of Vacuum	C <sup>2</sup> /(J m)
$\Psi_0$	Zeta Potential	V
$\kappa$	Inverse Debye Length	m <sup>-1</sup>
S <sub>0</sub>	Interparticle Distance	m

$$\kappa = \left[ \frac{e^2 N_A z I}{\epsilon \epsilon_0 k_B T} \right]^{0.5} \quad (6-5)$$

$$I = \frac{1}{2} \sum z_i^2 C_i \quad (6-6)$$

In the calculations for the inverse Debye length, the variable I is calculated using the ion valences,  $z_i$ , and the concentration of those ions,  $C_i$  (in units of mol/m<sup>3</sup>) that are determined based on the composition of the aqueous media. The remaining components of the calculation of inverse Debye length are constants whose definitions and values are listed in Table 6.5 and the temperature, T, in Kelvin.

Table 6.5. Definitions and values for constants used to calculate inverse Debye length.

Symbol	Definition	Value	Units
k <sub>B</sub>	Boltzmann Constant	1.38066×10 <sup>-23</sup>	J/K
e	Elementary Charge	1.6×10 <sup>-19</sup>	C

$\epsilon$	Dielectric Constant of Water	80.1	
$\epsilon_0$	Permittivity of Vacuum	$8.85 \times 10^{-12}$	$C^2/(J \cdot m)$
$N_A$	Avogadro's Number	$6.022 \times 10^{23}$	$mol^{-1}$

Equations 6-1 through 6-6 together constitute classical DLVO theory. To determine particle stability, the net interaction energy is plotted against distance for a pair of particles. As interparticle distance falls below  $\sim 1$  nm, Van der Waals forces tend to become exponentially stronger resulting in large negative energies indicating cohesion of particles. Electrostatic forces can create a local maximum that acts as an energy barrier preventing particles from reaching the critical distance at which Van der Waals forces are dominant. When local maximum values energies exceed  $\sim 1.5 k_B T$ , the energy of Brownian motion of particles<sup>54, 236</sup>, they are less likely to move near enough to adhere to one another. Classical DLVO theory can be a reliable approximation of the behavior of particles in aqueous media with varying ionic concentrations. However, it does not account for coated particles, whether they be covered in adsorbed protein or coated in a polymer. While the electrostatic forces are accounted for (since they are based on measured potentials), the changes in Van der Waals forces due to surface coatings are not predicted. These can be accounted for using theory postulated by Vold.<sup>238</sup> This model considers an increase in size due to the addition of material to a particle's surface and further calculates Van der Waals forces between particles, the adsorbate, and the medium as a modification to the Van der Waals interaction shown in Equation 6-7.

$$\Phi_{VDW} = \frac{(A_M^{0.5} - A_A^{0.5})^2 f_A(x,y) + (A_A^{0.5} - A_P^{0.5})^2 f_P(x,y) + 2(A_M^{0.5} - A_A^{0.5})(A_A^{0.5} - A_P^{0.5}) f_{PA}(x,y)}{-12} \quad (6-7)$$

In the above equation,  $A_A$ ,  $A_M$ , and  $A_P$  are Hamaker constants for the adsorbate, media, and particle respectively. The  $f$  functions are the same as in Equation 6-1, where  $x$

and  $y$  are defined such that in  $f_A$  there are 2 spheres of radius  $r+\delta$  separated by a distance  $S_0$ , in  $f_P$  the radius is  $r$  and the separation is  $S_0+2\delta$ , and in  $f_{PA}$  there are 2 spheres of radius  $r$  and  $r+\delta$  respectively separated by a distance  $S_0+\delta$ . To simplify this equation, it was assumed that adsorbates formed a monolayer.

While these equations now account for electrostatic forces and complex Van der Waals interactions between particles, adsorbates, and media, there is one further component that can contribute to particle stability that is not accounted for here, hydration. As discussed previously, for zwitterionic materials, and for proteins, the presence of multiple charged groups on a macromolecule such as a polymer or a protein creates a hydrophilic environment that often have little to no net surface charge. For systems where a hydrophilic material is present on the exterior of a particle, strong hydration can result in a required energy to displace solvent molecules for particles to move close together. To account for the stabilizing effect of well hydrated surfaces, Equation 6-8 is used to calculate a hydration energy  $\Phi_H$  based on work by Marčelja and Radić<sup>239</sup>, and incorporated into the energy balance (Equation 6-3) as demonstrated by Dávalos et al. forming Equation 6-9.<sup>31</sup>

$$\Phi_H = \pi r N_A C_H C_i \lambda^2 \exp\left(-S_0/\lambda\right) \quad (6-8)$$

$$\Phi_{Net} = \Phi_{VDW} + \Phi_{Elec} + \Phi_H \quad (6-9)$$

In the above equations,  $C_H$  is the hydration constant (in Joules) of the adsorbate and  $\lambda$  is the decay length (in m)<sup>31, 240</sup>. The hydration constant is proportional to the strength of the adsorbate's hydration and is positive for hydrophilic materials. Thus, we have developed a modified DLVO model that includes modifications to the Van der

Waals forces to account for the presence of an adsorbed monolayer, and the inclusion of hydration energy as an additional stabilizing force.

The classic DLVO model was initially generated, and validated against published work on silver nanoparticles,<sup>54</sup> producing matching results. The model was then applied to gold nanoparticles in saline. The model was modified using the adjustment of the Van der Waals calculation for a coated surface as described in Eq 6-7 to account for the presence of a polymer coating. The coating thickness was set to be half the difference in hydrodynamic diameter of coated versus uncoated gold particles as measured by DLS, and the Hamaker constant for poly(3-[dimethyl(2-methacryloyloxyethyl)ammonium] propanesulfonate) ( $1 \times 10^{-18}$  J) in water was used for pMPC assuming that the two polymers are highly similar in their interactions.<sup>241</sup> This assumed similarity is based on similarities in structure as illustrated by the monomer structure for 3-[dimethyl(2-methacryloyloxyethyl)ammonium] propanesulfonate in Figure 6.15.

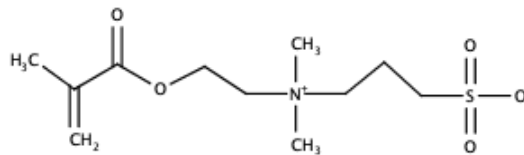


Figure 6.15. Monomer structure of 3-[dimethyl(2-methacryloyloxyethyl)ammonium] propanesulfonate

The cationic and anionic groups are swapped, and the anionic group is sulfate rather than phosphate. These were assumed to have little effect on the Hamaker constant. Finally, strong hydration was added to the model as described in Eq. 6-8, using a decay length of 1.2 nm. The value for  $C_H$  was set based on experimental observations. Having observed that pMPC-coated gold nanoparticles remain stable in saline suspension over long time

periods, the value of  $C_H$  was solved iteratively to satisfy the condition that a local maximum for  $\Phi_{Net}$  from 0-10 nm be greater than or equal to  $1.5k_B T$ . The initial guess for  $C_H$  was based on the reported  $C_H$  value for IgG ( $1.7 \times 10^{-20}$  J), and resulted in a  $C_H$  value for pMPC of  $1.2 \times 10^{-19}$  J. A comparison of the three models for pMPC-coated gold nanoparticles is illustrated in Figure 6.16.

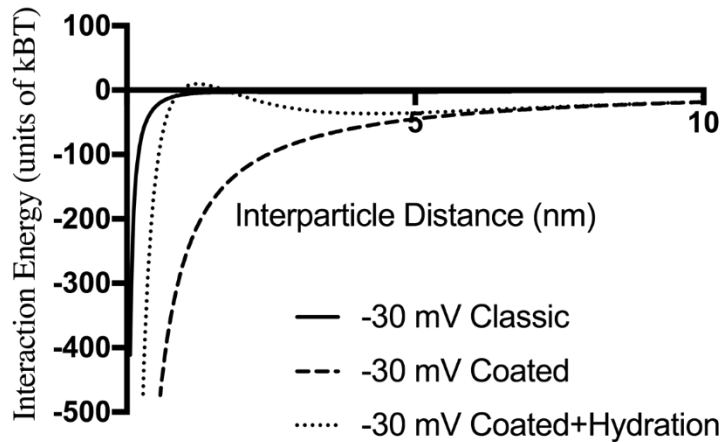


Figure 6.16. Comparison of classic DLVO, Coated DLVO, and Coated DLVO+Hydration models for 100 nm gold nanoparticles in saline.

Figure 6.16 highlights that a particle coating can lower the interaction energy between particles leading to aggregation, and that significant strong hydration can be in contributing to particle stability. This is especially true in the case of zwitterionic materials with low net surface charge, as the hydration effects must provide repulsive forces in the absence of strong electrostatic repulsion to maintain stability.

### 6.3.5 Cell Responses to Coated and Uncoated Gold Nanoparticles

Gold nanoparticles, reactants, and polymers were assessed for their effects on lung cell viability. The RAFT agent was the only component that reduced cell viability *in*



*in vitro* in a dose-dependent manner (Figure 6.17). However, once incorporated into a polymer no toxicity was observed. The RAFT agent makes up a small fraction of polymer by mass, and once combined with gold nanoparticles, the RAFT-agent fraction of coated particle mass is further overshadowed by the dense gold core. pMPC-coated gold nanoparticles induced no measurable toxicity in lung cells at any of the doses applied.

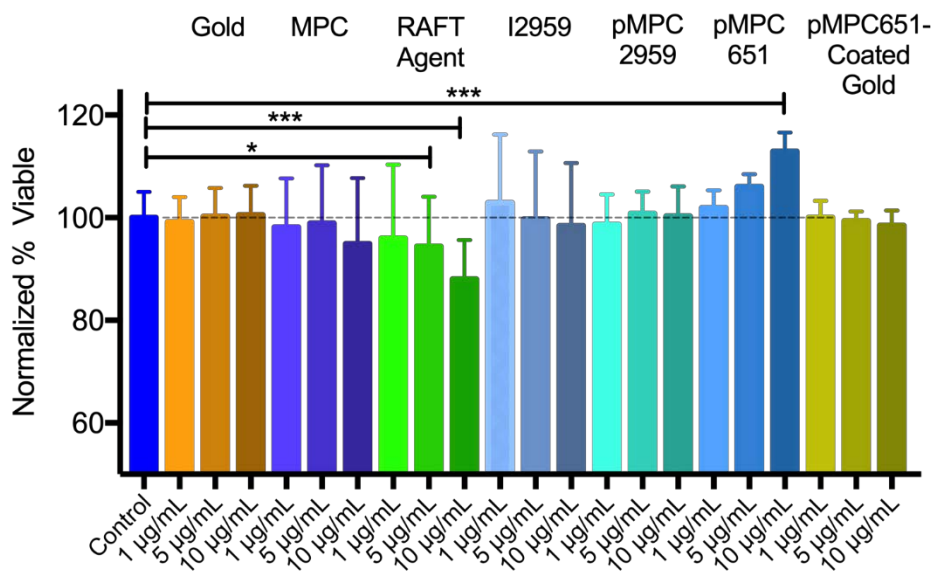


Figure 6.17. Measurement of the toxicity of the various components that may be present in coated gold nanoparticle suspensions exposed to cells. Gold, RAFT agent, I-2959, and pMPC 2959:  $n=4$ , 3 replicates. MPC:  $n=4$ , 4 replicates. pMPC 651 and pMPC 651-coated gold:  $n=1$ , 3 replicates. Error Bars=SD.

Cellular uptake/association of gold nanoparticles as measured by ICP-MS analysis of exposed cells identified a dose-dependent relationship between applied dose and the mass of gold associated with cells after exposure (Figure 6.18), which is consistent with previous reports of gold uptake using ICP analysis.<sup>242</sup> Analyses were performed using 6:1 coated and uncoated gold nanoparticles exposed to serum and BALF. As illustrated in Figure 6.18, similar linear trends were observed with dose for all exposures. For particles

exposed to serum, the pMPC I651-coated gold was most associated with cells while the uncoated gold was least associated. pMPC I2959-coated gold association was lower than pMPC I651-coated gold, but higher than bare gold. After exposure to BALF, particle uptake by A549 cells was identical regardless of coating or lack thereof. When pMPC I2959-coated gold particles were compared directly against uncoated gold without exposure to serum or BALF, the coated gold was found to associate more with the gold.

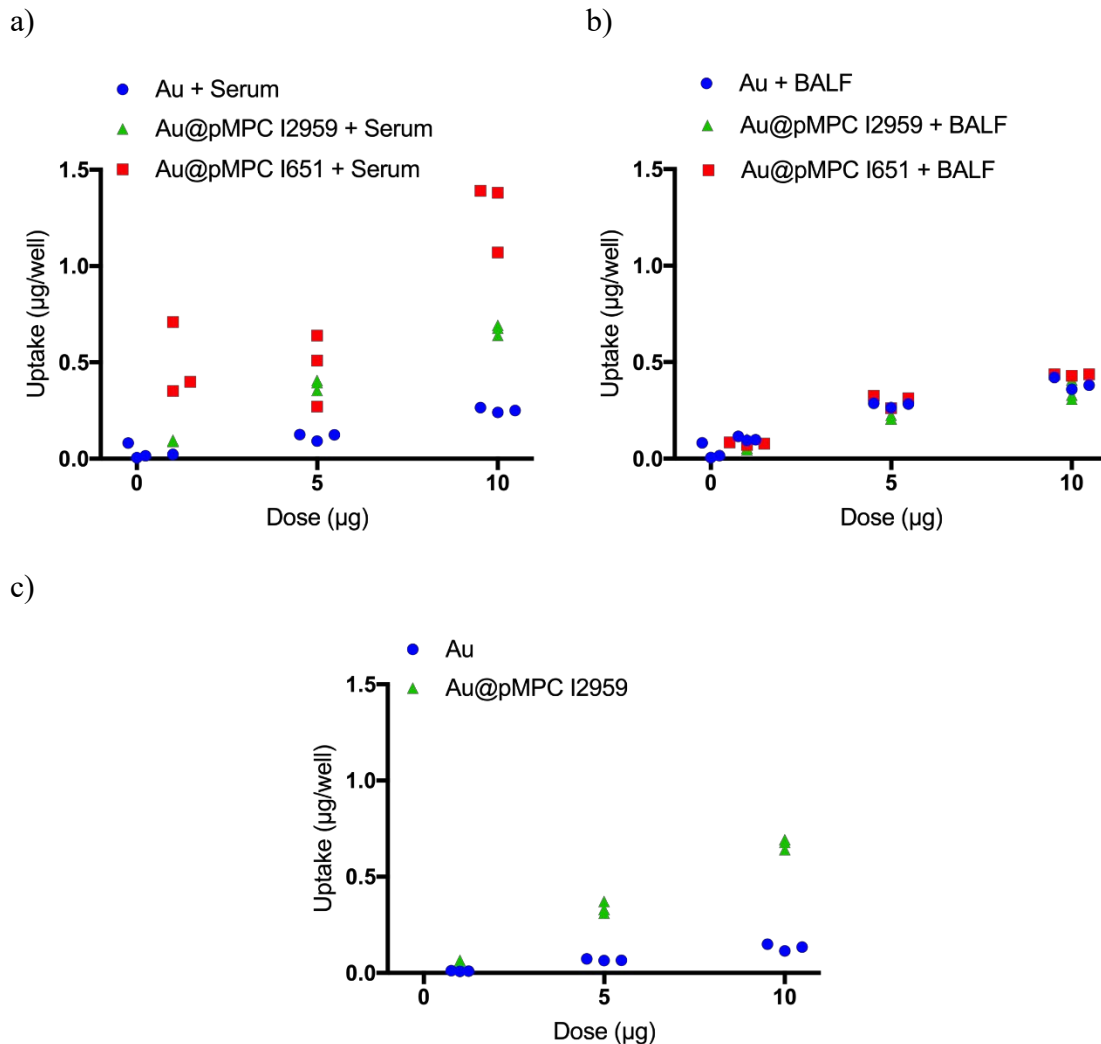


Figure 6.18. ICP-MS measurement of gold nanoparticle uptake in A549 cells with and without coating after exposure to a) serum or b) BALF. c) comparison of uptake of gold nanoparticles with and without pMPC I2959 coating. n=1, 3 replicates.

## 6.4 Discussion

GPC analysis identified that I-651 initiated polymers were large (~68 kDa), with I-2959 initiated polymers being larger (~148 kDa). These larger polymers may result in less-dense packing of polymer on the surface of gold due to steric hindrance. While these polymers were effective at both reducing nonspecific protein adsorption and increasing particle stability, reducing the size of these chains may further improve performance. Further, differences observed between polymers generated from the two initiators is likely due to differences in molecular weight between the polymers based on initiator.

When the mixing ratio used to coat polymers onto proteins was reduced to 6:1 polymer:gold (w/w), polymer coatings formed on the surfaces of gold particles. Unlike the high polymer-loading samples, these polymer coatings were not thick enough to cause shading in TEM images. The current density of the electron beam and the exposure time for image collection were maintained in a narrow range ensuring that imaging was consistent between samples, so it is unlikely that this shading phenomenon was an artifact of beam illumination. Additionally, the dispersion of particles in the TEM images was less agglomerated in these samples when compared to the 30:1 polymer:gold mass ratio or uncoated gold. This further highlights differences in these coatings and indicates that the observed increase in hydrodynamic diameter of particles in suspension is likely due to the formation of a polymer coating as opposed to aggregation.

When pure gold particles were exposed to protein-rich serum and BALF, particles tended to aggregate, and hydrodynamic size increased. When pMPC-coated particles were exposed to serum or BALF, they shrank. This was consistent whether studying the

optimized 6:1 or the 30:1 polymer:gold mass loading ratio. It appears that introduction of pMPC-coated gold nanoparticles into biological media can induce contraction of the pMPC layer. Contraction could be due to changes in ion environment or some effect of proteins on chain behavior. These size changes were accompanied by changes in zeta potential for these particles, which indicates a change in the double layer. This response in the polymer coating occurs while maintaining suspension stability in biological fluids.

The relative adsorption of proteins to pMPC-coated gold particles depended on the coating conditions. Gold particles coated in a 6:1 mass ratio of pMPC:gold adsorbed little to no measurable protein, whereas particles coated in a 30:1 mass ratio adsorbed similar levels of protein compared to bare gold. The reduction in protein adsorption observed in the 6:1 mass ratio coating of pMPC onto gold indicate that this is the more optimum coating ratio.

Cell responses to gold, pMPC, and components used to synthesize pMPC identified that the RAFT agent used was the only tested material that exhibited toxicity. This component is modified in the reaction, and the resulting polymer was found to be non-toxic. Additionally, the RAFT agent is further degraded after polymer synthesis. Polymer clean-up, whether performed directly from the reaction by use of dialysis or molecular thimbles or by washing the coated gold particles, should be considered to ensure no toxic components are present. Ethylamine, which is used to degrade the RAFT agent into thiol end-groups, is toxic and should be removed prior to any cell interactions.

In addition to being non-toxic to lung cells at the doses studied, an increase in uptake of pMPC I2959-coated gold nanoparticles was observed compared to gold in the absence of proteins. When coated and uncoated particles were exposed to serum or

BALF, cell uptake was impacted. Exposure to serum or BALF resulted in a small increase in uptake of bare gold. For pMPC I2959-coated gold particles, serum exposure had no effect on cell uptake, while BALF exposure resulted in a decrease in uptake. Considering the behavior of gold in biological fluids (Figure 6.19b), i.e. serum and BALF, it is possible that the aggregation and destabilization of uncoated gold nanoparticles may have unobserved consequences for particle interactions with cells, though none were observed with these metrics.

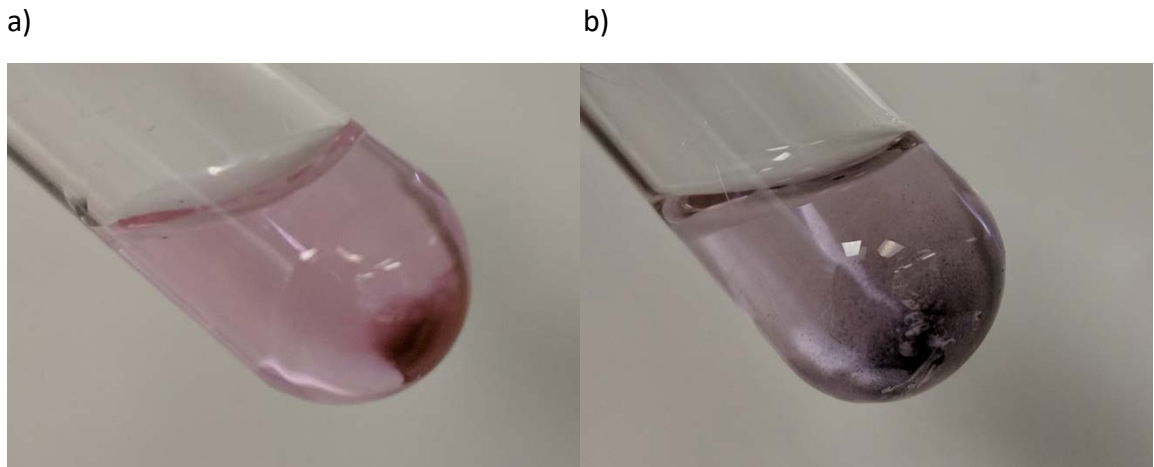


Figure 6.19. Illustration of observed differences between a) settled stable particles and b) aggregates observed during analysis and exposure to proteins.

## 6.5 Conclusion

The use of photopolymerization in the presence of a RAFT agent as a means of synthesizing pMPC-coated gold nanoparticles has been demonstrated here as a potential system for reducing particle interactions with proteins. These pMPC SAMs help maintain stability of gold nanoparticle suspensions, likely due to strong hydration of the phosphorylcholine moieties covering the polymer backbone. While this coating reduced interactions with proteins, pMPC did not affect uptake of gold particles by A549 alveolar epithelial cells or impact cell viability. The coatings on gold particles maintained higher

levels of cell association after serum exposure than after BALF exposure. In BALF, particles remained stable, and uptake was similar to that of uncoated gold. This system was designed to provide stability in lung fluids, while allowing entry into lung cells. Herein we have demonstrated a synthesis route to produce these polymers and demonstrated their ability to stabilize particles in serum and BALF without interfering with lung cell uptake, which makes this polymer coating a promising choice for potential use in pulmonary drug delivery.

## 7 Conclusions and Future Directions

### 7.1 Conclusions

This research investigated how inhaled particles interact in the lung environment. In the work presented, exploration of particle toxicity, particle influences on regulation of a cell receptor, particle interactions with proteins, and cellular uptake of particles by lung cells provide a better understanding of the behavior of inhaled particles in the airways. In particular, the development of methods to enhance the concentration of proteins from BALF provides an approach that can be utilized in many future studies to simulate the aqueous fluid environment in the respiratory airways.

In chapter 2, aerosols formed from the photooxidation of D5 were studied. Using an oxidative flow reactor equipped with UV lamps, water vapor was converted to OH. This reacted with gas-phase D5 resulting in oxidized products that formed aerosols. Particle size was characterized using SMPS and TEM, and the aerosols were found to be 32-89 nm in diameter. EDS spectra identified high silicon and oxygen content in the species deposited onto TEM grids. This confirmed that these aerosols were formed from D5. These particles were aerosolized onto lung cells (A549) at gas-phase concentrations ranging from 102-218  $\mu\text{g}/\text{mL}$  using a Vitrocell 6/12 exposure system. No toxicity attributable to this aerosol species was observed in these studies. After exposure, cells were rinsed to collect any secreted cytokines. No measurable cytokine production was observed using ELISA. These studies indicate that this environmental aerosol is not highly toxic to alveolar lung cell cultures.

In chapter 3, CuO, a component of urban PM, cigarette smoke, and e-cigarette vapor, was studied. CuO nanoparticles were imaged using TEM to verify their size

properties, and they were found to be aggregates of small primary particles around 20 nm in diameter. The *in vitro* toxicity range of CuO was explored in A549 cells. CuO was found to induce toxicity starting at concentrations of around 0.01 mg/mL, and complete cell death was observed above 1 mg/mL. Toxicity was found to be associated with visible changes in cell morphology, with cells undergoing apoptosis at higher concentrations. Within this range, cellular uptake of copper oxide was studied using ICP-MS and found to be linearly dose-dependent. After exposure to CuO particles, cells were lysed, and the lysate analyzed for PAFR using western blot. At higher doses, an increase in PAFR was observed in cell lysate. The effects of CuO on lung cell susceptibility to *S. pneumoniae* infection were studied. After exposure to CuO nanoparticles, lung cells were challenged with *S. pneumoniae*, and the number of colony-forming units attached or internalized was measured. No significant differences were observed in bacterial infectivity thus far. Bacterial growth was found to be unaffected by CuO doses at concentrations relevant to the bacterial challenge. These studies indicate that CuO nanoparticles are toxic to lung cells and may have additional effects on lung cells beyond immediate toxicity through upregulation of PAFR.

In chapter 4, a selection of proteins known to be expressed at higher levels in lung fluids were selected to investigate impacts on particles. The effects of BSA and lysozyme on polystyrene particles were studied. Lysozyme was found to cause large aggregates and large polydispersity. Lysozyme was also found to significantly alter the zeta potential of 200 nm and 1  $\mu$ m particles compared to all other exposure conditions. Lysozyme reduced cell association with both 200 nm and 1  $\mu$ m particles. Using gold nanoparticles, the role of pH in the adsorption of BSA, IgG, lactoferrin, and lysozyme was studied. Different



proteins were found to result in different levels of aggregation regardless of pH. This appeared to be related to protein zeta potentials and the composition of amine and carboxylate groups within a protein's primary structure. Using DLVO theory, the effects of proteins on gold nanoparticle stability in suspension were explored. Based on the conditions of exposure, DLVO theory accurately predicted aggregation behavior for all proteins and buffers studied. These studies demonstrate that proteins that are present at elevated levels in lung fluids can strongly influence particle stability in an aqueous environment.

In chapter 5, particles exposed to serum and BALF were explored to identify differences in how particles behave in blood compared to lung fluids. To establish a more physiologically relevant model system for pulmonary drug delivery, a method was developed to partially reconstitute BALF to much higher protein concentrations. Such an approach to *in vitro* modeling of particle behavior in the pulmonary environment has not been previously reported. Using a salt extraction followed by a solvent evaporation, a process for concentrating BALF was demonstrated. Using various surface-functionalized polystyrene particles, the impacts of serum and rBALF on particle aggregation, surface charge, and cellular responses were measured. Significant differences in aggregation behavior were observed in serum and rBALF for some of the particle functionalities studied. For most particle types studied, significant differences were observed between zeta potentials of particles exposed to these two fluids. These two fluids were both found to reduce particle-cell association *in vitro* for most particles studied, and in some surface functionalized particles, significant differences in cell responses to particles exposed to serum or rBALF were observed. This illustrates the need to study how particles interact

in lung fluids in the context of drug delivery, and provides here a useful approach to such studies using clinically-derived materials.

In chapter 6, an approach to synthesizing zwitterionic pMPC-coated gold nanoparticles to resist aggregation and adsorption of proteins was developed, and the resulting polymer tested. Using a photoinitiated polymerization in the presence of a RAFT agent, a thiol-terminated pMPC was synthesized. Using NMR, the chemistry of the resulting polymer was confirmed, and conversion was studied using Raman spectroscopy. Using a 6:1 mass ratio of polymer to gold, self-assembled monolayers were formed onto gold nanoparticles. Gold nanoparticles were characterized using TEM with and without polymer on the surface, which helped identify the optimum coating. These coated particles were more stable in saline and in the presence of serum or BALF. Protein adsorption to the surfaces of coated and uncoated gold particles was measured, and the coatings were found to reduce adsorption. The polymer was found to be non-toxic to lung cells, and polymer-coated gold nanoparticle uptake by lung cells was found to be unaffected by these coatings. *In vitro* cell uptake measurements identified no significant difference between coated and uncoated gold nanoparticles at the doses studied. This study demonstrated the utility of a pMPC coating for particle delivery in the lungs and demonstrated a simple approach to polymer synthesis to exploit thiol-gold chemistry.

BALF has herein been identified as a useful model system for studying the behavior of foreign materials that deposit in the respiratory airways. A process for increasing the concentration of airway proteins has been demonstrated utilizing a buffer exchange to reduce salt content followed by evaporation to decrease volume. This

process resulted in large increases in total protein concentration in BALF samples, which were nearer physiologically relevant concentrations.

## 7.2 Future Directions

### 7.2.1 Aerosols Produced Via Atmospheric Photooxidation of cVMS

Further investigations into cellular interactions with aerosols produced by photooxidation of these products could be performed. The large uncertainties in cell viability measurements coupled with unknown sources of toxicity in gaseous products from the OFR leave some uncertainties in these results. Modifications to the cell viability assay may aid in reducing measurement error. Direct application of assay reagent to cells affixed to transwell membranes would reduce potential errors in removal of cells from the transwell membrane for analysis. Further incubation of the cells after exposure prior to assessing viability could also allow more time for cells to respond to particles deposited on their surfaces. Additionally, analysis of gas-phase components would identify other potential sources of toxicity. While ozone was removed, there may be other molecules in the gas stream that could reduce cell viability. The use of GC-MS to analyze these components could identify or eliminate such components as potential causes of cell death.

As high levels of toxicity were not observed, progression to animal studies may further clarify the potential impacts these aerosols can have on lung health. Moving into mouse exposures would provide data on how such aerosols impact health *in vivo*. Moving into animal models also would allow for measurement of accumulation of materials in target organs, and identification of clearance mechanisms, if they exist.

### 7.2.2 Copper Oxide Nanoparticle Impacts on Lung Health

In these studies, copper oxide nanoparticles were found to be toxic. From western blot, there were some indications that a component of cellular response to these particles is increased expression of PAFR. Further studies of PAFR expression in response to these particles could be performed. As an alternative and complementary technique to Western Blot, ELISA could be utilized to measure with high sensitivity the presence of PAFR in cell lysate. Selection of a reference protein for normalization of the data analogous to the use of actin in the western blots would likely be needed for such protocols.

To increase understanding of PAFR-mediated infections with *S. Pneumoniae*, PAFR expression could be enhanced in lung cells using small activating RNA molecules to induce gene transcription.<sup>243, 244</sup> This would provide a positive control for increased bacterial infectivity in studies investigating receptor upregulation by CuO or any other material of interest. Bacterial adhesion could be further studied by blocking the PAFR receptor to verify its role in bacterial infectivity.

### 7.2.3 Impacts of Lung-Abundant Proteins on Particle Behavior

In these studies, protein interactions with particles were found to result in aggregation and changes in surface charge. Using the gold platform, ICP-MS studies could be performed to further examine effects of these proteins on cellular uptake of gold nanoparticles. The selection of proteins could be widened as well. Other proteins elevated in the lungs, such as IgM,  $\alpha$ -amylase, Club cell protein, and more could be added. These studies would further inform how proteins that are abundant in the lungs may impact particle fate in the body. To better understand adsorption, replicating these studies at higher particle concentrations could be used to increase the change in concentration of

proteins in solution before and after particle introduction. This may allow more meaningful information to be determined about a given protein's affinity for adsorbing to a particle. To combat the destabilization of gold in saline at various pH in the absence of proteins, adjustments to the aqueous phase could be made to improve the stability of these particles. This could include adjusting the salinity, or the addition of citric acid or other stabilizers to the mixture. Future work should minimize the use of multiple buffers during processing, as ionic components from these buffers may affect how particles and proteins interact.

#### 7.2.4 Reconstituted BALF to Study Inhaled Particles

These studies demonstrated an approach to studying particle behavior in the lungs by using BALF as a model fluid environment. BALF was herein demonstrated to be concentrated over tenfold to study particle behavior using a buffer exchange to reduce salts followed by evaporation of water to concentrate. While this method was demonstrated to be effective, it is also time and labor intensive, involving the processing of BALF in a large number of small volumes during the desalting phase. An alternative for concentrating BALF proteins could be the use of tangential flow filtration (TFF). TFF is used for exchange of buffers and the concentration of proteins in commercial and pharmaceutical settings.<sup>245, 246</sup> BALF can be recirculated through a membrane with a low molecular weight cutoff similar to a dialysis membrane. Over time, water and salts will permeate through the membrane, leaving behind the proteins. This process could be performed under refrigeration or with the sample reservoir attached to a chilled water line to keep samples cool, removing the need for extended processing of BALF at room temperature or at elevated temperatures used to evaporate water. This method could be

used to process entire samples of lung lavage, or even a large pooled sample to produce a model lung fluid with a high protein concentration. Sample pooling of BALF is another avenue that should be explored. Variability between people based on genetics can impact research that deals with proteins. Through sample pooling, a more representative lung fluid could be obtained.

Using reconstituted BALF, protein corona fingerprinting similar to previous work in plasma<sup>50, 55, 194, 247</sup> could be performed to analyze coronas that form around particles in the respiratory airways. Proteomic analyses of BALF would doubtless enhance scientific understanding of the processes that occur when inhaled particles interact with fluids in the lungs. Using proteomic techniques, a model approach to investigating systemic delivery through the lungs could be performed. For example, particles coated in BALF proteins that are subsequently transferred to serum should be studied to determine whether the protein coronas that form in the lung space remain dominant on the surface after transport into a fluid environment, such as blood, with a different proteome. Time-resolution of such exchange processes are especially important relative to phenomena such as circulation half-life.

#### 7.2.5 pMPC-Coatings for Drug Delivery in the Lungs

These studies identified the utility of pMPC self-assembled monolayers on gold nanoparticles at enhancing stability in BALF and serum. Further studies of these coatings could probe decreasing polymer length to form small brushes on the surface of gold particles to assess the effects of chain length on coating efficacy. This could be achieved by increasing initiator concentration or decreasing monomer concentration. Further development of copolymers that incorporate the MA and MP monomers to tune polymer

charge could be performed. In the polymerization of MPC, conversion of monomer may be increased. Sparging the reaction mixture with nitrogen and polymerizing under a nitrogen blanket may result in increased conversion. Oxygen can cause termination in free radical polymerizations, so efforts to remove it from the system may enhance conversion. Illumination time and lamp intensity could also be adjusted to increase conversion in this reaction.

To improve polymer characterization, polymer molecular weight measurements could be carried out a GPC with dual-detector system. Such a system with light scattering and differential refractive index monitoring is designed to combine the information gathered from the two detecting systems to determine the polymer molecular weight. This is based on the software using Mark-Houwink-Sakurada correlations which normalize GPC results based on intrinsic viscosity under the assumption of polymers moving through the system as a random coil.<sup>248</sup> With a well-calibrated dual-detector GPC system, molecular weight determinations could be made with more accuracy and without the need to create standard curves.

## Appendix

### A.1 Flow Cytometry Data

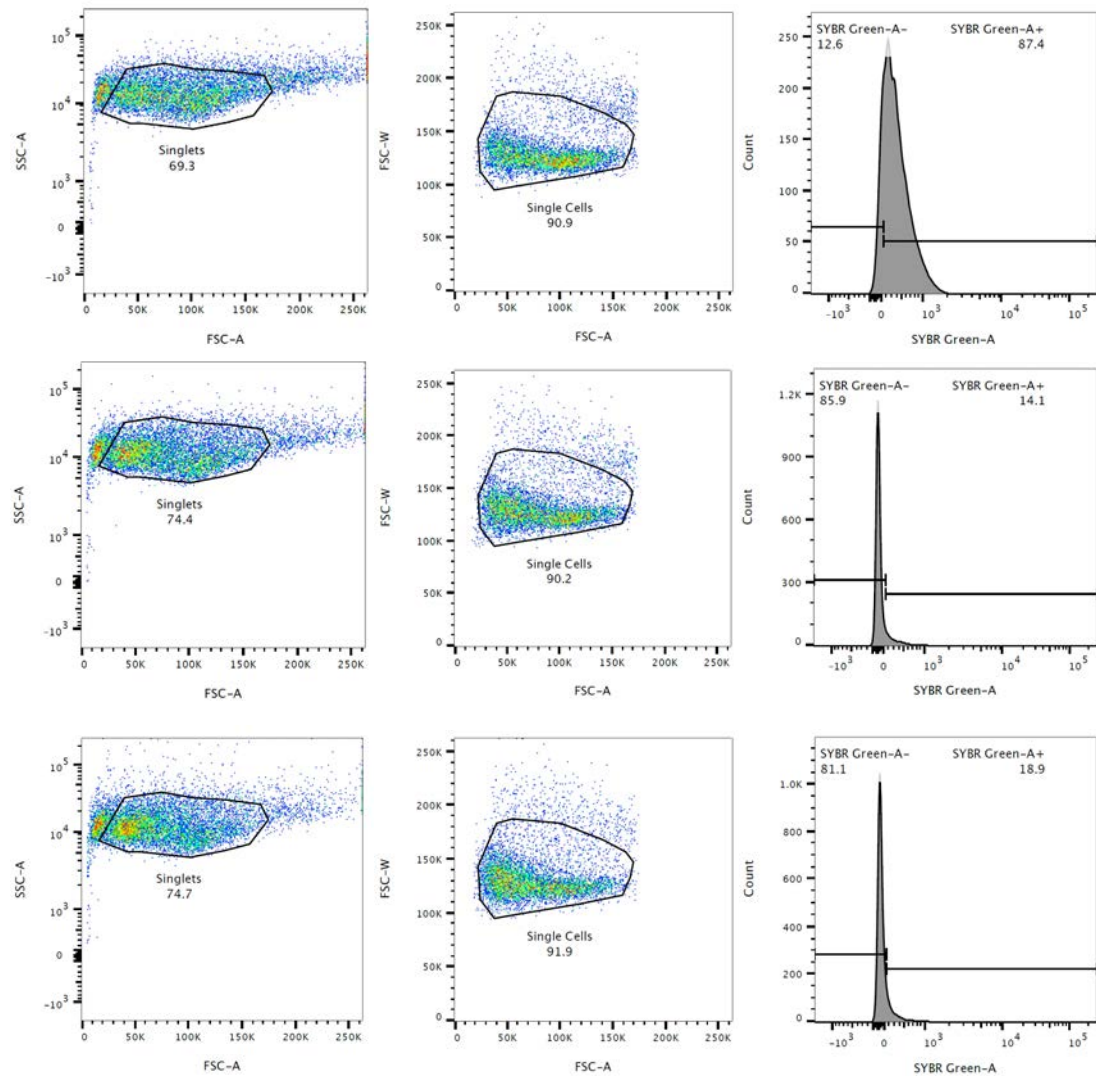


Figure A.1 Flow cytometry data for a-c) untreated, d-f) serum-treated, and g-i) BALF-treated 200 nm PPS particles exposed to A549 cells.



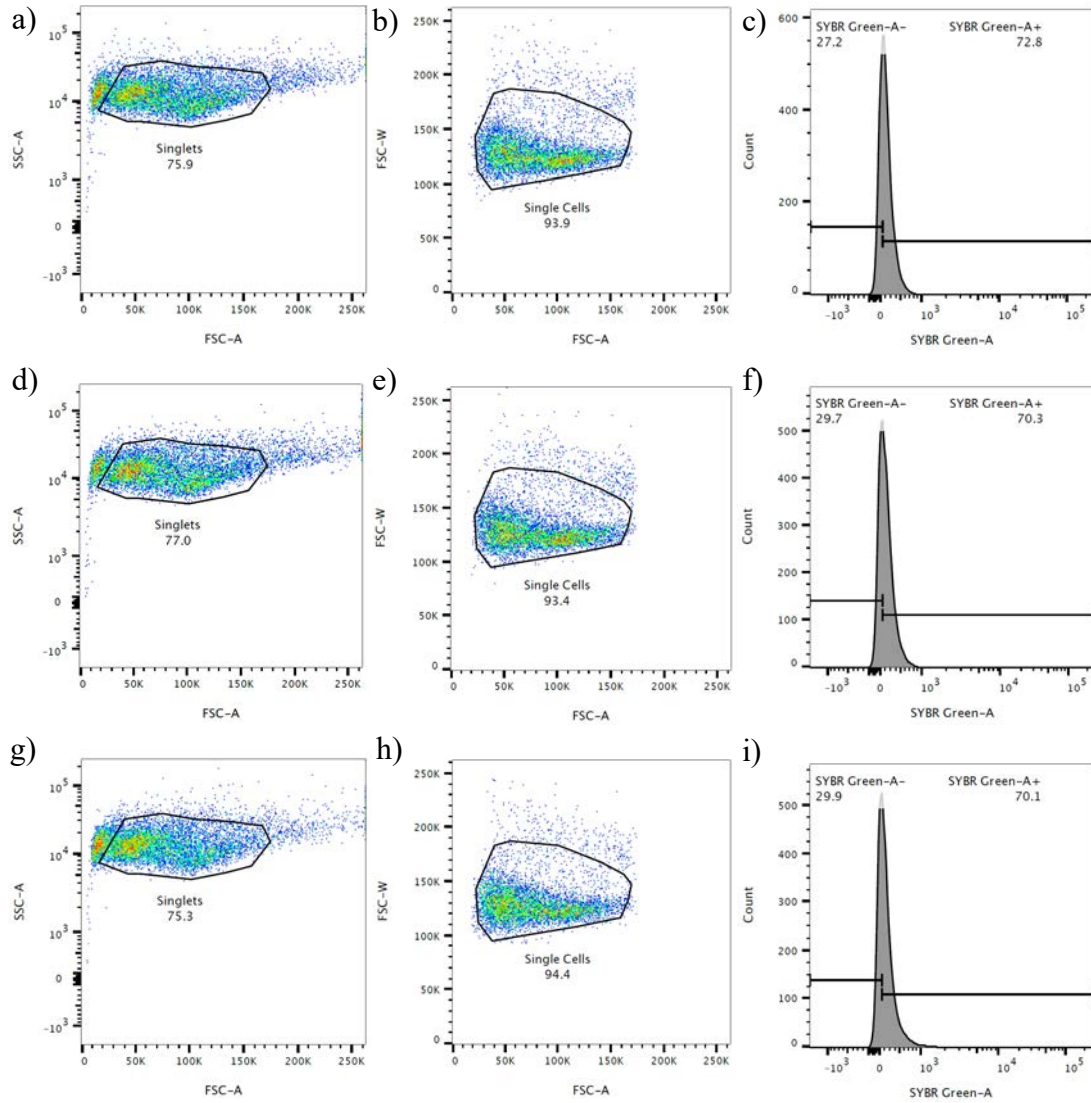


Figure A.2. Flow cytometry data for a-c) untreated, d-f) serum-treated, and g-i) BALF-treated 200 nm CML particles exposed to A549 cells.

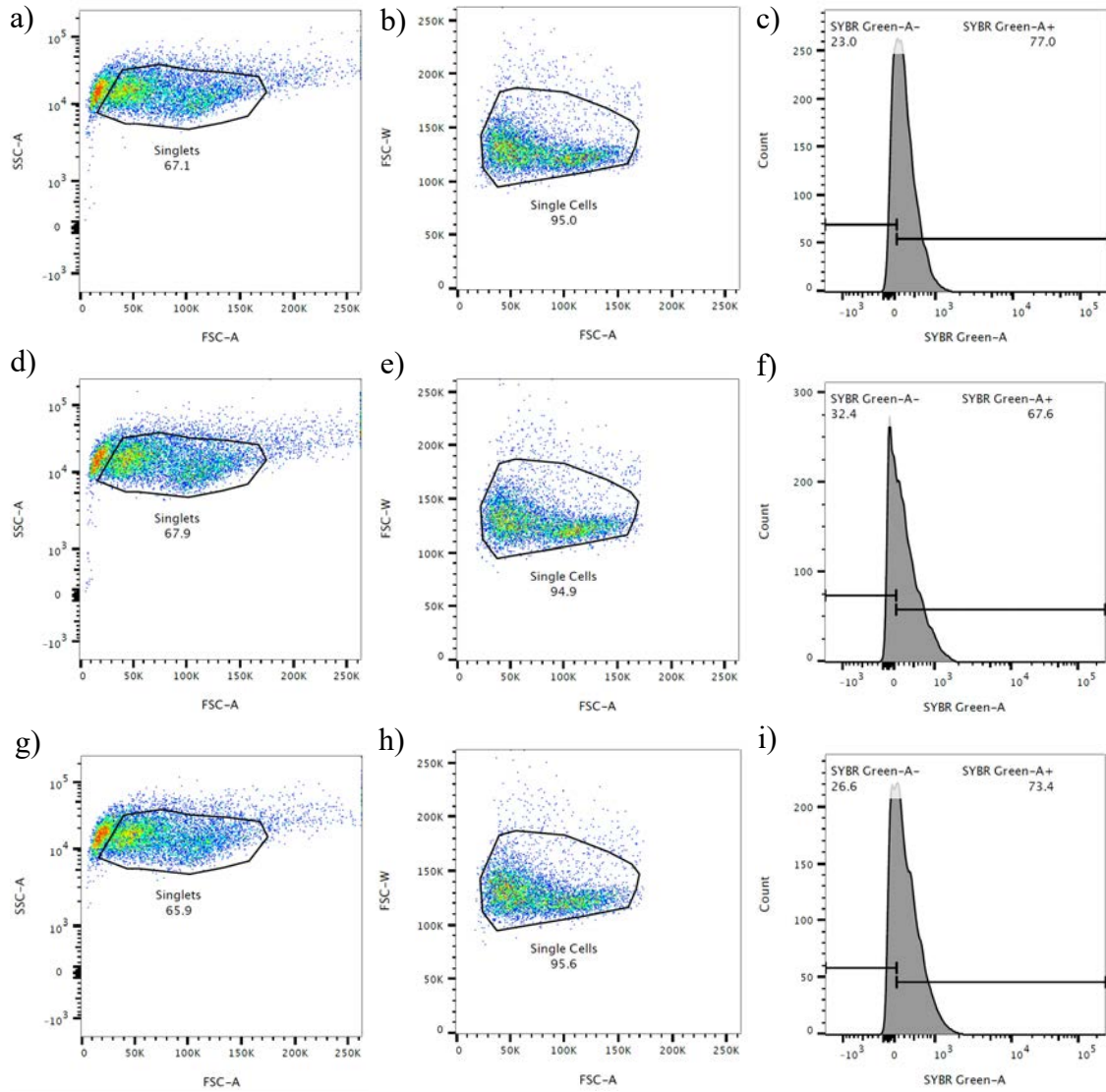


Figure A.3. Flow cytometry data for a-c) untreated, d-f) serum-treated, and g-i) BALF-treated 200 nm APS particles exposed to A549 cells.

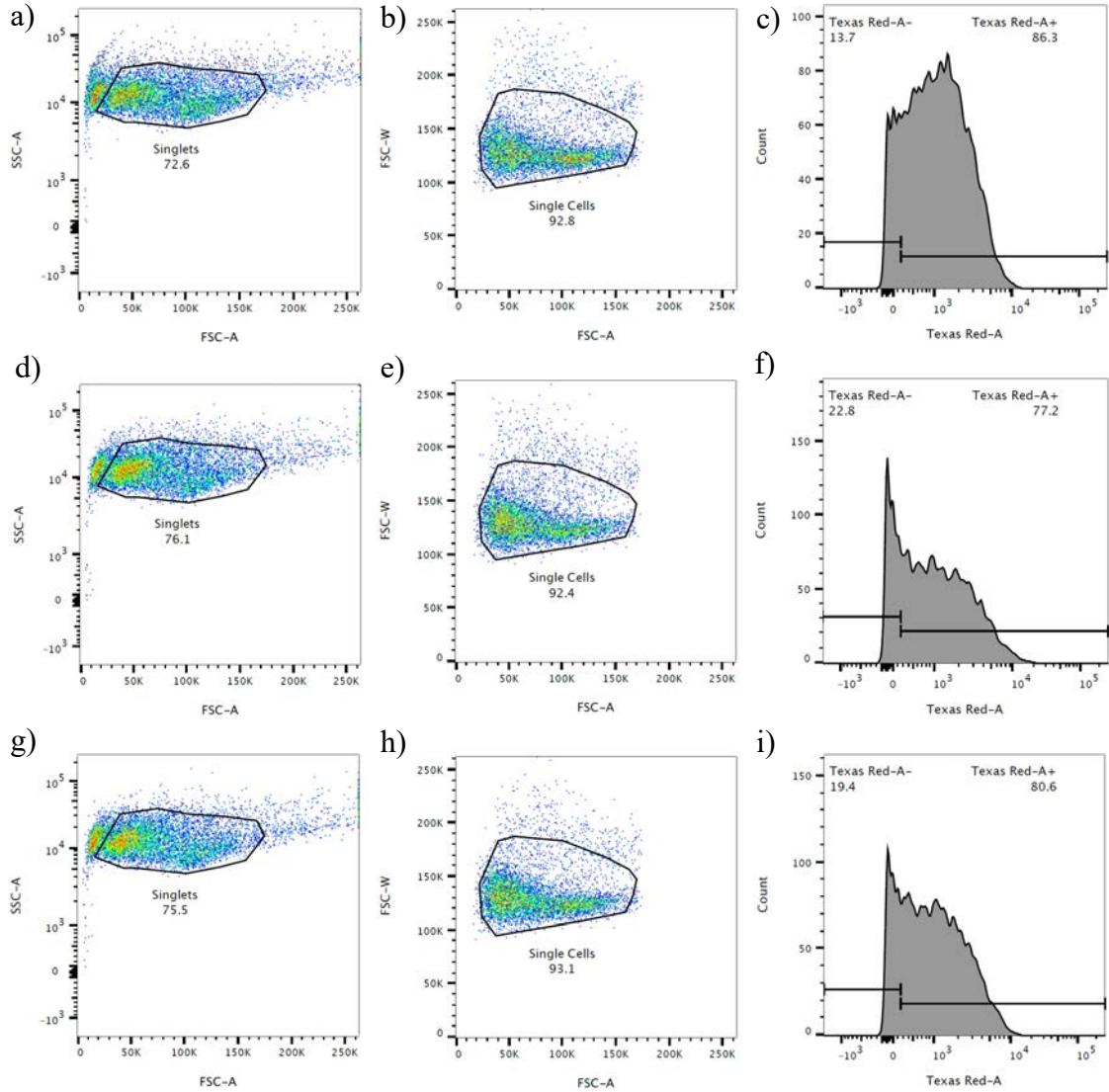


Figure A.4. Flow cytometry data for a-c) untreated, d-f) serum-treated, and g-i) BALF-treated 500 nm CML particles exposed to A549 cells.

## References

1. Ferkol, T.; Schraufnagel, D., The global burden of respiratory disease. *Annals of the American Thoracic Society* **2014**, *11*, (3), 404-406.
2. Troeger, C.; Forouzanfar, M.; Rao, P. C.; Khalil, I.; Brown, A.; Swartz, S.; Fullman, N.; Mosser, J.; Thompson, R. L.; Reiner, R. C., Jr.; Abajobir, A.; Alam, N.; Alemayohu, M. A.; Amare, A. T.; Antonio, C. A.; Asayesh, H.; Avokpaho, E.; Barac, A.; Beshir, M. A.; Boneya, D. J.; Brauer, M.; Dandona, L.; Dandona, R.; Fitchett, J. R. A.; Gebrehiwot, T. T.; Hailu, G. B.; Hotez, P. J.; Kasaeian, A.; Khoja, T.; Kisosoon, N.; Knibbs, L.; Kumar, G. A.; Rai, R. K.; El Razek, H. M. A.; Mohammed, M. S. K.; Nielson, K.; Oren, E.; Osman, A.; Patton, G.; Qorbani, M.; Roba, H. S.; Sartorius, B.; Savic, M.; Shigematsu, M.; Sykes, B.; Swaminathan, S.; Topor-Madry, R.; Ukwaja, K.; Werdecker, A.; Yonemoto, N.; El Sayed Zaki, M.; Lim, S. S.; Naghavi, M.; Vos, T.; Hay, S. I.; Murray, C. J. L.; Mokdad, A. H., Estimates of the global, regional, and national morbidity, mortality, and aetiologies of lower respiratory tract infections in 195 countries: a systematic analysis for the Global Burden of Disease Study 2015. *The Lancet Infectious Diseases* **2017**, *17*, (11), 1133-1161.
3. Cohen, A. J.; Anderson, H. R.; Ostro, B.; Pandey, K. D.; Krzyzanowski, M.; Künzli, N.; Gutschmidt, K.; III, C. A. P.; Romieu, I.; Samet, J. M.; Smith, K. R. *Chapter 17: Urban Air Pollution*; World Health Organization: World Health Organization, 2004; p 81.
4. Robinson, B. M., Malignant pleural mesothelioma: an epidemiological perspective. *Annals of Cardiothoracic Surgery* **2012**, *1*, (4), 491-496.
5. Castranova, V.; Vallyathan, V., Silicosis and coal workers' pneumoconiosis. *Environmental Health Perspectives* **2000**, *108*, (Suppl 4), 675-684.
6. Kreiss, K.; Gomaa, A.; Kullman, G.; Fedan, K.; Simoes, E. J.; Enright, P. L., Clinical bronchiolitis obliterans in workers at a microwave-popcorn plant. *The New England journal of medicine* **2002**, *347*, (5), 330-8.
7. Grigg, J.; Walters, H.; Sohal, S. S.; Wood-Baker, R.; Reid, D. W.; Xu, C.-B.; Edwinsson, L.; Morissette, M. C.; Stampfli, M. R.; Kirwan, M.; Koh, L.; Suri, R.; Mushtaq, N., Cigarette smoke and platelet-activating factor receptor dependent adhesion of *Streptococcus pneumoniae* to lower airway cells. *Respiratory Infections* **2012**, *67*, 908-913.
8. Mushtaq, N.; Ezzati, M.; Hall, L.; Dickson, I.; Kirwan, M.; Png, K. M. Y.; Mudway, I. S.; Grigg, J., Adhesion of *Streptococcus pneumoniae* to human airway epithelial cells exposed to urban particulate matter. *Journal of Allergy and Clinical Immunology* **2011**, *127*, 1236-1242.
9. Miyashita, L.; Suri, R.; Dearing, E.; Mudway, I.; Dove, Rosamund E.; Neill, D. R.; Van Zyl-Smit, R.; Kadioglu, A.; Grigg, J., E-cigarette vapour enhances pneumococcal adherence to airway epithelial cells. *European Respiratory Journal* **2018**, *51*, (2).
10. Mushtaq, N.; Ezzati, M.; Hall, L.; Dickson, I.; Kirwan, M.; Png, K. M. Y.; Mudway, I. S.; Grigg, J., Adhesion of *Streptococcus pneumoniae* to human airway epithelial cells exposed to urban particulate matter. *Journal of Allergy and Clinical Immunology* **2011**, *127*, (5), 1236-1242.e2.

11. Grigg, J.; Walters, H.; Sohal, S. S.; Wood-Baker, R.; Reid, D. W.; Xu, C.-B.; Edvinsson, L.; Morissette, M. C.; Stämpfli, M. R.; Kirwan, M.; Koh, L.; Suri, R.; Mushtaq, N., Cigarette smoke and platelet-activating factor receptor dependent adhesion of *Streptococcus pneumoniae* to lower airway cells. *Thorax* **2012**, *67*, (10), 908-913.
12. FDA, Approval Package for NDA 50-753 (TOBI). In Research, C. F. D. E. A., Ed. FDA, 1997.
13. FDA, FDA Briefing Document: Ciprofloxacin Dispersion for Inhalation (DI) Meeting of the Antimicrobial Drugs Advisory Committee (AMDAC). In Committee, A.-I. D. A., Ed. 2018.
14. Weibel, E. R.; Gomez, D. M., Architecture of the human lung. Use of quantitative methods establishes fundamental relations between size and number of lung structures **1962**, *137*, (3530), 577-585.
15. Frohlich, E., The role of surface charge in cellular uptake and cytotoxicity of medical nanoparticles. *International Journal of Nanomedicine* **2012**, *7*, 5577-5591.
16. Patton, J. S.; Byron, P. R., Inhaling medicines: delivering drugs to the body through the lungs. *Nature Reviews Drug Discovery* **2007**, *6*, 67.
17. Lai, S. K.; Wang, Y. Y.; Wirtz, D.; Hanes, J., Micro- and macrorheology of mucus. *Advanced Drug Delivery Reviews* **2009**, *61*, (2), 86-100.
18. Forbes, I. I., Human airway epithelial cell lines for in vitro drug transport and metabolism studies. *Pharmaceutical science & technology today* **2000**, *3*, (1), 18-27.
19. Irwin, R. S.; Augustyn, N.; French, C. T.; Rice, J.; Tedeschi, V.; Welch, S. J., Spread the word about the journal in 2013. *CHEST* **2013**, *143*, (1), 1-4.
20. Hinds, W. C., *Aerosol Technology: Properties, Behavior, and Measurement of Airborne Particles*. 2nd ed.; Wiley: 1999.
21. Patton, J. S.; Brain, J. D.; Davies, L. A.; Fiegel, J.; Gumbleton, M.; Kim, K.-J.; Sakagami, M.; Vanbever, R.; Ehrhardt, C., The particle has landed-characterizing the fate of inhaled pharmaceuticals. *Journal of Aerosol Medicine and Pulmonary Drug Delivery* **2010**, *23*, S71-S87.
22. Wert, S. E.; Whitsett, J. A.; Noguee, L. M., genetic disorders of surfactant dysfunction. *Pediatric and developmental pathology : the official journal of the Society for Pediatric Pathology and the Paediatric Pathology Society* **2009**, *12*, (4), 253-274.
23. Bell, D. Y.; Haseman, J. A.; Spock, A.; McLennan, G.; Hook, G. E., Plasma proteins of the bronchoalveolar surface of the lungs of smokers and nonsmokers. *The American review of respiratory disease* **1981**, *124*, (1), 72-9.
24. Wattiez, R.; Hermans, C.; Bernard, A.; Lesur, O.; Falmagne, P., Human bronchoalveolar lavage fluid: Two-dimensional gel electrophoresis, amino acid microsequencing and identification of major proteins. *ELECTROPHORESIS* **1999**, *20*, (7), 1634-1645.
25. Wattiez, R.; Falmagne, P., Proteomics of bronchoalveolar lavage fluid. *Journal of chromatography. B, Analytical technologies in the biomedical and life sciences* **2005**, *815*, (1-2), 169-78.
26. Chen, J.; Ryu, S.; Gharib, S. A.; Goodlett, D. R.; Schnapp, L. M., Exploration of the normal human bronchoalveolar lavage fluid proteome. *PROTEOMICS – Clinical Applications* **2008**, *2*, (4), 585-595.
27. Bowden, D. H., The alveolar macrophage. *Environmental health perspectives* **1984**, *55*, 327-341.

28. Koval, M., Tight junctions, but not too tight: fine control of lung permeability by claudins. *American journal of physiology. Lung cellular and molecular physiology* **2009**, 297, (2), L217-L218.
29. Gonda, I., Aerosols for delivery of therapeutic and diagnostic agents to the respiratory tract. *Critical reviews in therapeutic drug carrier systems* **1990**, 6, (4), 273-313.
30. Oberdörster, G.; Ferin, J.; Lehnert, B. E., Correlation between particle size, in vivo particle persistence, and lung injury. *Environmental health perspectives* **1994**, 102 Suppl 5, (Suppl 5), 173-179.
31. Davalos-Pantoja, L.; Ortega-Vinuesa, J. L.; Bastos-Gonzalez, D.; Hidalgo-Alvarez, R., Colloidal stability of IgG- and IgY-coated latex microspheres. *Colloids and surfaces. B, Biointerfaces* **2001**, 20, (2), 165-175.
32. Missana, T.; Adell, A., On the applicability of DLVO theory to the prediction of clay colloids stability. *Journal of Colloid and Interface Science* **2000**, 230, (1), 150-156.
33. Derjaguin, B.; Landau, L., Theory of the stability of strongly charged lyophobic sols and of the adhesion of strongly charged particles in solution of electrolytes. *Acta Physicochimica USSR* **1941**, 14, 29.
34. Verwey, E. J. W., Theory of the stability of lyophobic colloids. *The Journal of Physical and Colloid Chemistry* **1947**, 51, (3), 631-636.
35. Margenau, H., Van der waals forces. *Reviews of Modern Physics* **1939**, 11, (1), 1-35.
36. Moore, T. L.; Rodriguez-Lorenzo, L.; Hirsch, V.; Balog, S.; Urban, D.; Jud, C.; Rothen-Rutishauser, B.; Lattuada, M.; Petri-Fink, A., Nanoparticle colloidal stability in cell culture media and impact on cellular interactions. *Chemical Society Reviews* **2015**, 44, (17), 6287-6305.
37. Sharma, A.; Tan, S. N.; Walz, J. Y., Measurement of colloidal stability in solutions of simple, nonadsorbing polyelectrolytes. *Journal of Colloid and Interface Science* **1997**, 190, (2), 392-407.
38. Herrera, A. P.; Barrera, C.; Zayas, Y.; Rinaldi, C., Monitoring colloidal stability of polymer-coated magnetic nanoparticles using AC susceptibility measurements. *Journal of Colloid and Interface Science* **2010**, 342, (2), 540-9.
39. Lazzari, S.; Moscatelli, D.; Codari, F.; Salmona, M.; Morbidelli, M.; Diomede, L., Colloidal stability of polymeric nanoparticles in biological fluids. *Journal of nanoparticle research : an interdisciplinary forum for nanoscale science and technology* **2012**, 14, (6), 920-920.
40. Matusiak, J.; Grządka, E., Stability of colloidal systems-a review of the stability measurements methods. 2017; Vol. LXXII, p 33-45.
41. Abarca, C.; Ali, M. M.; Yang, S.; Dong, X.; Pelton, R. H., A Colloidal Stability Assay Suitable for High-Throughput Screening. *Analytical Chemistry* **2016**, 88, (5), 2929-2936.
42. Lynch, I.; Salvati, A.; Dawson, K. A., Protein-nanoparticle interactions: What does the cell see? *Nature Nanotechnol.* **2009**, 4, (9), 546-547.
43. Carrillo-Conde, B. R.; Ramer-Tait, A. E.; Wannemuehler, M. J.; Narasimhan, B., Chemistry-dependent adsorption of serum proteins onto polyanhydride microparticles differentially influences dendritic cell uptake and activation. *Acta Biomaterialia* **2012**, 8, (10), 3618-3628.

44. Vllasaliu, D.; Fowler, R.; Stolnik, S., PEGylated nanomedicines: recent progress and remaining concerns. *Expert Opinion on Drug Delivery* **2014**, *11*, (1), 139-154.
45. Rausch, K.; Reuter, A.; Fischer, K.; Schmidt, M., Evaluation of nanoparticle aggregation in human blood serum. *Biomacromolecules* **2010**, *11*, (11), 2836-2839.
46. Zhang, Z.; Zhang, M.; Chen, S.; Horbett, T. A.; Ratner, B. D.; Jiang, S., Blood compatibility of surfaces with superlow protein adsorption. *Biomaterials* **2008**, *29*, (32), 4285-91.
47. Bertrand, N.; Leroux, J. C., The journey of a drug-carrier in the body: an anatomo-physiological perspective. *Journal of Controlled Release* **2012**, *161*, (2), 152-63.
48. Alexis, F.; Pridgen, E.; Molnar, L. K.; Farokhzad, O. C., Factors affecting the clearance and biodistribution of polymeric nanoparticles. *Molecular Pharmaceutics* **2008**, *5*, (4), 505-515.
49. Davy, K. P.; Seals, D. R., Total blood volume in healthy young and older men. *Journal of applied physiology (Bethesda, Md. : 1985)* **1994**, *76*, (5), 2059-62.
50. Cedervall, T.; Lynch, I.; Foy, M.; Berggård, T.; Donnelly, S. C.; Cagney, G.; Linse, S.; Dawson, K. A., Detailed identification of plasma proteins adsorbed on copolymer nanoparticles. *Angewandte Chemie International Edition* **2007**, *46*, (30), 5754-5756.
51. Lynch, I.; Cedervall, T.; Lundqvist, M.; Cabaleiro-Lago, C.; Linse, S.; Dawson, K. A., The nanoparticle - protein complex as a biological entity; a complex fluids and surface science challenge for the 21st century. *Advances in Colloid and Interface Science* **2007**, *134-35*, 167-174.
52. Dawson, M.; Krauland, E.; Wirtz, D.; Hanes, J., Transport of polymeric nanoparticle gene carriers in gastric mucus. *Biotechnology Progress* **2004**, *20*, (3), 851-857.
53. Lynch, I.; Dawson, K. A., Protein-nanoparticle interactions. *Nano Today* **2008**, *3*, (1-2), 40-47.
54. Stebounova, L. V.; Guio, E.; Grassian, V. H., Silver nanoparticles in simulated biological media: a study of aggregation, sedimentation, and dissolution. *Journal of Nanoparticle Research* **2011**, *13*, (1), 233-244.
55. Walkey, C. D.; Olsen, J. B.; Song, F.; Liu, R.; Guo, H.; Olsen, D. W. H.; Cohen, Y.; Emili, A.; Chan, W. C. W., Protein corona fingerprinting predicts the cellular interaction of gold and silver nanoparticles. *ACS Nano* **2014**, *8*, (3), 2439-2455.
56. Albanese, A.; Chan, W. C. W., Effect of gold nanoparticle aggregation on cell uptake and toxicity. *ACS Nano* **2011**, *5*, (7), 5478-5489.
57. Mohr, K.; Sommer, M.; Baier, G.; Schottler, S.; Okwieka, P.; Tenzer, S.; Landfester, K.; Mailander, V.; Schmidt, M.; Meyer, R. G., Aggregation behavior of polystyrene-nanoparticles in human blood serum and its impact on the *in vivo* distribution in mice. *Journal of Nanomedicine & Nanotechnology* **2014**, (2), 1.
58. Malcolm, D. W.; Varghese, J. J.; Sorrells, J. E.; Ovitt, C. E.; Benoit, D. S. W., The effects of biological fluids on colloidal stability and siRNA delivery of a pH-responsive micellar nanoparticle delivery system. *ACS Nano* **2018**, *12*, (1), 187-197.

59. Müller, L. K.; Simon, J.; Rosenauer, C.; Mailänder, V.; Morsbach, S.; Landfester, K., The transferability from animal models to humans: Challenges regarding aggregation and protein corona formation of nanoparticles. *Biomacromolecules* **2018**, *19*, (2), 374-385.
60. Nuhn, L.; Gietzen, S.; Mohr, K.; Fischer, K.; Toh, K.; Miyata, K.; Matsumoto, Y.; Kataoka, K.; Schmidt, M.; Zentel, R., Aggregation behavior of cationic nanohydrogel particles in human blood serum. *Biomacromolecules* **2014**, *15*, (4), 1526-1533.
61. Kelsch, A.; Tomcin, S.; Rausch, K.; Barz, M.; Mailänder, V.; Schmidt, M.; Landfester, K.; Zentel, R., HPMA Copolymers as surfactants in the preparation of biocompatible nanoparticles for biomedical application. *Biomacromolecules* **2012**, *13*, (12), 4179-4187.
62. Hemmelmann, M.; Mohr, K.; Fischer, K.; Zentel, R.; Schmidt, M., Interaction of pHPMA-pLMA copolymers with human blood serum and its components. *Molecular Pharmaceutics* **2013**, *10*, (10), 3769-3775.
63. Ehrenberg, M. S.; Friedman, A. E.; Finkelstein, J. N.; Oberdorster, G.; McGrath, J. L., The influence of protein adsorption on nanoparticle association with cultured endothelial cells. *Biomaterials* **2009**, *30*, (4), 603-610.
64. Hu, S.; Loo, J. A.; Wong, D. T., Human body fluid proteome analysis. *Proteomics* **2006**, *6*, (23), 6326-53.
65. Galisteo-González, F.; Puig, J.; Martín-Rodríguez, A.; Serra-Domènech, J.; Hidalgo-Alvarez, R., Influence of electrostatic forces on IgG adsorption onto polystyrene beads. *Colloids and Surfaces B: Biointerfaces* **1994**, *2*, (4), 435-441.
66. Meder, F.; Brandes, C.; Treccani, L.; Rezwani, K., Controlling protein-particle adsorption by surface tailoring colloidal alumina particles with sulfonate groups. *Acta Biomaterialia* **2013**, *9*, (3), 5780-5787.
67. Rowe, G. E.; Margaritis, A.; Lan, Q.; Bassi, A. S.; Zhu, J. X., A new kinetic model of protein adsorption on suspended anion-exchange resin particles. *Biotechnology and Bioengineering* **1999**, *65*, (6), 613-621.
68. Gun'ko, V. M.; Mikhailova, I. V.; Zarko, V. I.; Gerashchenko, II; Guzenko, N. V.; Janusz, W.; Lebeda, R.; Chibowski, S., Study of interaction of proteins with fumed silica in aqueous suspensions by adsorption and photon correlation spectroscopy methods. *Journal of Colloids and Interface Science* **2003**, *260*, (1), 56-69.
69. Yoshimoto, K.; Hirase, T.; Madsen, J.; Armes, S. P.; Nagasaki, Y., Non-Fouling character of poly[2-(methacryloyloxy)ethyl phosphorylcholine]-modified gold surfaces fabricated by the 'grafting to' method: Comparison of its protein resistance with poly(ethylene glycol)-modified gold surfaces. *Macromolecular Rapid Communications* **2009**, *30*, (24), 2136-2140.
70. Baier, G.; Costa, C.; Zeller, A.; Baumann, D.; Sayer, C.; Araujo, P. H. H.; Mailänder, V.; Musyanovych, A.; Landfester, K., BSA adsorption on differently charged polystyrene nanoparticles using isothermal titration calorimetry and the influence on cellular uptake. *Macromolecular Bioscience* **2011**, *11*, (5), 628-638.
71. Schulze, C.; Schaefer, U. F.; Ruge, C. A.; Wohlleben, W.; Lehr, C. M., Interaction of metal oxide nanoparticles with lung surfactant protein A. *European Journal of Pharmaceutics and Biopharmaceutics* **2011**, *77*, (3), 376-83.



72. Tsai, D.-H.; DelRio, F. W.; Keene, A. M.; Tyner, K. M.; MacCuspie, R. I.; Cho, T. J.; Zachariah, M. R.; Hackley, V. A., Adsorption and conformation of serum albumin protein on gold nanoparticles investigated using dimensional measurements and in situ spectroscopic methods. *Langmuir* **2011**, *27*, (6), 2464-2477.
73. Huang, R.; Carney, R. P.; Stellacci, F.; Lau, B. L. T., Protein-nanoparticle interactions: the effects of surface compositional and structural heterogeneity are scale dependent. *Nanoscale* **2013**, *5*, (15), 6928-6935.
74. Wang, A.; Vo, T.; Le, V.; Fitzkee, N. C., Using hydrogen–deuterium exchange to monitor protein structure in the presence of gold nanoparticles. *The Journal of Physical Chemistry B* **2014**, *118*, (49), 14148-14156.
75. Wang, A.; Vangala, K.; Vo, T.; Zhang, D.; Fitzkee, N. C., A three-step model for protein–gold nanoparticle adsorption. *The Journal of Physical Chemistry C* **2014**, *118*, (15), 8134-8142.
76. Wang, A.; Perera, Y. R.; Davidson, M. B.; Fitzkee, N. C., Electrostatic interactions and protein competition reveal a dynamic surface in gold nanoparticle-protein adsorption. *The journal of physical chemistry. C, Nanomaterials and interfaces* **2016**, *120*, (42), 24231-24239.
77. Givens, B. E.; Xu, Z.; Fiegel, J.; Grassian, V. H., Bovine serum albumin adsorption on SiO<sub>2</sub> and TiO<sub>2</sub> nanoparticle surfaces at circumneutral and acidic pH: A tale of two nano-bio surface interactions. *Journal of Colloid and Interface Science* **2017**, *493*, 334-341.
78. van Vlerken, L. E.; Vyas, T. K.; Amiji, M. M., Poly(ethylene glycol)-modified nanocarriers for tumor-targeted and intracellular delivery. *Pharm Res* **2007**, *24*, (8), 1405-14.
79. Gref, R.; Luck, M.; Quellec, P.; Marchand, M.; Dellacherie, E.; Harnisch, S.; Blunk, T.; Muller, R. H., 'Stealth' corona-core nanoparticles surface modified by polyethylene glycol (PEG): influences of the corona (PEG chain length and surface density) and of the core composition on phagocytic uptake and plasma protein adsorption. *Colloids and Surfaces B-Biointerfaces* **2000**, *18*, (3-4), 301-313.
80. Abuchowski, A.; McCoy, J. R.; Palczuk, N. C.; van Es, T.; Davis, F. F., Effect of covalent attachment of polyethylene glycol on immunogenicity and circulating life of bovine liver catalase. *Journal of Biological Chemistry* **1977**, *252*, (11), 3582-6.
81. Zhang, P.; Sun, F.; Liu, S.; Jiang, S., Anti-PEG antibodies in the clinic: Current issues and beyond PEGylation. *Journal of controlled release : official journal of the Controlled Release Society* **2016**, *244*, (Pt B), 184-193.
82. Grenier, P.; Viana, I. M. d. O.; Lima, E. M.; Bertrand, N., Anti-polyethylene glycol antibodies alter the protein corona deposited on nanoparticles and the physiological pathways regulating their fate in vivo. *Journal of Controlled Release* **2018**, *287*, 121-131.
83. Murphy, K. P.; Travers, P.; Walport, M.; Janeway, C., *Janeway's Immunobiology*. Garland Science: New York, 2012.
84. Kane, R. S.; Deschatelets, P.; Whitesides, G. M., Kosmotropes form the basis of protein-resistant surfaces. *Langmuir* **2003**, *19*, (6), 2388-2391.
85. Nowinski, A. K.; White, A. D.; Keefe, A. J.; Jiang, S., Biologically inspired stealth peptide-capped gold nanoparticles. *Langmuir* **2014**, *30*, (7), 1864-1870.

86. Shao, Q.; He, Y.; White, A. D.; Jiang, S., Different effects of zwitterion and ethylene glycol on proteins. *The Journal of Chemical Physics* **2012**, *136*, (22), 225101.
87. Shao, Q.; Jiang, S., Molecular understanding and design of zwitterionic materials. *Advanced Materials* **2015**, *27*, (1), 15-26.
88. Sundaram, H. S.; Han, X.; Nowinski, A. K.; Brault, N. D.; Li, Y.; Ella-Menye, J. R.; Amoaka, K. A.; Cook, K. E.; Marek, P.; Senecal, K.; Jiang, S., Achieving one-step surface coating of highly hydrophilic poly(carboxybetaine methacrylate) polymers on hydrophobic and hydrophilic surfaces. *Advanced Material Interfaces* **2014**, *1*, (6), n/a.
89. Zhang, L.; Cao, Z.; Bai, T.; Carr, L.; Ella-Menye, J. R.; Irvin, C.; Ratner, B. D.; Jiang, S., Zwitterionic hydrogels implanted in mice resist the foreign-body reaction. *Nature Biotechnology* **2013**, *31*, (6), 553-6.
90. Zhou, W.; Shao, J.; Jin, Q.; Wei, Q.; Tang, J.; Ji, J., Zwitterionic phosphorylcholine as a better ligand for gold nanorods cell uptake and selective photothermal ablation of cancer cells. *Chemistry Communications (Cambridge)* **2010**, *46*, (9), 1479-81.
91. Bai, J.; Wang, T. T.; Wang, Y. C.; Jiang, X. E., Effects of nanoparticle surface ligands on protein adsorption and subsequent cytotoxicity. *Biomaterials Science* **2014**, *2*, (4), 493-501.
92. Schlenoff, J. B., Zwitteration: Coating surfaces with zwitterionic functionality to reduce nonspecific adsorption. *Langmuir* **2014**, *30*, (32), 9625-9636.
93. Laughlin, R. G., Fundamentals of the zwitterionic hydrophilic group. *Langmuir* **1991**, *7*, (5), 842-847.
94. Young, G.; Bowers, R.; Hall, B.; Port, M., Clinical comparison of Omaficon A with four control materials. *The CLAO journal : official publication of the Contact Lens Association of Ophthalmologists, Inc* **1997**, *23*, (4), 249-58.
95. Salvage, J. P.; Smith, T.; Lu, T.; Sanghera, A.; Standen, G.; Tang, Y.; Lewis, A. L., Synthesis, characterisation, and in vitro cellular uptake kinetics of nanoprecipitated poly(2-methacryloyloxyethyl phosphorylcholine)-b-poly(2-(diisopropylamino)ethyl methacrylate) (MPC-DPA) polymeric nanoparticle micelles for nanomedicine applications. *Applied Nanoscience* **2016**, *6*, (7), 1073-1094.
96. Yusa, S.-i.; Fukuda, K.; Yamamoto, T.; Ishihara, K.; Morishima, Y., Synthesis of well-defined amphiphilic block copolymers having phospholipid polymer sequences as a novel biocompatible polymer micelle reagent. *Biomacromolecules* **2005**, *6*, (2), 663-670.
97. Cao, Z.; Zhang, L.; Jiang, S., Superhydrophilic zwitterionic polymers stabilize liposomes. *Langmuir* **2012**, *28*, (31), 11625-11632.
98. Leigh, B. L.; Cheng, E.; Xu, L.; Andresen, C.; Hansen, M. R.; Guymon, C. A., Photopolymerizable zwitterionic polymer patterns control cell adhesion and guide neural growth. *Biomacromolecules* **2017**, *18*, (8), 2389-2401.
99. Diaz Blanco, C.; Ortner, A.; Dimitrov, R.; Navarro, A.; Mendoza, E.; Tzanov, T., Building an antifouling zwitterionic coating on urinary catheters using an enzymatically triggered bottom-up approach. *ACS Applied Materials & Interfaces* **2014**, *6*, (14), 11385-11393.
100. Rücker, C.; Kümmerer, K., Environmental chemistry of organosiloxanes. *Chemical Reviews* **2015**, *115*, (1), 466-524.
101. Mojsiewicz-Pienkowska, K.; Krenczkowska, D., Evolution of consciousness of exposure to siloxanes-review of publications. *Chemosphere* **2018**, *191*, 204-217.

102. Wang, D.-G.; Norwood, W.; Alaei, M.; Byer, J. D.; Brimble, S., Review of recent advances in research on the toxicity, detection, occurrence and fate of cyclic volatile methyl siloxanes in the environment. *Chemosphere* **2013**, *93*, (5), 711-725.
103. Janecek, N. J.; Hansen, K. M.; Stanier, C. O., Comprehensive atmospheric modeling of reactive cyclic siloxanes and their oxidation products. *Atmospheric Chemistry and Physics Discussions* **2017**, 1-27.
104. Navea, J. G.; Young, M. A.; Xu, S.; Grassian, V. H.; Stanier, C. O., The atmospheric lifetimes and concentrations of cyclic methylsiloxanes octamethylcyclotetrasiloxane (D4) and decamethylcyclopentasiloxane (D5) and the influence of heterogeneous uptake. *Atmospheric Environment* **2011**, *45*, (18), 3181-3191.
105. Horii, Y.; Kannan, K., Survey of organosilicone compounds, including cyclic and linear siloxanes, in personal-care and household products. *Archives of Environmental Contamination and Toxicology* **2008**, *55*, (4), 701-10.
106. McDonald, B. C.; de Gouw, J. A.; Gilman, J. B.; Jathar, S. H.; Akherati, A.; Cappa, C. D.; Jimenez, J. L.; Lee-Taylor, J.; Hayes, P. L.; McKeen, S. A.; Cui, Y. Y.; Kim, S.-W.; Gentner, D. R.; Isaacman-VanWertz, G.; Goldstein, A. H.; Harley, R. A.; Frost, G. J.; Roberts, J. M.; Ryerson, T. B.; Trainer, M., Volatile chemical products emerging as largest petrochemical source of urban organic emissions. *Science* **2018**, *359*, (6377), 760-764.
107. Tang, X.; Misztal, P. K.; Nazaroff, W. W.; Goldstein, A. H., Siloxanes Are the Most Abundant Volatile Organic Compound Emitted from Engineering Students in a Classroom. *Environmental Science & Technology Letters* **2015**, *2*, (11), 303-307.
108. Johnson, W., Jr.; Bergfeld, W. F.; Belsito, D. V.; Hill, R. A.; Klaassen, C. D.; Liebler, D. C.; Marks, J. G., Jr.; Shank, R. C.; Slaga, T. J.; Snyder, P. W.; Andersen, F. A., Safety assessment of cyclomethicone, cyclotetrasiloxane, cyclopentasiloxane, cyclohexasiloxane, and cycloheptasiloxane. *International Journal of Toxicology* **2011**, *30*, (6 Suppl), 149S-227S.
109. SCCS, Opinion on cyclomethicone octamethylcyclotetrasiloxane (cyclotetrasiloxane, D4) and decamethylcyclopentasiloxane (cyclopentasiloxane, D5). **2010**.
110. Xu, L.; Shi, Y.; Wang, T.; Dong, Z.; Su, W.; Cai, Y., Methyl siloxanes in environmental matrices around a siloxane production facility, and their distribution and elimination in plasma of exposed population. *Environmental Science & Technology* **2012**, *46*, (21), 11718-11726.
111. Reddy, M. B.; Dobrev, I. D.; McNett, D. A.; Tobin, J. M.; Utell, M. J.; Morrow, P. E.; Domoradzki, J. Y.; Plotzke, K. P.; Andersen, M. E., Inhalation dosimetry modeling with decamethylcyclopentasiloxane in rats and humans. *Toxicological Sciences* **2008**, *105*, (2), 275-285.
112. Rowe, V. K.; Spencer, H. C.; Bass, S. L., Toxicological studies on certain commercial silicones and hydrolyzable silane intermediates. *Journal of Industrial Hygiene and Toxicology* **1948**, *30*, (6), 332-52.
113. Albanus, L.; Björklund, N. E.; Gustafsson, B.; Jönsson, M., Forty days oral toxicity of 2,6-cis-diphenylhexamethylcyclotetrasiloxane (KABI 1774) in beagle dogs with special reference to effects on the male reproductive system. *Acta Pharmacologica et Toxicologica* **1975**, *36*, (s3), 93-130.

114. Atkinson, R., Kinetics of the gas-phase reactions of a series of organosilicon compounds with hydroxyl and nitrate(NO<sub>3</sub>) radicals and ozone at 297 ± 2 K. *Environmental Science & Technology* **1991**, *25*, (5), 863-866.
115. Sommerlade, R.; Parlar, H.; Wrobel, D.; Kochs, P., Product analysis and kinetics of the gas-phase reactions of selected organosilicon compounds with OH radicals using a smog chamber-mass spectrometer system. *Environmental Science & Technology* **1993**, *27*, (12), 2435-2440.
116. Wu, Y.; Johnston, M. V., Molecular characterization of secondary Aerosol from oxidation of cyclic methylsiloxanes. *Journal of The American Society for Mass Spectrometry* **2016**, *27*, (3), 402-409.
117. Wu, Y.; Johnston, M. V., Aerosol formation from OH oxidation of the volatile cyclic methyl siloxane (cVMS) decamethylcyclopentasiloxane. *Environmental Science & Technology* **2017**, *51*, (8), 4445-4451.
118. Bzdek, B. R.; Horan, A. J.; Pennington, M. R.; Janecek, N. J.; Baek, J.; Stanier, C. O.; Johnston, M. V., Silicon is a frequent component of atmospheric nanoparticles. *Environmental Science & Technology* **2014**, *48*, (19), 11137-11145.
119. Yucuis, R. A.; Stanier, C. O.; Hornbuckle, K. C., Cyclic siloxanes in air, including identification of high levels in Chicago and distinct diurnal variation. *Chemosphere* **2013**, *92*, (8), 905-910.
120. Genualdi, S.; Harner, T.; Cheng, Y.; MacLeod, M.; Hansen, K. M.; van Egmond, R.; Shoeib, M.; Lee, S. C., Global distribution of linear and cyclic volatile methyl siloxanes in air. *Environmental Science & Technology* **2011**, *45*, (8), 3349-3354.
121. Xu, S.; Wania, F., Chemical fate, latitudinal distribution and long-range transport of cyclic volatile methylsiloxanes in the global environment: A modeling assessment. *Chemosphere* **2013**, *93*, (5), 835-843.
122. Janecek, N. J.; Hansen, K. M.; Stanier, C. O., Comprehensive atmospheric modeling of reactive cyclic siloxanes and their oxidation products. *Atmospheric Chemistry and Physics* **2017**, *17*, (13), 8357-8370.
123. McLachlan, M. S.; Kierkegaard, A.; Hansen, K. M.; van Egmond, R.; Christensen, J. H.; Skjøth, C. A., Concentrations and fate of decamethylcyclopentasiloxane (D5) in the atmosphere. *Environmental Science & Technology* **2010**, *44*, (14), 5365-5370.
124. Xiao, R.; Zammit, I.; Wei, Z.; Hu, W.-P.; MacLeod, M.; Spinney, R., Kinetics and mechanism of the oxidation of cyclic methylsiloxanes by hydroxyl radical in the gas phase: an experimental and theoretical study. *Environmental Science & Technology* **2015**, *49*, (22), 13322-13330.
125. Chandramouli, B.; Kamens, R., The photochemical formation and gas-particle partitioning of oxidation products of decamethyl cyclopentasiloxane and decamethyl tetrasiloxane in the atmosphere. *Atmospheric Environment* **2001**, *35*, 87-95.
126. Latimer, H. K.; Kamens, R. M.; Chandra, G., The atmospheric partitioning of decamethylcyclopentasiloxane (D5) and 1-hydroxynonamethylcyclopentasiloxane (D4TOH) on different types of atmospheric particles. *Chemosphere* **1998**, *36*, (10), 2401-2414.

127. Navea, J.; Xu, S.; Stanier, C.; A. Young, M.; H. Grassian, V., Heterogeneous uptake of octamethylcyclotetrasiloxane (D4) and decamethylcyclopentasiloxane (D5) onto mineral dust aerosol under variable RH conditions. *Atmospheric Environment* **2009**, *43*, 4060-4069.
128. Whelan, M. J.; Estrada, E.; van Egmond, R., A modelling assessment of the atmospheric fate of volatile methyl siloxanes and their reaction products. *Chemosphere* **2004**, *57*, (10), 1427-1437.
129. Holder, A. L.; Carter, B. J.; Goth-Goldstein, R.; Lucas, D.; Koshland, C. P., Increased cytotoxicity of oxidized flame soot. *Atmospheric Pollution Research* **2012**, *3*, (1), 25-31.
130. Li, Q.; Shang, J.; Zhu, T., Physicochemical characteristics and toxic effects of ozone-oxidized black carbon particles. *Atmospheric Environment* **2013**, *81*, 68-75.
131. Lambe, A. T.; Ahern, A. T.; Williams, L. R.; Slowik, J. G.; Wong, J. P. S.; Abbatt, J. P. D.; Brune, W. H.; Ng, N. L.; Wright, J. P.; Croasdale, D. R.; Worsnop, D. R.; Davidovits, P.; Onasch, T. B., Characterization of aerosol photooxidation flow reactors: heterogeneous oxidation, secondary organic aerosol formation and cloud condensation nuclei activity measurements. *Atmospheric Measurement Techniques* **2011**, *4*, (3), 445-461.
132. Balharry, D.; Sexton, K.; Bérubé, K. A., An in vitro approach to assess the toxicity of inhaled tobacco smoke components: Nicotine, cadmium, formaldehyde and urethane. *Toxicology* **2008**, *244*, (1), 66-76.
133. Wu, J.; Wang, Y.; Liu, G.; Jia, Y.; Yang, J.; Shi, J.; Dong, J.; Wei, J.; Liu, X., Characterization of air-liquid interface culture of A549 alveolar epithelial cells. *Brazilian Journal of Medical and Biological Research* **2018**, *51*, (2), e6950.
134. Fiegel, J.; Ehrhardt, C.; Schaefer, U. F.; Lehr, C.-M.; Hanes, J., Large porous particle impingement on lung epithelial cell monolayers - Toward improved particle characterization in the lung. *Pharm. Res.* **2003**, *20*, 788-796.
135. Kang, E.; Root, M. J.; Toohey, D. W.; Brune, W. H., Introducing the concept of Potential Aerosol Mass (PAM). *Atmospheric Chemistry and Physics* **2007**, *7*, (22), 5727-5744.
136. Kang, E.; Toohey, D. W.; Brune, W. H., Dependence of SOA oxidation on organic aerosol mass concentration and OH exposure: experimental PAM chamber studies. *Atmos. Chem. Phys.* **2011**, *11*, (4), 1837-1852.
137. Leith, D.; Miller-Lionberg, D.; Casuccio, G.; Lersch, T.; Lentz, H.; Marchese, A.; Volckens, J., Development of a transfer function for a personal, thermophoretic nanoparticle sampler. *Aerosol Science And Technology* **2014**, *48*, (1), 81-89.
138. Loret, T.; Peyret, E.; Dubreuil, M.; Aguerre-Chariol, O.; Bressot, C.; le Bihan, O.; Amodeo, T.; Trouiller, B.; Braun, A.; Egles, C.; Lacroix, G., Air-liquid interface exposure to aerosols of poorly soluble nanomaterials induces different biological activation levels compared to exposure to suspensions. *Particle and Fibre Toxicology* **2016**, *13*, (1), 58.
139. Chortarea, S.; Clift, M. J. D.; Vanhecke, D.; Endes, C.; Wick, P.; Petri-Fink, A.; Rothen-Rutishauser, B., Repeated exposure to carbon nanotube-based aerosols does not affect the functional properties of a 3D human epithelial airway model. *Nanotoxicology* **2015**, *9*, (8), 983-993.

140. Schneider, C. A.; Rasband, W. S.; Eliceiri, K. W., NIH Image to ImageJ: 25 years of image analysis. *Nature Methods* **2012**, *9*, 671.
141. Jing, X.; Park, J. H.; Peters, T. M.; Thorne, P. S., Toxicity of copper oxide nanoparticles in lung epithelial cells exposed at the air-liquid interface compared with in vivo assessment. *Toxicology In Vitro* **2015**, *29*, (3), 502-11.
142. Kim, J. S.; Peters, T. M.; O'Shaughnessy, P. T.; Adamcakova-Dodd, A.; Thorne, P. S., Validation of an in vitro exposure system for toxicity assessment of air-delivered nanomaterials. *Toxicology in Vitro* **2013**, *27*, (1), 164-173.
143. da Roza, R. A. *Particle size for greatest penetration of HEPA filters - and their true efficiency*; United States, 1982; p 17.
144. Phares, D. J.; Rhoads, K. P.; Johnston, M. V.; Wexler, A. S., Size-resolved ultrafine particle composition analysis 2. Houston. *Journal of Geophysical Research: Atmospheres* **2003**, *108*, (D7).
145. Alink, G. M.; de Boer, R. M.; Mol, J.; Temmink, J. H., Toxic effects of ozone on human cells in vitro, exposed by gas diffusion through teflon film. *Toxicology* **1980**, *17*, (2), 209-18.
146. Poma, A.; Colafarina, S.; Aruffo, E.; Zarivi, O.; Bonfigli, A.; Di Bucchianico, S.; Di Carlo, P., Effects of ozone exposure on human epithelial adenocarcinoma and normal fibroblasts cells. *PLOS ONE* **2017**, *12*, (9), e0184519.
147. Uhlson, C.; Harrison, K.; Allen, C. B.; Ahmad, S.; White, C. W.; Murphy, R. C., Oxidized phospholipids derived from ozone-treated lung surfactant extract reduce macrophage and epithelial cell viability. *Chemical Research in Toxicology* **2002**, *15*, (7), 896-906.
148. Chowdhury, P. H.; He, Q.; Lasitza Male, T.; Brune, W. H.; Rudich, Y.; Pardo, M., Exposure of lung epithelial cells to photochemically aged secondary organic aerosol shows increased toxic effects. *Environmental Science & Technology Letters* **2018**, *5*, (7), 424-430.
149. Gualtieri, M.; Øvrevik, J.; Holme, J. A.; Perrone, M. G.; Bolzacchini, E.; Schwarze, P. E.; Camatini, M., Differences in cytotoxicity versus pro-inflammatory potency of different PM fractions in human epithelial lung cells. *Toxicology in Vitro* **2010**, *24*, (1), 29-39.
150. Crestani, B.; Cornillet, P.; Dehoux, M.; Rolland, C.; Guenounou, M.; Aubier, M., Alveolar type II epithelial cells produce interleukin-6 in vitro and in vivo. Regulation by alveolar macrophage secretory products. *Journal of Clinical Investigation* **1994**, *94*, (2), 731-740.
151. Yang, J.; Hooper, W. C.; Phillips, D. J.; Talkington, D. F., Regulation of proinflammatory cytokines in human lung epithelial cells infected with *mycoplasma pneumoniae*. *Infection and Immunity* **2002**, *70*, (7), 3649-3655.
152. Organization", W. H., WHO indoor air quality guidelines: household fuel combustion. In WHO Document Production Services: Geneva, Switzerland, 2014.
153. Clark, S. E.; Snow, J.; Li, J.; Zola, T. A.; Weiser, J. N., Phosphorylcholine allows for evasion of bactericidal antibody by *Haemophilus influenzae*. *PLoS Pathogens* **2012**, *8*, (3), e1002521.
154. Cundell, D. R.; Gerard, N. P.; Gerard, C.; Idanpaan-Heikkila, I.; Tuomanen, E. I., *Streptococcus pneumoniae* anchor to activated human cells by the receptor for platelet-activating factor. *Nature* **1995**, *377*, (6548), 435-438.

155. Swords, W. E.; Buscher, B. A.; Li, K. V. S.; Preston, A.; Nichols, W. A.; Weiser, J. N.; Gibson, B. W.; Apicella, M. A., Non-typeable *Haemophilus influenzae* adhere to and invade human bronchial epithelial cells via an interaction of lipooligosaccharide with the PAF receptor. *Mol. Microbiol.* **2000**, *37*, (1), 13-27.
156. Smani, Y.; Docobo-Pérez, F.; López-Rojas, R.; Domínguez-Herrera, J.; Ibáñez-Martínez, J.; Pachón, J., Platelet-activating factor receptor initiates contact of *Acinetobacter baumannii* expressing phosphorylcholine with host cells. *The Journal of Biological Chemistry* **2012**, *287*, (32), 26901-26910.
157. Hergott, C. B.; Roche, A. M.; Naidu, N. A.; Mesaros, C.; Blair, I. A.; Weiser, J. N., Bacterial exploitation of phosphorylcholine mimicry suppresses inflammation to promote airway infection. *The Journal of Clinical Investigation* **2015**, *125*, (10), 3878-3890.
158. Aruoja, V.; Dubourguier, H.-C.; Kasemets, K.; Kahru, A., Toxicity of nanoparticles of CuO, ZnO and TiO<sub>2</sub> to microalgae *Pseudokirchneriella subcapitata*. *Science of The Total Environment* **2009**, *407*, (4), 1461-1468.
159. Wang, H.; Huang, Y.; Tan, Z.; Hu, X., Fabrication and characterization of copper nanoparticle thin-films and the electrocatalytic behavior. *Analytica Chimica Acta* **2004**, *526*, (1), 13-17.
160. Kim, J. S.; Adamcakova-Dodd, A.; O'Shaughnessy, P. T.; Grassian, V. H.; Thorne, P. S., Effects of copper nanoparticle exposure on host defense in a murine pulmonary infection model. *Particle and Fibre Toxicology* **2011**, *8*, (1), 29.
161. Ji, H., Lysis of cultured cells for immunoprecipitation. *Cold Spring Harbor Protocols* **2010**, *2010*, (8), pdb.prot5466.
162. Monroy, C. A.; Doorn, J. A.; Roman, D. L., Modification and functional inhibition of regulator of G-protein signaling 4 (RGS4) by 4-hydroxy-2-nonenal. *Chem. Res. Toxicol.* **2013**, *26*, (12), 1832-1839.
163. Yu, Y.; Zhang, X.; Hong, S.; Zhang, M.; Cai, Q.; Zhang, M.; Jiang, W.; Xu, C., The expression of platelet-activating factor receptor modulates the cisplatin sensitivity of ovarian cancer cells: a novel target for combination therapy. *British Journal of Cancer* **2014**, *111*, (3), 515-524.
164. Yuan, D.; Xu, S.; He, P., Enhanced permeability responses to inflammation in streptozotocin-induced diabetic rat venules: Rho-mediated alterations of actin cytoskeleton and VE-cadherin. *American Journal of Physiology: Heart and Circulatory Physiology* **2014**, *307*, (1), H44-H53.
165. Chiavolini, D.; Pozzi, G.; Ricci, S., Animal models of *Streptococcus pneumoniae* disease. *Clinical Microbiology Reviews* **2008**, *21*, (4), 666-685.
166. Grigg, J.; Walters, H.; Sohal, S. S.; Wood-Baker, R.; Reid, D. W.; Xu, C. B.; Edvinsson, L.; Morissette, M. C.; Stampfli, M. R.; Kirwan, M.; Koh, L.; Suri, R.; Mushtaq, N., Cigarette smoke and platelet-activating factor receptor dependent adhesion of *Streptococcus pneumoniae* to lower airway cells. *Thorax* **2012**, *67*, (10), 908-13.
167. Liu, X.; Tang, J.; Wang, L.; Giesy, J. P., Mechanisms of oxidative stress caused by CuO nanoparticles to membranes of the bacterium *Streptomyces coelicolor* M145. *Ecotoxicology and environmental safety* **2018**, *158*, 123-130.
168. Tang, Y.; He, R.; Zhao, J.; Nie, G.; Xu, L.; Xing, B., Oxidative stress-induced toxicity of CuO nanoparticles and related toxicogenomic responses in *Arabidopsis thaliana*. *Environmental pollution (Barking, Essex : 1987)* **2016**, *212*, 605-614.

169. Amiri, M.; Etemadifar, Z.; Daneshkazemi, A.; Nateghi, M., Antimicrobial effect of copper oxide nanoparticles on some oral bacteria and candida species. *Journal of dental biomaterials* **2017**, *4*, (1), 347-352.
170. Hans, M.; Erbe, A.; Mathews, S.; Chen, Y.; Solioz, M.; Mücklich, F., Role of copper oxides in contact killing of bacteria. *Langmuir* **2013**, *29*, (52), 16160-16166.
171. Rogers, D. F., Physiology of Airway Mucus Secretion and Pathophysiology of Hypersecretion. *Respiratory Care* **2007**, *52*, (9), 1134-1149.
172. Ehrenberg, M.; McGrath, J. L., Binding between particles and proteins in extracts: implications for microrheology and toxicity. *Acta Biomaterialia* **2005**, *1*, (3), 305-315.
173. Bangs Laboratories, I., Adsorption to microspheres. In Bangs Laboratories, I., Ed. 2013; Vol. TechNote 204, pp 1-5.
174. Rubasinghege, G.; Kyei, P. K.; Scherer, M. M.; Grassian, V. H., Proton-promoted dissolution of  $\alpha$ -FeOOH nanorods and microrods: Size dependence, anion effects (carbonate and phosphate), aggregation and surface adsorption. *Journal of Colloid and Interface Science* **2012**, *385*, (1), 15-23.
175. Mudunkotuwa, I. A.; Minshid, A. A.; Grassian, V. H., ATR-FTIR spectroscopy as a tool to probe surface adsorption on nanoparticles at the liquid–solid interface in environmentally and biologically relevant media. *Analyst* **2014**, *139*, (5), 870-881.
176. Shibata, C. T.; Lenhoff, A. M., TIRF of salt and surface effects on protein adsorption: I. Equilibrium. *Journal of Colloid and Interface Science* **1992**, *148*, (2), 469-484.
177. Tu, M. H. Lipooligosaccharide-Modified Polymeric Particles for Targeted Pulmonary Drug Delivery. PhD Thesis. University of Iowa, University of Iowa, 2015.
178. Furmanski, P.; Li, Z. P.; Fortuna, M. B.; Swamy, C. V.; Das, M. R., Multiple molecular forms of human lactoferrin. Identification of a class of lactoferrins that possess ribonuclease activity and lack iron-binding capacity. *The Journal of experimental medicine* **1989**, *170*, (2), 415-29.
179. Abraham, G. N.; Podell, D. N.; Wistar, R.; Johnston, S. L.; Welch, E. H., Immunological and structural properties of human monoclonal IgG cryoglobulins. *Clinical and Experimental Immunology* **1979**, *36*, (1), 63-70.
180. Huangfu, X.; Ma, J., Influence of biomacromolecules on the stability of colloidal manganese dioxide. In *Advances in the Environmental Biogeochemistry of Manganese Oxides*, American Chemical Society: 2015; Vol. 1197, pp 185-198.
181. Rahman, A.; Brown, C. W., Effect of pH on the critical micelle concentration of sodium dodecyl sulphate. *Journal of Applied Polymer Science* **1983**, *28*, (4), 1331-1334.
182. Rejman, J.; Oberle, V.; Zuhorn, I. S.; Hoekstra, D., Size-dependent internalization of particles via the pathways of clathrin- and caveolae-mediated endocytosis. *Biochemical Journal* **2004**, *377*, (Pt 1), 159-169.
183. Qing, H.; Yanlin, H.; Fenlin, S.; Zuyi, T., Effects of pH and metal ions on the conformation of bovine serum albumin in aqueous solution An attenuated total reflection (ATR) FTIR spectroscopic study. *Spectrochimica Acta Part A: Molecular and Biomolecular Spectroscopy* **1996**, *52*, (13), 1795-1800.
184. Fine, D. H., Lactoferrin: A roadmap to the borderland between caries and periodontal disease. *Journal of Dental Research* **2015**, *94*, (6), 768-776.
185. The UniProt Consortium, UniProt: the universal protein knowledgebase. *Nucleic Acids Research* **2017**, *45*, (D1), D158-D169.



186. Bastus, N. G.; Comenge, J.; Puentes, V., Kinetically controlled seeded growth synthesis of citrate-stabilized gold nanoparticles of up to 200 nm: size focusing versus Ostwald ripening. *Langmuir* **2011**, *27*, (17), 11098-105.
187. Bates, R. G.; Pinching, G. D., Resolution of the dissociation constants of citric acid at 0 to 50°, and determination of certain related thermodynamic functions. *Journal of the American Chemical Society* **1949**, *71*, (4), 1274-1283.
188. Al-Johani, H.; Abou-Hamad, E.; Jedidi, A.; Widdifield, C. M.; Viger-Gravel, J.; Sangaru, S. S.; Gajan, D.; Anjum, D. H.; Ould-Chikh, S.; Hedhili, M. N.; Gurinov, A.; Kelly, M. J.; El Eter, M.; Cavallo, L.; Emsley, L.; Basset, J.-M., The structure and binding mode of citrate in the stabilization of gold nanoparticles. *Nature Chemistry* **2017**, *9*, 890.
189. Zhang, S.; Sun, Y., A model for the salt effect on adsorption equilibrium of basic protein to dye-ligand affinity adsorbent. *Biotechnology Progress* **2004**, *20*, (1), 207-214.
190. Poleunis, C.; Rubio, C.; Compère, C.; Bertrand, P., Role of salts on the BSA adsorption on stainless steel in aqueous solutions. II. ToF-SIMS spectral and chemical mapping study. *Surface and Interface Analysis* **2002**, *34*, (1), 55-58.
191. Cantarero, L. A.; Butler, J. E.; Osborne, J. W., The adsorptive characteristics of proteins for polystyrene and their significance in solid-phase immunoassays. *Analytical Biochemistry* **1980**, *105*, (1), 375-382.
192. Valle-Delgado, J. J.; Molina-Bolívar, J. A.; Galisteo-González, F.; Gálvez-Ruiz, M. J.; Feiler, A.; Rutland, M., Interactions between bovine serum albumin layers adsorbed on different substrates measured with an atomic force microscope. *Physical Chemistry Chemical Physics* **2004**, *6*, (7), 1482-1486.
193. Gripon, C.; Legrand, L.; Rosenman, I.; Vidal, O.; Robert, M. C.; Boué, F., Lysozyme-lysozyme interactions in under- and super-saturated solutions: a simple relation between the second virial coefficients in H<sub>2</sub>O and D<sub>2</sub>O. *Journal of Crystal Growth* **1997**, *178*, (4), 575-584.
194. Lundqvist, M.; Stigler, J.; Elia, G.; Lynch, I.; Cedervall, T.; Dawson, K. A., Nanoparticle size and surface properties determine the protein corona with possible implications for biological impacts. *Proceedings of the National Academy of Sciences* **2008**.
195. Aillon, K. L.; Xie, Y.; El-Gendy, N.; Berkland, C. J.; Forrest, M. L., Effects of nanomaterial physicochemical properties on in vivo toxicity. *Advanced Drug Delivery Reviews* **2009**, *61*, (6), 457-66.
196. Panicker, G.; Ye, Y.; Wang, D.; Unger, E. R., Characterization of the human cervical mucous proteome. *Clinical Proteomics* **2010**, *6*, (1-2), 18-28.
197. Noël-Georis, I.; Bernard, A.; Falmagne, P.; Wattiez, R., Database of bronchoalveolar lavage fluid proteins. *Journal of Chromatography B* **2002**, *771*, (1-2), 221-236.
198. Ensign, L. M.; Cone, R.; Hanes, J., Nanoparticle-based drug delivery to the vagina: A review. *Journal of Controlled Release* **2014**, *190*, (0), 500-514.
199. Ruge, C. A.; Schaefer, U. F.; Herrmann, J.; Kirch, J.; Cañadas, O.; Echaide, M.; Pérez-Gil, J.; Casals, C.; Müller, R.; Lehr, C.-M., The interplay of lung surfactant proteins and lipids assimilates the macrophage clearance of nanoparticles. *PLoS ONE* **2012**, *7*, (7), e40775.

200. Bangs Laboratories, I., Polymer microspheres. In Bangs Laboratories, I., Ed. 2016; Vol. Tech Note 100, pp 1-2.
201. Claudia, M.; Kristin, Ö.; Jennifer, O.; Eva, R.; Eleonore, F., Comparison of fluorescence-based methods to determine nanoparticle uptake by phagocytes and non-phagocytic cells in vitro. *Toxicology* **2017**, *378*, 25-36.
202. Support, B. L. T., Synthesis of Amine-Functionalized Polystyrene Particles. In Discussion of amine-functionalized polystyrene. ed.; King, B., Ed. 2018.
203. Thermo/Invitrogen Aliphatic Amine Latex Beads, 2% w/v, 0.2 µm: Product Overview. <https://www.thermofisher.com/order/catalog/product/A37356?SID=srch-srp-A37356> (September 02),
204. Wood, B., Certificate of analysis: Aliphatic Amine latex, 2% w/v 0.2 µm. In Molecular Probes Inc.: Molecular Probes Inc., 2012.
205. Chen, S.; Zheng, J.; Li, L.; Jiang, S., Strong resistance of phosphorylcholine self-assembled monolayers to protein adsorption: Insights into nonfouling properties of zwitterionic materials. *Journal of the American Chemical Society* **2005**, *127*, (41), 14473-14478.
206. Edmondson, S.; Nguyen, N. T.; Lewis, A. L.; Armes, S. P., Co-Nonsolvency effects for surface-initiated poly(2-(methacryloyloxy)ethyl phosphorylcholine) brushes in alcohol/water mixtures. *Langmuir* **2010**, *26*, (10), 7216-7226.
207. Ruiz, L.; Hilborn, J. G.; Léonard, D.; Mathieu, H. J., Synthesis, structure and surface dynamics of phosphorylcholine functional biomimicking polymers. *Biomaterials* **1998**, *19*, (11), 987-998.
208. Yuan, J.-J.; Schmid, A.; Armes, S. P.; Lewis, A. L., Facile synthesis of highly biocompatible poly(2-(methacryloyloxy)ethyl phosphorylcholine)-coated gold nanoparticles in aqueous solution. *Langmuir* **2006**, *22*, (26), 11022-11027.
209. Zhou, Y.; Kong, Y.; Kundu, S.; Cirillo, J. D.; Liang, H., Antibacterial activities of gold and silver nanoparticles against Escherichia coli and bacillus Calmette-Guérin. *Journal of Nanobiotechnology* **2012**, *10*, 19-19.
210. Mohamed, M. M.; Fouad, S. A.; Elshoky, H. A.; Mohammed, G. M.; Salaheldin, T. A., Antibacterial effect of gold nanoparticles against Corynebacterium pseudotuberculosis. *International Journal of Veterinary Science and Medicine* **2017**, *5*, (1), 23-29.
211. Wernicki, A.; Puchalski, A.; Urban-Chmiel, R.; Dec, M.; Stęgierska, D.; Dudzic, A.; Wójcik, A., Antimicrobial properties of gold, silver, copper and platinum nanoparticles against selected microorganisms isolated from cases of mastitis in cattle. *Medycyna Weterynaryjna* **2014**, *70*, (9), 564-567.
212. Vimbela, G. V.; Ngo, S. M.; Frazee, C.; Yang, L.; Stout, D. A., Antibacterial properties and toxicity from metallic nanomaterials. *International journal of nanomedicine* **2017**, *12*, 3941-3965.
213. Pensa, E.; Cortés, E.; Corthey, G.; Carro, P.; Vericat, C.; Fonticelli, M. H.; Benítez, G.; Rubert, A. A.; Salvarezza, R. C., The chemistry of the sulfur-gold interface: in search of a unified model. *Accounts of Chemical Research* **2012**, *45*, (8), 1183-1192.
214. Turkevich, J.; Stevenson, P. C.; Hillier, J., A study of the nucleation and growth processes in the synthesis of colloidal gold. *Discussions of the Faraday Society* **1951**, *11*, (0), 55-75.

215. Frens, G., Controlled nucleation for the regulation of the particle size in monodisperse gold suspensions. *Nature* **1973**, *241*, (105), 20.
216. Sigma-Aldrich *Preparing Self-Assembled Monolayers (SAMs) A Step-by-Step Guide for Solution-Based Self-Assembly* 2010, 2010; pp 1-3.
217. Bain, C. D.; Evall, J.; Whitesides, G. M., Formation of monolayers by the coadsorption of thiols on gold: variation in the head group, tail group, and solvent. *Journal of the American Chemical Society* **1989**, *111*, (18), 7155-7164.
218. Laibinis, P. E.; Nuzzo, R. G.; Whitesides, G. M., Structure of monolayers formed by coadsorption of two n-alkanethiols of different chain lengths on gold and its relation to wetting. *The Journal of Physical Chemistry* **1992**, *96*, (12), 5097-5105.
219. Surface and particle modification via the RAFT process: Approach and properties. In *Handbook of RAFT Polymerization*.
220. Lowe, A. B. M., Charles L, RAFT polymerization in homogeneous aqueous media: initiation systems, RAFT agent stability, monomers, and polymer structures. In *Handbook of RAFT Polymerization*, Barner-Kowollik, C., Ed. Wiley: September 16, 2008; pp 235-284.
221. Ferreira, P.; Coelho, J. F. J.; Almeida, J. F.; Gil, M. H., Photocrosslinkable Polymers for Biomedical Applications, Biomedical Engineering - Frontiers and Challenges. *InTech*: 2011.
222. Scaiano, J. C.; Stamplecoskie, K. G.; Hallett-Tapley, G. L., Photochemical Norrish type I reaction as a tool for metal nanoparticle synthesis: importance of proton coupled electron transfer. *Chemical Communications* **2012**, *48*, (40), 4798-4808.
223. Ligon, S. C.; Liska, R.; Stampfl, J.; Gurr, M.; Mülhaupt, R., Polymers for 3D printing and customized additive manufacturing. *Chemical reviews* **2017**, *117*, (15), 10212-10290.
224. Mironi-Harpaz, I.; Wang, D. Y.; Venkatraman, S.; Seliktar, D., Photopolymerization of cell-encapsulating hydrogels: crosslinking efficiency versus cytotoxicity. *Acta Biomaterialia* **2012**, *8*, (5), 1838-48.
225. Jockusch, S.; Landis, M. S.; Freiermuth, B.; Turro, N. J., Photochemistry and photophysics of  $\alpha$ -hydroxy ketones. *Macromolecules* **2001**, *34*, (6), 1619-1626.
226. Efficiency of a photopolymerization reaction. *Photoinitiators for Polymer Synthesis*, p 112.
227. Samanta, D.; McRae, S.; Cooper, B.; Hu, Y.; Emrick, T.; Pratt, J.; Charles, S. A., End-Functionalized phosphorylcholine methacrylates and their use in protein conjugation. *Biomacromolecules* **2008**, *9*, (10), 2891-2897.
228. Hsiue, G.-H.; Lo, C.-L.; Cheng, C.-H.; Lin, C.-P.; Huang, C.-K.; Chen, H.-H., Preparation and characterization of poly(2-methacryloyloxyethyl phosphorylcholine)-block-poly(D,L-lactide) polymer nanoparticles. *Journal of Polymer Science Part A: Polymer Chemistry* **2007**, *45*, (4), 688-698.
229. Thompson, K. L.; Bannister, I.; Armes, S. P.; Lewis, A. L., Preparation of biocompatible sterically stabilized latexes using well-defined poly(2-(methacryloyloxy)ethyl phosphorylcholine) macromonomers. *Langmuir* **2010**, *26*, (7), 4693-4702.
230. Ji, X.; Song, X.; Li, J.; Bai, Y.; Yang, W.; Peng, X., Size control of gold nanocrystals in citrate reduction: the third role of citrate. *Journal of the American Chemical Society* **2007**, *129*, (45), 13939-13948.

231. Kimling, J.; Maier, M.; Okenve, B.; Kotaidis, V.; Ballot, H.; Plech, A., Turkevich method for gold nanoparticle synthesis revisited. *The Journal of Physical Chemistry B* **2006**, *110*, (32), 15700-15707.
232. Kumar, S.; Gandhi, K. S.; Kumar, R., Modeling of formation of gold nanoparticles by citrate method. *Industrial & Engineering Chemistry Research* **2007**, *46*, (10), 3128-3136.
233. Turkevich, J.; Stevenson, P. C.; Hillier, J., The formation of colloidal gold. *The Journal of Physical Chemistry* **1953**, *57*, (7), 670-673.
234. Schulz, F.; Homolka, T.; Bastus, N. G.; Puentes, V.; Weller, H.; Vossmeier, T., Little adjustments significantly improve the Turkevich synthesis of gold nanoparticles. *Langmuir* **2014**, *30*, (35), 10779-84.
235. Verwey, E. J. W.; Overbeek, J. T. G., Theory of the stability of lyophobic colloids. *Elsevier, Amsterdam* **1948**.
236. Farnoud, A. M. Interaction of polymeric particles with surfactant interfaces. PhD Thesis. University of Iowa, University of Iowa, 2013.
237. Aasim, M.; Bibi, N. S.; Vennapusa, R. R.; Fernandez-Lahore, M., Extended DLVO calculations expose the role of the structural nature of the adsorbent beads during chromatography. *Journal of separation science* **2012**, *35*, (9), 1068-78.
238. Vold, M. J., The effect of adsorption on the van der waals interaction of spherical colloidal particles. *Journal of Colloid Science* **1961**, *16*, (1), 1-12.
239. Marčelja, S.; Radić, N., Repulsion of interfaces due to boundary water. *Chemical Physics Letters* **1976**, *42*, (1), 129-130.
240. Salou, M.; Siffert, B.; Jada, A., Study of the stability of bitumen emulsions by application of DLVO theory. *Colloids and Surfaces A: Physicochemical and Engineering Aspects* **1998**, *142*, (1), 9-16.
241. Shi, C.; Yan, B.; Xie, L.; Zhang, L.; Wang, J.; Takahara, A.; Zeng, H., Long-Range hydrophilic attraction between water and polyelectrolyte surfaces in oil. *Angewandte Chemie International Edition* **2016**, *55*, (48), 15017-15021.
242. Klingberg, H.; B. Oddershede, L.; Loeschner, K.; Larsen, E. H.; Loft, S.; Møller, P., Uptake of gold nanoparticles in primary human endothelial cells. *Toxicology Research* **2015**, *4*, (3), 655-666.
243. Voutila, J.; Reebye, V.; Roberts, T. C.; Protopapa, P.; Andrikakou, P.; Blakey, D. C.; Habib, R.; Huber, H.; Saetrom, P.; Rossi, J. J.; Habib, N. A., Development and mechanism of small activating RNA targeting CEBPA, a novel therapeutic in clinical trials for liver cancer. *Molecular therapy : the journal of the American Society of Gene Therapy* **2017**, *25*, (12), 2705-2714.
244. Vaschetto, L. M., RNA activation: A diamond in the rough for genome engineers. *Journal of Cellular Biochemistry* **2018**, *119*, (1), 247-249.
245. Shire, S. J.; Shahrokh, Z.; Liu, J., Challenges in the development of high protein concentration formulations. *Journal of Pharmaceutical Sciences* **2004**, *93*, (6), 1390-1402.
246. Musumeci, T.; Leonardi, A.; Bonaccorso, A.; Pignatello, R.; Puglisi, G., Tangential flow filtration technique: An overview on nanomedicine applications. *Pharmaceutical nanotechnology* **2018**, *6*, (1), 48-60.

247. Lynch, I.; Dawson, K. A.; Linse, S., Detecting cryptic epitopes created by nanoparticles. *Science's STKE : signal transduction knowledge environment* **2006**, 2006, (327), pe14.
248. Keary, C. M., Characterization of METHOCEL cellulose ethers by aqueous SEC with multiple detectors. *Carbohydrate Polymers* **2001**, 45, (3), 293-303.